DEVELOPMENT OF ELECTROCATALYSTS AND MEMBRANES FOR THE COGENERATION OF ELECTRICITY AND VALUABLE CHEMICALS

Nick Daems

Supervisors:
Prof. Dr. Paolo P. Pescarmona
Prof. Dr. Ivo F.J. Vankelecom

Members of the Examination Committee:
Prof. Dr. Dirk Springael (chairman)
Prof. Dr. Philippe Vereecken, KU Leuven
Prof. Dr. Maarten Roeffaers, KU Leuven
Prof. Dr. Jin Won Seo, KU Leuven
Dr. Yolanda Alvarez-Gallego, VITO

Dissertation presented in partial fulfilment of the requirements for the degree of Doctor of Bioscience Engineering

November 2016

Doctoraatsproefschrift nr. 1385 aan de faculteit Bio-ingenieurswetenschappen van de KU Leuven

Dankwoord

Een doctoraat is niet iets dat je op je eentje doet. Gedurende de laatste vier jaar heb ik hulp gekregen van heel wat mensen en ik zou graag van deze kans gebruik maken om ze allemaal te bedanken. Allemaal hebben ze het mede mogelijk gemaakt dit doctoraat tot een goed einde te brengen.

Paolo en Ivo, bedankt om mij te overtuigen en om mij een kans te geven om dit doctoraat te kunnen doen. Bedankt ook om me doorheen deze vier jaren van hard werk te helpen met jullie eindeloze raad, steun en geduld. Jullie waren altijd beschikbaar voor de talrijke en leerrijke discussies en om mij van nieuwe inzichten en opties te voorzien daar waar ik dit nodig had. Zonder jullie bijdragen zou dit werk niet hetzelfde geweest zijn. Daarnaast zou ik ook graag het Agentschap voor Innovatie door Wetenschap en Technologie (IWT) willen bedanken voor de financiële steun in de vorm van een doctoraatsbeurs.

Next, I would also like to thank Xia for her help and guidance during my master thesis, which helped me to convince myself to start a Ph.D. in this field. I am also very grateful for her support during the starting period of my Ph.D. which helped me find my way around and to get the project started smoothly. Een bijzondere bedanking gaat ook uit naar Patrick, Benny en Annick van de VUB en Bart en Tom van de UA voor de mooie samenwerking in dit domein van onderzoek en voor hun hulp om het elektrochemische gedeelte van mijn onderzoek te verduidelijken waar nodig en mijn kennis hieromtrent uit te breiden. Tom en Annick, jullie wil ik ook nog extra bedanken om mij de mogelijkheid te bieden om jullie opstellingen te gebruiken voor het uitvoeren van mijn elektrochemische testen.

Voor hun hulp bij de karakterisatie van mijn materialen zou ik ook graag mijn dank uiten aan Kitty en Isabelle voor de XPS en Raman metingen, aan Maarten voor de SEM/EDX metingen, aan Maria en Cédric voor de TEM metingen, Gina voor de N_2-fysisorptie metingen en Cédric, Eric en Christine voor de XRD en SAXS metingen. Daarnaast wil ik ook Marnix en Bart van de VUB en Stef, Johan, Dirk en Paul bedankt voor hun technische ondersteuning bij het maken en repareren van mijn opstellingen en Annelies, Lieve, Birgit, Inge en Ines voor hun hulp bij het administratieve gedeelte.

Dan wil ik nog Philippe bedanken als assessor voor zijn raad en zijn nuttige bijdragen in de loop van mijn project en zijn kritische kijk op mijn werk dat mij telkens deed nadenken wanneer ik met hem samenzat. También quiero dar las gracias a Yolanda; en primer lugar, por analizar mis catalizadores para la reducción de óxido de nitrógeno, y también por su evaluación exhaustiva de mis datos y por sus ideas para mejorar mi tesina.

Ik zou ook graag nog mijn collega's van het COK en in het bijzonder de collega's van de membraangroep bedanken voor de uitstekende werkomgeving en hun vriendschap. In het bijzonder zou ik hier ook zeker Cédric willen bedanken om de vele TEM en XRD metingen te doen telkens wanneer ik deze nodig had. Speciale dank gaat ook uit naar Roel, Free, Brecht, Jeroen, Michiel en nog zovele meer om mijn middagpauzes aangenaam te maken. Besides this I woud also like to thank my colleagues at the VUB (especially Patrick, Benny, Jon, Lucía, and Xinhua) and at the UA (especially Bart, Tom and Jonas) to accompany me to the ISE conferences and make them more fun to go to.

Zonder de steun van mijn vrienden en familie was ik nooit zo ver geraakt. Dus ook hun zou ik graag bedanken. Mama, papa, Melissa en Eileen, ik weet dat ik het jullie soms niet gemakkelijk heb gemaakt op momenten dat er een deadline in de buurt kwam, dus bedankt om mij steeds te steunen in mijn werk.

Por último, Sara, no se me ocurre olvidarme de ti. Gracias por ayudarme a mejorar mis dibujos y esquemas, sin ti mis artículos no hubieran sido lo mismo. Y más importante aún, gracias por tu paciencia conmigo y por tu apoyo, especialmente en los días de más estrés, como antes de una conferencia o una fecha importante. Sin ti no lo hubiera conseguido.

Nick Daems
17-11-2016

Abstract

A lot of economically valuable chemicals are obtained in industry through oxidation and reduction reactions. While many of these processes are highly exothermic, liberating energy as heat, they generally do not reach high energy efficiencies because most of this liberated energy cannot be recovered efficiently. Fuel cells offer the possibility to produce these chemicals through electrochemical reactions while converting the released energy into electricity, thus offering a clear advantage over the conventional production process. Another drawback of many of the current industrial processes is a rather low selectivity and as a consequence, a lot of raw materials are lost and an extensive downstream processing is required to purify the product stream. By controlling the potential in a fuel cell, the electrochemical approach offers a possibility to drive the reaction to a desired product and thus to increase the selectivity. The ultimate aim of this Ph.D. thesis was to develop suitable electrocatalysts and proton-exchange membranes for this electrochemical cogeneration approach, which would allow the use of fuel cells for a simultaneous and efficient production of electricity and industrially important chemicals. Since the currently applied electrocatalysts (typically based on noble metals) and proton-exchange membranes (Nafion®) are too expensive to allow a wide-spread commercialisation, cheaper alternatives were investigated in this work. As alternative to the noble metals, two types of non-noble metal-containing or even metal-free electrocatalysts were developed: (1) non-noble, abundant transition metals (Cu, Co or Fe) supported on N-doped carbons and (2) metal-free ordered mesoporous carbons doped with nitrogen, boron or phosphorus. Polyvinylidene membranes grafted with sulphonated polystyrene (PVDF-g-PSSA) were selected and investigated as alternative to the commercial Nafion® membrane. The selected electrocatalysts were tested for three target reactions, each producing a relevant product, (1) reduction of oxygen to hydrogen peroxide, (2) reduction of nitric oxide to hydroxylamine and (3) reduction of nitrobenzene to aniline.

In a first phase of the research, ordered mesoporous carbons doped with nitrogen (NOMCs) were studied as electrocatalysts for the oxygen reduction reaction (ORR) because of two main reasons, (1) N-doped carbons have already been reported in the literature as efficient metal-free electrocatalysts for the reduction of oxygen to water in an alkaline environment and (2) ordered mesoporous carbons have the additional advantage of resulting in a high surface area combined with easy accessible active sites compared to microporous materials as graphene. The NOMCs were synthesised according to a novel nanocasting method from two low cost precursors. They were thoroughly characterised and their electrochemical performance was evaluated in a half-cell setup. In alkaline environment, the best NOMC electrocatalyst achieved a much superior kinetic current density in the ORR compared to previously reported N doped carbon materials, and displayed high selectivity for a two-electron reduction process. Furthermore, long-term chronoamperometric tests revealed that the synthesised electrocatalysts also exhibit an excellent long-term stability. The best NOMC was further selected as electrocatalyst to perform a thorough investigation of the influence of the ink composition and the applied amount on the electrocatalytic performance for the oxygen reduction reaction. This study was deemed necessary because the contribution of the electrode composition and preparation on the ORR performance is generally underestimated. It was found that the factor with the largest impact was the catalyst loading: by increasing it an increased selectivity towards water was observed. The results of this study allowed to determine the optimal electrode composition to get the best ORR performance for electricity generation. Using this procedure as standard for the preparation of electrodes would be of enormous help as it would enable a meaningful comparison

between different literature results, which is thus far hindered by the wide variety in electrode compositions that can be found throughout the literature.

In the second phase, N-doped carbons containing different contents of iron were studied as electrocatalysts for the electrochemical production of hydroxylamine in a NO-H_2 fuel cell. They were selected based on an investigation of the state of the art, which made it possible to define the desirable features for the selective reduction of NO to NH_2OH. First of all, the presence of isolated metal centres as active sites is an important prerequisite. Secondly, the isolated metal should have at least two accessible oxidation states, in order to successfully adsorb NO. Finally, the presence of an extended delocalised π-system in the electrocatalyst will grant high electrical conductivity. Moreover, our iron composite electrocatalyst containing N-doped carbon (Fe-PANI-AC) offers several advantages compared to iron phthalocyanine (FePc) supported on carbon materials: (1) the synthesis is straightforward and easily upscalable; (2) it makes use of inexpensive, available chemicals; and (3) several parameters (pyrolysis temperature, metal content and type) can be easily modified in order to optimise the electrochemical performance. The electrocatalysts were evaluated by chronoamperometry in a fuel cell with a 6 or 18% NO in N_2 feed. While at low NO concentration the Fe-PANI-ACs could not outperform the most promising electrocatalyst reported so far, at higher NO concentration the performance of Fe-PANI-ACs was much superior to that of the reference material (33% increase in selectivity to hydroxylamine, 1.5 times more power generated and an almost three times larger hydroxylamine production rate). Furthermore, they displayed an excellent stability under the operating conditions. To speed up the screening of the electrocatalysts an attempt was also made to construct a setup to test the electrochemical performance of four electrocatalysts at the same time with a rotating disk setup for the NO reduction reaction. However, due to recurring problems with the setup this work was eventually stopped.

Next, based on recent reports proving the possibility to use Cu nanoparticles supported on multi-walled carbon nanotubes for the electrochemical reduction of nitrobenzene, non-noble metal-containing (Co, Fe or Cu) supported on N-doped carbons were investigated as electrocatalysts for the reduction of nitrobenzene to aniline. By replacing the undoped support with a N-doped carbon, it was attempted to increase the selectivity towards aniline: on one side, by creating extra active sites in the carbon framework as a consequence of the nitrogen doping; on the other hand, by incorporating N, different metal configurations (metal coordinated to nitrogen, oxides, …) can be expected. The desired selectivity increase was successfully achieved. Indeed, the best performing electrocatalyst (Cu-PANI-AC) exhibited a superior electrocatalytic behaviour compared to the literature electrocatalysts, since a higher selectivity to aniline was achieved and a lower overpotential was necessary to initiate the reduction reaction. Through chronoamperometry experiments a conversion of 54% and a selectivity of 82% towards aniline was achieved in an acidic environment at -0.75 V vs. Fc^+/Fc. Since a possible role in the nitrobenzene reduction of the N-containing sites alone could not be completely excluded, also the metal-free ordered mesoporous carbons doped with B, P or N were tested for this purpose. These specific dopant elements were chosen because their incorporation into the carbon framework is facilitated by their similar size to carbon and, furthermore, because they have either a higher or a lower electronegativity than carbon, which will have an influence on the electronic properties of carbon and thus on its electrocatalytic performance. It was discovered that each element had its own advantage, boron lead to the highest kinetic currents, phosphorus resulted in a lower overpotential and nitrogen resulted in the highest selectivity towards aniline. Overall, the NOMC resulted in the best performance: a value of six for the electron transfer number, a kinetic current density of

-33 mA cm^{-2} and an onset potential of -0.31 V vs. Fc^{+}/Fc, hereby outperforming the Cu-containing electrocatalyst. This clearly demonstrated that a metal is not strictly necessary to reduce nitrobenzene towards aniline.

Finally, the synthesis of PVDF-g-PSSA membranes was optimised by selecting and varying the parameters that were considered having the most impact on the proton conductivity, which is the most crucial factor for their application in fuel cells. Three different steps were optimised, (1) the dehydrofluorination reaction was optimised with respect to the number of double bonds that could be generated, (2) the grafting with polystyrene was enhanced and (3) the sulphonation reaction was maximised to incorporate a higher number of proton-exchange groups. According to the literature, these membranes already offer a competing value for the proton conductivity with respect to the commercial Nafion® membranes, especially at elevated temperatures, but at a lower cost. However, since no attempt was made to optimise the different steps in its synthesis method, we assumed that higher conductivities could be achieved. Indeed, it was discovered that a 4-fold increase in conductivity could be obtained. Compared to Nafion®, a three times higher proton conductivity was achieved and this difference increased to 6-fold at 80°C. This clearly demonstrates the benefits of this study and the applicability of these membranes as potential replacement for Nafion® in fuel cells. Furthermore, since PVDF membranes are known as chemically, physically and thermally stable membranes with possible implementations in various filtration applications, it was investigated if the grafting could enhance the separation properties of these membranes. Besides extending the applicability of these membranes to extremely alkaline pH's, the grafting with sulphonated polystyrene also enhanced the rejection of salts (NaCl to 60% and $MgSO_4$ to 75%).

Samenvatting

Veel economisch waardevolle chemicaliën worden in de industrie bekomen via oxidatie- of reductiereacties. Hoewel veel van deze processen erg exotherm zijn en dus energie vrijgeven in de vorm van warmte, bereiken ze in het algemeen geen hoge energie-efficiëntie omdat de meeste van de vrijgelaten energie niet efficiënt gerecupereerd kan worden. Brandstofcellen bieden de mogelijkheid om deze chemicaliën te produceren via elektrochemische reacties en tegelijkertijd de vrijgelaten energie om te zetten in elektriciteit. Daarom bieden ze dus een duidelijk voordeel ten opzichte van de conventionele processen. Een ander nadeel van veel van de huidige industriële processen is een vrij lage selectiviteit. Bijgevolg gaat een groot deel van de ruwe materialen verloren en is er nood aan een extensieve verdere verwerking om de productstroom op te zuiveren. Via de controle over de potentiaal in een brandstofcel biedt de elektrochemische aanpak een mogelijkheid om de reactie in de richting van de gewenste producten te duwen en als dusdanig de selectiviteit te verhogen. Het uiteindelijke doel van deze doctoraatsthesis was de ontwikkeling van geschikte elektrokatalysatoren en proton-uitwisselingsmembranen voor deze elektrochemische cogeneratie. Dit zou het gebruik van brandstofcellen voor de simultane en efficiënte productie van elektriciteit en industrieel belangrijke chemicaliën toestaan. Vermits de huidige elektrokatalysatoren (typisch gebaseerd op edelmetalen) en proton-uitwisselingsmembranen (Nafion®) te duur zijn om een brede commercialisatie toe te staan, werden goedkopere alternatieven onderzocht in dit werk. Als alternatief voor edelmetalen, werden twee types elektrokatalysatoren ontwikkeld, die ofwel niet-edele metalen bevatten ofwel metaalvrij waren: (1) niet-edele, veelvoorkomende overgangsmetalen (Cu, Co of Fe) afgezet op N-gedopeerde koolstofmaterialen en (2) metaalvrije geordende mesoporeuze koolstofmaterialen gedopeerd met stikstof, boor of fosfor. Polyvinylideenfluoride membranen geënt met gesulfoneerd polystyreen (PVDF-g-PSSA) werden geselecteerd en onderzocht als alternatief voor het commerciële Nafion® membraan. De geselecteerde elektrokatalysatoren werden getest voor drie doelreacties, welke allemaal tot een waardevol product leiden: (1) de reductie van zuurstof tot waterstofperoxide, (2) de reductie van stikstofmonoxide tot hydroxylamine en (3) de reductie van nitrobenzeen tot aniline.

In de eerste fase van het onderzoek werden geordende mesoporeuze koolstofmaterialen gedopeerd met stikstof (NOMCs) onderzocht als elektrokatalysatoren voor de reductie van zuurstof (ORR) omwille van twee redenen, (1) N-gedopeerde koolstofmaterialen werden reeds gerapporteerd in de literatuur als efficiënte metaalvrije elektrokatalysatoren voor de reductie van zuurstof tot water in basisch milieu en (2) geordende mesoporeuze koolstofmaterialen hebben het voordeel dat ze een groot oppervlak combineren met eenvoudig toegankelijke actieve plaatsen in vergelijking met microporeuze materialen zoals grafeen. De NOMCs werden bereid via een nieuwe “nanocasting” methode, vertrekkende vanuit goedkope reagentia. Ze werden grondig gekarakteriseerd en hun elektrochemische prestatie werd onderzocht in een halfcel opstelling. In alkalische omgeving bereikte de beste NOMC elektrokatalysator een superieure kinetische stroomdichtheid voor de ORR in vergelijking met eerder gerapporteerde N-gedopeerde koolstofmaterialen, en gaf de katalysator een hoge selectiviteit voor de twee-elektron reductie. Bovendien toonden chronoamperometrische testen aan dat de gesynthetiseerde elektrokatalysatoren ook beschikken over een uitstekende lange termijn stabiliteit. De beste NOMC werd verder geselecteerd als elektrokatalysator om een grondig onderzoek uit te voeren naar de invloed van de samenstelling van de inkt en de aangebrachte hoeveelheid hiervan op de elektrokatalytische prestaties in de zuurstof reductie reactie. Dit onderzoek werd nodig

geacht omdat de bijdrage van de elektrodesamenstelling en -bereiding op de ORR prestatie in het algemeen onderschat wordt. De factor met de grootste impact bleek de hoeveelheid katalysator te zijn. Meer katalysator leidde tot een verhoogde selectiviteit naar water. De resultaten van deze studie stonden toe de optimale elektrodesamenstelling te bepalen voor een zo goed mogelijke prestatie in de ORR met als doel de opwekking van elektriciteit. Het gebruik van deze procedure als standaard voor de bereiding van elektrodes zou een enorme hulp inhouden omdat het een betekenisvolle vergelijking tussen verschillende resultaten in de literatuur mogelijk zou maken. Tot dusver wordt dit verhinderd door de grote variatie in elektrodesamenstelling die kan gevonden worden doorheen de literatuur.

In een tweede fase werden N-gedopeerde koolstofmaterialen met verschillende hoeveelheid ijzer bestudeerd als elektrokatalysatoren voor de elektrochemische productie van hydroxylamine in een NO-H_2 brandstofcel. Belangrijke eigenschappen voor een selectieve reductie van NO tot NH_2OH, waren de aanwezigheid van geïsoleerde metaalcentra als actieve plaatsen, en minstens twee toegankelijke oxidatietoestanden op de geïsoleerde metalen om goed NO te kunnen adsorberen. Ten slotte zorgde de aanwezigheid van een uitgebreid gedelokaliseerd π-systeem in de elektrokatalysator voor een hoge elektrische geleidbaarheid. De ontwikkelde elektrokatalysator, samengesteld uit ijzer en N-gedopeerde koolstof (Fe-PANI-AC), biedt enkele belangrijke voordelen ten opzichte van ijzerftalocyanine afgezet op koolstof: (1) de synthese is eenvoudig en makkelijk te verschalen; (2) goedkope, eenvoudig beschikbare chemicaliën worden gebruikt, en (3) verschillende parameters (pyrolyse temperatuur, metaalgehalte en type) kunnen gemakkelijk aangepast worden om de elektrochemische prestaties te optimaliseren. De elektrokatalysatoren werden geëvalueerd met chronoamperometrie in een brandstofcel met een voeding van 6 of 18% NO in N_2. Hoewel de Fe-PANI-ACs de beste reeds gepubliceerde elektrokatalysatoren niet konden overtreffen bij lage NO concentratie, waren de prestaties bij hogere NO concentratie veruit superieur ten opzichte van referentiematerialen (stijging van 33% wat betreft selectiviteit naar hydroxylamine, opwekking van 1.5 keer meer energie en een bijna drie keer grotere hydroxylamine productiesnelheid). Bovendien vertoonden ze een uitstekende stabiliteit onder de werkingsomstandigheden. Om het testen van de elektrokatalysatoren te versnellen, werd getracht een opstelling te bouwen die het gelijktijdig testen van vier verschillende elektrokatalysatoren voor de NO reductie reactie zou toestaan. Als gevolg van terugkerende problemen met deze opstelling werd dit werk uiteindelijk echter stopgezet.

Vervolgens werden niet-edele metalen afgezet op N-gedopeerde koolstofmaterialen onderzocht als elektrokatalysatoren voor de reductie van nitrobenzeen tot aniline Dit onderzoek is gebaseerd op recent onderzoek dat de mogelijkheid weergaf om Cu nanopartikels afgezet op koolstofnanobuizen te gebruiken voor de elektrochemische reductie van nitrobenzeen. Door de niet gedopeerde steunlaag te vervangen door een N-gedopeerd koolstofmateriaal, werd getracht de selectiviteit naar aniline te verhogen: enerzijds door de creatie van extra actieve plaatsen in de koolstofstructuur als gevolg van de stikstofincorporatie; anderzijds om door de incorporatie van stikstof andere metaalconfiguraties te creëren (metaal gecoördineerd met stikstof, oxides, …). De best presterende elektrokatalysator (Cu-PANI-AC) vertoonde een superieur elektrokatalytisch gedrag in vergelijking met de elektrokatalysatoren uit de literatuur, vermits een hogere selectiviteit naar aniline bekomen werd en een lagere overpotentiaal nodig was om de reductie reactie te initialiseren. Door middel van chrono-amperometrie experimenten werd een conversie van 54% en een selectiviteit van 82% naar aniline bekomen in een zure omgeving en met een potentiaal van -0.75 V vs. Fc^+/Fc. Vermits een mogelijke rol van de N-

bevattende plaatsen in de nitrobenzeenreductie niet volledig kon uitgesloten worden, werden ook de metaalvrije geordende mesoporeuze koolstofmaterialen gedopeerd met B, P of N onderzocht voor dit doel. Deze specifieke elementen werden gekozen omdat hun incorporatie in de koolstofstructuur vergemakkelijkt wordt door hun grootte die gelijkaardig is aan die van koolstof. Bovendien hebben ze ofwel een hogere of een lagere elektronegativiteit dan koolstof, welke een invloed zal hebben op de elektronische eigenschappen van koolstof en dus op de elektrochemische prestaties. Elk element bleek zijn eigen voordeel te hebben: boor leidde tot de hoogste kinetische stromen, fosfor resulteerde in een lagere overpotentiaal en stikstof gaf de hoogste selectiviteit naar aniline. In het algemeen gaf de NOMC het beste resultaat: een elektrontransfergetal van zes, een kinetische stroomdichtheid van -33 mA cm^{-2} en een startpotentiaal van -0.31 V vs. Fc^{+}/Fc. Dit overtrof dan ook de elektrokatalysator met koper, hetgeen er duidelijk op wijst dat een metaal niet strikt noodzakelijk is om nitrobenzeen te reduceren tot aniline.

Tot slot werd de synthese van PVDF-g-PSSA membranen geoptimaliseerd door parameters te te variëren die de grootste impact zouden hebben op de protongeleidbaarheid, welke de cruciale factor is voor hun toepassing in brandstofcellen. Drie verschillende stappen werden geoptimaliseerd: (1) de dehydrofluorinatiereactie werd geoptimaliseerd met betrekking tot het aantal dubbele bindingen dat gevormd kon worden, (2) het enten met polystyreen werd verbeterd en (3) de sulfoneringsreactie werd gemaximaliseerd om een hoger aantal proton-uitwisselingsgroepen te verwerken in de uiteindelijke structuur. In vergelijking met Nafion® werd een vijf keer hogere protongeleidbaarheid bekomen en dit verschil steeg nog verder bij 80°C (negen keer hoger). Dit bewijst duidelijk de voordelen en de toepasbaarheid van deze membranen als mogelijke vervanger van Nafion® in brandstofcellen. Vermits PVDF-membranen gekend zijn als chemisch, fysisch en thermisch stabiele membranen met mogelijke applicaties in verschillende filtratietoepassingen, werd ook onderzocht of deze membranen konden gebruikt worden bij extreme pH-condities en of de membranen zo dens konden worden gemaakt via de enting dat zelfs zouten konden worden weerhouden. Effectief bleek dat de filtratie-eigenschappen van de membranen onveranderd bleven na een lange termijn behandeling bij hoge (14) en lage (0) pH. Bovendien werd de zoutretentie verhoogd tot 60% voor NaCl en 75% voor $MgSO_4$.

List of abbreviations and symbols

AC	Activated Carbon
AEMFC	Anion-Exchange Membrane Fuel Cell
APS	Ammonium persulphate
ATR-FTIR	Attenuated Total Reflectance-Fourier Transform Infrared spectroscopy
BET	Brunauer–Emmett–Teller
BJH	Barrett-Joyner-Halenda
BOMC	B-doped Ordered Mesoporous Carbon
BPO	Benzoyl peroxide
CCD	Charge-Coupled Device
DFT	Density Functional Theory
DHN	Dihydroxynaphthalene
DMFC	Direct Methanol Fuel Cell
DOE	Department of Energy
EASA	Electrochemically Active Surface Area
EDX	Enery-Dispersive X-ray
EN	Electronegativity
EXAFS	Extended X-ray Absorption Fine Structure
FEP	Fluorinated Ethylene Propylene
FePc	Iron-phthalocyanine
FT-IR	Fourier Transform-Infrared
FWHM	Full Width at Half Maximum height
GC	Gas Chromatography
GDL	Gas Diffusion Layer
HAADF	High-Angle Annular Dark-Field
HOR	Hydrogen Oxidation Reaction
ICP/MS	Inductively Coupled Plasma/Mass Spectrometry
IEC	Ion-Exchange Capacity
IP-PSD	Image Plate Position Detector
K-L	Koutécky-Levich
LSV	Linear Sweep Voltammetry
NF	Nanofiltration
NMP	N-methyl-2-pyrrolidone
NOMC	N-doped Ordered Mesoporous Carbon
NSB	Nitrosobenzene
MEA	Membrane Electrode Assembly
MWCNTS	Multiwalled Carbon Nanotubes
OCP	Open Circuit Potential
OMC	Ordered Mesoporous Carbon
ORR	Oxygen Reduction Reaction
PANI	Polyanline
PEMFC	Proton-Exchange Membrane Fuel cell
PHA	Phenylhydroxylamine
POMC	P-doped Ordered Mesoporous Carbon
PSD	Pore Size Distribution
PSS	Polystyrene sulphonic acid

PTFE	Polytetrafluoroethylene
PVDF	Polyvinylidene fluoride
PVDF-g-PS	Polyvinylidene fluoride grafted with polystyrene
PVDF-g-PSSA	Polyvinylidene fluoride grafted with sulphonated polystyrene
RB	Rose Bengal
RDE	Rotating Disk Electrode
RRDE	Rotating Ring Disk Electrode
SAXS	Small Angle X-ray Scattering
SBA-15	Santa Barbara Amorphous 15
SEM	Scanning Electron Microscopy
SHE	Standard Hydrogen Electrode
STEM	Scanning Transmission Electron Microscope
TEOS	Tetraethyl orthosilicate
TEM	Transmission Electron Microscopy
TGA	Thermogravimetric Analysis
THF	Tetrahydrofuran
ToF-SIMS	Time-of-Flight Secondary Ion Mass Spectrometry
V_{SHE}	Voltage with respect to the Standard Hydrogen Electrode
XANES	X-ray Absorption Near-Edge Spectral
XRD	X-ray Diffraction
XPS	X-ray Photoelectron Spectroscopy

List of Publications and Conference Presentations

Publications

N. Daems,* X. Sheng,* I.F.J. Vankelecom, P.P. Pescarmona, Metal-free doped carbons as electrocatalysts for the oxygen reduction reaction in fuel cells. **J. Mater. Chem. A**, 2 (2014) 4085-4110 (*Equal contribution). Impact factor: 8.3, citations: 164, highly cited.

X. Sheng,* N. Daems,* B. Geboes, M. Kurttepeli, S. Bals, T. Breugelmans, A. Hubin, I.F.J. Vankelecom, P.P. Pescarmona, N-doped ordered mesoporous carbons prepared by a two-step nanocasting strategy as highly active and selective electrocatalysts for the reduction of O_2 to H_2O_2. **Appl. Catal. B: Environ.**, 176-177 (2015) 212-224 (*Equal contribution). Impact factor: 8.3, citations: 14.

N. Daems,* X. Sheng,* Y. Alvarez-Gallego, I.F.J. Vankelecom, P.P. Pescarmona, Iron-containing N-doped carbon electrocatalysts for the cogeneration of hydroxylamine and electricity in a H_2-NO fuel cell. **Green Chem.**, 18 (2016) 1547-1559 (*Equal contribution). Impact factor: 8.5, citations: 2.

International conference presentations

Nick Daems, Xia Sheng, Bart Geboes, Tom Breugelmans, Annick Hubin, Ivo F.J. Vankelecom, Paolo P. Pescarmona, “Doped ordered mesoporous carbons as electrocatalysts for the oxygen reduction reaction”, 65th Annual Meeting of the International Society of Electrochemistry, Lausanne, Switzerland, 1-5 September 2014, (*poster*).

Nick Daems, Bart Geboes, Tom Breugelmans, Ivo F.J. Vankelecom, Paolo P. Pescarmona, “Doped ordered mesoporous carbons for the oxygen reduction reaction”, The Netherlands’ Catalysis and Chemistry Conference 16th edition, Noordwijkerhout, The Netherlands, 2-4 March 2015, (*oral*).

Nick Daems, Patrick Steegstra, Annick Hubin, Ivo F.J. Vankelecom, Paolo P. Pescarmona, “N-doped graphitic carbons as electrocatalysts for the synthesis of hydroxylamine with cogeneration of electricity”, 16th Topical meeting of the International Society of Electrochemistry, Angro dos Reis, Brasil, 22-26 March 2015, (*oral*).

Nick Daems, Xia Sheng, Yolanda Alvarez-Gallego, Ivo F.J. Vankelecom, Paolo P. Pescarmona, “Iron-containing N-doped composite carbon materials for the cogeneration of electricity and hydroxylamine in a NO-H_2 fuel cell”, 3rd International Symposium on Green Chemistry, La Rochelle, France, 3-7 May 2015, (*oral*).

Nick Daems, Jonatan Wouters, Ivo F.J. Vankelecom, Paolo P. Pescarmona, “Non-noble metal-containing doped graphitic carbons as electrocatalysts for the cogeneration of electricity and aniline”, 66th Annual Meeting of the International Society of Electrochemistry, Taipei, Taiwan, 4-9 October 2015, (*oral*).

Nick Daems, Sam Milis, Ivo F.J. Vankelecom, Paolo P. Pescarmona, “Synthesis of membrane electrode assemblies for proton-exchange-membrane fuel cells”, 66th Annual Meeting of the International Society of Electrochemistry, Taipei, Taiwan, 4-9 October 2015, (*poster*).

Nick Daems, Jonatan Wouters, Ivo F.J. Vankelecom, Paolo P. Pescarmona, “Non-noble metals @ nitrogen-doped carbons as electrocatalysts for the cogeneration of electricity and aniline”, The Netherlands’ Catalysis and Chemistry Conference 17th edition, Noordwijkerhout, The Netherlands, 7-9 March 2016, (*oral*).

Nick Daems, Ivo F.J. Vankelecom, Paolo P. Pescarmona, “Doped ordered mesoporous carbons as electrocatalysts for the cogeneration of electricity and aniline”, 67th Annual Meeting of the International Society of Electrochemistry, The Hague, The Netherlands, 22-26 August 2016, (*oral*).

Table of contents

Chapter 1

Introduction and scope of the thesis

This chapter is partially based on the review paper entitled "Metal-free doped carbons as electrocatalysts for the oxygen reduction reaction in fuel cells" by Nick Daems, Xia Sheng,* Ivo F.J. Vankelecom, and Paolo P. Pescarmona, published in the Journal of Materials Chemistry A, 2014, **2**, 4085-4110 DOI: 10.1039/C3TA14043A (* equal contribution).*

Author contribution

Structure of the review defined and developed by N. Daems, X. Sheng and P. P. Pescarmona. Manuscript written by N. Daems. Valuable additions and suggestions were made by X. Sheng. The editing of the article was done by P. P. Pescarmona and I. F. J. Vankelecom.

1.1 Fuel cells

In the course of history, human beings have always depended on nature for their energy. In the beginning nature's energy was only used to give us warmth or to prepare food (camp fires). Later on nature's energy was also applied to make our work easier (e.g. windmills or watermills to produce flour). However, it is only since 1750 and the industrial revolution that nature's energy in the form of non-renewable resources, like natural gas, coal and petroleum, has been used on a large scale. In 2012 the energy consumption was estimated at 579 10^{18} J a year and this figure is expected to rise up until 860 10^{18} J a year by 2040, mainly thanks to countries as China and India. 78% of this energy will still be delivered through petroleum, natural gas and coal (Energy Information Administration (E.I.A.), 2016). However, there are two main problems linked with this continued dependency on fossil fuels, (1) their stock is limited and since it is expected that the maximum oil production peak will be reached in the near future, oil production will no longer be able to follow its demand thanks to the growing population and industrialisation and (2) their combustion is paired with emission of greenhouse gases as CO_2, which can have a disastrous impact on the environment (global warming, tsunamis, etc.). The best strategy to avoid these problems is to turn to renewable sources for our energy supply and in this context fuel cells have been attracting a lot of attention worldwide. A fuel cell is a device that can convert chemical energy directly into electricity without combustion processes and with high energy conversion efficiencies. They are based on an exergonic redox reaction, which is carried out as two half-reactions, occurring in two separate compartments, an anodic and a cathodic compartment separated by an electrolyte. Several fuel cell configurations exist and they are generally classified based on the electrolyte and the used fuel. Polymer electrolyte fuel cells (proton-exchange-membrane (PEM) or anion-exchange membrane (AEM) fuel cells and direct methanol fuel cells (DMFC)) are the most widely investigated type of fuel cells because they offer the possibility to work at lower operation temperature and have longer life spans compared to for example high temperature solid-oxide fuel cells.[1,2]

The major components of a fuel cell are the electrodes and the membrane. Both the anode and the cathode generally consist of two layers: the active layer, composed of the electrocatalyst and a polymer binder, and the gas diffusion layer (GDL). The polymer binder is necessary to provide a good interaction between the membrane and the active layer. The purpose of the GDL is three-fold: it acts as a support for the active layer, conducts electrons away from the anode and towards the cathode, and it provides a diffusion path for reagents to reach the active site and for reaction products to be removed. Therefore, the GDL has to be porous, conductive and hydrophobic. Commonly applied GDL materials are porous carbon cloths.[3,4] Electricity is generated in a fuel cell as a consequence of the free electrons, which are generated at the anode and move towards the cathode over an external circuit. The membrane is a necessary component of the fuel cell since it avoids direct contact between the reagents in order to provide a current. Additionally, electrolytes (either a proton or an anion-exchange membrane) allow protons or hydroxyl ions to pass from the half-cell where they are generated to the other half-cell where they are consumed. The membrane thus has to be charged (either positively or negatively) to allow ion transport, be dense enough to avoid reagent cross-over and be insulating to force electron transport across the external circuit and generate a current. Electrocatalysts are used at both electrodes to increase the reaction rates.

In the most common fuel cell configuration or the PEMFC, hydrogen is oxidised at the anode while at the cathode oxygen (either pure or in air) is reduced according to the following equations and the respective standard reduction potentials (at 298 K and at 1 bar).[5]

1) Anode:
   a. Acidic: $2H_2 \longrightarrow 4H^+ + 4e^-$ $E° = 0.0\ V_{SHE}$
   b. Alkaline: $2H_2 + 4OH^- \longrightarrow 4H_2O + 4e^-$ $E° = -0.83\ V_{SHE}$
2) Cathode:
   a. Acidic: $O_2 + 4H^+ + 4e^- \longrightarrow 2H_2O$ $E° = 1.23\ V_{SHE}$
   b. Alkaline: $O_2 + 2H_2O + 4e^- \longrightarrow 4OH^-$ $E° = 0.40\ V_{SHE}$

When the hydrogen is supplied from renewable energy sources, fuel cells are a promising source of renewable energy, which could seriously alleviate our future dependency on fossil fuels for energy liberation. Furthermore, the environmental problems related with the use of fossil fuels (CO_2 emission) can be avoided since the only byproduct of this process is water, making it an environmentally clean process. In the conventional and most commonly applied fuel cells, Pt supported on activated carbon (Pt/C) is generally used as electrocatalyst, both at the anodic and at the cathodic side, and Nafion® is used as the electrolyte.

Even though a lot of effort has been invested in the last decades to enhance the fuel cell efficiency such that it can successfully be implemented in practice, two major problems remain which impede widespread commercialisation: cost and lifetime.[2,6] The main factors contributing to the fuel cell cost and lifetime are the membrane (Nafion®) and the electrocatalysts (Pt). Both Pt and Nafion® contribute significantly to the cost. Pt is a rare, noble metal, and the ever-increasing demand renders it an expensive resource. Nafion® is a fluoropolymer, with a difficult and rather expensive synthesis process. On the other hand, the fuel cell lifetime is governed by several factors, including membrane degradation, platinum deactivation (by dissolution and agglomeration or by poisoning) and support corrosion. The timescale of these processes is strongly influenced by the operation conditions of the fuel cell. The important parameters include amongst other the impurities in the feed (e.g. CO traces in the H_2 feed can block active Pt sites), operating voltage and current (e.g. some voltages induce hydrogen peroxide generation which can degrade the membrane, others promote carbon corrosion and yet others result in alloy leaching into the membrane, decreasing its conductivity), temperature and its operation mode (continuous or intermittent).[1,2,6,7]

Solutions to the above-mentioned problems and current ongoing investigations to improve or replace the currently applied electrocatalysts and membranes will be discussed in paragraph 1.2 and 1.3 for the electrocatalysts and the membranes, respectively.

1.1.1 Cogeneration of electricity and valuable chemicals

Besides for being used as a renewable energy source, fuel cells also allow the possibility of cogeneration, where industrially relevant chemicals and electricity can be generated simultaneously in a fuel cell setup. In the chemical industry, many products are obtained through thermodynamically favourable reactions. For such exergonic reactions ($\Delta G° < 0$), the process is accompanied by the liberation of energy, generally in the form of heat. This energy is often not utilised efficiently and it can sometimes even be problematic to remove it safely. An interesting strategy to convert this waste of energy into useful energy and at the same time generate valuable chemicals is the electrochemical cogeneration process. All reagents that can be oxidised or reduced in an electrochemical way qualify for being produced in an electrochemical cell. If the selected redox process is exergonic, the synthesis of the target chemical will cogenerate electricity in a similar manner to what occurs in a

standard H_2/O_2 fuel cell, but with the advantage that valuable chemicals will be obtained instead of water. An additional advantage of this approach is its potential to allow a more local chemical production, in direct vicinity of its consumption point, which would significantly reduce the costs.[8] This Ph.D. project thus investigates a sustainable and economically attractive electrochemical alternative to industrially important chemical processes.

Throughout the course of this Ph.D. project, three alternative reduction reactions were investigated: the reduction of (1) oxygen to hydrogen peroxide, (2) nitrogen monoxide to hydroxylamine, and (3) nitrobenzene to aniline.

Hydrogen peroxide production

Whereas a high selectivity toward water is required if the sole interest of using fuel cells is electricity generation, a highly selective 2-electron reduction to hydrogen peroxide could also be attractive from the cogeneration point of view. H_2O_2 is one of the most important green chemical oxidants with a broad range of applications.[9,10] The hydrogen peroxide production is expected to reach 5.7 M tons per year by 2020 and its main consumption point is in the paper and chemical industry.[8] Currently, H_2O_2 is mainly synthesised from H_2 and O_2 through the anthraquinone process, which suffers from several disadvantages as a high cost, suitable only for large scale applications and not environmentally friendly.[8,11,12] It is therefore highly desirable to develop a more environmentally friendly and economically more attractive process. The electrochemical approach combines both aspects. It performs the reduction of O_2 to hydrogen peroxide in the absence of solvents while generating electricity. Furthermore, compared to the direct synthesis of H_2O_2 from a direct contact between hydrogen and oxygen, it avoids the danger of explosion by performing the hydrogen oxidation and the oxygen reduction in separate cells.[8,10–12] The overall reactions in acidic environment are:

1) Anode:

$$H_2 \rightarrow 2H^+ + 2e^- \qquad E^0 = 0\ V_{SHE}$$

2) Cathode:

$$O_2 + 2H^+ + 2e^- \rightarrow H_2O_2 \qquad E^0 = 0.70\ V_{SHE}$$

Hydroxylamine production

The second target chemical, hydroxylamine, can also be obtained by the cogeneration approach by replacing the oxygen reduction reaction with the reduction of nitrogen monoxide (NO). In industry, hydroxylamine is widely applied in the synthesis of caprolactam, the main application of which is in the production of Nylon-6.[13–17] Worldwide approximately 1 M ton per year of hydroxylamine is produced, through the hydrogenation of nitric oxide or nitric acid, with Pt/C as catalyst.[13–18] Substituting the current technology with the cogeneration approach would have the advantage of generating electricity, and could also allow a cost reduction if different and cheaper catalysts than the currently applied Pt-based catalysts are employed. The possibility to use a H_2-NO fuel cell for the cogeneration of hydroxylamine and electricity was first investigated by Langer *et al.*[19] in '91 and has hardly been further developed since then.[13–15,17] The overall reactions in acidic environment are:

3) Anode:

$$1.5H_2 \rightarrow 3H^+ + 3e^- \qquad E^0 = 0\ V_{SHE}$$

4) Cathode:

$$NO + 3H^+ + 3e^- \rightarrow NH_2OH \qquad E^0 = 0.38\ V_{SHE}$$

Aniline production

A final target product of this Ph.D. project is aniline, which is an industrially relevant chemical, particularly, as a reagent for the synthesis of polyurethane.[20,21] In 2010, the worldwide aniline production amounted to 2.3 M tons, of which 66% is used in the polyurethane production.[18] Nowadays, aniline is most commonly produced through the hydrogenation of nitrobenzene over Raney Nickel catalysts. However, in order to achieve sufficient conversion and aniline selectivity, slightly elevated temperatures (35-50°C), high H_2 pressures and long reaction times are required.[20,21] These problems could possibly be avoided with the electrochemical approach since it offers an additional possibility to control the reaction rate and the selectivity, namely through the electrical potential, which does not take away the importance of finding better catalysts but merely allows extra control. Haber *et al.* first investigated the electrochemical nitrobenzene reduction and it has been further developed since then.[22–25] The overall reactions in acidic environment are:

5) Anode:

$$3H_2 \rightarrow 6H^+ + 6e^- \qquad E^0 = 0\ V_{SHE}$$

6) Cathode:

$$PhNO_2 + 6H^+ + 6e^- \rightarrow PhNH_2 + 2H_2O \qquad E^0 = 0.82\ V_{SHE}$$

For all these reactions, the design of a suitable electrocatalyst is essential for optimising conversion rate and, thus the generation of electricity, but also to control and optimise the selectivity towards the target product, as various side-products are possible in each case. The importance of an electrocatalyst in a fuel cell can be understood when considering that the amount of electricity that can be produced with a fuel cell does not depend only on the potential difference between the two half-cells, but also on the activation energy (or overpotential) that has to be overcome for each half-reaction to occur at the electrodes. The higher this overpotential is, the lower the efficiency of the fuel cell for producing electricity. A good electrocatalyst is thus a material that allows decreasing the overpotential of a half-reaction. The electrocatalyst can also help improving the selectivity towards a target product, by favouring a specific reaction pathway. Importantly, an electrocatalyst should also be highly stable under the operating conditions. A study into the currently applied fuel cell electrocatalysts and their alternatives will be performed as part of section 1.2.

Another essential component of the fuel cell is the membrane. As was mentioned above, it allows protons or hydroxyl anions to pass from one half-cell to the other while avoiding reagents to interact directly with each other or electrons to pass across the membrane, as this would lead to a reduction in the electricity generation. The currently applied membranes and their alternatives will be highlighted in section 1.3.

1.2 Electrocatalysts

While the cogeneration of electricity and industrially valuable chemicals, like hydroxylamine, aniline and hydrogen peroxide, is interesting from an economical point of view, research in this area is still rather limited. A much more studied fuel cell is the PEMFC, which, as mentioned above, consists of two half-cells separated by a positively charged proton-exchange membrane. At the anode hydrogen is oxidised to protons, which travel across the membrane to the cathode where they reduce oxygen ideally to water. Since the oxygen reduction reaction (ORR) is the rate limiting step (higher overpotential than the hydrogen oxidation reaction (HOR)), the research on cost-effective electrocatalysts has mainly been focused on the cathode catalysts.[26–28] The ORR can generally follow two pathways. The first is a four-electron reduction of oxygen directly to water (1.1) and the second is the less

efficient two-step two-electron reduction with hydrogen peroxide as an intermediate ((1.2) and (1.3)).

$$O_2 + 4H^+ + 4e^- \longrightarrow 2H_2O \quad (1.1)$$

$$O_2 + 2H^+ + 2e^- \longrightarrow H_2O_2 \quad (1.2)$$

$$H_2O_2 + 2H^+ + 2e^- \longrightarrow 2H_2O \quad (1.3)$$

In this case, electrocatalysts are used to facilitate the four-electron reduction pathway in order to maximise the electricity generated by the fuel cell.[29] Furthermore, the production of hydrogen peroxide can lead to corrosion of the fuel cell components.[30] Currently, three approaches are being pursued in order to reduce the electrocatalyst costs for the ORR: (1) reduction of the Pt-loading, (2) development of non-noble metal catalysts and (3) synthesis of metal-free catalysts.

1.2.1 Pt-based electrocatalysts

Currently, Pt is still the most commonly applied electrocatalyst for PEMFCs, because it is the most active material to date both in the ORR and in the HOR. For the ORR, this is evidenced by the so-called volcano plot, which plots the activity as a function of the binding energy between oxygen and metal specie (see figure 1.1).

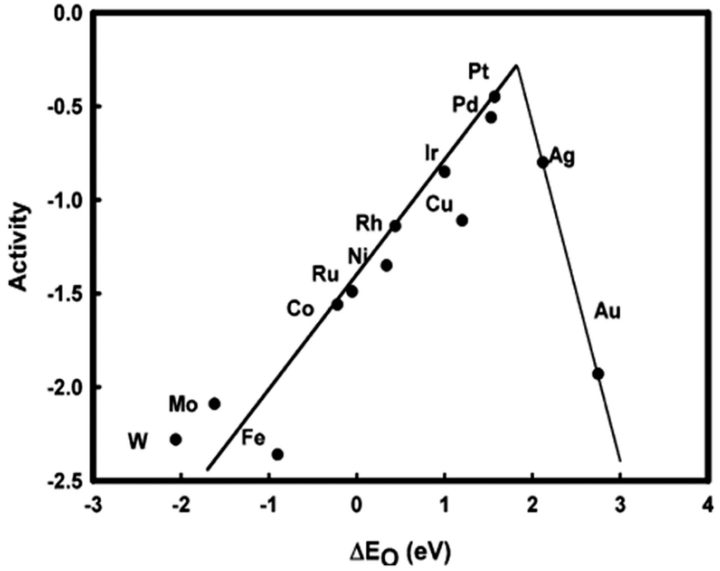

Figure 1.1: ORR activity plotted as a function of the oxygen binding energy according to Norskøv *et al.*.[31]

According to this figure, the binding energy between metal and oxygen can neither be too high nor too low. If oxygen is bonded too strongly (left-hand side), the reaction rate is limited by desorption of O and OH species. On the other hand, when the oxygen-metal bond is too weak (right-hand side), the dissociation of O_2 or the transfer of proton and electrons to adsorbed O_2, is the rate-limiting step. Ideally, an electrocatalyst should be found that binds oxygen less strongly than Pt by approximately 0.2 eV.[26,32]

The ORR mechanism on Pt electrodes has been extensively studied in the past. Two possible mechanisms have been proposed: (1) the dissociative mechanism (1.4) and the associative mechanism (1.5). In the former, the O-O bond is broken upon adsorption, while in the latter, oxygen is adsorbed in its molecular form. As a consequence, the associative mechanism can give rise to the production of hydrogen peroxide if the desorption process is energetically favorable compared to the further reduction to water.[31,33]

The dissociative mechanism at low current densities (1.4):

$$1/2O_2 + Pt \leftrightarrow Pt\text{-}O_{ads}$$

$$Pt\text{-}O_{ads} + H^+ + e^- \leftrightarrow Pt\text{-}OH_{ads}$$

$Pt\text{-}OH_{ads} + H^+ + e^- \rightarrow H_2O + Pt$

The associative mechanism at high current densities (1.5):

$O_2 + Pt \leftrightarrow Pt\text{-}O_{2,ads}$

$Pt\text{-}O_{2,ads} + H^+ + e^- \leftrightarrow Pt\text{-}HO_{2,ads}$

$Pt\text{-}HO_{2,ads} + H^+ + e^- \rightarrow H_2O + Pt\text{-}O_{ads}$

$Pt\text{-}O_{ads} + H^+ + e^- \leftrightarrow Pt\text{-}OH_{ads}$

$Pt\text{-}OH_{ads} + H^+ + e^- \rightarrow H_2O + Pt$

However, since the Pt-utilisation target for 2015, was set by the Department of Energy (DOE) at 0.2 g of Pt per kW at 55% efficiency for PEMFC stacks for transportation, the use of bulk platinum as electrocatalyst is not sustainable. Indeed, if an annual production of 100 million PEMFC cars is assumed, the Pt demand would rise up to 1000 tons per year which can clearly not be met by the global Pt production of about 200 tons per year. Furthermore, this would most likely lead to a significant increase of the Pt cost, which would make the Pt catalyst alone responsible for up to 56% of the PEMFC cost. Therefore, it is important to reduce the costs related to the electrocatalysts.[34] The Pt loading can be reduced by utilising a support on which small Pt nanoparticles are deposited with a high dispersion, by alloying Pt with other metals, or by developing novel Pt structures.[1,32,35–37] To further enhance the electrocatalytic activity of Pt nanoparticles the synthesis approach is designed in such a way that only the high index facets of Pt, possessing a high density of under-coordinated atoms, steps, edges, and kinks, are exposed, generating more active reduction sites.[26,32,38,39] However, a major disadvantage of the high index facets is that they are less stable under fuel cell conditions, since defects are active sites for crystal growth and agglomeration. Alloying Pt with transition metals is a solution for this problem. Adding a small amount of alloy metals improves the activity and the stability of the catalysts while at the same time also reducing the Pt usage.[39] The important factors that influence the ORR activity of the alloys are their composition (surface uniformity, alloy metal dispersion), ordering and morphology (shape). The origin of activity enhancement of Pt alloys lays in the modification of the electronic structure of the Pt surface. This modification results in in a better chemisorption of oxygen (weaker metal-oxygen bond) than when compared to pure Pt, and is caused by a ligand effect (electronic charge-transfer between alloy and metal) and a geometric effect (lattice strain).[26,28] Both result in a shift in energy levels of the Pt d-states, which has a major influence on the bond strengths between metal and intermediates.[32,40] A volcano-type relation was also established for the Pt alloy electrocatalysts and it was discovered that the Pt_3Co alloy had an optimal metal-oxygen bond strength and therefore, exhibited the highest ORR activity.[41]

A major disadvantage of Pt alloy nanoparticles, is the susceptibility towards leaching out of the alloy metals in an acidic environment, making them intrinsically instable in the fuel cell environment. This problem could be solved with the so-called core-shell structured electrocatalysts, consisting of a non-noble metal core, which is covered with a thin Pt shell. This Pt shell inhibits the dissolution of alloy metals and increases the stability. Furthermore, this technique also further decreases the electrocatalyst cost since only the outmost layer of the nanoparticle consists of the noble Pt metal further reducing the Pt usage.[28,42,43]

However, the Pt-based electrocatalysts still suffer from the intrinsic high cost of Pt and the deactivation problems. Thus, in order to make the commercialisation of fuel cells possible in the long term, research should be focused on completely replacing Pt.

1.2.2 Non-noble metal-based electrocatalysts

Many of the initial attempts to replace Pt for the ORR focused on the development of electrocatalysts based on non-noble metals, including transition metal complexes, conductive polymer-based electrocatalysts, transition metal chalcogenides, metal oxides, carbides or nitrides and enzymatic compounds.[26,44] In terms of ORR activity, the most promising non-precious metal-based electrocatalysts are transition metals supported on N-doped carbons (M-N_x/C, with M = Co, Fe, Ni, etc and x = 2 or 4).[26,28,34,44–46] In 1965, Jasinski discovered that cobalt phthalocyanine was an active ORR electrocatalyst in alkaline environment.[47] In the next few years, it was discovered that a variety of metal-N_4 complexes either as such or supported were active both in acidic and alkaline environment. Furthermore, these electrocatalysts also exhibit a higher tolerance to poisoning compared to commercial Pt catalysts.[35,48–55]

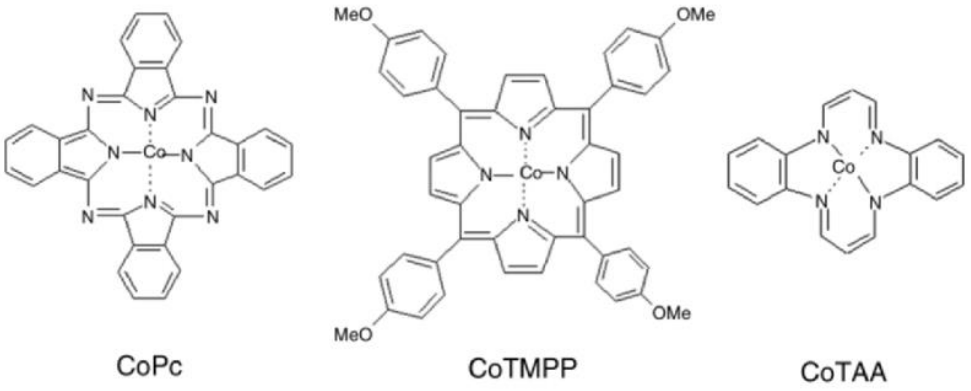

Figure 1.2: Structure of some active metal-macrocycles; from left to right: cobalt phthalocyanine, cobalt tetramethoxy phenyl porphyrin and cobalt dibenzo-tetra-aza-annulen.

However, these macrocyclic-based electrocatalysts have few disadvantages: a rather low activity compared to Pt/C especially in acidic environment, a low stability of the ligand, especially in the presence of H_2O_2, and the rather high cost of some metal complexes. A heat treatment (400 to 1000°C) under N_2 (pyrolysis) of the supported metal complexes can help improving their stability (by generating a graphitic carbon structure) and their selectivity towards water (by increasing the number of ORR active sites).[56–62] The activity and selectivity enhancement that was observed after a thermal treatment of this type of electrocatalysts could only be explained by changes in the atomic configuration of the macrocycles.[44,46] This makes it difficult to predict the structure of the ORR active site and several different and opposing configurations have been proposed. The conflicting configurations obtained by different groups are most likely a consequence of the differences in the synthesis conditions (i.e. pyrolysis temperature and duration, transition metal, macrocycle, carbon support), making it difficult to compare various electrocatalysts.[45,61] van Veen *et al.* proposed that the M-N_4 moieties serve as the active sites and thus have to be conserved in the final material. This can be achieved by applying moderate pyrolysis temperatures (500-600°C).[59] Yeager *et al.* on the other hand, believed that the active sites are formed after a contact between the decomposed macrocycle with the electrolyte, generating M-N_x-C-type active sites.[60,63] Finally, Wiesener proposed that the metal ions do not form part of the final active site but that they merely facilitate the formation of active sites by catalysing the decomposition of the macrocycles to yield nitrogen-doped graphitic carbons.[62]

As a consequence of the different active sites, it was postulated that these expensive macrocycles could be replaced with a combination of a separate nitrogen- and metal-

containing precursor and a high surface area carbon material. The first example of an ORR active electrocatalyst based on this idea was prepared from polyacrylonitrile, Fe or Co salts and Vulcan XC-72.[64]

For the above-mentioned non-noble metal-containing electrocatalyst, it is thus clear that there are four important factors contributing to their catalytic ORR activity: (1) the nitrogen source, (2) the transition metal species, source and content, (3) the carbon support and (4) the pyrolysis temperature and duration.[65]

The exact composition of the active site, however, remains a matter of debate up until now and several different structures have been proposed so far.[26,28,34,44,45] Through time-of-flight secondary ion mass spectrometry (ToF-SIMS), Dodelet *et al.* initially proposed active sites in the form of M-$N_xC_y^+$, which are composed of a combination between a transition metal ion, nitrogen functional groups and a carbon support.[54] In the case of Fe, two distinct active sites were observed, FeN_2/C and FeN_4/C (Figure 1.3 (a) and (b), respectively). In a more recent study, their active site configuration was revised to the FeN_{2+2}/C configuration, which bridges two adjacent graphitic planes primarily across micropores (Figure 1.3 (c)).[54,66,67] These results were later confirmed by additional ^{57}Fe Mösbauer, X-ray absorption near-edge spectral (XANES) and extended X-ray absorption fine structure analysis (EXAFS)[68–71] and by theoretical density functional theory (DFT) calculations.[72–74].

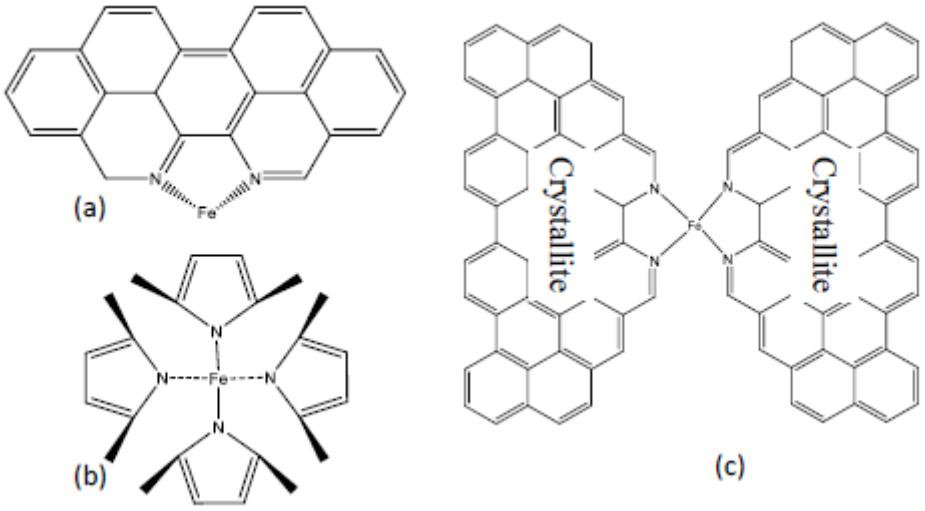

Figure 1.3: FeN_2/C (a) and FeN_4/C (b) active sites and (c) revised FeN_{2+2}/C active sites structure present in micropores (adapted from Ref. 64).

ToF-SIMS performed on Co-based electrocatalysts revealed that only CoN_4/C species could be observed, while CoN_2/C did not appear. Furthermore, no clear correlation between a specific Co-containing site and the ORR activity was established. Instead, all sites containing cobalt, irrespective of the configuration, contributed equally to the ORR activity. This is in clear contrast with the Fe-based materials where a dominant active site could be determined.[54,75]

Furthermore, it was generally observed that M-N_X-C electrocatalysts with cobalt as metal generated more hydrogen peroxide than those with iron and this could be explained by the molecular orbital theory. The d_{z^2} orbital of the metal ion will bind the oxygen molecule thanks to its suitable symmetry for overlap. Back-bonding will occur between the empty or partially filled π anti-boding orbitals of oxygen and the filled d_{xz} or d_{yz} orbitals of the metal, which have approximately the same energy. The d_{z^2} orbitals of Fe are unoccupied while that of Co contains one electron. The oxygen reduction will occur faster through partial electron transfer

from d_{xz} or d_{yz} to oxygen and this back-bonding occurs faster if the d_{xz} and d_{yz} orbitals are filled and if the d_{z^2} orbital is empty. Since the transfer of electrons from oxygen to the d_{z^2} orbital from the metal lowers the energy of the π anti-bonding orbitals and raises the energy of the d_{xz} and d_{yz} orbitals, a better overlap between these orbitals for back-bonding is achieved. Thus, oxygen reduction will be faster and will proceed directly to water through a four electron pathway in the case of iron and less so in the case of cobalt as less electrons can be transferred to the d_{z^2} orbital for the latter, resulting in a worse overlap.[76]

Finally, the nature of the carbon support present during the synthesis of these M-N_x/C electrocatalysts has a significant influence on the ORR activity and stability of the resulting material. The most important parameters influencing the electrocatalytic behaviour are the N content and the micropore content.[34,44,77]

1.2.3 "Metal-free" doped carbon materials

Doped carbons are carbon-based materials containing significant amounts of other elements besides carbon, hydrogen and oxygen, such as nitrogen, boron or phosphorus and other less common elements as selenium, sulphur or halogens. The use of carbon-based materials has several advantages including a tunable surface chemistry, a high conductivity, a good stability under the applied conditions and a relatively low cost.[2,78] Besides their promising ORR activity, doped carbon materials also exhibit a higher stability and poisoning resistance than Pt/C.[79]

Carbon materials can be chemically doped by two approaches: (1) substitutional doping, which leads to a substitution of carbon atoms in sp^2 configuration by heteroatoms, and (2) functionalisation with a gas, organic molecules or metals on the carbon surface.[80] The effect of the doping on the properties of the carbon materials is mainly associated with three features of the dopant element: (1) the number of electrons in the external shell, (2) the electronegativity and (3) the size. The most common dopant element is nitrogen since it has a similar size to carbon and one electron more than carbon in the external shell. Other dopant elements, e.g. boron, phosphorus, selenium, sulphur and various halogens have also been reported but they have not been studied as extensively as nitrogen doping. A schematic representation of a N-doped carbon is given in Fig. 1. Nitrogen can generally be found in four bonding configurations: pyridinic N, pyrrolic N, graphitic N and oxidised pyridinic N. Pyridinic N (N1) and pyrrolic N (N2) atoms are located at edge or defect sites. They do not increase the number of electrons in the delocalised π-system. Graphitic N (N3-N4) atoms substitute carbon atoms within the graphitic structure. Therefore, they have the same configuration as graphitic carbon atoms but they introduce extra electrons in the delocalised π-system. N3 is located at the edge while N4 is found in the bulk of the graphitic carbon framework. Pyridinic N can also be present in its oxidised form (N5) (Figure 1.4).[81,82]

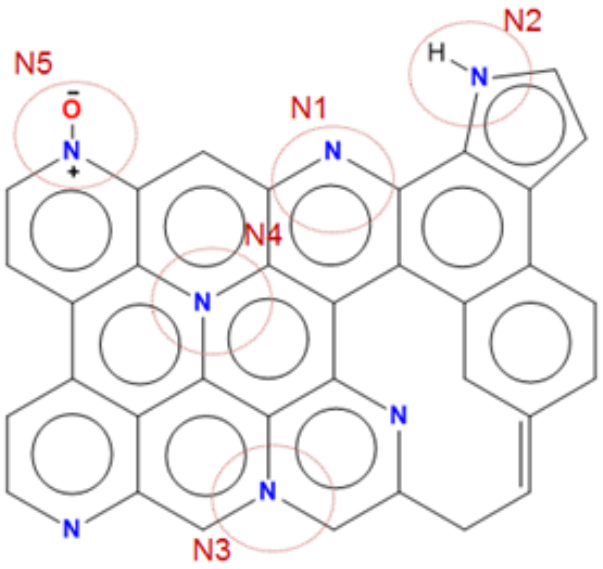

Figure 1.4: Representation of N-doped carbon material.

It has been observed that incorporation of nitrogen enhances the electron-donor or basic capacities of the carbon material, thereby enhancing its ORR activity.[1,83–85] The enhanced basicity can be related to the lone electron pair of pyridinic N and to the presence of more electrons in the delocalised π-orbitals of the carbon framework due to the higher number of electrons of nitrogen atoms. π-electrons can perform a nucleophilic attack on oxygen and the more π-electrons the system contains, the higher the oxygen reduction activity.[1] The exact nature of the active sites in N-doped carbons is still a matter of debate.[26,45] Some researchers assume that pyridinic N is involved in the ORR activity[86–90], while others propose graphitic N.[91,92] Another study suggests that both sites might be equally important for the ORR since it was proposed that graphitic and pyridnic N sites interconvert during the ORR.[93] In addition, it has also been observed that other properties besides the type of nitrogen site influence the ORR activity, like the amount of carbon edge sites, the total N content, the surface area and the degree of graphitisation.[85,93] Yet others also propose that both pyridinic and graphitic N influence the ORR activity but different aspects: on one hand, pyridinic N was found to improve the onset potential, while graphitic N on the other hand enhances the limiting current density.[27,94]

Two main approaches are employed for doping carbon materials: (1) direct doping during the synthesis of the carbon material or “in situ” doping and (2) post-synthesis doping of an “as-synthesised” carbon material with a dopant source (e.g. NH_3). The latter technique will only lead to surface doping of the material, while the former could lead to a more homogeneous doping of the carbon material. The final composition, structure and activity of all these materials depend on the specific synthesis conditions.

Other dopants than nitrogen (i.e. boron, phosphorus, sulphur, selenium and halogens) have also been used to synthesise doped carbon materials with high ORR activity and stability. A rather large difference in electronegativity (EN) exists between carbon and boron or phosphorus. As a consequence, the ORR activity of these doped carbons can be related to the disruption of the uniformity of the charge distribution of the material. Boron and phophorus tend to donate electrons to carbon, thus creating a partial positive charge on the dopant atoms. On the other hand, nitrogen, which has higher EN than carbon, tends to receive electrons from carbon, thus generating a partial positive charge on the carbon atoms.[26,95,96] In all cases, formation of partial positive and partial negative charges can favour

the interaction with O_2 and its adsorption on the carbon-based material. When sulphur and selenium (having a similar EN to carbon) are used as dopant species another explanation for the enhanced ORR activity has to be proposed. In this case DFT studies showed that the local spin density was altered, generating carbon atoms with high spin densities, which facilitates oxygen adsorption and reduction.[78,97] Another influence of the larger dopant atoms (as P and S) is that they might induce more strain and defect sites in the carbon lattice as a consequence of their mismatch in size within the graphitic carbon plane.[78,97] The introduction of halogens inside the carbon framework is a rather recent development. Jeon *et al*. recently obtained several edge-halogenated (Cl, Br and I) graphene types. It is noteworthy that even though the EN decreased in the order of Cl > Br > I, the ORR activity of the doped graphene increased in the order of decreasing EN. This is in contradiction with the charge transfer mechanism at the origin of the ORR activity of other doped carbons. However, due to the larger relative size of iodine compared to Br and Cl, its valence electrons are more loosely bound and can more easily generate local charges in the carbon framework, thus resulting in a more efficient charge transfer between halogen and oxygen and a higher ORR activity.[98] For all kinds of dopants, it was recently determined, no matter what effect they have (charge disruption, generating high spin density, creating more defects), the variation in adsorption energies is determined by the coupling between the adsorbate's orbitals and E_{diff}, or the difference in energy between the lowest valence orbital of the active atom and the highest valence orbital of the carbon framework. Upon adsorption of (O, OH or OOH), bonding and antibonding states are formed between active site and adsorbed species. A lower valence band of the active atom results in higher filling of the antibonding states and as a consequence the adsorbate-carbon interaction is destabilised. A higher valence band on the other hand increases the bond strength between adsorbate and carbon. The optimal ORR activity, will be the result of an intermediate bonding strength as was already evidenced for the noble metals (*vide supra*).[96,99] Dual- and even ternary-doped carbons have recently been reported to further enhance the ORR activity, owing to the synergistic effects between the different heteroatoms generating a larger asymmetrical spin and charge density into the carbon framework.[85,100–103]

A tentative ORR mechanism has recently been proposed based on DFT calculations.[93] Based on the adsorption energy of oxygen on carbon atoms and on the energy barrier for the first electron transfer (rate determining step[97]), the most likely active site of N-doped graphene was proposed. Carbon atoms located at a site on the edge and next to a valley graphitic N atom showed the lowest energy barrier for the first electron transfer, together with a low (though not the lowest) end-on oxygen adsorption energy. An ORR mechanism was then proposed based on the reaction energies of the various steps (Figurer 1.5).[93]

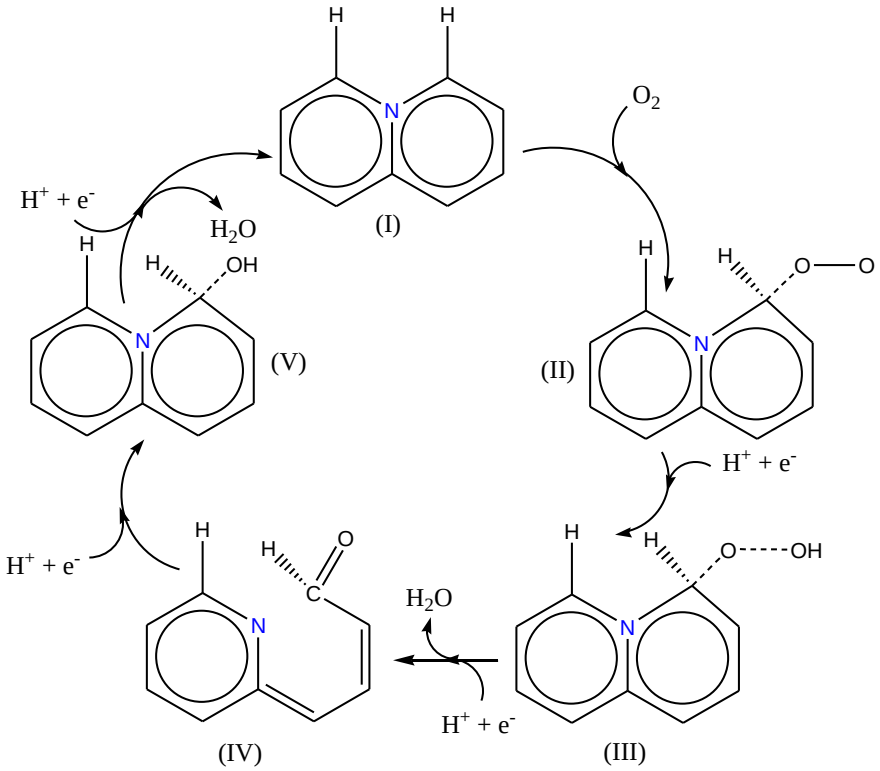

Figure 1.5: ORR mechanism on N-doped graphene nanoribbons as proposed by Kim *et al.* [93]. Adapted from ref. 93.

The four-electron pathway would be followed in this case because the O-O bond length in step (III) is longer than that of C-O: therefore it will be more easily broken and free OOH-species (and H_2O_2) will rarely be produced. In step (III), H_2O is released and the remaining adsorbed oxygen atom will cause the C-N bond to be cleaved (experimentally observed) producing a stable CHO group and pyridinic N species (IV). This mechanism thus suggests that both the graphitic and the pyridinic N configuration are important species for the four-electron reduction of oxygen to water.[93]

Unfortunately, this proposal was made under the assumption that the ORR occurs under acidic conditions. However, from experimental results, it is known that N-doped carbon electrocatalysts perform better under basic conditions. Therefore, it would be highly relevant to model the ORR mechanism for alkaline conditions.

It is important to thoroughly verify whether or not the above-mentioned electrocatalysts are actually metal-free since these claims have two major shortcomings. (1) For example, most carbon nanotubes are prepared with metals as growth catalysts, leaving behind a certain residual number of metallic impurities in the final material. (2) Often, the performed characterisations are not sufficiently sensitive to claim that a catalyst is metal-free. XPS is not sensitive enough (detection limit of 0.1 wt%), more accurate techniques are inductively coupled plasma/mass spectrometry (ICP/MS) or X-ray fluorescence.[45,104,105] It is often impossible to remove these residual metal contents even after thorough acid washing, especially from carbon nanotubes where they are covered by several carbon layers. Since these residual metallic impurities dominate the carbon electrochemistry, even at levels as low as 100 ppm (0.01 wt%), these claims of “metal-free” ORR electrocatalysts are often incorrect.[45,104–106] However, not all residual metal content is active and to verify whether the remaining metal content participates in the ORR, a poisoning experiment should be

performed. Since CN^- ions are known to poison several metal species, especially iron, by strongly adsorbing on them, a clear difference in ORR activity should be seen in the presence of CN^- if the remaining metal species are actively contributing to the ORR performance.[107]

1.3 Membranes

Another essential component of the PEMFC is the proton-exchange membrane, which should ideally have the following properties: (1) high proton conductivity, (2) low reagent permeability, (3) high resistance to electron transport, (4) sufficient stability under fuel cell operating conditions, (5) good water transport at low swelling degree and (6) a low cost. The importance of the membrane lays in the structure of the membrane electrode assembly (MEA) and more in specific in the membrane/active layer interface. The reaction kinetics are controlled by this interface since it provides the three-phase contact (reagent gas, active site and hydrated protons) where the fuel cell reactions take place.[108] Currently, Nafion®, a perfluorinated sulphonic acid based ionomer developed at the end of the 1960s by DuPont as a modification of Teflon, is still the standard membrane in fuel cells.[6,108] Nafion® has high proton conductivity, especially at low temperatures and high humidities, and it shows decent chemical and physical stabilities.[109,110]

Water is very important for the proton conductivity inside Nafion® membranes since it controls the availability of its proton transport paths. At low water content, only isolated water domains exist and, as a consequence, the membrane is not proton conductive. At a certain water content, these isolated domains become randomly connected and proton conductivity can start. However, most of the water will still be present close to the sulfonic groups and thus a rather high activation energy is still required for the proton transport. When the water content further increases the water channels become wider and wider and proton conductivity increases due to a higher proton mobility.[108] The first drawback of Nafion® is linked with this water necessity for good proton conductivity. At temperatures above 100°C and below 0°C, the proton conductivity is too low.[109] Other disadvantages of Nafion® include: (1) high cost,[110] (2) membrane degradation in the presence of H_2O_2[111] and (3) the membrane conductivity may decrease significantly in the presence of contaminating multi-charge ions (e.g. Fe or Co ions leached out from the electrocatalyst) since they can form stronger bonds with the sulfonic acid groups than protons, which will inevitably lead to a lower proton conductivity.[6]

Nafion® membranes are prone to chemical degradation through a reaction with hydroxyl ($^\bullet OH$) or peroxyl ($^\bullet OOH$) radicals, which can be generated in the presence of H_2O_2 and trace amounts of for example Fe ions.[111] The end groups of Nafion® are particularly sensitive to radical attack since they are only partially fluorinated. For example, CF_2COOH could be degraded by the following reactions (1.6-1.8).[6,111]

$$R\text{-}CF_2COOH + {}^\bullet OH \longrightarrow R\text{-}CF_2{}^\bullet + CO_2 + H_2O \quad (1.6)$$

$$R\text{-}CF_2{}^\bullet + {}^\bullet OH \longrightarrow R\text{-}CF_2OH \longrightarrow R\text{-}COF + HF \quad (1.7)$$

$$R\text{-}COF + H_2O \longrightarrow R\text{-}COOH + HF \quad (1.8)$$

In order to overcome these drawbacks, a wide range of alternative proton-exchange membranes has been developed in the last decades with as common aim to obtain economically more attractive and more stable membranes that can operate at elevated temperatures and low relative humidities with a high proton conductivity.[108,109,112] Ideally, a PEM should combine a high proton conductivity with a good stability against swelling or

shrinkage. To meet both criteria, a membrane should consist of a hydrophobic, stable backbone containing hydrophilic proton-conducting channels across the membrane. A high proton conductivity is promoted by a strong acidity, high ion-exchange capacity (IEC) and high proton mobility. Special care has to be taken to not increase the IEC too far since this might result in dissolution of the membrane once it comes into contact with water.[109]

Briefly, the largest groups of alternatives to Nafion® include the following. (1) Polystyrene-sulphonic acid membranes, which have as advantage that they are rather inexpensive but they are insufficiently stable under fuel cell conditions. Furthermore, due to a lower amount of available sulphonic acid groups, their proton conductivity remains below that of Nafion®.[113] (2) Sulphonated polyimide membranes, which form a second group of promising replacements for Nafion® due to their high chemical and physical stability,[114] their lower cost, their lower degree of swelling at intermediate temperatures (40-100°C) and finally but most importantly their possibility to achieve proton conductivities higher than Nafion® at elevated temperatures.[115] Their major drawbacks are a low stability in water due to the susceptibility of the imide-links to hydrolysis[116] and a low conductivity at low water contents.[117] (3) Poly(benzimidazole)-based membranes impregnated with phosphoric acid have received attention as well due to their high mechanical and thermal stability[118] as well as high conductivities at 160-180°C.[119] However, the high phosphoric acid contents required to reach these high conductivities decrease the mechanical strength of the membrane,[120] increase the gas permeability[121] and phosphoric acid leaching could inhibit the electrocatalyst and corrode the electrodes.[122] (4) The last group comprises all kinds of sulphonated membranes with aromatic carbon backbone as poly(arylene ethers), polysulphones, polysulphone-ethers or polyphenylsulphones. They gained a lot of interest due to their high physical and chemical stability and low cost.[108] The most commonly studied sulphonated poly(arylene ethers) are sulphonated poly(arylene ether ketone)s and sulphonated poly(ether ether ketone)s. The latter group has been reported to reach conductivities up to 0.1 S cm^{-1}.[123] Their drawback is a lower stability against peroxides.[124]

To increase the stability of polystyrene sulphonic acid membranes, styrene sulphonic acid monomers can be grafted onto a more stable backbone polymer as polyvinylidene fluoride (PVDF). While these materials (PVDF grafted with sulphonated polystyrene, otherwise known as PVDF-g-PSSA) have already been studied and promising conductivities (up to 0.13 S cm^{-1}) were already obtained for these kind of materials[109,125–128] there is still room for improvement.

The alkaline counterpart of PEMFCs, AEMFCs, offer several advantages over the acidic fuel cells. (1) Under alkaline conditions, the anode and cathode reaction kinetics are faster, which allows for the use of non-noble metal or metal-free electrocatalysts, seriously reducing the fuel cell cost.[55] (2) Easier water management (fuel crossover and cathode flooding) as a consequence of the ion and water transport towards the anode.[129] (3) Lower corrosion tendencies in alkaline environment; and (4) faster methanol and ethanol electrooxidation, which have the advantage of being easier to store and transport and which have a higher energy value compared to hydrogen.[5,7,112,130,131] Unfortunately, the use of alkaline exchange membranes still faces some challenges before they can completely replace PEMs. (1) The basic functional groups (NR_4^+) are much less stable than their acidic counterparts, especially at temperatures above 60°C because they can be replaced by OH^- ions through a direct nucleophilic attack.[132] (2) A lower ionic conductivity than that of acidic PEMs, which is a consequence of the four times lower diffusion coefficient of OH^- ions when compared to H^+ ions. In order to obtain similar conductivities an AEM should thus have a four times higher IEC. Unfortunately, this would lead to a significantly increased membrane swelling and thus a

loss of mechanical properties.[7,133,134] (3) The presence of CO_2 impurities in the feed might severely decrease the membrane conductivity by producing CO_3^{2-} or HCO_3^- ions, which bind strongly with the quaternary ammonium groups of the membrane reducing the amount of OH^- exchange sites.[135]

While research has come a long way since the first success of the alkaline fuel cells (as power source of the Gemini and Apollo spacecrafts[7]), there is still a long way to go before they become economically viable alternatives to the PEMFCs. The currently most used commercially available alkaline membrane are those developed by Tokuyama.

Generally, AEMs are subdivided into homogeneous and heterogeneous membranes. The former consist of a single phase backbone with covalently attached cationic sites, while the latter have an inert backbone with embedded hydroxide salts or other composites (e.g. functionalised SiO_2).[136]

For the homogeneous membranes, three different methods exist to fix the cationic sites to the polymer backbone. (1) In direct polymerisation, a functionalised monomer is directly (co-)polymerised, followed by quaternisation and OH^- exchange.[137–139] (2) Grafting is the most effective method reported thus far and it includes the grafting of a monomer onto the existing polymer backbone, followed by a functionalisation.[129] (3) Chemical modification of a polymer with cationic groups prior to or after casting it into an AEM.[134,140–144]

As was mentioned above, the most common method to increase the conductivity of AEMs when compared to PEMs and despite their lower ionic diffusion coefficient, is to increase the IEC by synthesising membranes with a higher number of cationic groups. However, this would induce significant membrane swelling and a concomitant decrease of the mechanical strength of the membrane. At elevated temperatures, the membranes might even dissolve. A possible solution is to cross-link the membranes but then they lose their solubility properties and as a consequence ionomer solutions, which are essential for the MEA preparation, can no longer be obtained.[134] Recently, two interesting strategies have been proposed to increase the membrane conductivity without compromising mechanical properties. The first one is a short-range cross-linking mechanism for AEMs with a high number of cationic moieties, which only allows cross-linking between polymer chains when they are in close contact, which will never occur in solution. The second approach designs the membranes such that hydrophilic domains group together as a consequence of the presence of extra hydrophobic side-chains. This would result in locally increased ion concentrations, which in turn enhance the OH^- conduction.[134]

1.4 Thesis aims

The ultimate aim of this Ph.D. is to develop novel, efficient and durable electrocatalysts and membranes for improved fuel cell performance with cogeneration of valuable chemicals. Achieving this goal would have a strong impact on the current chemical industry. This Ph.D. is focused on three relevant reactions in which valuable chemicals can be produced with cogeneration of electricity: (1) the reduction of oxygen to hydrogen peroxide, (2) the reduction of nitrogen monoxide to hydroxylamine and (3) the reduction of nitrobenzene to aniline. For all these reactions, the design of an improved electrocatalyst and membrane is of essential importance in order to optimise the generation of electricity, as well as to control the selectivity to the product of interest, since each reaction includes several side-products. The development, evaluation and understanding of such improved electrocatalysts and membranes for the different reactions under investigation was the main target of this Ph.D. thesis.

As a first step in this research, a suitable electrocatalyst has to be found for the electrochemical production of each target product. Two types of electrocatalysts were investigated (1) non-noble metals supported on N-doped carbons and (2) metal-free doped ordered mesoporous carbon materials. They were synthesised, characterised by several analysis techniques and tested for their electrocatalytic performance using a three-electrode electrochemical setup. The most optimal electrocatalyst is determined by the following set of electrochemical parameters: (1) selectivity towards the target product, (2) kinetic and limiting current density, (3) onset potential and (4) half-wave potential. The physicochemical characterisation can then be used to link the composition and structure of the electrocatalysts to their electrochemical performance with as aim to further understand their behaviour and possibly further optimise them.

In a second step of this doctoral work, a cheaper alternative for Nafion® as proton-exchange membrane was developed by optimising the different steps in the synthesis of PVDF-g-PSSA membranes (PVDF synthesis, dehydrofluorination, grafting and sulphonation) separately in order to obtain the most optimal PEM in terms of ion exchange capacity and proton conductivity. While the main interest into these enhanced and cheaper proton-exchange membranes originates from the fuel cell industry, which has as ultimate aim the commercialisation of PEMFCs for electricity generation, the cogeneration approach can also benefit from enhanced membrane properties. Indeed, a faster proton transport would increase the conversion rate and a higher stability and a lower cost will speed up their commercialisation process as well. Furthermore, as these membranes have promising properties to be applied as pH-resistant nanofiltration membranes, this doctoral work also nvestigated their performance as nanofiltration membranes after prolonged exposure to extreme pH's.

1.5 Thesis outline

This thesis focuses on the design, development and evaluation of inexpensive, alternative electrocatalysts and proton-exchange membranes for the cogeneration of electricity and industrially valuable chemicals. New synthesis approaches were developed and established procedures were optimised to prepare different classes of noble-metal-free electrocatalysts. The resulting materials were successfully applied in the electrochemical cogeneration approach.

For the first target product, namely hydrogen peroxide, doped carbon materials were employed. Doped carbon materials are widely reported for the oxygen reduction reaction as inexpensive alternatives for Pt nanoparticles supported on activated carbon, although generally with lower selectivities to water. In this work, N-doped ordered mesoporous carbons were prepared through a new nanocasting approach with as aim to improve the activity towards the oxygen reduction reaction. While this approach did result in enhanced activity, it also resulted in a shift in the selectivity of the oxygen reduction reaction in favour of hydrogen peroxide, which is beneficial for our cogeneration approach. SBA-15 was used as a template and aniline and dihyroxynaphthalene were used as N- and/or C-precursors. In **Chapter 2**, the electrocatalytic performance of two N-doped ordered mesoporous carbons, prepared with different amounts of dihyroxynaphthalene, are compared and the difference in performance is explained based on a thorough investigation of the physicochemical properties of the different materials. The best material offered an excellent prospect for the cogeneration of electricity and hydrogen peroxide due to its superior selectivity (≈100%), high kinetic current density and excellent long-term stability. When comparing our results to the literature, we encountered some difficulties as a consequence of the wide variety in the

composition and applied amount of electrocatalyst ink in the work performed by different groups. Therefore, a thorough investigation of the influence of the ink composition and the applied amount on the oxygen reduction reaction was performed with a rotating ring-disk setup for the N-doped carbons in **Chapter 3**.

As a second target reaction of this Ph.D., the reduction of nitrogen monoxide to hydroxylamine was studied. In **Chapter** 4, Fe-containing N-doped carbons, prepared from inexpensive metal salts and aniline, were tested for the first time in a half and a single cell setup as electrocatalysts for the reduction of diluted nitric oxide. These materials were chosen not only because the synthesis method is straightforward and easily upscalable, but also because they possess the desirable properties for the selective reduction of NO to hydroxylamine. They consist of isolated metal sites, which is important for a high selectivity and their extended delocalised π-system provides them with good electron conductivity, which is an important asset in a fuel cell setup. In attempt to move to the industrially more relevant conditions (100% NO feed) and to speed-up the electrocatalyst screening, a setup with four operating rotating disc electrodes was constructed at the Vrije Universiteit Brussel. In **Appendix 1**, the successes and setbacks of this setup are discussed.

In **Chapter 5**, the use of N-doped carbons as support for metal nanoparticles (copper, iron or cobalt) for the cogeneration of electricity and aniline (final target product) was investigated for the first time. It was discovered that the selectivity towards aniline was drastically improved as compared to the selectivity over copper nanoparticles supported on multi-walled carbon nanotubes as described in literature. This drastic improve suggested that metals might not be essential to obtain a material active in the nitrobenzene reduction reaction. Therefore, in **Chapter 6**, the applicability of ordered mesoporous carbons doped with different elements (B, P or N) as electrocatalysts for the electrochemical production of aniline was investigated for the first time. The synthesised materials were fully characterised and tested for the reduction in a half-cell setup.

For all of these reactions, whether they occur in alkaline or acidic medium, another important component to complete the fuel cell setup is the electrolyte. Currently, the most commonly applied electrolyte is Nafion®, which is a proton-exchange membrane. However, this fluorinated membrane has a high cost and is not sufficiently stable in the acidic fuel cell environment. Therefore, in **Chapter 7**, the synthesis of another known membrane, polyvinylidene fluoride grafted with sulphonated polystyrene, was optimised with respect to its ion-exchange capacity and proton conductivity. Unprecedented conductivities were achieved proving the benefits of a step-by-step optimisation of a reported synthesis method. The optimised membranes even outperformed Nafion® and thus offer a promising cheaper alternative as proton-exchange membranes for application in fuel cells. In **Chapter 8**, the applicability of these membranes as pH-resistant nanofiltration membranes was tested since it was discovered that the grafting increased the chemical stability of the already stable polyvinylidene fluoride membranes to a pH of 14.

Finally, the general conclusions and future perspectives are presented in **Chapter 9**.

Chapter 2

N-doped ordered mesoporous carbons prepared by a two-step nanocasting strategy as highly active and selective electrocatalysts for the reduction of O_2 to H_2O_2

Abstract

A new, two-step nanocasting method was developed to prepare N-doped ordered mesoporous carbon (NOMC) electrocatalysts for the reduction of O_2 to H_2O_2. Our strategy involves the sequential pyrolysis of two inexpensive and readily available N and C precursors, *i.e.* aniline and dihydroxynaphthalene (DHN), inside the pores of a SBA-15 hard silica template to obtain N-doped graphitic carbon materials with well-ordered pores and high surface areas (764 and 877 m^2/g). By tuning the ratio of carbon sources to silica template, it was possible to achieve an optimal filling of the pores of the SBA-15 silica and to minimise carbon species outside the pores. These NOMC materials displayed outstanding electrocatalytic activity in the oxygen reduction reaction, achieving a remarkably enhanced kinetic current density compared to state-of-the-art N-doped carbon materials (-16.7 mA cm^{-2} at -0.35V vs. Ag/AgCl in a 0.1 M KOH solution as electrolyte). The NOMC electrocatalysts showed high selectivity towards the two-electron reduction of oxygen to hydrogen peroxide and excellent long-term stability.

Based on:

X. Sheng, N. Daems, B. Geboes, M. Kurttepeli, S. Bals, T. Breugelmans, A. Hubin, I.F.J. Vankelecom, P.P. Pescarmona, *Appl. Catal. B Environ.*, 176 (2015) 212-224.

Author contribution

The original idea of this research was developed by X. Sheng and P. P. Pescarmona. Electrocatalyst synthesis was done by N. Daems. Physicochemical characterisation was done by N. Daems under supervision of X. Sheng. The manuscript wat written by X. Sheng and N. Daems and edited by P.P. Pescarmona. TEM measurements were performed by M. Kurttepeli under the supervision of S. Bals. B. Geboes performed the electrochemical characterisation under the supervision of T. Breugelmans and A. Hubin. The whole work was supervised by P. P. Pescarmona and I. F. J. Vankelecom.

2.1 Introduction

The development of suitable technologies for the sustainable conversion of energy is a crucial challenge faced by the human society. Fuel cells are very attractive power sources with applications ranging from stationary power generation in industry to portable power for mobile applications. The high efficiency of fuel cells stems from the conversion of the chemical energy of a thermodynamically favourable reaction into electricity. A commonly used reaction for this purpose involves the oxidation of hydrogen and the reduction of oxygen, with water as the product. The electrochemical reduction of O_2 to H_2O occurs through the transfer of four electrons (2.1), whereas the partial reduction of O_2 to H_2O_2 involves the transfer of two electrons (2.2).

$O_2 + 4\ H^+ + 4\ e^- \rightarrow 2\ H_2O$ (*acidic env.*) $E^0 = 1.23$ V (2.1)
$O_2 + 2\ H_2O + 4\ e^- \rightarrow 4\ OH^-$ (*basic env.*) $E^0 = 0.40$ V
$O_2 + 2\ H^+ + 2\ e^- \rightarrow H_2O_2$ (*acidic env.*) $E^0 = 0.70$ V (2.2)
$O_2 + H_2O + 2\ e^- \rightarrow HO_2^- + OH^-$ (*basic env.*) $E^0 = -0.06$ V

The oxygen reduction reaction (ORR) is not only important for H_2-O_2 fuel cells but also for direct methanol fuel cells and for metal-air batteries. Since the kinetics of the cathodic ORR are sluggish compared to the anodic reaction, research efforts have focussed on the development of active, selective and cost-effective electrocatalysts for the cathode.[145]. The selectivity of the electrocatalyst in the ORR is of prime importance. A high selectivity towards the 4-electron reduction of oxygen to water is desired if the target is to maximise the generation of electricity.[145] On the other hand, a highly selective 2-electron reduction to hydrogen peroxide can also be attractive because it would allow the cogeneration of a useful product and of electricity. This last approach can provide a sustainable and economically advantageous way to produce industrially relevant chemicals that are prepared through a redox reaction with $\Delta G < 0$ (*i.e.* $E > 0$), by converting the energy that is generally dissipated in the form of heat into electricity.[23] H_2O_2 is one of the most important chemical commodity products, used as a green oxidant in a large variety of applications.[9] However, because of the high cost and hazardous nature of its standard production through the anthraquinone process, the development of an environmentally friendly process based on hydrogen and oxygen as reactants is highly desired. The electrochemical approach has the relevant advantage of performing the reduction of O_2 and the oxidation of H_2 in two separate cells, thus avoiding the contact between the two reagents and making the process intrinsically safer compared to the direct reaction of H_2 with O_2. Different designs of H_2/O_2 fuel cells for the synthesis of H_2O_2 have been proposed, with the electrolyte being an acidic solution, a basic solution or a solid polymeric membrane.[11,146] The latter option allows obtaining neutral and electrolyte-free solutions of H_2O_2. An essential factor for the development of fuel cells for the cogeneration of chemicals and electricity is the identification of suitable electrocatalysts. The choice of the electrocatalyst is crucial for obtaining high selectivity towards the 2-electron reduction of O_2 to H_2O_2 and to avoid further electrochemical reduction of H_2O_2 to H_2O by another 2-electron reduction (2.3) or the chemical disproportionation reaction of H_2O_2 (2.4).[147]

$H_2O_2 + 2\ H^+ + 2\ e^- \rightarrow 2\ H_2O$ (*acidic env.*) $E^0 = 1.76$ V (2.3)
$H_2O + HO_2^- + 2\ e^- \rightarrow 3\ OH^-$ (*basic env.*) $E^0 = 0.86$ V
$2\ H_2O_2 \rightarrow 2\ H_2O + O_2$ (2.4)

A variety of electrocatalysts has been developed for the oxygen reduction reaction, either to H_2O or to H_2O_2.[12,148,149] The benchmark electrocatalysts for this reaction consist of noble metal particles, typically Pt, supported on carbon, which show high activity in terms of produced current and display high selectivity towards the full reduction of O_2 to H_2O.[150–152] Although the use of noble metals in the form of supported nanoparticles allowed increasing the efficiency of the electrocatalysts per gram of the very expensive metal, the cost and the stability of these materials still represent serious limitations for their practical application.[153] Therefore, alternative types of electrocatalysts have been sought. Initial attempts to replace Pt focused on the development of electrocatalysts based on non-noble metals. Pyrolysed carbon-supported transition metal complexes forming metal-N_x chelates (with x = 2 or 4; *e.g.* phthalocyanines) exhibited the most promising results in terms of ORR activity.[154,155] However, these catalysts have two disadvantages: low stability and, in general, lower activity than Pt-based catalysts. Recently, nitrogen-doped carbon materials have drawn great interest as an alternative to conventional Pt-based electrocatalysts.[156] These metal-free materials can reach competitive electrocatalytic activity in the ORR and exhibit long-term stability.[78] Their unique electronic properties are derived from the conjugation between the orbitals of the nitrogen lone-pair electrons and the graphitic π-system. N-doped carbon materials can be prepared in different morphologies, among which N-doped ordered mesoporous carbons (NOMCs) are particular attractive for catalytic applications because they are characterised by regular arrays of uniform mesopores that lead to a material with extremely high specific surface area (500-1900 $m^2\ g^{-1}$).[80,153,157]. Moreover, the size of the pores in the mesocale (typically between 2 and 50 nm) is favourable for the diffusion of reactants and products through the catalyst.[153] As for all carbon materials, NOMCs combine high electrical and thermal conductivity with high stability.

In this work, we present a new nanocasting strategy for the synthesis of highly active, selective and stable N-doped ordered mesoporous carbon electrocatalysts for the reduction of O_2 to H_2O_2. The synthesis method is based on the use of two inexpensive and readily available carbon precursors, *i.e.* aniline and dihydroxynaphthalene (DHN), which are sequentially introduced into the pores of mesoporous SBA-15 silica as a hard template. In our strategy, the pores of SBA-15 are covered with a monolayer of aniline, which is then polymerised and pyrolysed, followed by filling of the remaining pores space with dihydroxynaphthalene, by another pyrolysis step and finally by the removal of the silica template (Figure 1). In this way, N-doping will be limited to the surface of the material. DHN was chosen to complete the filling of the pores of the SBA-15 template because it has an extensive aromatic structure, with the target of favouring the formation of a graphitic structure, and because its hydroxyl groups can easily interact with N through hydrogen bridges. The two hydroxyl groups can also react with the SBA-15 silanol groups that might still be available, leading to grafting of the aromatic species through a dehydration reaction.[158] Two NOMC materials were prepared by tuning the amount of DHN employed in the synthesis. The obtained materials presented the desired array of parallel channels leading to high specific surface area (up to 877 $m^2\ g^{-1}$) and displayed excellent electrocatalytic properties in the oxygen reduction reaction to H_2O_2.

2.2 Experimental

2.2.1 Preparation of SBA-15

The SBA-15 hard template was prepared according to a procedure reported in literature[159] using triblock copolymer Pluronic P123 (BASF) as structure directing agent and

tetraethylorthosilicate (TEOS, Acros organics) as silica source in acidic solution. The molar ratio of the components in the synthesis mixture was 1 SiO_2: 0.0167 Pluronic P123: 1.05 glycerol: 9.2 HCl: 188 H_2O. All chemicals were used without further purification. In a typical synthesis, 1.8 g of P123 and 1.8 g of glycerol were stirred overnight at 35°C in a 1 M HCl aqueous solution prepared by diluting concentrated HCl (37%, VWR) with distilled water. Next, 3.87 g of TEOS was added dropwise to the solution, which was then stirred for 5 min. Afterwards, the mixture was allowed to react for 24 h at 35°C under static conditions followed by a hydrothermal treatment at 100°C for 24 h in a closed polypropylene bottle, again under static conditions. The solid products were collected by filtration, washed with distilled water, and dried at 80°C overnight. The resulting powders were gently ground and calcined at 550 °C for 5 h to remove the organic structure directing agent.

2.2.2 Preparation of the NOMC materials

The N-doped ordered mesoporous carbon (NOMC) materials were prepared using a two-step procedure. First, aniline was polymerised inside the pores of SBA-15. The amount of aniline employed in this step was chosen in order to cover the SBA-15 surface with an aniline monolayer. For this purpose, the molecular cross-sectional area (σ) of aniline was calculated to be equal to 31.0 $Å^2$ from the formula:

$$\sigma = f\left(\frac{M}{\rho N_A}\right)^{\frac{2}{3}}$$

where *f* is a constant, equal to 1.091 for a close-packed liquid monolayer, M is the molecular mass of aniline (93.13 g mol^{-1}), ρ is the density of aniline at 20 °C (1.02 g cm^{-3}) and N_A is the Avogadro constant ($6.022 \cdot 10^{23}$ mol^{-1}).[160] The value of σ for aniline is very similar to that for benzene (30.7 Å²). However, for practical applications, the value of the cross-sectional area of benzene is generally corrected to 43 $Å^2$.[160] We applied the same correction and used a value of 43 $Å^2$ for our calculations. Dividing the surface area of 0.5 g of SBA-15 (413 m^2) by 43 $Å^2$ we obtain that 1.6 mmol of aniline are needed to achieve a monolayer on the SBA-15 surface. Therefore, 0.15 ml (1.6 mmol, Janssen Chimica) of aniline and 0.44 g (1.9 mmol) of the radical initiator ammonium persulfate (APS, Sigma-Aldrich) were added to a suspension of 0.5 g of SBA-15 in 250 ml of a 0.5 M HCl aqueous solution, and stirred for 24 h in an ice bath. Afterwards, the solvent was removed in a rotary evaporator and the sample was dried in an oven at 100°C. The sample was then placed into a quartz U-tube where it underwent pyrolysis for 3 h at 900°C (with a heating rate of 3 °C min^{-1}) under N_2 flow (1 cm^3 s^{-1}). This low N_2 flow rate was chosen in order to avoid excessive vaporisation and loss of aniline. In the second step of the procedure, the obtained grey solid was mixed with the selected amount of 2,3-dihydroxynaphthalene (DHN, 98% Sigma-Aldrich, b.p. ~354°C, ρ = 1.33 g cm^{-3}) in acetone as a solvent (5 ml) and stirred for 24 h at room temperature. Two different amounts of DHN were used: 0.36 g (2.3 mmol, NOMC-L) or 0.46 g (2.9 mmol, NOMC-H), corresponding to a 1:1.4 and 1:1.8 molar ratio between aniline and DHN. After evaporation of the solvent, the composite material was thermally treated for 2 h at 300 °C under N_2 flow (3 °C min^{-1}, 1 cm^3 s^{-1}). Next, the sample was washed 3 times with acetone, collected by filtration and dried in a vacuum oven at 60°C. A final pyrolysis was then performed for 5 h at 900°C (heating rate: 3 °C min^{-1}) under N_2 flow (1 cm^3 s^{-1}). Finally, the silica template was removed by suspending the black solid in a 2.5 wt% NaOH solution in a 1:1 mixture of EtOH/H_2O while stirring for 8 h under reflux and under N_2 flow. The NOMC material in the form of a black solid was then collected by filtration and dried for 24 h in a vacuum oven at 100°C.

In order to investigate the influence of DHN on the ORR activity, an extra electrocatalyst was prepared following the same procedure described above but without the addition of DHN (NOMC-no-DHN).

2.2.3 Physicochemical characterisation of the NOMC materials

Small-angle X-ray scattering (SAXS) patterns of the NOMCs were recorded at room temperature by using a SAXSess mc^2 instrument (Anton Paar, Graz, Austria) with line-collimated Cu*Kα* ($\lambda_{K\alpha}$ = 0.154 nm) radiation and a 2D imaging plate detector. "SAXSquant" software was used to model the subtraction of the background (empty sample holder).[161] The SAXS patterns were plotted as a function of 2θ. The 2θ value is related to the scattering vector (q, in nm^{-1}), which is often used in SAXS patterns, by the following equation: $q = 4\pi\sin(\theta)/\lambda$.[162] Wide-angle X-ray diffraction (XRD) patterns were measured on a STOE Stadi P instrument using Cu*Kα* radiation. Nitrogen adsorption–desorption isotherms were measured at 77 K on a Micromeritics Tristar 3000. The pore size distributions were determined using the Barrett-Joyner-Halenda (BJH) method applied to the adsorption branch of the isotherm, whereas the Brunauer-Emmett-Teller (BET) method was used to calculate the surface area of the samples.[163] The Dumas-method was used for elemental analysis to determine the percentages of N and C: the NOMC materials were subjected to an oxidative combustion process at 900 °C, and the produced gases were detected with a thermal conductivity detector (Vario Max CN, Elementar).[164] Transmission electron microscopy was done partly at EMAT, and partly at MTM-KU Leuven, using a FEI Tecnai G2 operated at 200 kV (EMAT) and a Philips FEG CM200 operated at 200 kV, respectively. Samples were prepared by dispersing the powders in ethanol and placing several drops of the dispersion onto a holey carbon grid. The samples were visualised using electron tomography, performed by collecting a tilt series of 2-dimensional images using high-angle annular dark-field scanning transmission electron microscopy (HAADF-STEM) over an angular range of ±72° with a tilt increment of 2°. After the alignment of the projection images, a 3-dimensional reconstruction was obtained using the simultaneous iterative reconstruction technique (SIRT)[165] implemented in the FEI Inspect3D software. X-ray photoelectron spectroscopy (XPS) was used to determine the elemental composition at the surface of the NOMCs and to give information about the molecular environment of the different atoms. The analysis was carried out on a Physical Electronics PHI 1600 multi-technique system using an Al *Kα* (1486.6 eV) monochromatic X-ray source, which was operated at 15 kV and 150W at a pressure of $2 \cdot 10^{-9}$ Torr. The graphitic C 1s band at 284.6 eV was taken as internal standard, in order to correct possible deviations caused by electric charging of the samples. The multipack software was used for the deconvolution and integration of the XPS spectra. Room-temperature Raman spectra were recorded on a LabRAM HR Evolution-Horiba Scientific system with a green laser (532 nm). Deconvolution and peak integration was performed by using the PeakFit v4.12 software.

2.2.4 Electrochemical characterisation of the NOMC materials

The electrocatalytic activity of the NOMCs in the oxygen reduction reaction was evaluated by means of rotating disc electrode (RDE) linear sweep voltammetry (LSV). The commercially available Pt/C (20 wt% Pt on Vulcan XC 72 purchased from Alfa Aesar), which is commonly employed as benchmark electrocatalyst for the ORR, was used as a reference for comparison with the synthesised NOMCs.[79] LSV measurements were conducted at various rotating speeds (400 to 2500 rpm). The experiments were carried out at room temperature in a conventional three-electrode cell with a Radiometer EDI-101 rotating disc

electrode connected to an Autolab PGSTAT 302F potentiostat. An Ag/AgCl (saturated KCl) reference electrode was used in combination with a Pt counter electrode. The reference electrode has an internal salt bridge filled with 0.1 M KOH. A Luggin capillary is present between the compartment of the reference electrode and the working electrode. A glassy carbon RDE (with a surface area of 0.283 cm^2) was employed as an inert carrier for the working electrode. Catalyst ink solutions were prepared by suspending 2 mg of electrocatalyst powder in 1.5 ml of solvent (1:1 volume mixture of isopropanol and H_2O). 5 µl of catalyst ink was then deposited onto the glassy carbon surface, yielding an approximate catalyst loading of 25 µg cm^{-2}. After drying, a thin Nafion® film was applied by depositing 7 µl of a 0.05 wt% Nafion® solution (diluted with 1:1 isopropanol with water from a 5 wt% Nafion® solution in a mixture of perfluorosulfonic acid with lower aliphatic alcohols from Aldrich) followed by a final drying step at room temperature. The ORR was performed under alkaline conditions using an aqueous 0.1 M KOH electrolyte solution saturated with O_2. The saturation of the electrolyte solution with O_2 was achieved by bubbling O_2 gas for 10 min, after which O_2 flow was maintained just above the solution during the whole voltammetric measurement. The potential was varied from 0.2 to -1.2 V vs. Ag/AgCl at a potential sweep rate of 10 mV s^{-1}. Before each blank measurement, N_2 was bubbled into the electrolyte solution for 30 min, in order to remove the remaining O_2. Each measurement was performed three times and the average values are reported.

Cyclic voltammograms (CV) of NOMC-H and NOMC-L were recorded on a glassy-carbon electrode in either N_2-saturated or O_2-saturated 0.1 M KOH aqueous solutions, by varying the potential between 0.2 and -1.0 V at a scan rate of 50 mV s^{-1}. Chronoamperometric tests were carried out at a fixed potential of -0.4 V in O_2-saturated 0.1 M KOH at a rotation rate of 1600 rpm during 5 h. The features of the cell and the preparation of the working electrode were as in the LSV experiments (*vide supra*).

The current densities were calculated using the geometric surface area of the glassy carbon electrode as the actual surface area of the electrode cannot be determined accurately. The actual surface area depends on the specific surface area of the porous electrocatalyst and on the amount of electrocatalyst and binder that are deposited on the disk. This implies that the obtained values of kinetic current density include contributions of both the intrinsic activity (per surface unit) and of the surface area of the electrocatalyst. This allows a meaningful ranking of the performance of different electrocatalytic materials. It should be noted that this is conceptually different from reports in which the kinetic current density is normalised through the electrochemically active surface area (EASA), in which case only the intrinsic activity is evaluated.

2.3 Results and discussion

2.3.1 Synthesis and physicochemical characterisation of the NOMC electrocatalysts

A novel, two-step nanocasting method was designed and applied to the synthesis of N-doped ordered mesoporous carbon (NOMC) materials using readily available and inexpensive N and C sources (aniline and 2,3-dihydroxynaphthalene). The synthesis of N-doped mesoporous carbons by nanocasting typically consists in filling the pores of an inorganic solid template with suitable C and N precursors, followed by pyrolysis and removal of the inorganic template to produce a carbon negative, *i.e.* a material in which the carbon part corresponds to the pores of the inorganic template and the voids correspond to the walls of the template.[79,166,167] For application as electrocatalysts for the

ORR, highly aromatic large molecules (*e.g.* porphyrin derivatives) have been employed as precursors for the formation of the ordered carbon framework.[79,153] The NOMCs prepared with this approach display excellent ORR activity but the high price and often complex synthesis of highly aromatic large molecules represent a serious limitation for the up-scaling of the fabrication of these NOMCs. Therefore, the development of an accessible and affordable method for the synthesis of NOMCs with enhanced electrocatalytic performance in the oxygen reduction reaction (ORR) is a highly attractive target. Our two-step synthetic procedure is illustrated in Figure 2.1. This original strategy differs from the known nanocasting methods because it aims at generating a carbon material in which N-doping is mainly occurring at the surface and with a carbonaceous core having high graphitic degree, which would provide high electrical conductivity. For this purpose, an N precursor (aniline) and a C precursor (2,3-dihydroxynaphthalene) were sequentially introduced and pyrolysed into the pores of SBA-15 mesoporous silica, which is widely used as hard template for nanocasting.[153] Aniline was selected as N-containing precursor because it can be easily polymerised and it contains an aromatic ring in its structure. DHN was employed to complete the filling of the SBA-15 pores because it has a more extended aromatic structure compared to aniline, and this feature is expected to facilitate the graphitisation process upon pyrolysis.[168] Both molecules can be easily introduced into the pores of the template as their size is small compared to that of the mesopores of SBA-15. Moreover, the polymerisation of aniline, the high boiling point of DHN (~354°C) and the ability of these compounds to interact with each other and with the silanol groups at the surface of SBA-15, are all expected to promote carbonisation over evaporation during the pyrolysis steps.[169] SBA-15 was chosen as template for the nanocasting because it displays high specific surface area originating from its hexagonal array of parallel mesopores, and can be prepared with micropores connecting the parallel channels. This latter feature is essential for the generation of ordered mesoporous carbon structures because it leads to the formation of carbon bridges that prevent agglomeration of the carbon rods after removal of the silica template (Figure 2.1), thus leading to a carbon material with high surface area.[153] The textural features of the prepared SBA-15 were characterised by N_2-physisorption (Table 2.1 and Figure 2.2). The material presents the anticipated high surface area and the desired combination of meso- and micropores. Transmission electron microscopy (TEM) confirms the successful formation of the characteristic hexagonal array of parallel mesopores of SBA-15 (Figure 2.3.A). In the next step, aniline was introduced into the pores of SBA-15, and then polymerised. The added amount of aniline was chosen to form only an adsorbed monolayer on the pore walls of SBA-15, with the aim of achieving an N-containing carbon layer after pyrolysis at 900 °C. The obtained material was impregnated with 2,3-dihydroxynaphthalene (DHN), after which a self-assembly dehydration reaction occurred in the pores at 300 °C under N_2. A careful tuning of the amount of DHN is essential to achieve a complete filling of the pores with DHN, while avoiding an excessive loading that would lead to the formation of carbonaceous species outside the pores of the silica template. For this purpose, two different amounts of DHN were employed, leading to a sample prepared with lower amount of DHN (NOMC-L, with a 1:1.4 molar ratio between aniline to DHN) and one with higher amount (NOMC-H, with a 1:1.8 molar ratio between aniline and DHN). These amounts were calculated based on the total pore volume of the SBA-15 (Table 2.1) minus the volume of aniline that was added in the first step, and considering that part of the aniline employed in the first step is lost at 350-400 °C during the heating-up phase of the thermal treatment at 900 °C. After a second treatment at 900 °C to pyrolyse the DHN precursor, the silica template was removed by treatment with a NaOH solution that induces

the conversion of the Si-O-Si bonds into Si-OH and Si-O$^-$ species.[170] The successful removal of the silica template was confirmed by XPS analysis (see Table 2.2).

Table 2.1. Structural and textural properties of SBA-15 and NOMCs

	S_{BET}[a] ($m^2\ g^{-1}$)	Total pore volume[b] ($cm^3\ g^{-1}$)	Micropore Volume[c] ($cm^3\ g^{-1}$)	Mesopore Volume[d] ($cm^3\ g^{-1}$)	Pore size[b] (nm)	d_{100}[e] (nm)	a_0[f] (nm)	Wall thickness[g]
SBA-15	826	0.76	0.12	0.64	7.5	10.7	12.4	4.9
NOMC-H	877	0.56	0.06	0.50	3.3	9.0	10.3	7.0
NOMC-L	764	0.54	0.01	0.53	3.3	9.0	10.3	7.0
NOMC-no-DHN	761	0.78	0.06	0.72	4.3	n.d.	n.d.	n.d.

[a] S_{BET}: BET surface area. [b] Total pore volume and pore size determined by the BJH method. [c] Micropore volume, calculated by the t-plot method (Figure S2.1).[171] [d] Mesopore volume = total pore volume - micropore volume. [e] d-spacing calculated on the basis of the following formula $\lambda = 2d_{100}\sin\theta$. [f] Unit cell constant calculated by the equation $a_0 = 2d_{100}/\sqrt{3}$, where d_{100} is the spacing of the (100) planes of a hexagonal array of pores. [g] Wall thickness = a_0 - pore size.
n.d. = not determined.

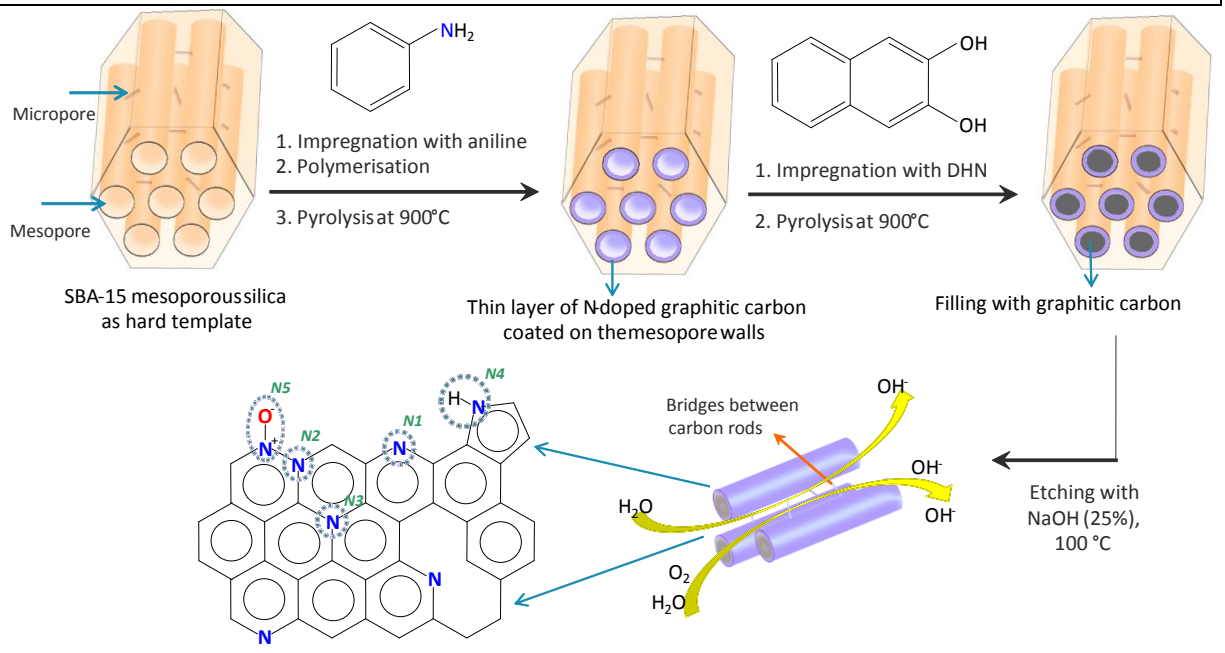

Figure 2.1. Schematic illustration of the formation of a NOMCs with a layer of N-doped carbon at the surface and a fully carbonaceous core, using SBA-15 as hard template. The possible configurations of N atoms in the NOMC material are indicated: pyridinic N (*N1*), graphitic N (*N2-N3*), pyrrolic N (*N4*) and oxidised pyridinic N (*N5*).

The employed synthesis strategy was successful for preparing the desired N-doped ordered mesoporous carbon (NOMC) materials with a well-defined ordered carbon framework and high specific surface area, as demonstrated through a combination of characterisation techniques. The BET surface areas of NOMC-H and NOMC-L determined by N_2-physisorption are high among NOMCs prepared by introducing an N-containing carbon source in SBA-15 (*in-situ* method),[79,172] reaching a value of 877 $m^2\ g^{-1}$ for NOMC-H (Table 2.1). These high surface areas are ascribed to the tuning of the amounts of the N and C precursor relative to the amount of silica template. The analogous adsorption-desorption

isotherms of the two NOMC samples (Figure 2.2) are of type IV with a clear hysteresis loop at p/p^0= 0.4-0.9, indicating the mesoporous character of the materials.[160,169] The insets show narrow pore size distribution curves, corresponding to a rather uniform mesopore size around 3.3 nm (Table 2.1). However, the less steep hysteresis loop of the NOMCs when compared to that of the SBA-15 template (Figure 2.2), indicates the presence of pores with different sizes. It is thus possible that some of the SBA-15 pores are not completely filled during the synthesis, resulting in the creation of carbon tubes instead of carbon rods and creating a second type of pores. For the remainder of this thesis and for simplicity, the carbon rods and tubes are considered under the common name, carbon rods. The formation of the hexagonal arrays of parallel carbon rods with a regular spacing is unequivocally demonstrated by the TEM images (Figure 2.3.B and D) and by electron tomography (Figure 2.4.A and B) of NOMC-H and NOMC-L. The presence of graphitic layers within the aligned carbon rods was evidenced by HR-TEM (Figure 2.4.C and D). These graphitic layers are organised in small, local domains, without a preferential orientation of the domains within the rod. The parallel array of long channels of NOMC-H and NOMC-L evidenced by TEM corresponds to long carbon rod structures when observed on the micrometer scale by SEM (Figure 2.5). Besides the desired ordered mesoporous carbon framework, the TEM images of the NOMCs evidence the presence of small areas of unstructured carbon. These species probably originate from DHN that remained outside the pores of SBA-15 during the synthesis. Indeed, these disordered carbon species are observed in larger amount in NOMC-H, for which a higher ratio of DHN to aniline was employed (compare B and C with D and E in Figure 2.3). This observation can be related to the larger micropore volume of NOMC-H (Table 2.1), originating from the pyrolysis of DHN that was not confined into the silica pores, whereas the mesopore volume of the two NOMC materials is similar. The presence of this microporosity also explains the higher surface area of NOMC-H compared to NOMC-L (877 $m^2\ g^{-1}$ vs. 764 $m^2\ g^{-1}$).

The 2D-hexagonal ordering of the prepared NOMCs was confirmed by SAXS (Figure 2.6.A). The typical SAXS pattern of the SBA-15 silica used as template corresponds to a 2D-hexagonal P6mm space group with a strong peak correlated with the (100) plane at 0.84° and two other weak peaks due to the (110) and (200) planes at 1.44° and 1.66°, respectively. The SAXS patterns of the NOMCs also show the characteristic diffraction peaks corresponding with the ordered hexagonal structure. However, these signals have a low intensity and the reflections of the (110) and (200) planes are almost indiscernible: this can be caused by a lower degree of order in the structure of the NOMCs compared to that of SBA-15 or by 'accidental extinctions' related to the specific sizes of the rods and pores.[173,174] The (100) peaks of the NOMCs are shifted to higher 2θ value (0.97°) compared to that of SBA-15, corresponding to a d-spacing of 9.0 nm for the NOMCs and of 10.7 nm for SBA-15 (Table 2.1). The smaller d-spacing of the NOMCs is related to a shrinkage of the framework of the material during pyrolysis and upon dissolution of the silica template.[175] Since the mesoporous carbon material is produced inside the SBA-15 channels, the diameter of the carbon rods should correspond to the pores of SBA-15 whereas the voids of the resulting NOMC originate from the SBA-15 walls after removal of the silica template. Indeed, the diameter of the carbon rods (7 nm) matches well with the mesopore size of the SBA-15 (7.5 nm), whereas the voids of the NOMCs (3.3 nm) are smaller compared to the wall thickness of the silica template (4.9 nm), as a consequence of the above-mentioned shrinkage.

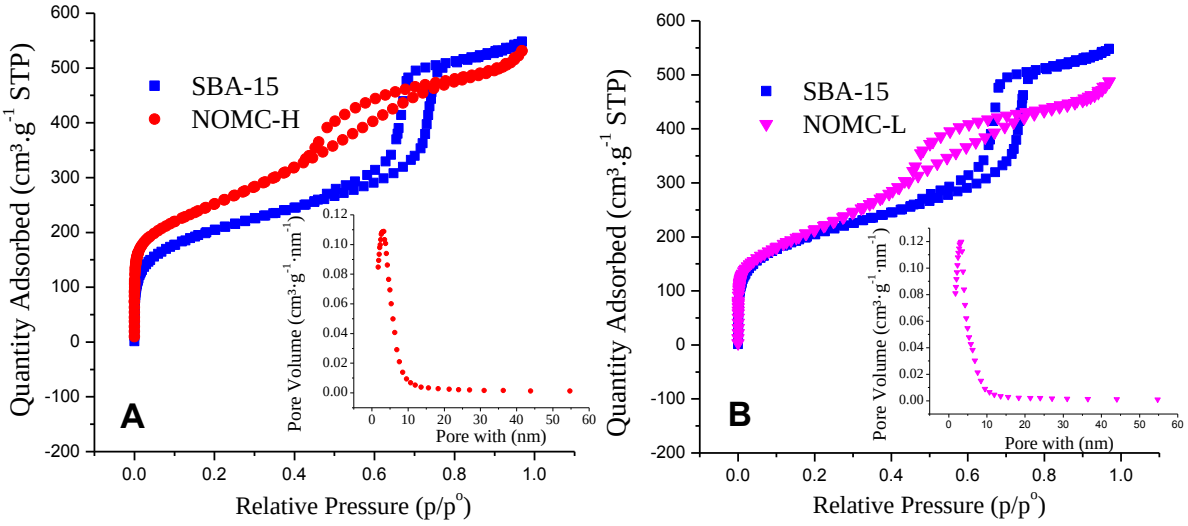

Figure 2.2. N_2 adsorption-desorption isotherms of NOMC-H (A) and NOMC-L (B) compared with the SBA-15 hard template. The insets are the respective BJH pore size distributions.

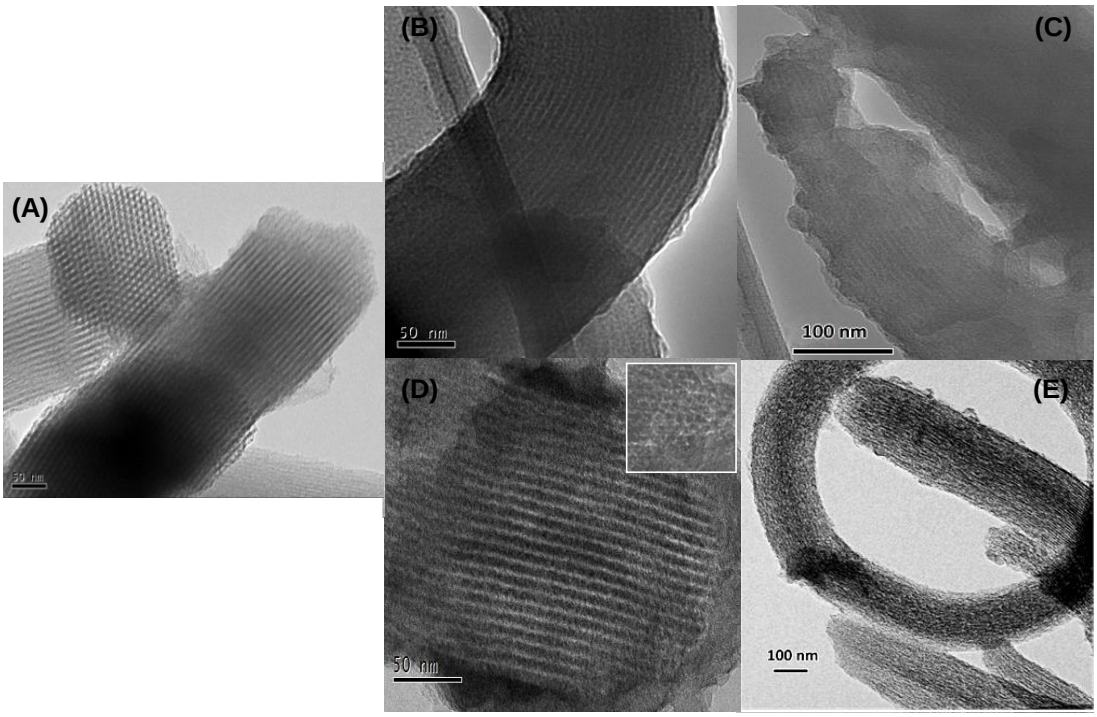

Figure 2.3. TEM images of: SBA-15 (A); NOMC-H (B and C); NOMC-L (D and E). The inset in (D) is the enlarged area of a top view of the hexagonal array of mesopores.

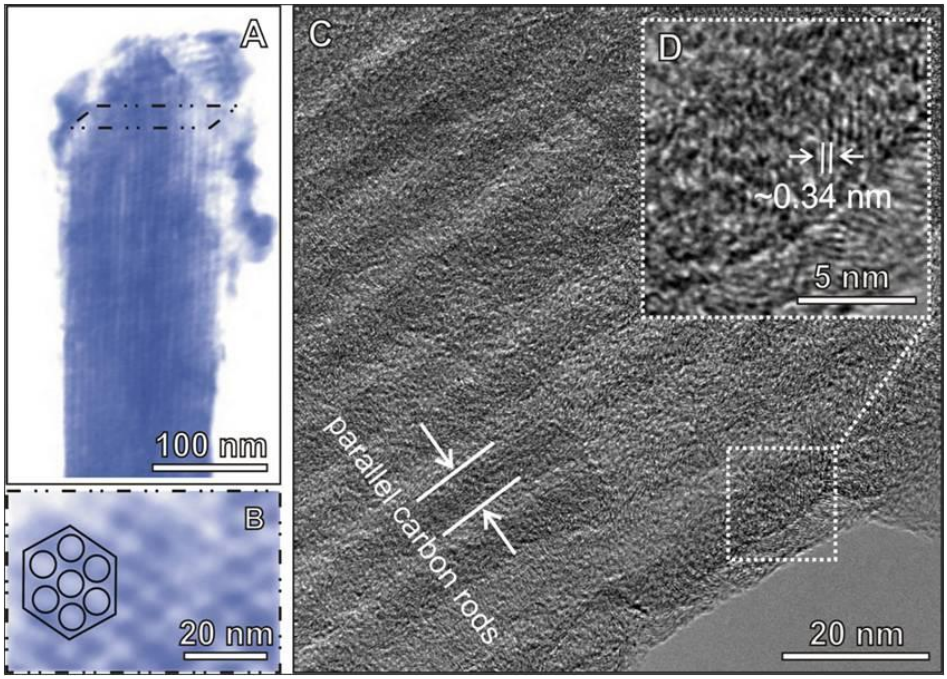

Figure 2.4. Reconstructions by electron tomography of the NOMC-L sample along different orientations (A and B). HR-TEM images of NOMC-L (C and D), with indication of the position of the parallel carbon rods and of the graphitic layers (~0.34 nm spacing).

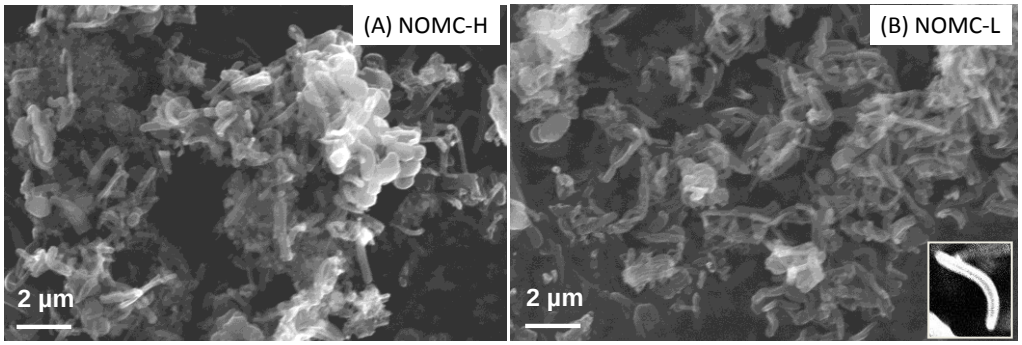

Figure 2.5. SEM images of NOMC-H (A) and NOMC-L (B). The inset is a zoomed image of a single tubular carbon structure.

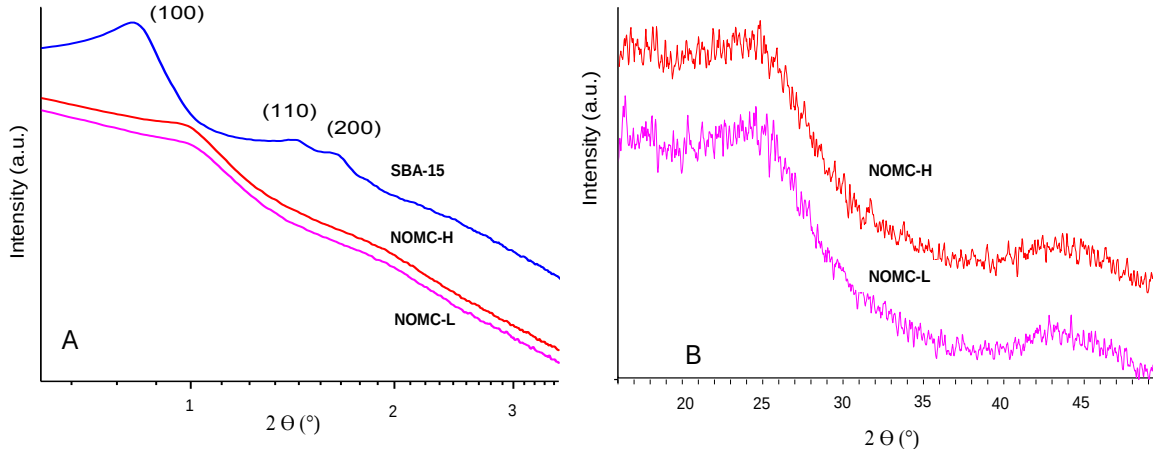

Figure 2.6. SAXS patterns of SBA-15 and of the NOMCs (A) and XRD patterns of the NOMCs (B).

The formation of an electrically conductive graphitic structure within the carbon rods of the NOMC materials would be an asset in view of an electrocatalytic application. The two peaks at 24.1° and at 42.3° in the wide-angle XRD patterns of the synthesised NOMCs (Figure 2.6.B) are characteristic for the (002) and (101) graphitic planes, respectively. As expected considering the nanoscale of the rods constituting the NOMCs and the HR-TEM data discussed above, the two peaks are rather broad, indicating a relatively low degree of crystallinity of the graphitic carbon structure.[175] Complementary information about the degree of graphitisation of the NOMCs is provided by Raman spectroscopy (Figure 2.7). The formation of graphitic structures within the carbon framework is clearly evidenced by the presence of an intense and narrow band at 1604 cm^{-1} (G-band), which is assigned to the planar C=C stretching vibration mode in an ideal graphitic layer. The position of this band is shifted to lower wavenumbers in N-doped carbon materials compared to undoped carbons, due to a change in the electronic structure of the carbon framework originating from n-type doping.[153] The other band at 1330 cm^{-1} (D-band) is correlated with structural defects and disordered structures at the edges of the sp^2 domain. The ratio of the areas of the D and G bands (A_D/A_G) is inversely proportional to the graphitic degree. The A_D/A_G values of NOMC-H and NOMC-L, *i.e.* 1.5 and 1.3 (Table 2.2), are in the same range as N-doped carbon nanotubes and relatively high compared with previously reported N-doped graphite.[153] This confirms that the rods constituting the NOMCs have a graphitic character, though the graphitisation degree is lower compared to the extensive layers of graphite. The higher graphitic degree of NOMC-L compared to NOMC-H shows that the higher amount of DHN employed in the synthesis of the latter material generated a less graphitic structure, which could correspond to the disordered carbon species observed by TEM (*vide supra*). Besides the two major G- and D-bands, deconvolution of the Raman spectra indicates the presence of two additional peaks centred at 1200 and 1510 cm^{-1} (Figure 2.7), which are respectively attributed to carbon atoms outside a perfectly planar graphitic network (such as aliphatic species) and to five-member rings or heteroatoms integrated in the graphite sheet.[176] In line with the lower graphitic degree of NOMC-H mentioned above, the relative contribution of these two bands is slightly higher for NOMC-H than for NOMC-L. Although the graphitic degree of the two NOMC materials is lower compared to graphite, impedance measurements performed on glassy carbon disc electrodes coated with an ink of NOMC-H, NOMC-L or graphite showed that the electrical resistance of the electrodes based on the NOMC materials lies in the same range as that of an electrode based on pure graphite under the employed experimental conditions (Table S2.1).

Table 2.2. Carbon, nitrogen and oxygen contents and I_D/I_G ratio of the prepared NOMCs.

	C (wt%)[a]	N (wt%)[a]	O (wt%)[a]	Si (wt%)[a]	I_D/I_G[b]
NOMC-H	87	3.0 (theor. 3.8)	9.7	< 1	1.5
NOMC-L	87	3.4 (theor. 4.5)	9.2	0.0[c]	1.3
NOMC-no-DHN	87	5.7 (theor. 15.0)	6.7	1.0	n.d.

[a]Determined by XPS. [b]Determined from the deconvolution of the Raman spectra (measured with a laser with λ = 532 nm). [c] No Si signal was detected. n.d. = not determined .

The composition of the NOMCs and the configuration of the N atoms were investigated by means of X-ray photoelectron spectroscopy (XPS). The higher N-content of NOMC-L compared to NOMC-H (Table 2.2) is a direct consequence of the higher aniline to DHN ratio employed in the former. For both NOMC materials, the N-contents measured by XPS are lower than the theoretical value. This is attributed to the observed partial loss of aniline/polyaniline during pyrolysis (*vide supra*). Nitrogen can occupy different sites within the graphitic structure of carbon materials (*N1*-*N5* in Figure 2.1).[78] Each of these nitrogen bonding configurations can be characterised based on the position of the N1s peaks in the XPS spectrum of the N-doped carbon material. The N1s signal can be deconvoluted into four peaks (Figure 2.8), which are assigned to pyridinic N (398.5 eV, *N1*), pyrrolic N (400.5 eV, *N4*), graphitic N (401.1 eV, *N2* and *N3*) and oxidised pyridinic N (> 402.8 eV, *N5*).[176,177] Both graphitic and pyridinic N atoms have been proposed to be involved in the electrocatalytic activity of N-doped carbon materials in the ORR, but the exact nature of the active sites is still debated.[93,145,153,178] Our NOMC materials present graphitic and pyridinic N atoms as the two major species, with the former being more abundant, and show similar relative amounts of each of the N-configurations (Table 2.3).

The NOMC materials discussed above were prepared with a tailored strategy involving the sequential addition and pyrolysis of aniline and dihydroxynaphthalene. To investigate whether the use of DHN in the synthesis is essential, we prepared a reference material following the same procedure used for NOMC-H and NOMC-L but without the addition of DHN (NOMC-no-DHN). The obtained material also displays an ordered, hexagonal array of carbon rods (Figure S2.2) and high specific surface area with a narrow pore size distribution centred at 4.3 nm (Table 2.1 and Figure S2.3). The absence of DHN as precursor might lead to an incomplete filling of the carbonaceous rods, which fits with the larger micropore volume of NOMC-no-DHN compared to NOMC-L (Table 2.1). The fact that NOMC-no-DHN was prepared using exclusively aniline as precursor implies that this material has a larger N-content compared to NOMC-H and NOMC-L, as proven by XPS analysis (Table 2.2 and Figure S2.4). The deconvolution of the N1s signal of NOMC-no-DHN shows that this material contains a larger fraction of graphitic N and a lower fraction of pyridinic N compared to the other NOMCs (Table 2.3 and Figure S2.4). It can be concluded that DHN does play an important role in the synthesis of the NOMC material. The physicochemical differences between these NOMCs are reflected by their different electrocatalytic performance, which will be discussed in the following section.

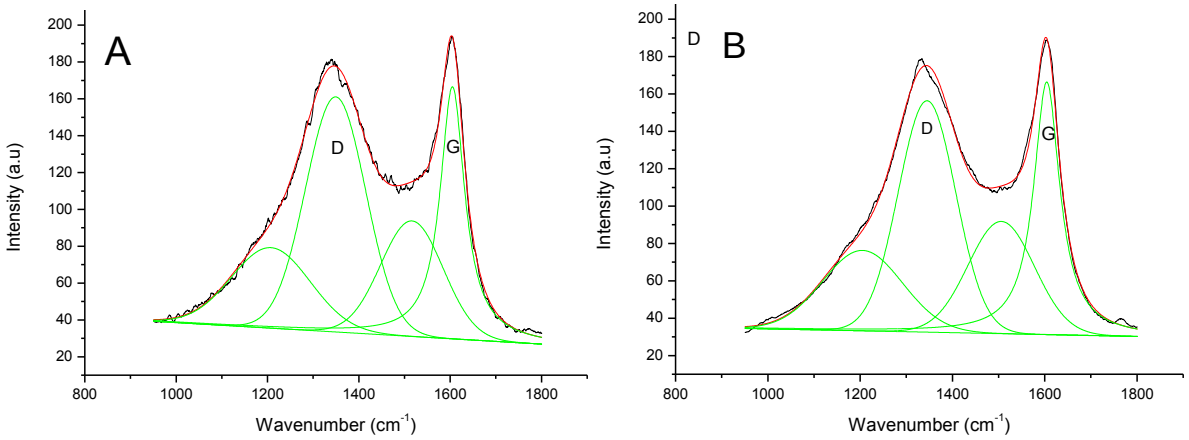

Figure 2.7. Deconvoluted Raman spectra for NOMC-H (A) and NOMC-L (B).

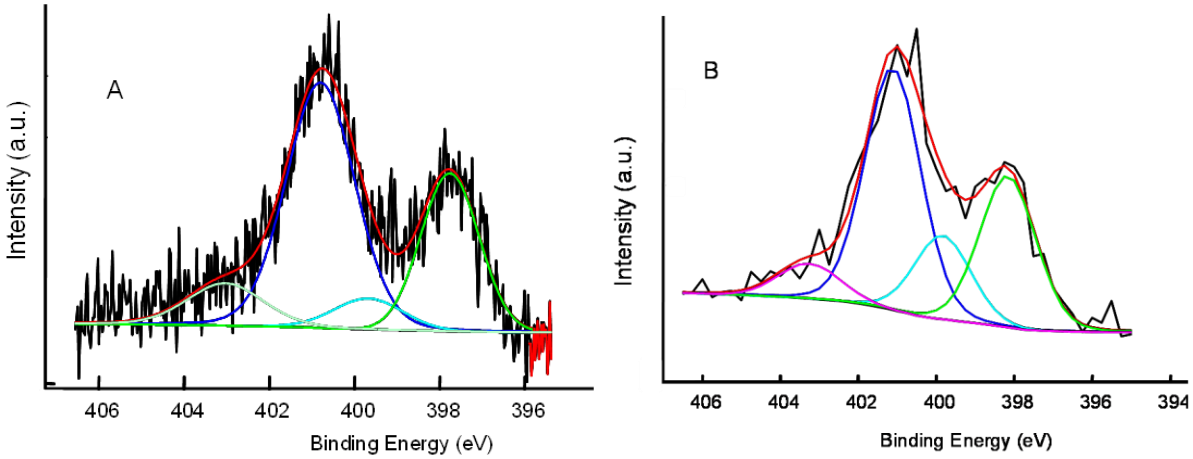

Figure 2.8. Deconvolution of the N1s XPS peak of NOMC-H (A) and NOMC-L (B).

Table 2.3. Binding energies (B.E.) and relative amounts of the various N species in the NOMCs.

	Pyridinic N (398-399.3 eV)			Pyrrolic N (399.8-401.2 eV)			Graphitic N (401.1-402.7 eV)			Oxidised pyridinic N (> 402.8 eV)		
	B.E. (eV)	Area%	wt%	B.E. (eV)	Area%	wt%	B.E. (eV)	Area%	wt%	B.E. (eV)	Area%	wt%
NOMC-H	398.0	33	0.99	399.8	11	0.34	401.0	48	1.44	403.3	7.4	0.22
NOMC-L	398.2	29	1.00	399.8	16	0.55	401.1	47	1.60	403.3	7.3	0.25
NOMC-no-DHN	398.9	26	1.48	400.2	8.9	0.51	401.7	56	3.20	403.6	8.7	0.50
wt%: weight %.												

2.3.2 Electrocatalytic performance of the NOMC materials in the ORR

The electrocatalytic activity of N-doped carbon materials in the oxygen reduction reaction is generally attributed to the higher electronegativity of N compared to C, which leads to a polarisation of the C-N bonds into $C(\delta^+)$-$N(\delta^-)$, thus altering the electronic properties of the carbon material and creating sites for interaction with O_2.[177] Moreover, the incorporation of nitrogen into the carbon material enhances its electron-donor properties.[179] Both graphitic N and pyridinic N have been proposed to contribute to the electrocatalytic activity of N-doped carbon materials, but the exact role of these two types of sites in the reaction mechanism and their influence on the selectivity towards the partial reduction to H_2O_2 or the complete reduction to H_2O are still a matter of debate.[82,91,153] The NOMC materials prepared with our two-step approach display promising features for electrocatalytic application in the ORR: they have high specific surface area and regular mesopores, a graphitic character and N atoms both in graphitic and pyridinic configuration. The performance of NOMC-H and NOMC-L as electrocatalysts for the ORR was studied in a three electrode cell set-up in an aqueous 0.1 M KOH solution. The first electrochemical analysis was performed by cyclic voltammetry (CV) under static conditions (Figure 2.9). CV curves obtained with both NOMCs show only the capacitive background of the electrochemical double layer if the electrolyte was saturated with an inert gas as N_2 (dotted curve in Figure 2.9).[180] When O_2 was introduced in the solution, two reduction peaks appeared at -0.24 and -0.84 V vs. Ag/AgCl for NOMC-L, which are characteristic for a two-step oxygen reduction reaction, with two electrons being exchanged in each step.[181] Comparing the performance of NOMC-H with that of NOMC-L, it

can be seen that the peaks are slightly shifted to less negative potentials for NOMC-L, implying a smaller ORR overpotential for NOMC-L compared to NOMC-H.

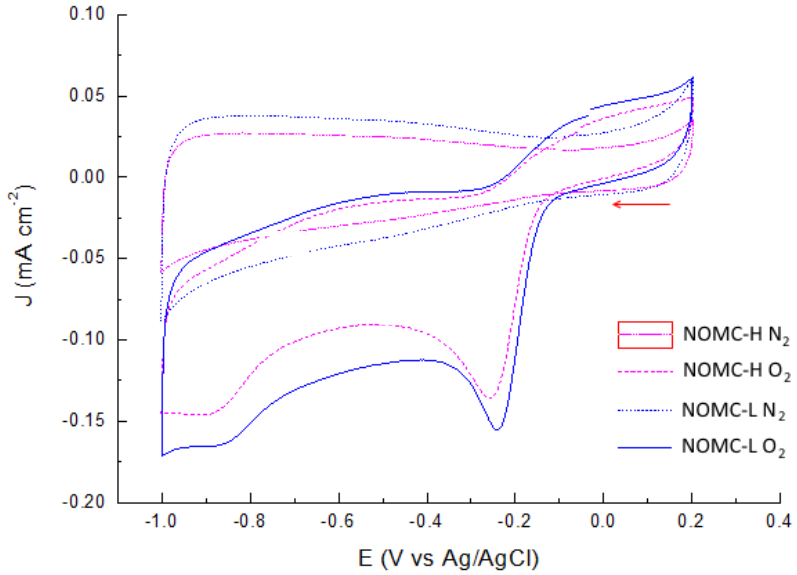

Figure 2.9. Cyclic voltammograms of NOMC-H and NOMC-L on a glassy-carbon RDE electrode in N_2 and O_2-saturated 0.1 M KOH solution between 0.2 and -1.0 V at a scan rate of 50 mV s^{-1}.

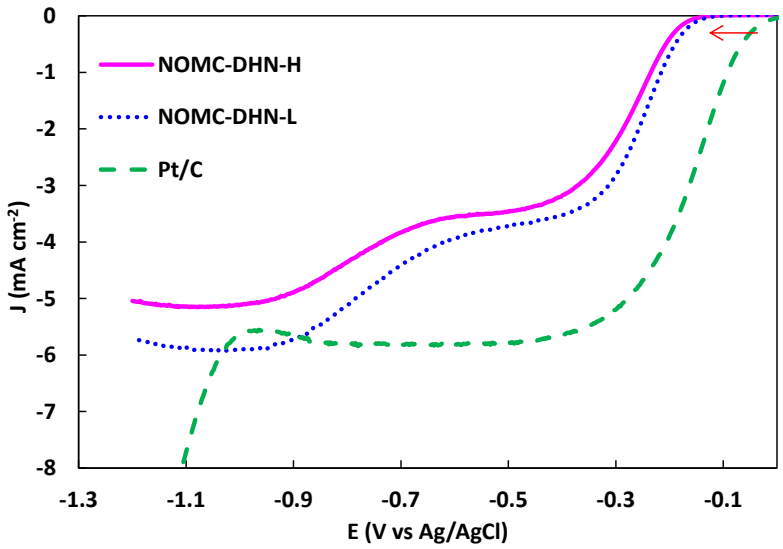

Figure 2.10. Linear sweep voltammograms for the NOMC electrocatalysts and for a standard Pt/C electrode, recorded in an O_2-saturated 0.1 M KOH solution at a scan rate of 10 mVs^{-1} and with a rotation speed of 2500 rpm.

The electrocatalytic behaviour of the two NOMCs was further investigated by linear sweep voltammetry (LSV) measurements at various rotation speeds, which were carried out in an O_2-saturated 0.1 M KOH solution in a three electrode cell set-up equipped with a rotating disk electrode (RDE). The kinetics of the reduction process for the two NOMCs were compared to those of a standard Pt/C electrocatalyst (20 wt% Pt on Vulcan XC 72, Alfa Aesar). The Pt/C electrocatalyst exhibited a one-step oxygen reduction pathway with an onset potential at 0.045 V vs. Ag/AgCl (Figure 2.10). In contrast, both NOMC electrocatalysts exhibit two reduction steps with a more negative onset potential, approximately -0.1 V for the first reduction and -0.6 V for the second reduction (Figure 2.10). The two NOMC electrocatalysts

have similar yet slightly different onset potentials, indicating that the nature of their active sites is analogous. This is in agreement with the similar relative amounts of N atoms in each of the possible configurations in the two materials (*vide supra*). NOMC-L produces a higher diffusion-limited current than NOMC-H (Figure 2.10), which is correlated to the difference in the number of exchanged electrons at the plateau (-0.5 V vs Ag/AgCl). The number of transferred electrons (*n*) in the ORR over the investigated catalysts was calculated based on the Koutécky-Levich (K-L) equations (Eq. 2.1-2.3):[79]

$$\frac{1}{J} = \frac{1}{J_K} + \frac{1}{J_D} = \frac{1}{J_K} + \frac{1}{B\omega^{1/2}} \qquad \text{(Eq. 2.1)}$$

where J is the measured current density, which is related to the kinetic current density (J_K) and the diffusion-limited current density (J_D), and ω is the angular velocity of the rotating electrode. B and J_K are given by Eq. 2.2 and 2.3:

$$B = 0.62nFC_0(D_0)^{2/3}v^{-1/6} \qquad \text{(Eq. 2.2)}$$

$$J_K = nFkC_0 \qquad \text{(Eq. 2.3)}$$

where F is the Faraday constant, *k* is the electron transfer rate constant (at a certain potential), C_0 is the bulk concentration of O_2 ($1.2 \cdot 10^{-6}$ mol cm^{-3}), *v* is the kinematic viscosity of the electrolyte (0.01cm^2 s^{-1}) and D_0 is the diffusion coefficient ($1.9 \cdot 10^{-5}$ cm^2 s^{-1}).[79]

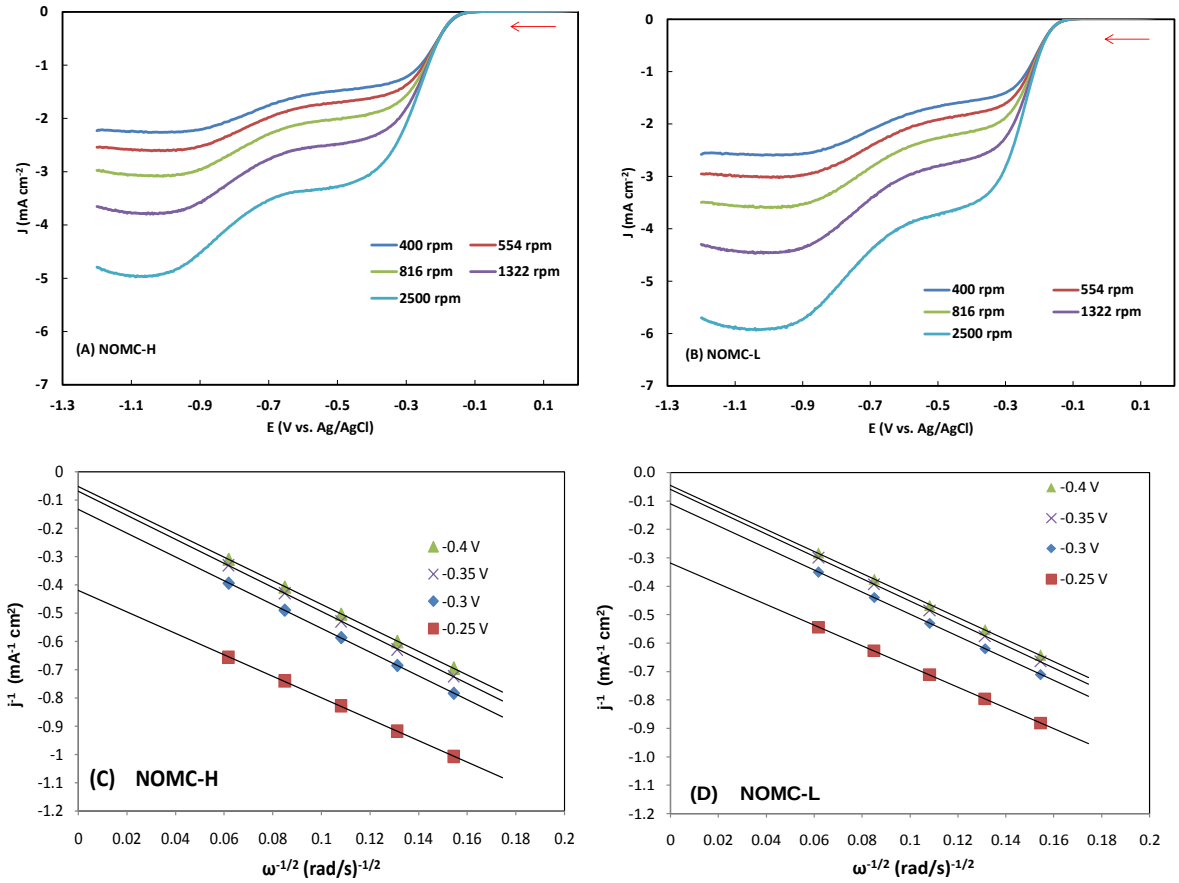

Figure 2.11. LSV curves for the NOMC electrocatalysts recorded in an O_2-saturated 0.1 M KOH solution with a scan rate of 10 mV s^{-1} at different rotation speeds (A and B), and the corresponding Koutécky-Levich plots (J^{-1} vs. $\omega^{-1/2}$) at different electrode potentials for NOMC-H (C) and NOMC-L (D).

K-L plots were generated on the basis of the LSV curves at various rotation speeds (Figure 2.11.A and B). The resulting K-L plots (Figure 2.11.C and D) for the two NOMC electrocatalysts at various potentials (from -0.25 to -0.4 V vs. Ag/AgCl) exhibit good linearity and all present very similar slopes, indicating a similar number of electrons transferred in the ORR in that potential range. The average number of exchanged electrons (*n*) calculated from the value of the slope using Eq. 2 was found to be 2.1-2.4 for the two NOMC materials in the selected potential range (Figure 2.12). These values are close to 2, indicating that H_2O_2 is produced with high selectively on our electrocatalysts. The first reaction step over the NOMCs is thus attributed to the reduction of O_2 to H_2O_2, which is an electrochemical intermediate, whereas the second step is assigned to the second 2-electron reduction reaction, where H_2O_2 is further reduced to H_2O at the electrode.[182] A well-defined plateau corresponding to the diffusion-controlled region is observed for both NOMCs between -0.4 and -0.6 V vs. Ag/AgCl in the LSV plots. The presence of this plateau means that the two reduction steps are clearly separated over these NOMCs (no mixed reactions).[176] In this work, the goal was to achieve high selectivity towards H_2O_2; hence the observed 2-electron exchange process is required. The formation of H_2O_2 during the LSV measurement was confirmed by the Merck peroxide test.[156] The number of exchanged electrons for the Pt/C catalyst was calculated to be 3.9-4.0 (Figure S2.5), which demonstrates that the 4-electron reduction of O_2 to H_2O is the main reaction on this electrocatalyst, in agreement with previous reports.[79,183]

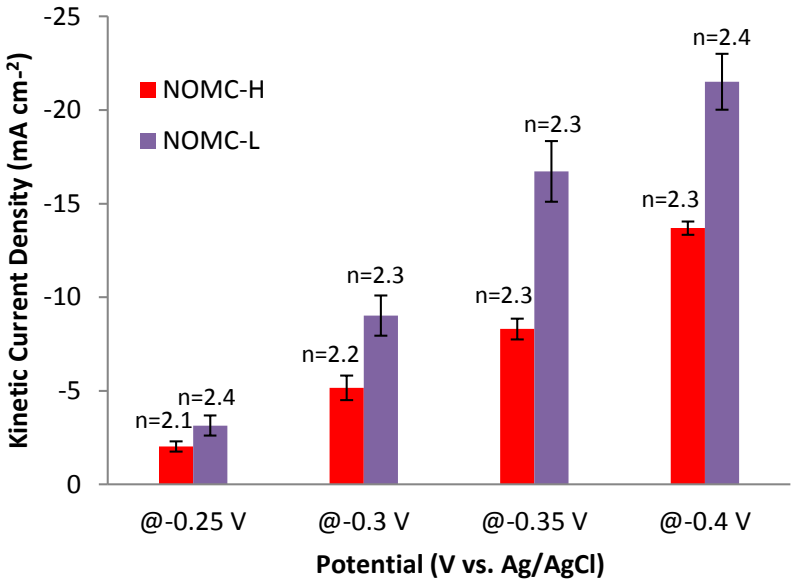

Figure 2.12. Kinetic current density and number of exchanged electrons for NOMC-H and NOMC-L at the selected potentials. All measurements were performed at least three times and the average values are reported.

The activity of the electrocatalysts was evaluated on the basis of the kinetic current density in the mixed kinetics region (-0.25 to -0.4 V vs. Ag/AgCl, see Figure 2.12). The kinetic current density at a certain potential can be determined from the intercept of the K-L plots with the y-axis (Eq. 1). NOMC-L consistently shows a better performance than NOMC-H. For NOMC-L, a J_K of -16.7±1.6 mA cm^{-2} was obtained at -0.35 V vs. Ag/AgCl, which is twice as high as that of NOMC-H at the same potential (-8.3±0.6 mA cm^{-2}). The better electrocatalytic performance of NOMC-L compared to NOMC-H can be correlated to the physicochemical

features of the two materials. NOMC-L has a higher N-content, a higher degree of graphitisation and a lower micropore volume compared to NOMC-H (Table 2.1 and 2.2). The higher N-content leads to the creation of more active sites, particularly considering that N is preferentially located at the surface of the material in our synthesis strategy. Graphitic and pyridinic N atoms are the most abundant configurations in both NOMC materials, in line with the proposed involvement of these species in the electrocatalytic activity of N-doped carbons.[178] The higher graphitic degree of NOMC-L is expected to lead to an increase in the electrical conductivity, and thus to promote a higher current density, but also to improve the durability of the electrocatalyst in the ORR.[176] Finally, it has been proposed that the ORR mainly occurs in the mesopores of the electrocatalyst, whereas micropores can be detrimental.[184] Furthermore, the unstructured carbon species that were observed in larger amounts in NOMC-H could infiltrate into the mesopores when the catalyst powder is suspended into a solution during the electrode preparation process, and this could lead to partial blockage of the mesopores thus hindering the diffusion of the reactant to the active sites. Although the NOMC with the lower amount of DHN (NOMC-L) displays better electrocatlytic performance, the use of DHN in the synthesis method is very important for the ORR activity of the NOMC. This was demonstrated by preparing an NOMC using only aniline to cover the pore surface of the SBA-15 template (NOMC-no-DHN). Linear sweep voltammetry (Figure S2.6) showed that the electrocatalytic performance of NOMC-no-DHN was markedly worse than that of the two NOMCs prepared by using DHN, as evidenced by the much lower absolute value of kinetic current density (Table 2.4). The inferior results obtained with NOMC-no-DHN can be correlated to the presence of microporosity and to the different relative amounts of N atoms with graphitic and pyridinic configuration compared to NOMC-H and NOMC-L (*vide supra*). Moreover, it has been reported that too high N-content can cause disruption of the π-system, thus reducing the electron conductivity of the material.[153] Therefore, the high N-content of NOMC-no-DHN might be detrimental to the ORR activity of the electrocatalyst. Further investigation would be required to determine the specific influence of each of these factors.

Table 2.4. Electrocatalytic properties of various N-doped carbon materials for the ORR in an alkaline electrolyte [all potentials are expressed vs. Ag/AgCl and the average values are reported for our electrocatalysts].

Entry	Electrocatalyst	J_k (mA cm^{-2})	*n*	Onset potential (V vs. Ag/AgCl)
1	NOMC-H	-8.3 at -0.35 V	2.3	-0.1
2	NOMC-L	-16.7 at -0.35 V	2.3	-0.1
3	NOMC-no-DHN	-3.1 at -0.35 V	2.3	-0.1
4	Ref. graphene oxide[185]	-3.7 at -0.5 V	2.4	-0.2
5	Ref. N-graphene oxide[185]	-4.2 at -0.5 V	2.6	-0.2
6	Ref. NOMC-750[79]	-7 at -0.35 V	2.6	-0.1
7	Ref. NOMC-900[79]	-9 at -0.35 V	3.9	-0.1

Notably, the kinetic current density obtained with NOMC-L is not only superior to that with NOMC-H and NOMC-no-DHN, but also much higher (in absolute value) than that found with previously reported N-doped carbon materials (Table 2.4 and Figure 2.12)[46,79,185] including the state-of-the-art NOMC electrocatalyst prepared using a large aromatic dye molecule,[79] which was tested under exactly the same conditions and with the same electrode loading (25 $\mu g_{catalyst}$ cm^{-2}) as used in this work. The improved kinetic current over NOMC-L compared to the NOMC from the literature is most likely caused by the higher surface area and the excellent ordering of the mesopores in NOMC-L, which both lead to an easier diffusion of O_2 through the pores and thus to enhanced accessibility of the active sites. The superior kinetic current density measured at -0.35 V over NOMC-L is even more remarkable when considering that at this potential the catalyst promotes a 2-electron reduction step (n = 2.3), while the best NOMC reported in the literature promotes a 4-electron reduction (n = 3.9, see entry 2 and 7 in Table 2.4). It can be concluded that NOMC-L is an excellent electrocatalyst for the oxygen reduction reaction to H_2O_2. The high selectivity of our NOMC materials towards the reduction of molecular oxygen to H_2O_2 indicates that during the reduction process the O-O bond of the adsorbed O_2 is not weakened to the point of causing its rupture, and the desorption of H_2O_2 after the 2-electron reduction is favoured over the further reduction to water. This is an indication that the adsorption of O_2 on the surface of our NOMCs is weaker compared to that on Pt, which is known to promote the dissociation of the O-O bond, thus leading to higher selectivity towards the complete reduction of oxygen to water.[153]

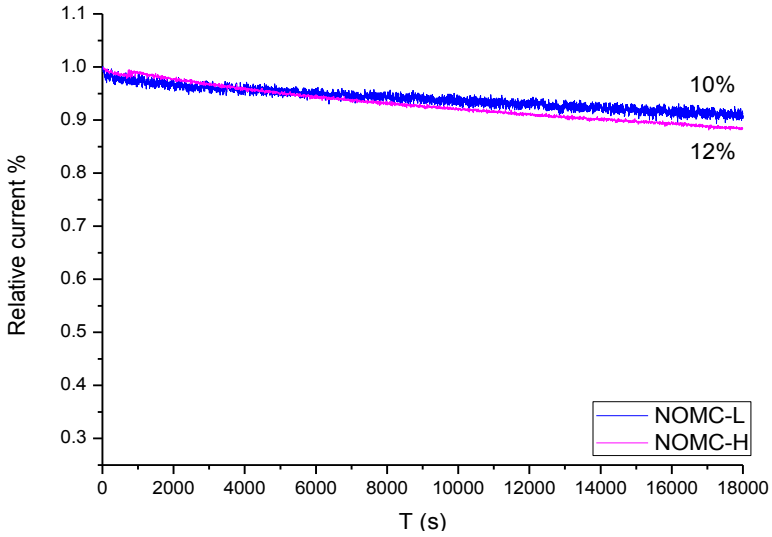

Figure 2.13. Relative current density vs. time (J-t) plot based on chronoamperometric measurements of NOMCs at -0.4 V vs. Ag/AgCl in O_2-saturated 0.1 M KOH at a rotation speed of 1600 rpm.

Finally, the stability of NOMC-L and NOMC-H was tested by chronoamperometric measurements at a constant potential of -0.4 V vs. Ag/AgCl for 5 h in a 0.1 M KOH solution saturated with O_2 at a rotation rate of 1600 rpm (Figure 2.13). Remarkably, the performance loss after 5 h was only 10% for NOMC-L and 12% for NOMC-H. This is the smallest degree of deactivation reported so far for NOMC electrocatalysts for the ORR, compared to the 15% decrease after 5 h observed with the optimum N-doped graphitic carbon material as electrocatalyst reported in the literature, and to the much more severe deactivation typically observed with standard Pt/C electrocatalysts.[79,183]

2.4 Conclusions

Metal-free N-doped ordered mesoporous carbon materials with high surface area and graphitic character were successfully prepared by means of a novel, two-step nanocasting method, and proved to be outstanding electrocatalysts for the oxygen reduction reaction. The NOMCs were synthesised with an accessible method using inexpensive N and C precursors (aniline and DHN), which is an important advantage towards the potential up-scaling of the fabrication of these materials. A careful control of the amounts of aniline and DHN and of the synthesis conditions allowed preparing a material with a high N-content (up to 3.4 wt%) and a well-defined ordered mesoporous framework consisting of interconnected N-doped carbon rods with uniform size. The best NOMC electrocatalyst achieved a much superior kinetic current density in the ORR compared to previously reported N-doped carbon materials, and displayed high selectivity for a two-electron reduction process. This is highly promising for application in a fuel cell that could produce a useful chemical as H_2O_2 while cogenerating electricity. Importantly, a chronoamperometric test demonstrated that the optimum NOMC electrocatalyst also displays high long-term stability.

Suppporting information

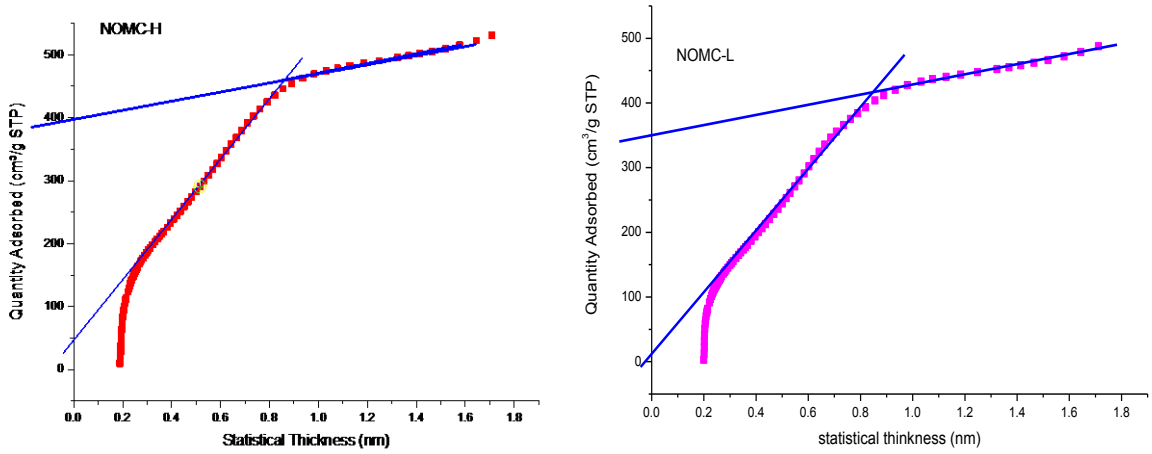

Figure S2.1. t-plot of NOMC-H and NOMC-L.

Table S2.1. Resistance of the glassy carbon disk electrode as such, or coated with an ink of NOMC-H, NOMC-L or graphite. The resistance values were obtained from impedance measurements carried out in a two-electrode setup (each reported value is the average of the results of two measurements). The counter electrode was a Pt mesh and the working electrode was a glassy carbon disk with or without an ink of NOMC-H, NOMC-L or graphite. The ink was made and applied in a similar manner as has been mentioned in the experimental part. A 0.5 M solution of sulphuric acid was used as electrolyte.

	Resistance (Ohm)
Empty glassy carbon disk	3.24 (*i.e.* equal to the resistance of the electrolyte)
Glassy carbon + graphite ink	3.63
Graphite ink	0.39
Glassy carbon + NOMC-H ink	3.53
NOMC-H ink	0.29
Glassy carbon + NOMC-L ink	3.53
NOMC-L ink	0.29

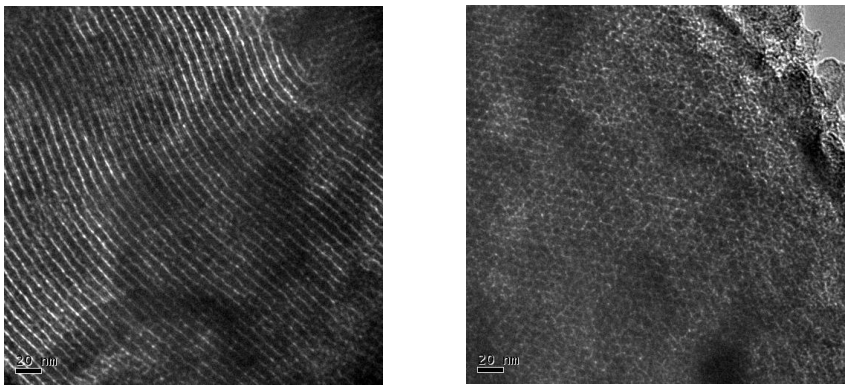

Figure S2.2. TEM images of NOMC-no-DHN.

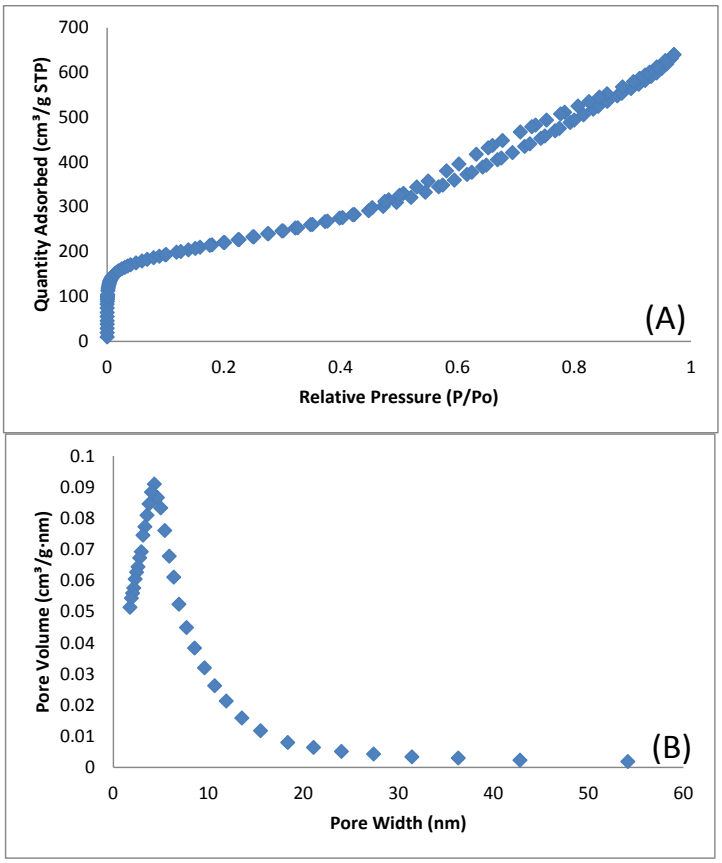

Figure S2.3. N_2 adsorption-desorption isotherms (A) and the respective BJH pore size distribution (B) for NOMC-no-DHN.

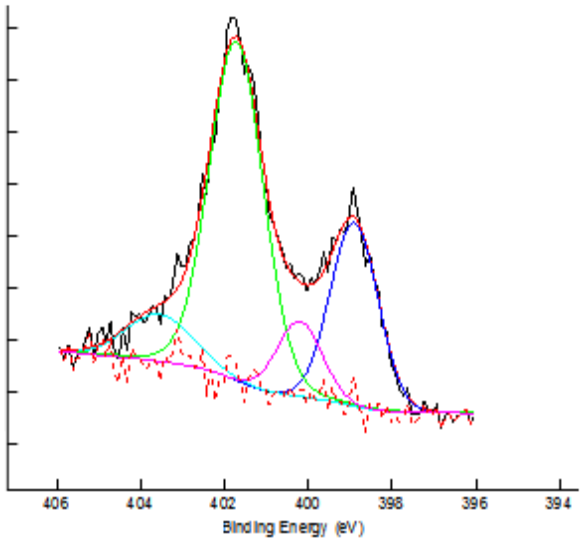

Figure S2.4. Deconvolution of the N1s XPS peak of NOMC-no-DHN.

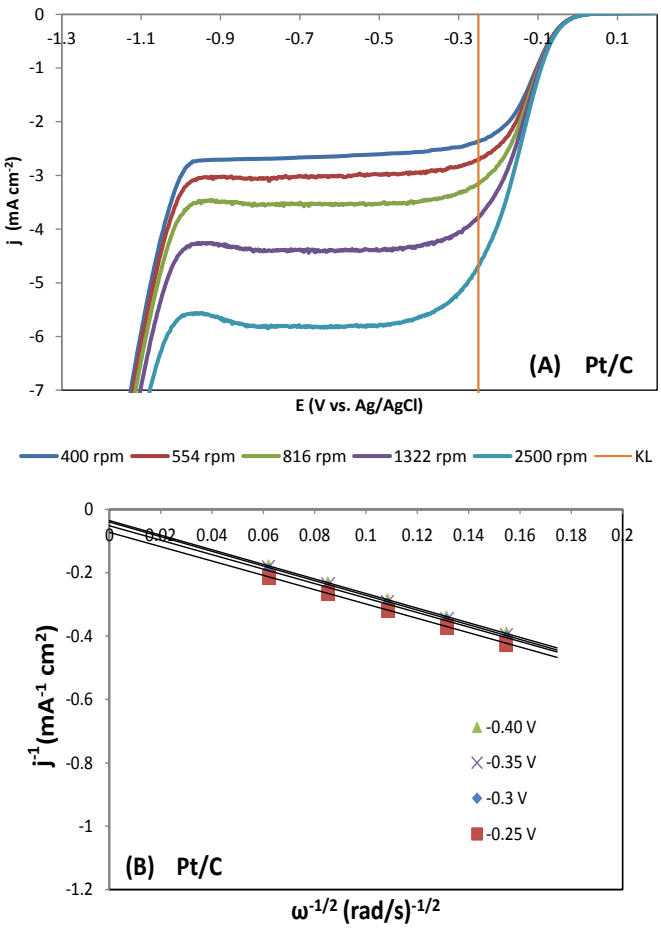

Figure S2.5. (A) RDE voltammograms of the Pt/C electrode recorded in an O_2-saturated 0.1 M solution of KOH with a scan rate of 10 mV s^{-1} at different rotation rate; (B) the corresponding Koutécky-Levich plots (J^{-1} vs. $\omega^{-1/2}$) at different electrode potentials.

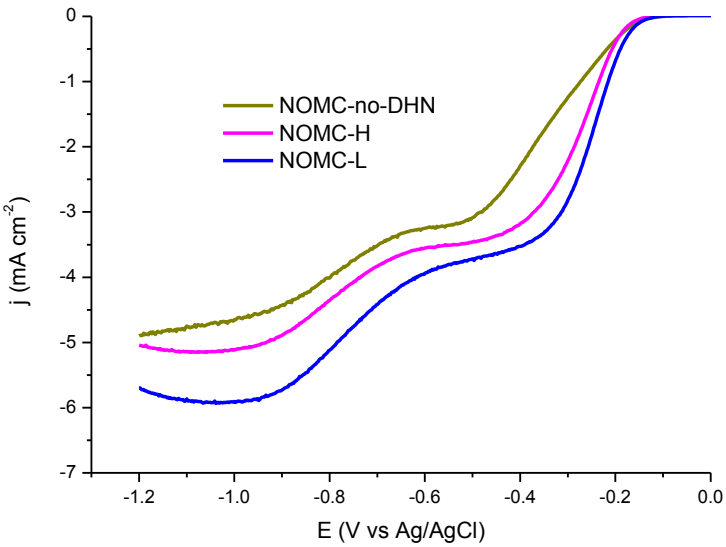

Figure S2.6. Comparison of linear sweep voltammograms of NOMC-no-DHN, NOMC-L and NOMC-H electrocatalysts, recorded in an O_2-saturated 0.1 M KOH solution at a scan rate of 10 mV s^{-1} and with a rotation speed of 2500 rpm.

Chapter 3

Influence of electrode composition and preparation on the electrocatalytic performance of N-doped ordered mesoporous carbons in the alkaline oxygen reduction reaction

Abstract

We report a systematic study of the influence of the composition and preparation method of the electrocatalyst layer deposited on the rotating (ring)disk electrodes used in the investigation of the oxygen reduction reaction (ORR). The inks used to prepare this layer consist of a suspension of the electrocatalyst and of a solution containing a binder, which can be employed in different relative and absolute amounts. In order to investigate the generally underestimated role of these factors on the ORR performance of metal-free electrocatalyts, we synthesised a nitrogen-doped ordered mesoporous carbon material through a nanocasting method. The activity and selectivity of this electrocatalyst in the oxygen reduction reaction were studied as a function of the loading of electrocatalyst and binder, of the type of binder and of the order of addition of the components of the layer. It was discovered that the use of an anion-exchange polymer (Fumion FAA-3®) as binder instead of the commonly employed proton conductive Nafion® was beneficial for the selectivity towards hydrogen peroxide. On the other hand, it was observed that the selectivity towards water increased with the catalyst loading. The formation of water could also be favoured by increasing the loading of binder (Nafion®) above 1.11 µg cm^{-2} at constant catalyst loading, although this caused a decrease in the current generation. The results of this study prove the crucial effect of the composition and preparation method of the layer on the electrocatalytic performance of NOMCs, both in terms of generated current (activity) and number of exchanged electrons (selectivity).

Based on:

N. Daems, I.F.J. Vankelecom, P.P. Pescarmona, *submitted to Journal of Power Sources.*

Author contribution

The original idea of this research was developed by N. Daems and P. P. Pescarmona. Electrocatalyst synthesis, electrochemical tests and writing of the article were done by N. Daems. Valuable discussions to understand and interpret the results were held with P. P. Pescarmona, who also supervised the whole work together with I.F.J. Vankelecom.

3.1 Introduction

In recent years, research about renewable energy sources has experienced a considerable boost mainly due to the rising societal awareness concerning greenhouse gas emissions and their environmental impact. Another important factor driving this research is the fossil fuel depletion.[186] In this context, increasing research endeavours focussed on proton exchange membrane fuel cells (PEMFCs), which generate electricity by exploiting the energy liberated by the electrochemical reduction of oxygen coupled to the oxidation of hydrogen. However, the commercialisation of these fuel cells is still hampered by the high cost and the poor stability of the oxygen reduction reaction (ORR) electrocatalysts, which are currently based on supported nanoparticles of Pt or Pt-alloys. These limitations stimulated the search for alternative electrocatalysts for the ORR.[150,151,153,187] Initially, the attempts mainly focused on pyrolysed carbon-supported transition metal complexes, but neither the stability nor the activity of these electrocatalysts reached the desired levels. The research further shifted to metal-free doped carbon materials, which reached similar ORR performance to the Pt-based electrodes in alkaline environments, but much higher long-term stability. In acidic environment they are not yet competitive enough to replace Pt-based electrodes.[78,154–156]. Both in acidic and in alkaline environment, the reduction of O_2 to H_2O can occur either through a direct mechanism involving the transfer of four electrons (3.1) or via a sequential mechanism with hydrogen peroxide as an intermediate (3.2).

$O_2 + 4H^+ + 4e^- \longrightarrow 2H_2O$		(pH < 7)	$E^\circ = 1.23$ V	(Eq. 3.1)
$O_2 + 2H_2O + 4e^- \longrightarrow 4OH^-$		(pH > 7)	$E^\circ = 0.40$ V	
$O_2 + 2H^+ + 2e^- \longrightarrow H_2O_2$		(pH < 7)	$E^\circ = 0.70$ V	(Eq. 3.2A)
$O_2 + H_2O + 2e^- \longrightarrow HO_2^- + OH^-$		(pH > 7)	$E^\circ = -0.08$ V	
$H_2O_2 + 2H^+ + 2e^- \longrightarrow 2\,H_2O$		(pH < 7)	$E^\circ = 1.78$ V	(Eq. 3.2B)
$HO_2^- + H_2O + 2e^- \longrightarrow 3OH^-$		(pH > 7)	$E^\circ = 0.87$ V	

If the sole purpose of the fuel cell is to generate electricity, an ideal electrocatalyst should promote the complete reduction with formation of water as final product. In this context, the formation of H_2O_2 is considered a drawback as it lowers the current generated per oxygen molecule. Furthermore, the decomposition of H_2O_2 releases radicals, which are known to damage the Nafion® membranes commonly applied in PEMFCs.[111,188–191] On the other hand, hydrogen peroxide is an industrially relevant chemical product (worldwide annual production of 3.8 million tonnes[192]) that can be used as a green oxidant in a broad range of applications.[9] Therefore, the selective reduction of O_2 to H_2O_2 can also be attractive from an economic point of view since it would allow cogeneration of electricity and of an industrially important commodity product.[187]

Due to the existence of Nafion® (a sulphonated fluoropolymer based on a tetrafluoroethylene backbone) as a commercially available, high-performance proton-exchange membrane, PEMFCs are the fuel cells that have received the most attention thus far. However, since it has been discovered that alkaline fuel cells allow the use of a much broader range of electrocatalytic materials for the ORR,[188] there has been an increased interest towards alkaline ORR[79,153] and anion exchange membranes.[134,193–195] In alkaline environment, anions have lower tendency to adsorb on the less positively charged electrode surface (due to the fact that the electrode potential is ~0.83V lower in alkaline medium).[196] This results in a higher number of available active sites for interacting with O_2.[197–199] Moreover, in alkaline environment the ORR can also take place through outer sphere reactions, which do not require O_2 to adsorb prior to reduction. In this mechanism, the bonds that are formed between mildly adsorbed OH^- ions and solvated oxygen allow tunnelling of

electrons from the electrode to the oxygen molecules and result in a faster initiation of the reaction.[188,196,200]

The expected impact of fuel cells and the challenges summarised above explain the growing research efforts dedicated to the development of enhanced electrocatalysts for the ORR.[34,46,78,153,201,202] Generally, the activity and selectivity of novel electrocatalysts in the ORR are first investigated with a rotating disk electrode (RDE) or a rotating ring-disk electrode (RRDE) in a half-cell setup.[203] Only the best performing materials are then used in membrane electrode assemblies (MEA), which are evaluated in complete fuel cells. Both the RDE and the RRDE techniques directly result in data on the ORR activity. With the RRDE technique, the selectivity can also be determined directly from the experiments based on a comparison of the ring and the disk current. The RDE uses the Koutécky-Levich equations to estimate the selectivity[204] based on the number of exchanged electrons. While these techniques allow an easy evaluation of the ORR performance, they may result in contradictory results (especially for the selectivity) for the same electrocatalyst.[150,205] This is a consequence of the variety of different conditions in which the electrocatalysts are tested. Important factors influencing the electrocatalytic performance are the scan rate (at higher rates slower reactions might be inhibited), the electrolyte type and concentration (acidic vs. alkaline; KOH vs. NaOH) and, most critically, the composition of the catalyst ink and the preparation of the electrode.[197,206] A study by Jin *et al.* on the influence of the electrolyte composition on the ORR performance revealed that the electrocatalytic activity decreases at increased electrolyte concentrations. This lower activity was ascribed to a lower oxygen solubility and diffusivity in the more viscous electrolytes. Furthermore, it was observed that KOH resulted in higher oxygen solubilities and diffusivities than NaOH, irrespective of the alkaline concentration.[198] The influence of the ink composition (e.g. solvent, binder content,[207] catalyst content[191,205] and duration of sonication) and of the electrode manufacturing (e.g. amount of ink added,[191] drying temperature and atmosphere) on the ORR behaviour were investigated for different metal-based electrocatalysts. The parameter that has probably the largest influence on the ORR performance of electrocatalyst is its loading on the electrode. Several studies have shown that the selectivity towards water increases with the loading of the electrocatalyst. This can be rationalised considering that at higher loadings the electrocatalyst layer is thicker and the produced H_2O_2 has to travel a larger distance prior to its release in the electrolyte: therefore, the probability to encounter another active site that promotes its further reduction to water increases.[97,190,191,205] However, if the ORR follows the direct four electron reduction mechanism, the amount of H_2O_2 that is generated should be insensitive to the catalyst loading since every O_2 molecule is adsorbed and reduced on the same active site without leaving it. By varying the catalyst loading, it is thus possible to discriminate between the direct four electron reduction and the sequential mechanism with H_2O_2 as an intermediate.[208] Another important factor is the influence of the binder content, which is typically an ionomer (e.g. Nafion®) that acts as binder for fixing the electrocatalyst on the glassy carbon support in the RDE and RRDE. The binder loading should be sufficiently high to prevent the electrocatalyst from falling off at high rotation speeds, though very high loadings should be avoided too, since they impose a higher transport limitation as a result of the larger distance that oxygen has to travel to reach the active site.[188,209] A more recent study showed that also the conductivity of the electrocatalyst itself has an impact on the selectivity. By varying the conductivity of a perovskite oxide or by adding different amounts of a conductive carbon, it was discovered that a more conductive environment resulted in a higher selectivity towards water ($4e^-$-pathway).[210]

Based on the above, it is important to investigate the influence of the ink composition and the electrode fabrication method on the overall ORR performance. While the role of some of these parameters has already been explored for Pt-based electrocatalysts,[211] non-noble metal-containing electrocatalysts[191] and CN_x materials,[205,206] a systematic study of all the relevant parameters is still lacking. Moreover, no study so far addressed the effect of the composition and preparation method of the electrocatalyst layer for the newer and very promising class of electrocatalysts consisting of N-doped ordered mesoporous carbons (NOMCs). Therefore, we decided to study the influence of the composition and fabrication method of the electrocatalyst layer on a NOMC that was previously developed by our group and that exhibited excellent activity and selectivity as electrocatalyst for the cogeneration of electricity and hydrogen peroxide in a fuel cell.[187] Based on the information that could be found in the literature (*vide supra*) and since the investigated electrocatalyst is devoid of metals, the study was performed in an alkaline environment and more specifically with an aqueous 0.1 M KOH solution as electrolyte. The influence of the binder and the catalyst loading (both at constant binder content and at constant binder-to-catalyst ratio) and the binder type were systematically evaluated over a wide range of values. Finally, we studied the effect of using an ink that contains both the binder and the catalyst instead of the conventional two-step preparation (catalyst and binder added separately). To prepare the inks, a 1:1 isopropanol:water volume mixture was chosen since a previous study demonstrated that this composition leads to the most stable suspensions (up to days without settling).[42]

3.2 Experimental

3.2.1 Synthesis of the electrocatalyst

A detailed description of the synthesis method of the NOMC electrocatalyst has been reported elsewhere.[187] A brief summary is given here. First, the SBA-15 mesoporous silica used as hard template was synthesised, calcined and impregnated with aniline. After polymerisation, the material was subjected to a first pyrolysis step for 3h at 900°C and the remaining pore volume was filled up with dihydroxynaphthalene, followed by a second pyrolysis step for 5h at 900°C. In a final step, the template was etched away by treatment with a 2.5 wt% solution of NaOH in EtOH/H_2O to obtain the N-doped ordered mesoporous carbon material that was used as electrocatalyst in this study.

3.2.2 Electrochemical study

The electrocatalytic performance of the NOMC in the oxygen reduction reaction as a function of the composition and fabrication method of the electrocatalyst layer was evaluated by means of linear sweep voltammetry (LSV) carried out with a rotating ring disk electrode (RRDE). LSV measurements were conducted at various rotation speeds (400-2500 rpm). The experiments were carried out at room temperature in a conventional three-electrode cell from Gamry with a modulated speed rotator of Pine and a rotating ring disk electrode connected to a Gamry Interface 1000 bipotentiostat. An Ag/AgCl (saturated KCl, E° = 0.197 V vs. SHE) reference electrode was used in combination with a Pt gauze counter electrode. The internal salt bridge of the reference electrode was filled with 0.1 M aqueous KOH. A glassy carbon, replaceable disk with a surface area of 0.196 cm^2 was employed as inert carrier for the working electrode. A Pt ring was used to detect and quantify the hydrogen peroxide that is produced during the ORR. The ORR was performed in an aqueous 0.1 M KOH electrolyte, which was previously saturated with O_2 by bubbling O_2 gas into the solution

for 30 min. Afterwards, O_2 saturation was maintained by a flow of O_2 just above the electrolyte during the whole voltammetry experiment. The potential of the disk was varied from 0.1 to -1.2 V vs. Ag/AgCl at a potential sweep rate of 10 mV s^{-1}. The Pt-ring potential was kept constant at 0.5 V, which is positive enough to reoxidise all the produced hydrogen peroxide back to oxygen. The ring currents are thus an indication for the hydrogen peroxide production.

The current densities were calculated based on the geometric surface area of the glassy carbon electrode as the actual surface area cannot be determined accurately. The actual surface area is a function of the specific surface area of the electrocatalyst, and of the amounts of electrocatalyst and of binder that are deposited on the disk. This implies that the obtained values of kinetic current density include contributions of both the intrinsic activity (per surface unit) and of the surface area of the electrocatalyst.[23]

The standard electrocatalyst ink solution was prepared by suspending 2 mg of electrocatalyst in 1.5 ml of a 1:1 volume mixture of isopropanol and water. This ink was sonicated for 1 h to obtain a homogeneous suspension. 3.47 µL ± 0.04 µL of electrocatalyst ink was then deposited with a pipette (Finnpipette F1, 0.5-5 µl) onto the disk surface, yielding an approximate catalyst loading of 25 µg cm^{-2}. After drying, a thin Nafion® film was applied by depositing 4.86 µl ± 0.04 µL of a 0.05 wt% Nafion® solution in 50/50 vol% isopropanol/water with the same type of pipette, followed by a final drying step at room temperature giving an approximate Nafion® loading of 1.11 µg cm^{-2}.

The standard procedure described above was modified in different ways to investigate the influence of various parameters on the ORR performance. First of all, the influence of the binder type was studied by employing either polystyrene sulphonic acid or Fumion FAA-3® ionomer from Fumatech instead of Nafion® (with a loading of 1.11 µg cm^{-2} in all cases). Next, the influence of the binder (Nafion®) loading on the performance was investigated by applying Nafion® loadings in a range from 0 to 44.4 µg cm^{-2}. The effect of the catalyst loading was also investigated by varying the final loading from 10 to 1000 µg cm^{-2}, either at a constant Nafion® loading (1.11 µg cm^{-2}) or at a constant electrocatalyst-to-Nafion® mass ratio (22.5). In all these studies, the different loadings were achieved by depositing different volumes of the standard electrocatalyst suspension and binder solution described above. A final variation to this standard method was made by adding both Nafion® and electrocatalyst to the same ink and adding them to the glassy carbon disk at the same time without modifying the final electrode composition.

All measurements were performed in duplicate and the average values and standard deviations are reported. For the onset potential and the half-wave potential the standard deviation was never larger than 0.01 and is therefore not reported in the rest of the paper.

The water uptake of Nafion® and Fumion FAA-3® were determined by immersing a sample (3 x 3 cm) that was cut from a commercial membrane (186 µm for Nafion® and 30 µm thickness Fumion FAA-3®) in a 250 ml beaker containing 125 ml of boiling water.

$$\text{Water uptake} = \frac{m_{wet} - m_{dry}}{m_{dry}} 100\% \qquad \text{(Eq. 3.3)}$$

where m_{dry} is the mass of the membrane sample after drying at 50°C in a vacuum oven overnight and m_{wet} is the mass of the membrane sample after equilibration for 1 h in boiling water at 100°C.

3.3 Results and discussion

We studied the influence of the ink composition and electrode fabrication method on the ORR activity and selectivity of an NOMC electrocatalyst with high surface area (764 m^2 g^{-1}) and uniform mesopores (average diameter of 3.3 nm).[187] The activity was assessed on the basis of the onset potential, the half-wave potential ($E_{1/2}$) and the kinetic current density measured with a rotating ring disk electrode in a half-cell setup. The onset potential was determined as the potential at which the current density exceeds 10μA cm^{-2} in the LSV plots. The onset potential is not expected to experience major influence from the investigated parameters since in principle it should only depend on the type of active sites. The half-wave potential was determined as the potential at which the first derivative of the LSV plots with respect to the potential reaches a maximum. The kinetic current density was determined based on the Koutécky-Levich (K-L) equations (3.4-3.6):

$$\frac{1}{J} = \frac{1}{J_K} + \frac{1}{J_D} = \frac{1}{J_K} + \frac{1}{B\omega^{1/2}} \quad \text{(Eq. 3.4)}$$

where J is the measured current density, which can be expressed in terms of kinetic current density (J_K) and diffusion-limited current density (J_D). ω Is the angular velocity of the RRDE. B and J_K are defined as follows:

$$B = 0.62nFC_0(D_0)^{2/3}v^{-1/6} \quad \text{(Eq. 3.5)}$$

$$J_K = nFkC_0 \quad \text{(Eq. 3.6)}$$

where F is the Faraday constant (96485 C mol^{-1}), *k* is the electron transfer rate constant (at a given potential), C_0 is the bulk O_2 concentration (1.2 x 10^{-6} mol cm^{-3}), v is the kinematic viscosity of the electrolyte (0.01 cm^2 s^{-1}) and D_0 is the diffusion coefficient of O_2 (1.9 x 10^{-5} cm^2 s^{-1}).[187] The kinetic current density can be determined from the intercept of the K-L plots.

The selectivity was assessed based on the number of exchanged electrons (*n*), which can be determined from the slope of the K-L plots, and on the amount H_2O_2 that is detected on the Pt ring, using the following equation:

$$\text{Sel.}H_2O_2(\%) = \frac{200 \times I_{ring}}{(N \times I_{disk}) + I_{ring}} \quad \text{(Eq. 3.7)}$$

where I_{ring} and I_{disk} are the currents collected on the Pt ring and on the catalyst-coated disk, respectively. N is the collection efficiency and was determined to be 0.22 for our RRDE system (electrocatalyst included) by using the Fc/Fc^+ redox couple. Equation (7) is valid under the assumption that only H_2O_2 and H_2O are produced from the oxygen reduction. The values of *n*, J_K and Sel.H_2O_2(%) were all determined at -0.35 V vs. Ag/AgCl, as this potential corresponds to the mixed kinetic-diffusion regime.[24,212]

3.3.1 Role of the type of ionomer used as binder

The influence of the type of ionomer that is used to bind the catalyst to the glassy carbon disk on the ORR performance was investigated here for the first time (Table 3.1 and Fig. S3.1, S3.2). A binder is utilised to grant the adhesion of the catalyst to the RDE at all employed rotation speeds. Ionomers were used as binders as this would facilitate the later application in an actual fuel cell, in which a ionomer is essential to transfer either protons or hydroxide ions between anode and cathode compartments. In this work, besides the most commonly applied Nafion® binder we studied another proton-conductive polymer, polystyrene sulphonic acid (PSSA) and a hydroxide-conductive polymer (Fumion FAA-3®). PSSA was

investigated to determine whether this cheaper proton-conductive ionomer could offer a similar performance to Nafion®. Fumion FAA-3® was chosen because PSSA and Nafion®, being both proton-conductive, would not be suitable for the membrane electrode assembly (MEA) in an alkaline fuel cell, which requires the transfer of hydroxide ions. While this investigation is important in view of a perspective application in an actual fuel cell, we also aim at finding out if the use of an anion- or a proton-exchange polymer has an influence on the ORR performance at the level of half-cell tests.

Table 3.1. Effect of the binder type on the ORR performance of the NOMC electrocatalyst, at -0.35 V vs. Ag/AgCl and recorded in an O_2-saturated 0.1 M KOH solution with a scan rate of 10 mV s^{-1} at 2500 rpm.

	n	J_K (mA cm^{-2})	Sel.H_2O_2 (%)	E_{Onset} (V)	$E_{1/2}$ (V)
Nafion®	2.2±0.1	-10.1±0.7	92±1	-0.07	-0.27
PSSA	2.2±0.1	-7.3±0.5	92±2	-0.05	-0.28
Fumion FAA-3®	2.0±0.1	-6.6±0.4	100±1	-0.04	-0.27

As expected, the onset potential did not vary considerably when the ionomer type was changed, though the difference in onset potential between Fumion FAA-3® and Nafion® seems statistically significant. On the other hand, the kinetic current density differed significantly between the three ionomers. We attribute the higher kinetic current density observed with Nafion® compared to Fumion FAA-3® to the higher affinity for water of the former, as indicated by the measured values of water uptake (37 wt.% for Nafion® and 26 wt.% for Fumion FAA-3®). A higher water uptake implies that more dissolved oxygen can reach the active sites. In turn, this can result in a higher kinetic current density. Also the ionic conductivity of the ionomers can be used to explain the influence of the binder type on the electrocatalyst performance. A proton-conductivity of 100 mS cm^{-1} has been reported for Nafion®,[213] whereas the value reported for PSSA was 70 mS cm^{-1}.[214] A hydroxide-conductivity of 50 mS cm^{-1} was measured for Fumion FAA-3®.[215] Based on the data available in literature the higher ion conductivity for Nafion® is directly related to the higher water uptake.[216,217] Although the trend in ion-conductivity corresponds to that followed by the kinetic current density (Table 1), it should be kept in mind that potassium ions rather than protons are expected to be transported through Nafion® and PSSA in the employed KOH solution.

The selectivity of the ORR shifted towards hydrogen peroxide (higher Sel.H_2O_2(%) and *n* closer to two, Table 3.1) when Fumion FAA-3® was used. This behaviour can be rationalised considering the different nature of the ionomer backbone, which is positively charged in Fumion FAA-3® and negatively in the other two. The positive charge can allow a faster removal of hydrogen peroxide, which is present as HO_2^- in an alkaline environment, from the active layer. On the other hand, the negatively charged backbone of Nafion® and PSSA can favour the retention of the HO_2^- ions for a longer time in the catalyst layer due to electrostatic repulsion, thus increasing the probability of further reduction of the peroxide anion to water.

These results demonstrate that the ionomer does not only play a role as binder but also significantly influences the ORR performance, both in terms of activity and selectivity of the electrocatalyst.

3.3.2 Influence of the binder loading

Besides the nature of the binder used in the ink, also its loading is expected to have a relevant impact on the electrocatalytic performance. Previous reports on silver nanowires and Pt/C demonstrated that the use of a binder is essential to guarantee the adhesion of the electrocatalyst to the electrode.[188,209] However, it is important that the ionomer loading is not too high, as this is generally detrimental for the ORR performance.[188,209] These observations were confirmed in this study for the NOMC using Nafion® as binder (see Figure 3.1, S3.3, S3.4 and Table 3.2).

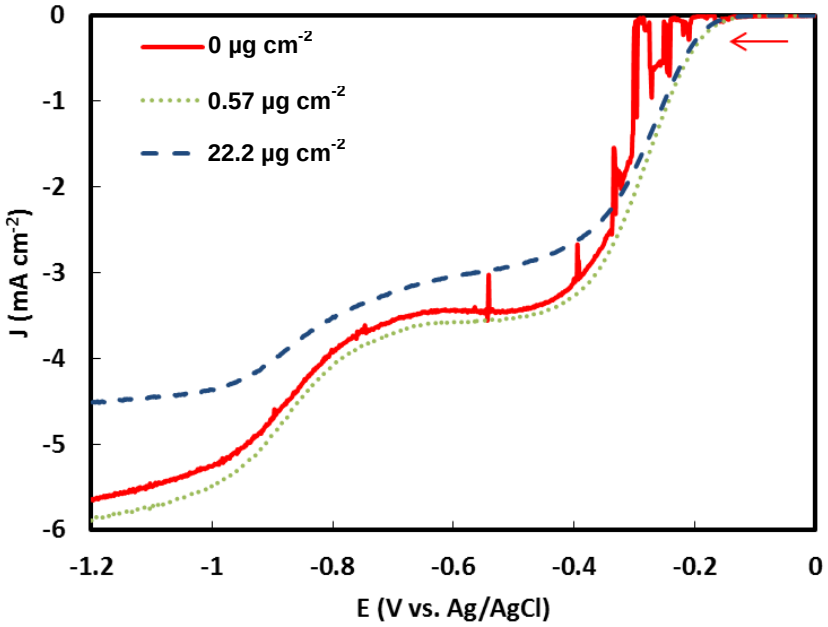

Figure 3.1. Impact of Nafion® loading on the electrocatalytic performance of NOMC, measured on a RRDE in an O_2-saturated 0.1 M KOH solution with a scan rate of 10 mV s^{-1} at 2500 rpm. The red arrow indicates the scan direction.

At high rotation speeds (2500 rpm) a high level of noise could be observed in the LSV plots for the electrodes prepared without Nafion® (Fig. 3.1), which was consistent with the observed release of the catalyst from the RRDE. This proves that a binder is necessary for the adhesion of the NOMC electrocatalyst to the electrode. A loading as low as 0.56 µg cm^{-2} is sufficient to efficiently attach the electrocatalyst to the electrode, so that it does not peel off even at high rotation rates. At low loadings, the impact of the binder on the electrocatalytic performance is negligible, as can be seen by comparing the results for binder loadings ≤ 1.11 µg cm^{-2} (Table 3.2 and Fig. 3.1 & S3.3). On the other hand, when the loading of binder is ≥ 2.22 µg cm^{-2}, it negatively influences the kinetic current density and the overall current generation (Table 3.2 and Fig. 3.1 & S3.3). This can be explained by the increased oxygen transport limitations, which are imposed by the thicker Nafion® layer. At this thickness, the diffusion of the oxygen molecules through the binder becomes slower than the actual reaction rate at the electrocatalyst surface, thus limiting the measured reaction rate.

Table 3.2. Influence of Nafion® loading on the ORR performance of the NOMC electrocatalyst, at -0.35 V vs. Ag/AgCl and recorded in an O_2-saturated 0.1 M KOH solution with a scan rate of 10 mV s^{-1} at 2500 rpm.

Loading (µg cm^{-2})	*n*	J_K (mA cm^{-2})	Sel.H_2O_2 (%)	E_{Onset} (V)	$E_{1/2}$ (V)
0	/	/	/	/	/
0.56	2.2±0.1	-9.9±0.2	91±1	-0.07	-0.28
1.11	2.2±0.1	-10.1±0.3	92±1	-0.07	-0.27
2.22	2.5±0.2	-4.6±0.5	74±2	-0.07	-0.31
22.2	2.7±0.1	-4.8±0.3	65±1	-0.06	-0.30
44.4	/	/	/	/	/

The onset potential does not differ significantly as a function of the binder loading and this means that the trend in the half-wave potential is connected to that of the kinetic current density (Table 3.2). For the electrodes prepared without Nafion®, the values for the different parameters could not be determined because of the noise. The selectivity towards hydrogen peroxide decreases (*n* increases, Sel.H_2O_2(%) decreases, see Table 23.) with an increase of the Nafion® loading above 1.11 µg cm^{-2}. This is attributed to electrostatic repulsion (*vide supra*): the thicker the Nafion® layer, the longer the HO_2^- ions will be retained in the catalytically active layer, thus favouring their further reduction. Finally, a Nafion® loading of 44.4 µg cm^{-2} was too high to generate any current. Most likely, the layer that oxygen had to cross to reach the active site became so thick as to fully prevent the ORR.

3.3.3 Influence of the electrocatalyst loading

The impact of the electrocatalyst loading on the ORR performance was investigated to determine which reduction mechanism, i.e. the direct four electron reduction or the stepwise two electron reduction with hydrogen peroxide as an intermediate, is the dominant one over the NOMC. A previous study showed that the number of exchanged electrons should not differ in function of the electrocatalyst loading if the four electron reduction mechanism is followed.[208] Since the selectivity towards water increases at higher catalyst loadings (*n* closer to 4 and lower Sel.H_2O_2(%), see Table 3.3 and Fig. S3.6), it is concluded that the path involving hydrogen peroxide as an intermediate is predominant in the ORR catalysed by our NOMC in basic medium. This is a consequence of the longer residence time of reagent and products in the active layer, which leads to a higher probability of the formed peroxide to encounter another active site and to get reduced further to H_2O prior to being released.

The overall current also increases with the electrocatalyst loading (Figure 3.2 and S3.5 to S3.7). The same trend is followed by the kinetic current density (up to 100 µg cm^{-2}, see Table 3.3). This increase is not only due to the higher number of active sites that is available at higher loadings, but also to the observed increase in number of exchanged electrons at higher electrocatalyst loading (J_K is proportional to *n*). If the magnitude of the current density is plotted as a function of the catalysts loading (Fig. 3.3), the first increase in electrocatalyst loading (from 10 to 22 µg cm^{-2}) leads to the expected increase in J_K (assuming proportionality to both catalyst loading and *n*). This is not the case if the electrocatalyst loading is further increased, which suggests that the reaction rate becomes limited by the rate of transport of O_2 to the catalyst.

Finally, since the type of active site did not differ when modifying the electrocatalyst loading, the onset potential did not change significantly either. Therefore, the trend in half-wave potential follows that of the kinetic current density. For the electrocatalyst loading of 1000 µg cm^{-2}, a decrease in *n* and J_K was observed. This was caused by the detachment of the electrocatalyst from the RRDE, which was visually observed at high rotation rates (> 2000 rpm). The Nafion® content was thus not sufficiently high to bind all the active material on the electrode at these rotation rates. This result stimulated us to explore also the influence of the electrocatalyst loading on the ORR performance at constant electrocatalyst-to-Nafion® ratio (see Table 3.4 and figure S3.8 and S3.9).

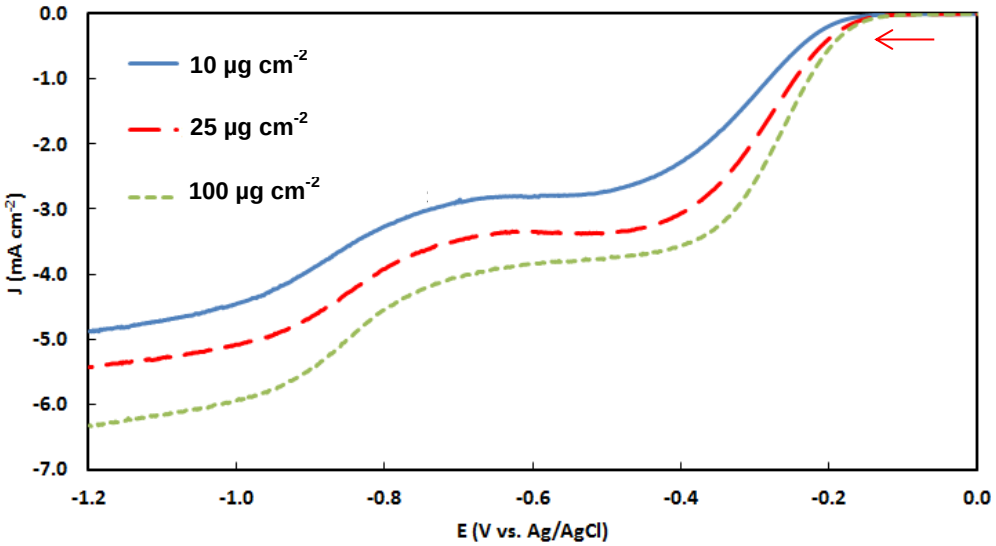

Figure 3.2. Impact of catalyst loading on the electrocatalytic performance of NOMC, recorded on a RRDE in an O_2-saturated 0.1 M KOH solution with a scan rate of 10 mV s^{-1} at 2500 rpm and at constant Nafion® loading (1.11 µg cm^{-2}). The red arrow indicates the scan direction.

Table 3.3. Influence of the electrocatalyst loading on the ORR performance of NOMC at constant Nafion® loading of 1.11 µg cm^{-2}, at -0.35 V vs. Ag/AgCl and recorded in an O_2-saturated 0.1 M KOH solution with a scan rate of 10 mV s^{-1} at 2500 rpm.

Loading (µg cm^{-2})	*n*	J_K (mA cm^{-2})	Sel.H_2O_2 (%)	E_{Onset} (V)	$E_{1/2}$ (V)
10	2.0±0.1	-3.8±0.2	99±1	-0.06	-0.31
22	2.2±0.1	-9.9±0.5	92±1	-0.06	-0.26
25	2.2±0.1	-10.1±0.3	92±1	-0.07	-0.27
50	2.6±0.2	-11.5±0.6	73±2	-0.05	-0.24
100	2.7±0.2	-13.7±1.2	67±2	-0.06	-0.24
1000	2.3±0.4	-6.4±0.5	85±5	-0.06	-0.31

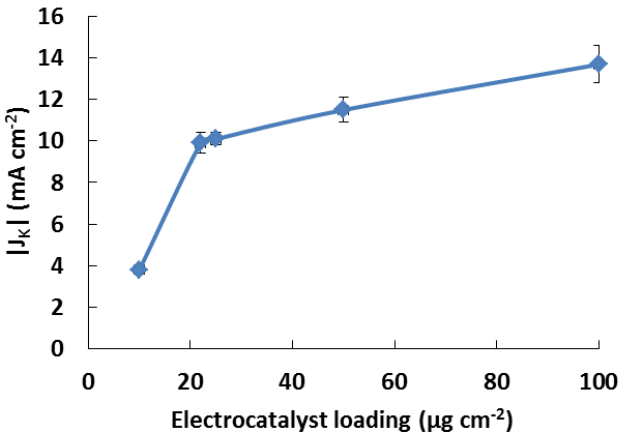

Figure 3.3. Kinetic current density as a function of electrocatalyst loading.

The trends observed by increasing the catalyst loading at constant electrocatalyst-to-Nafion® ratio are similar to those observed with fixed Nafion® amount: the selectivity to water increases (*n* increases and Sel.H_2O_2(%) decreases) whereas the onset potential does not differ significantly. However, the kinetic current density does not tend to increase with *n*, which was the case at constant Nafion® loading. This is a consequence of the negative impact of the increased Nafion® loading on the oxygen transport towards the active site (*vide supra*), which negatively influences the reaction rate.

Table 3.4. Influence of the electrocatalyst loading on the ORR performance at constant electrocatalyst-to-Nafion® mass ratio of 22.5, at -0.35 V vs. Ag/AgCl and recorded in an O_2-saturated 0.1 M KOH solution with a scan rate of 10 mV s^{-1} at 2500 rpm.

Loading (µg cm^{-2})	*n*	J_K (mA cm^{-2})	%H_2O_2	E_{Onset} (V)	$E_{1/2}$ (V)
10	2.1±0.1	-7.7±0.4	95±1	-0.06	-0.29
25	2.2±0.1	-10.1±0.3	92±1	-0.07	-0.27
50	2.7±0.2	-10.0±0.6	65±2	-0.05	-0.23
100	3.2±0.3	-10.3±0.3	40±4	-0.05	-0.23

3.3.4 Stepwise vs. simultaneous addition

Finally, it was investigated whether the electrocatalytic performance benefits from a separate addition of catalyst and Nafion® or if the same results can be obtained with a simultaneous addition without modifying the final electrode composition. The results in Table 3.5 show no clear difference between the two methods (see also Fig. S3.10 and S3.11). This means that the standard procedure for the preparation of the electrode can be simplified by adding electrocatalyst and binder simultaneously. This decrease in the number of experimental variables is also expected to lead to an increased reproducibility of the LSV tests.

Table 3.5. Comparison of performance in ORR between the stepwise and the simultaneous addition of binder and electrocatalyst, recorded on a RRDE in an O_2-saturated 0.1 M KOH solution with a scan rate of 10 mV s^{-1} at 2500 rpm.

Method	*n*	J_K (mA cm^{-2})	Sel.H_2O_2 (%)	E_{Onset} (V)	$E_{1/2}$ (V)
Stepwise	2.2±0.1	-10.1±0.3	92±1	-0.07	-0.27
Simultaneous	2.2±0.1	-10.1±0.2	93±1	-0.06	-0.26

3.4 Conclusions

The impact of the electrode composition on the ORR performance of an N-doped ordered mesoporous carbon electrocatalyst in 0.1 M KOH as electrolyte was investigated here for the first time. In agreement with literature reports on other electrocatalysts, an increase in the electrocatalyst loading resulted in a higher electron transfer number. By varying the type and loading of binder, it was concluded that the ORR performance is also influenced by the nature and amount of ionomer. The influence of the binder type had not yet been investigated thus far. It was determined that the selectivity towards water in an alkaline environment decreases when an anionomer is used as binder instead of a proton-exchange polymer. Furthermore, a correlation was found between the observed current density and the water uptake and ion-conductivity of the ionomer. The impact of the binder loading was studied with Nafion® and showed an increase in selectivity and a decrease in kinetic current density at higher Nafion® loadings. This agrees well with the results that have been reported with an anion-exchange polymer from Tokuyama (ionomer AS-4) used as binder for a silver nanowire electrocatalyst.[188] Finally, it was determined that the time and cost efficiency of the electrode fabrication process could be improved by simultaneously adding the catalyst and the binder to the electrode.

Based on the above trends it is possible to determine an optimal composition of the electrocatalyst layer both for the cogeneration of hydrogen peroxide and electricity and for the case when the sole purpose is electricity generation. For the former, Fumion FAA 3® should be used as ionomer, applying as low loadings as possible (*e.g.* 0.57 µg cm^{-2}) to avoid the negative effects on the current density and the selectivity. With respect to the catalyst, a lower loading also ensures a higher selectivity towards H_2O_2. On the other hand, for generating water the optimal composition of the electrocatalyst layer would be 100 µg cm^{-2} of NOMC and 4.44 µg cm^{-2} of Nafion®. Higher Nafion® loadings would have a negative impact on the current density, although possibly further increasing the selectivity. This relatively high loading is needed to increase the selectivity, though it also decreases the efficiency of the catalyst due to diffusion limitations.

This systematic study allowed establishing the relevance and the extent of the influence of the ink composition and the electrode fabrication method on the ORR performance of a metal-free NOMC electrocatalyst: the values for J_k varied between -3.8 and -13.7 mA cm^{-2} and those of *n* between 2.0 and 3.2, simply by changing the composition of the electrocatalyst layer. This study thus clearly underlines the need of taking these parameters into account when comparing different electrocatalysts. In this context, it would be advised to define a standard composition of the electrocatalyst layer to be used in RDE studies of novel electrocatalysts. Only in this way it would become possible to compare in a meaningful way the performance of novel electrocatalysts reported by different research groups. This

comparison is currently severely hampered by the wide variety in electrode compositions and preparation methods employed in different studies. Based on our results, we propose to use a Fumion FAA 3® loading of 0.56 µg cm^{-2}, an electrocatalyst loading of 25 µg cm^{-2} and the simultaneous addition of binder and catalyst as standard composition and preparation method of the electrocatalyst layer in the RDE-investigation of the oxygen reduction reaction in alkaline environment. The anion-exchange binder was chosen as this would offer an evaluation of the electrocatalytic performance in alkaline environment with as underlying idea to decide on its applicability in actual fuel cell technology. The catalyst and binder loadings were kept low as to limit the influence of the thickness of the active layer on the outcome of the ORR tests.

Supporting information

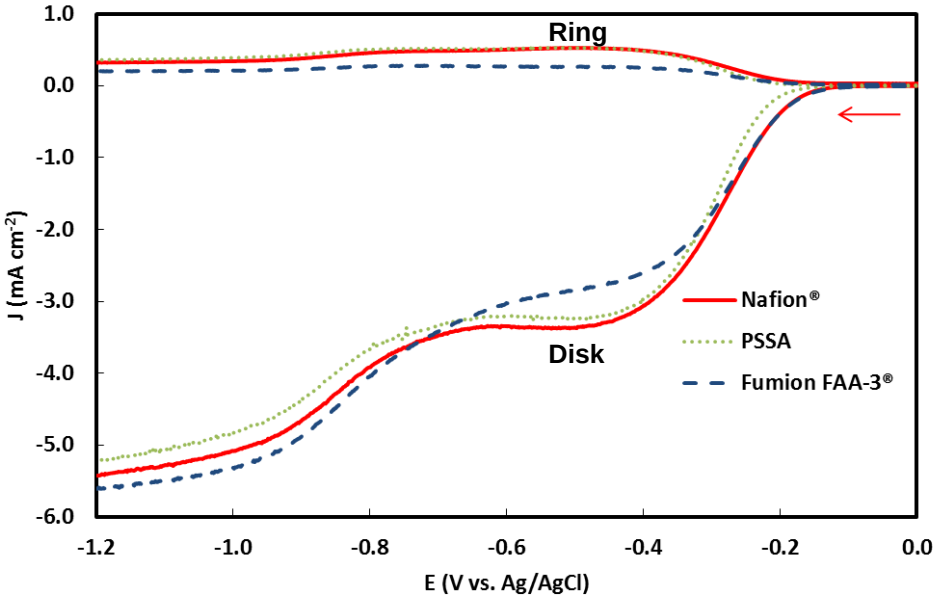

Figure S3.1. Impact of the binder type on the ring and disk currents of the NOMC electrocatalyst, recorded in an O_2-saturated 0.1 M KOH solution at a scan rate of 10 mVs^{-1} and with a rotation speed of 2500 rpm. The red arrow indicates the scan direction.

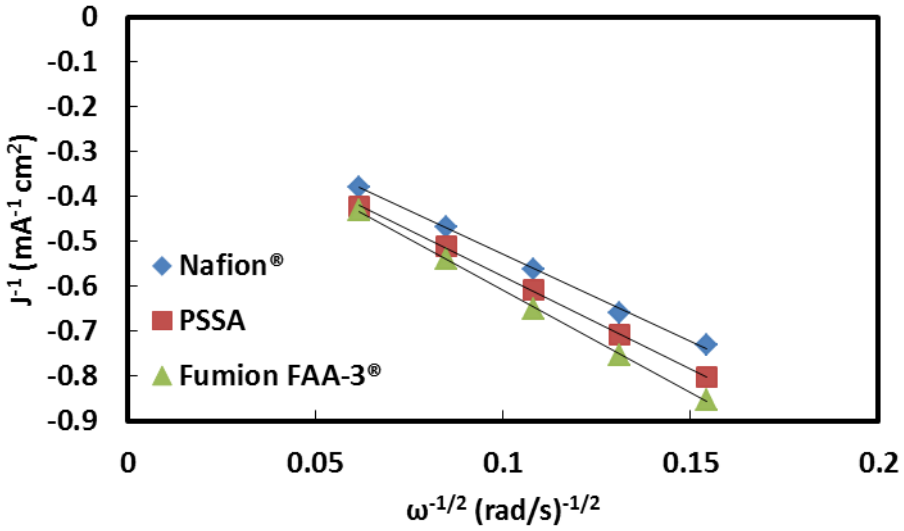

Figure S3.2. Impact of the binder type on the Koutécky-Levich plots as determined at -0.35 V vs. Ag/AgCl in an O_2-saturated 0.1 M KOH solution at a scan rate of 10 mV s^{-1}.

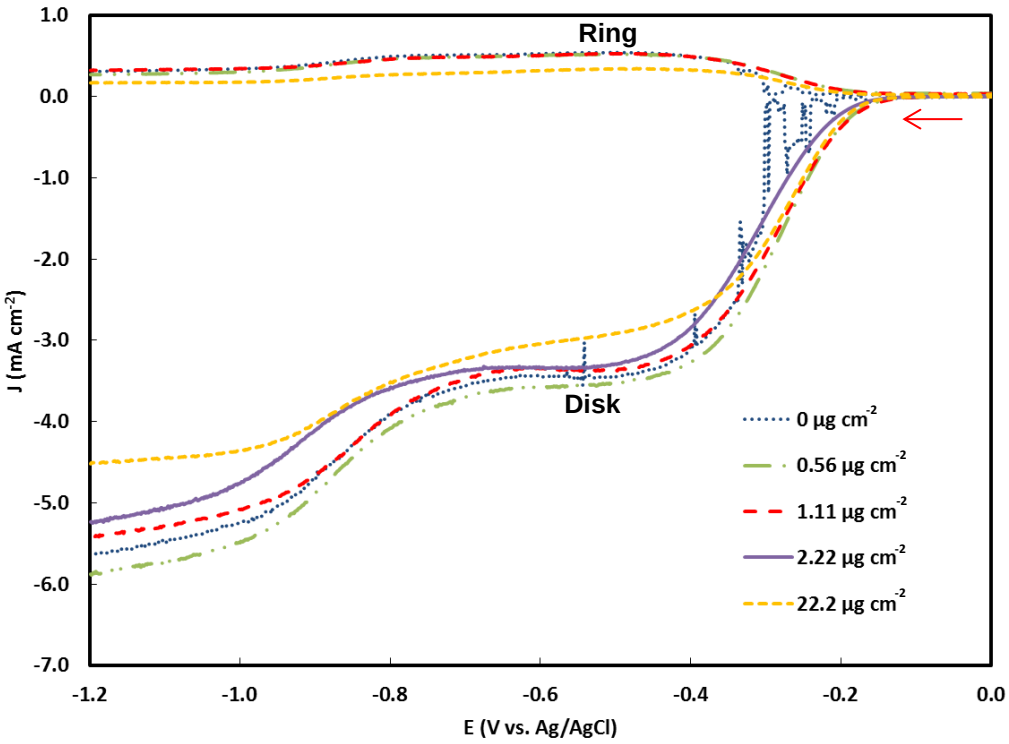

Figure S3.3. Impact of the Nafion® loading on the ring and disk currents of the NOMC electrocatalyst, recorded in an O_2-saturated 0.1 M KOH solution at a scan rate of 10 mVs^{-1} and with a rotation speed of 2500 rpm. The red arrow indicates the scan direction.

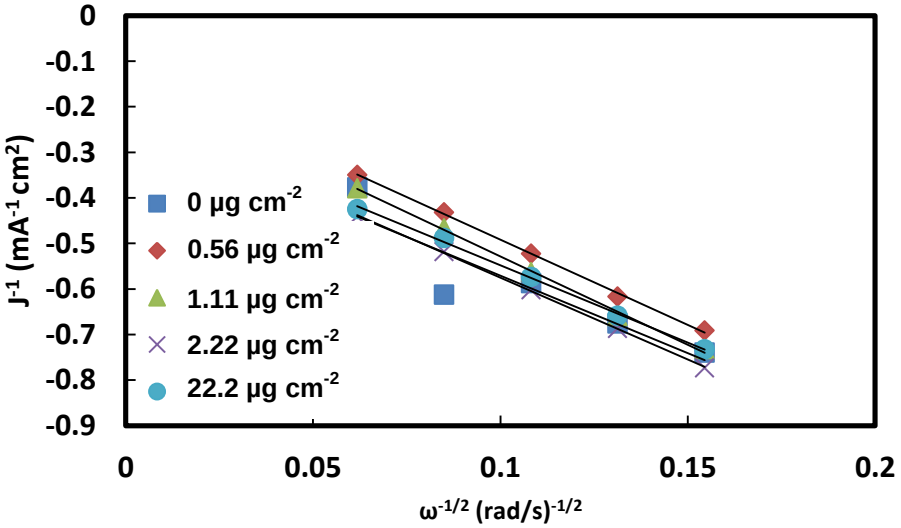

Figure S3.4. Impact of the Nafion® loading on the Koutécky-Levich plots as determined at -0.35 Vvs. Ag/AgCl in an O_2-saturated 0.1 M KOH solution at a scan rate of 10 mV s^{-1}.

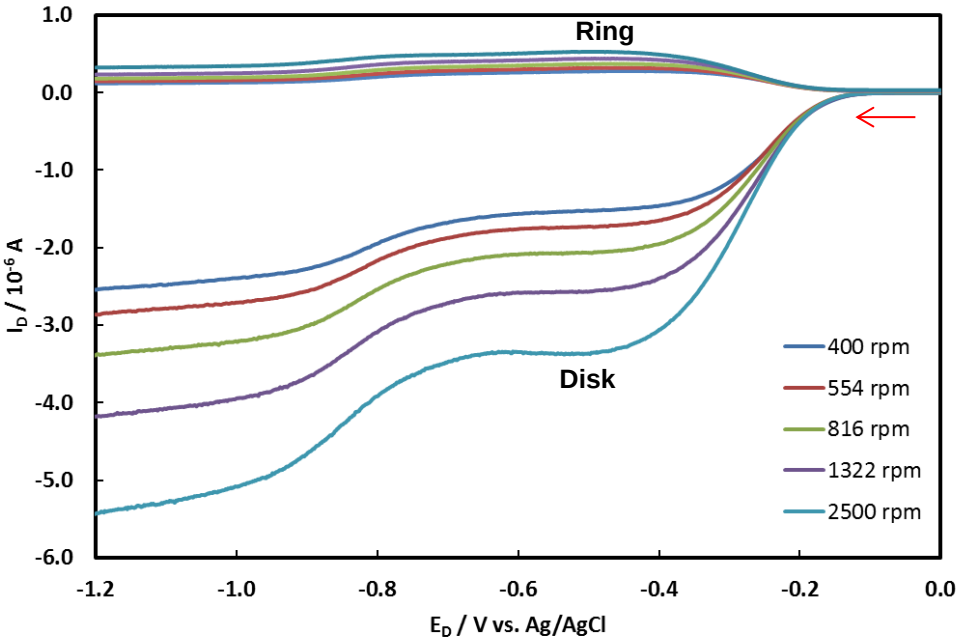

Figure S3.5. LSV plots of NOMC with an electrode composition of 25 µg cm^{-2} catalyst and 1.11 µg cm^{-2} Nafion® recorded in an O_2-saturated 0.1 M KOH solution at a scan rate of 10 mVs^{-1} at different rotation rates. The red arrow indicates the scan direction.

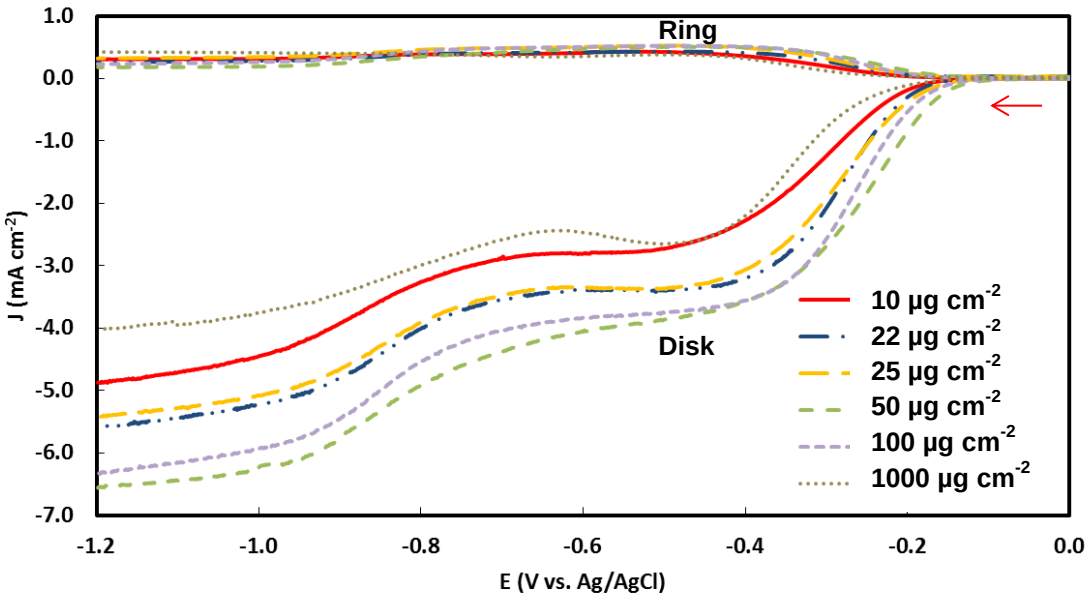

Figure S3.6. Impact of the electrocatalyst loading on the ring and disk currents of the NOMC electrocatalyst at constant Nafion® loading of 1.11 µg cm^{-2}, recorded in an O_2-saturated 0.1 M KOH solution at a scan rate of 10 mVs^{-1} and with a rotation speed of 2500 rpm. The red arrow indicates the scan direction.

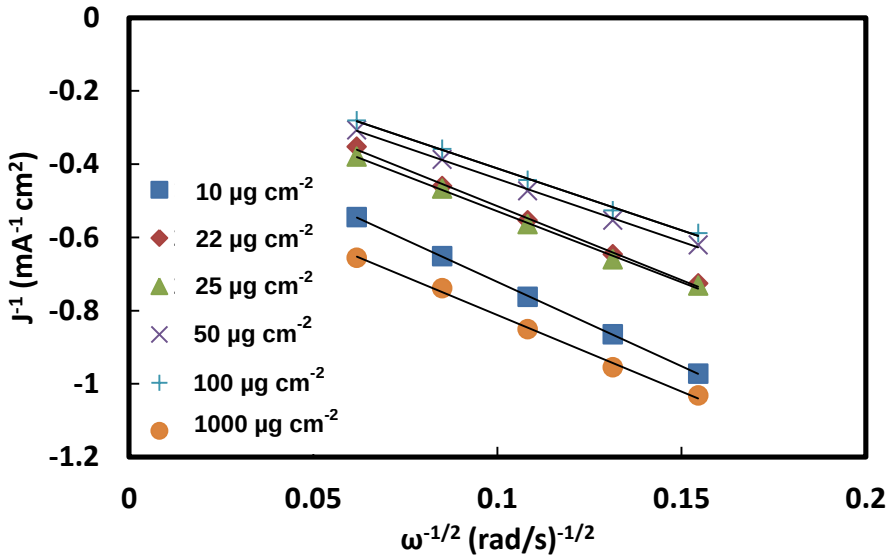

Figure S3.7. Impact of the electrocatalyst loading on the Koutécky-Levich plots at constant Nafion® loading of 1.11 µg cm^{-2} as determined at -0.35 Vvs. Ag/AgCl in an O_2-saturated 0.1 M KOH solution at a scan rate of 10 mV s^{-1}.

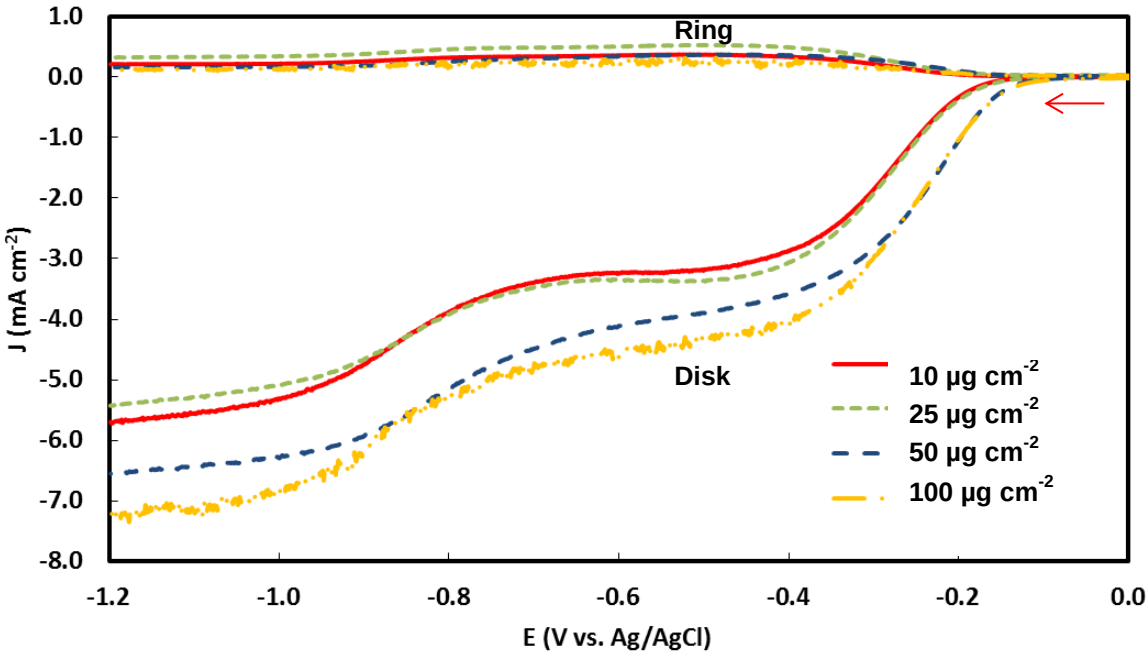

Figure S3.8. Impact of the electrocatalyst loading on the ring and disk currents of the NOMC electrocatalyst at constant electrocatalyst-to-Nafion® mass ratio of 22.5, recorded in an O_2-saturated 0.1 M KOH solution at a scan rate of 10 mVs^{-1} and with a rotation speed of 2500 rpm. The red arrow inidicates the scan direction.

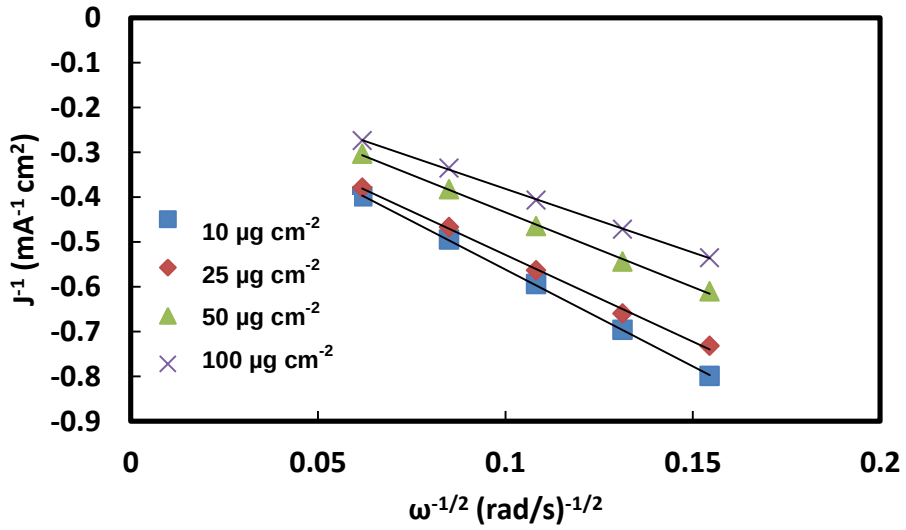

Figure S3.9. Impact of the electrocatalyst loading on the Koutécky-Levich plots at constant electrocatalyst-to-Nafion® mass ratio of 22.5 as determined at -0.35 Vvs. Ag/AgCl in an O_2-saturated 0.1 M KOH solution at a scan rate of 10 mV s^{-1}.

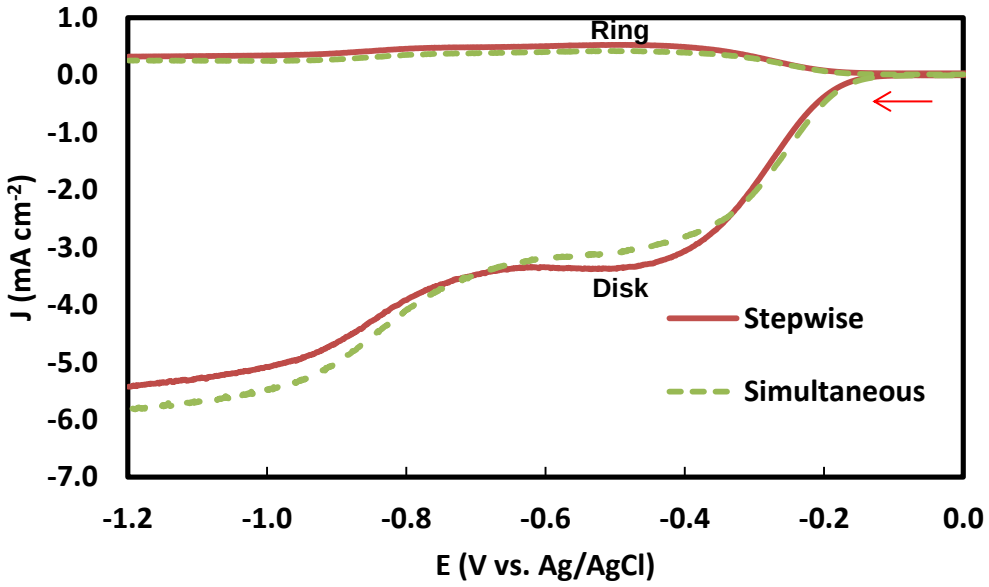

Figure S3.10. Impact of order of addition of the electrocatalyst and binder on the ring and disk currents of the NOMC electrocatalyst, recorded in an O_2-saturated 0.1 M KOH solution at a scan rate of 10 mVs^{-1} and with a rotation speed of 2500 rpm. The red arrow indicates the scan direction.

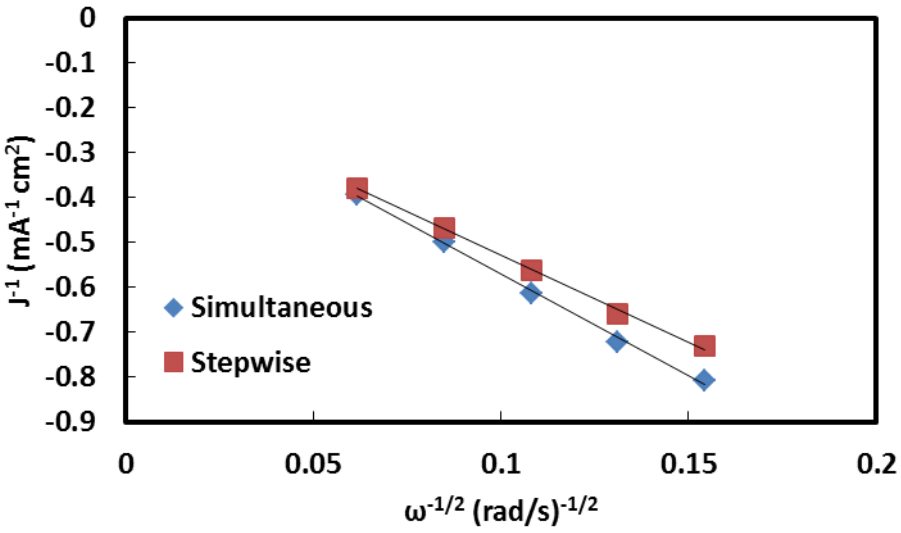

Figure S3.11. Impact of the order of addition of the electrocatalyst and binder on the Koutécky-Levich plots of the NOMC electrocatalyst as determined at -0.35 Vvs. Ag/AgCl in an O_2-saturated 0.1 M KOH solution at a scan rate of 10 mV s^{-1}.

Chapter 4

Iron-containing N-doped carbon electrocatalysts for the cogeneration of hydroxylamine and electricity in a NO-H_2 fuel cell.

Abstract

Iron-containing N-doped carbon materials were investigated as electrocatalysts for the cogeneration of hydroxylamine (NH_2OH) and electricity in a H_2-NO fuel cell. This electrochemical route for the production of hydroxylamine is a greener alternative to the present industrial synthesis, because it allows converting the energy released during the reaction into electricity. The studied electrocatalysts were prepared by pyrolysis of composites of activated carbon and polyaniline (PANI) incorporating Fe sites (Fe-PANI-AC). Characterisation with a combination of techniques (FT-IR and Raman spectroscopy, XRD, N_2-physisorption, XPS and ToF-SIMS) showed that the materials exhibit promising features as electrocatalysts for the NO reduction reaction, as they contain the desired isolated FeN_xC_y sites and have a relatively high degree of graphitisation, which grants good electrical conductivity. The performance of the Fe-PANI-AC electrocatalysts was investigated by means of linear sweep voltammetry (LSV) in a half cell setup and by chronoamperometry in a H_2-NO fuel cell setup and compared to that of a reference electrocatalyst consisting of iron phthalocyanine supported on activated carbon (FePc/AC). The Fe-PANI-AC electrocatalysts led to higher current density than FePc/AC under all studied conditions. At low NO concentration in the feed, FePc/AC displayed higher selectivity towards hydroxylamine, whereas the Fe-PANI-AC electrocatalysts were superior at higher NO concentration (*i.e.* at the industrially more relevant conditions), both in terms of production rate and of selectivity towards hydroxylamine. Moreover, the Fe-PANI-AC electrocatalysts exhibited high stability under the fuel cell operating conditions. In summary, Fe-PANI-ACs displayed very promising electrocatalytic performance in the reduction of NO to hydroxylamine and offered the additional advantage of being less expensive compared to the reference FePc/AC electrocatalyst or to a benchmark noble-metal-based electrocatalyst as Pt/AC.

Based on:

N. Daems, X. Sheng, Y. Alvarez-Gallego, I.F.J. Vankelecom, P.P. Pescarmona, Green Chem., 18 (2016) 1547-1559.

Author contributions

The original idea of this research was developed by X. Sheng. Electrocatalyst synthesis and physicochemical characterisation was done by N. Daems under the supervision of X. Sheng. Writing of the manuscript was done by N. Daems, with editing by P. P. Pescarmona. Electrochemical characterisation was performed by Y. Alvarez-Gallego. The data were analysed and interpreted by N. Daems in collaboration with X. Sheng and P. P. Pescarmona. The whole work was carried out under supervision of P. P. Pescarmona and I. F. J. Vankelecom.

4.1 Introduction

The depletion of raw materials reserves used for supplying chemicals and fuels is stimulating the chemical industry to pursue alternative technologies for increasing the efficiency of their production processes in terms of conversion, product selectivity and energy demands.[187,218] Currently, many industrial products are obtained through thermodynamically favourable reactions. For such exergonic reactions ($\Delta_r G < 0$), the process is accompanied by liberation of energy, generally in the form of heat. This energy is often not utilised efficiently and in some processes it can be problematic to remove it safely. A possible, greener alternative to conventional chemical processes is provided by electrochemical processes in which the energy released during the reaction is converted into electricity.[13,14,24,25,187,219,220] This approach is conceptually very attractive as it allows the cogeneration of electricity and useful chemical products in a fuel cell setup. All reagents that can be oxidised or reduced in an electrochemical way qualify for being produced in this type of electrochemical cells. Another advantage of an electrochemical production is the possibility of controlling the reaction rate and selectivity by means of the electrical potential.[15] In this work, this electrochemical cogeneration approach is applied to the reduction of nitric oxide (NO) to hydroxylamine, which is widely used in industry for the synthesis of cyclohexanone oxime. In turn this is used to produce caprolactam, the main application of which is in the production of nylon 6.[13–17] The annual worldwide hydroxylamine production for caprolactam synthesis amounts to about 0.9 million metric tons.[18] In industry, hydroxylamine is generally produced through the hydrogenation of high oxidation-state compounds of nitrogen, like nitric oxide or nitric acid, in a sulphuric acid solution with platinum supported on activated carbon as catalyst.[13–17] The as-synthesised hydroxylamine reacts immediately with sulphuric acid to produce the more stable and easier to handle hydroxylamine sulphate salt [$(NH_3OH)_2SO_4$]. This transformation is required since the hydroxylamine free base can decompose violently at temperatures above 50°C.[15] Substituting the current technology with an electrochemical production process would have the advantage of the cogeneration of electricity, and could also allow lowering the costs related to the catalyst if different active species than platinum are employed. The possibility of cogenerating NH_2OH and electricity in a H_2-NO fuel cell was first investigated by Langer *et al.*[19] and has been further developed since then.[13–15,17] The electrochemical cell typically consists of a porous anode and cathode placed in two compartments that are separated by a proton exchange membrane (PEM). Hydrogen is oxidised at the anode generating protons, which pass to the cathodic compartment through the PEM, and liberating electrons that flow to the cathode by means of the external circuit. Nitrogen monoxide is reduced at the cathode by means of the protons and electrons coming from the anode. The overall reactions are:

Anode:

$$H_2 \rightarrow 2H^+ + 2e^- \qquad E^0 = 0\ V \qquad (4.1)$$

Cathode:

$$2NO + 2H^+ + 2e^- \rightarrow N_2O + H_2O \qquad E^0 = 1.59\ V \qquad (4.2)$$

$$2NO + 4H^+ + 4e^- \rightarrow N_2 + 2H_2O \qquad E^0 = 1.68\ V \qquad (4.3)$$

$$NO + 3H^+ + 3e^- \rightarrow NH_2OH \qquad E^0 = 0.38\ V \qquad (4.4)$$

$$NO + 5H^+ + 5e^- \rightarrow NH_3 + H_2O \qquad E^0 = 0.73\ V \qquad (4.5)$$

Based on the above standard reduction potentials, it is clear that all these reduction reactions can lead to the cogeneration of electricity and nitrogen compounds. An important observation made during previous experimental studies, is that the selectivity depends strongly on the electrode potential. At low potentials (E_{cell} < 0.5 V vs. SHE), hydroxylamine and ammonia are the dominant products while at high potentials nitrous oxide is the main product. Nitrogen is mainly observed at intermediate potentials.[15,19,221,222] The most investigated electrocatalysts for the reduction of NO are based on noble metals like platinum, palladium and ruthenium supported on activated carbon.[14,219] These noble metal electrocatalysts lead to high conversions of NO but they lack a sufficiently high selectivity towards hydroxylamine.[13–16,19,221–223] This is mainly related to two side-reactions: (1) the further reduction of NH_2OH to NH_3; (2) the formation of N_2O through the reaction of two NHO species adsorbed on neighbouring sites on the Pt surface, with the elimination of a H_2O molecule. It was discovered that the selectivity of Pt electrocatalysts towards hydroxylamine could be significantly increased by covering it with sulphur. It was proposed that the presence of sulphur prevents breaking of the nitrogen-oxygen bonds during the reduction process, thus increasing the selectivity towards hydroxylamine by preventing N_2 and NH_3 formation.[15,19] A promising alternative class of electrocatalysts for the reduction of NO in a fuel cell is represented by transition metal complexes.[13] Iron-phthalocyanine, cobalt-phthalocyanine, vitamin B12, Prussian blue and cobalt-porphyrin have been investigated for this purpose.[17] Among them, iron phthalocyanine on activated carbon (FePc/AC) or on graphite (FePc/Gr) showed the most promising results with a selectivity up to 90% for NH_2OH.[13] Although the mechanism of the NO reduction on this kind of electrocatalysts is not yet fully understood, it was proposed that NO is reduced on FePc/Gr by means of three consecutive reduction steps, each adding one electron and one proton to the intermediate until finally hydroxylamine is released into the solution (Scheme 4.1). The observed high selectivity was ascribed to the relatively high distance between neighbouring iron sites, which are separated through phthalocyanine rings. This distance prevents the interaction of two NHO species adsorbed on adjacent sites, and thus limits the formation of the N_2O side-product. Furthermore, it was suggested that two neighbouring metal sites are needed in order to split the N-O bond, which is a requirement for the further reduction of NH_2OH to NH_3, making this reaction nearly impossible on this type of electrocatalysts. However, this hypothesis has not been proven so far.[13]

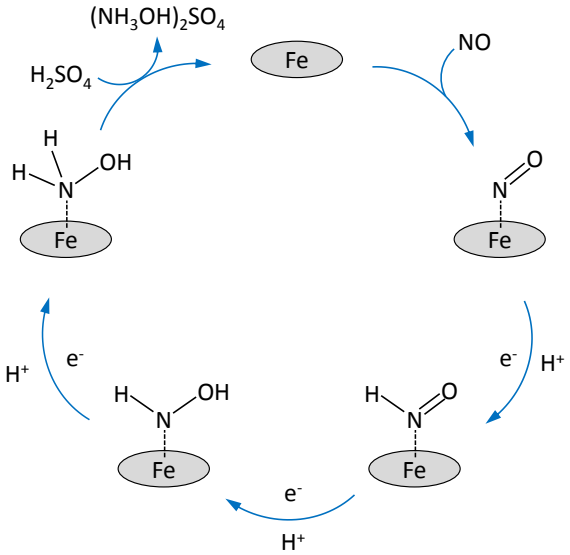

Scheme 4.1. Proposed mechanism for the reduction of NO to NH2OH over isolated Fe sites.

Based on the above discussion of the state of the art, it is possible to define the desirable features of electrocatalysts for the selective reduction of NO to NH_2OH. First of all, the presence of isolated metal centres as active sites is most likely an important requisite to selectively obtain hydroxylamine. Secondly, in order to successfully adsorb NO and initiate its reduction, it is important that the metal has at least two accessible oxidation states [e.g. Fe(II)/Fe(III)]. Finally, an extended delocalised π-system in the electrocatalyst will grant high electrical conductivity, which is an asset for a good electrocatalytic performance. In this work, we report polyaniline-derived Fe-containing N-doped carbon materials as electrocatalysts for the reduction of NO in half cell and fuel cell setups. These electrocatalysts were prepared by pyrolysing composite materials consisting of activated carbon and polyaniline (PANI), in which the N-atoms originating from PANI can coordinate Fe sites (Fe-PANI-AC, see Scheme 4.2).

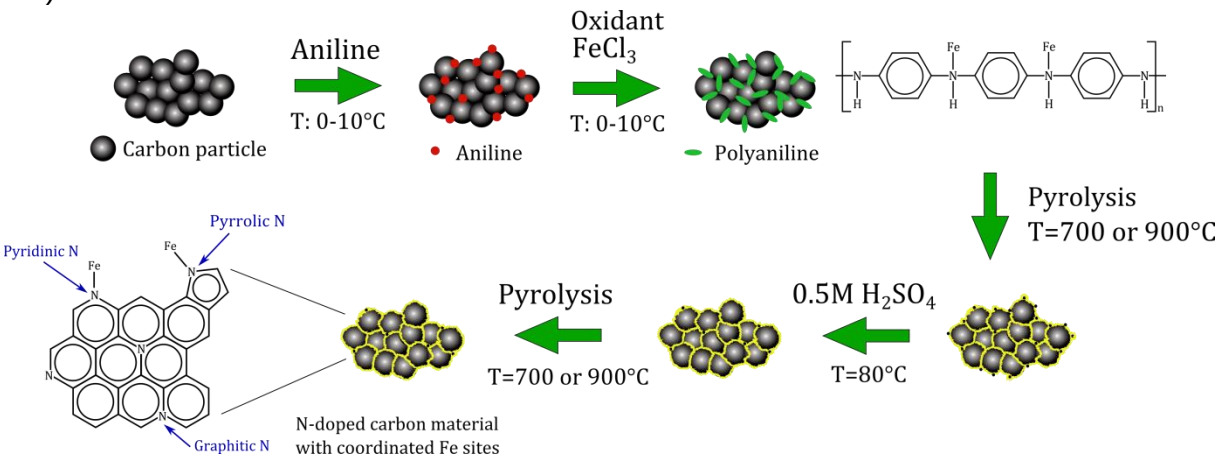

Scheme 4.2. Synthesis of the Fe-PANI-AC electrocatalysts.

This class of materials has been recently reported as a very promising type of electrocatalysts for the oxygen reduction reaction,[154,224] but also displays the above mentioned desirable features for the selective reduction of NO to NH_2OH. Moreover, Fe-PANI-ACs offer several advantages compared to FePc supported on carbon materials: (1) the synthesis is straightforward and easily upscalable; (2) compared to the expensive phthalocyanine, the synthesis of Fe-PANI-ACs makes use of inexpensive, available chemicals; and (3) several parameters (pyrolysis temperature, metal content and type) can be easily modified in order to optimise the activity and selectivity of the electrocatalyst. Polyaniline was preferred over other N-containing polymers such as polypyrrole because it contains phenyl groups, which are expected to generate more readily a graphitic structure, thus leading to a material with the desired high electrical conductivity.

4.2 Experimental

4.2.1 Materials

Aniline (99.8%, pure, Acros organics), activated carbon Norit® SX1G (878 $m^2\ g^{-1}$, Norit Americas inc., further referred to as AC(N)), activated carbon from Sigma-Aldrich (1300 $m^2\ g^{-1}$, further referred to as AC(S)), iron(III) chloride (97%, reagent grade, Sigma Aldrich), ammonium peroxydisulphate (98%, Acros Organics), sulphuric acid (>95%, Fisher Chemical), hydrochloric acid (≈37%, Fisher Chemical), iron(II) phthalocyanine (FePc, >95%, TCI Europe), 10% (wt/wt) Pt on charcoal type 18 (Johnson Matthey), polytetrafluoroethylene

(Teflon® PTFE 6N, Dupont), fluorinated ethylene propylene resin (Teflon® FEP 8000, Dupont), were used as received from commercial sources.

4.2.2 Synthesis of the electrocatalysts

Iron-containing N-doped graphitic carbon materials were synthesised according to a procedure described in literature.[154] In the first step, activated carbon (AC(S)) was treated with a 6M HCl aqueous solution for 24 h at room temperature to remove impurities. Next, 2.5 mL aniline was mixed with 0.5 g of the purified activated carbon and 0.5 M HCl at a temperature between 0 and 10°C. After 20 min, ammonium peroxydisulphate ($(NH_4)_2S_2O_8$, as oxidant) and iron chloride (1:1 or 1:4 molar ratio relative to aniline), were added to the reaction mixture. This suspension was stirred for 24 h. Next, the solvent was evaporated and the remaining solid was completely dried in a vacuum oven at 80°C overnight. In the next step, the material was subjected to a first pyrolysis under N_2 at 700 or 900°C for 1 h at a heating rate of 3.3°C min^{-1}. Afterwards, unstable species were mostly removed from the materials by means of a treatment in 0.5 M H_2SO_4 at 80°C for 8 h, followed by filtration, washing with deionised water and drying in a vacuum oven. Finally, the catalyst was subjected to a second pyrolysis for 3 h at the same temperature used in the first treatment. Two different electrocatalysts were prepared: (1) Fe-PANI-AC-1 at a pyrolysis temperature of 700°C and a metal to aniline ratio of 1:1 and (2) Fe-PANI-AC-2 at a pyrolysis temperature of 900°C and a metal to aniline ratio of 1:4.

As a reference, an iron phthalocyanine (FePc) electrocatalyst was prepared by dispersing a selected amount of FePc (0.3 wt% of iron) onto the activated carbon support (Norit SX1G) according to a literature procedure.[225] First, FePc was dispersed in concentrated H_2SO_4 and sonicated for 30 min. Next, AC(N) was added and the suspension was homogenised by ultrasonication to obtain a good dispersion of FePc on the carbon supports. Then the suspension was poured in deionised water, filtered, washed with deionised water until the pH was 7 and dried at 70°C in an oven under air overnight.

4.2.3 Physicochemical characterisation

FT-IR spectra were recorded on a Bruker IFS 66/v/S FT-IR spectrometer on KBr pellets in the range 400-4000 cm^{-1}. The spectrometer was controlled by OPUS version 4 software from Bruker. A STOE Stadi P Combi instrument was used in transmission mode to measure the X-ray diffraction (XRD) patterns. The instrument was used in high-throughput mode and was equipped with a Cu-Kα radiation source (λ = 1.54 Å) and a Kα1 Germanium Johann-type monochromator. A high-throughput image plate position detector (IP-PSD) from STOE was used as detector. The XRD instrument was controlled by the WinXPOW software (version 2.20) from STOE and all measurements were performed in a 2θ range from 0 to 75°. Nitrogen adsorption-desorption isotherms were measured at 77 K on a Micromeritics Tristar 3000. The pore size distributions were determined using the Barrett-Joyner-Halenda (BJH) method, whereas the Brunauer-Emmett-Teller (BET) method was used to calculate the surface area of the samples. Thermogravimetric analysis (TGA) was performed to determine the iron content. The measurements were carried out under O_2 flow on a TGA Q500 from TA instruments. The temperature was ramped with a heating rate of 5 °C min^{-1} until 1000 °C was reached, and then it was held constant until the mass change was smaller than 0.05% per min., after which the system was cooled down to room temperature. Previous reports showed by XRD that the residual red-orange powder is Fe_2O_3.[224] The residual weight can thus be used to determine the overall iron content of the sample. X-ray photoelectron spectroscopy (XPS) measurements were performed by a Physical Electronics PHI 1600

multi-technique system using an Al Kα (1486.6 eV) monochromatic X-ray source, which was operated at 15 kV and 150 W at a base pressure of $2 \cdot 10^{-9}$ Torr. The graphitic C 1s band at 284.6 eV was taken as internal standard, in order to correct possible deviations caused by electric charging of the samples. The multipack software was used for the deconvolution and integration of the XPS spectra. Room-temperature Raman spectra were recorded on a Dilor XY spectrometer from HORIBA Jobin Yvon Inc.. The spectroscope was equipped with an Olympus BH 2 microscope, a monochromator, a filter and charge-coupled detector with liquid nitrogen cooling (CCD3000 with a resolution of 2 cm^{-1}). A beam originating from an argon/krypton mixed gas laser at a wavelength of 514 nm (Coherent Innova 70C) was sent to the sample. Deconvolution and peak integration was performed by using the Igor pro software. Time of Flight Secondary Ion Mass Spectroscopy (ToF-SIMS) was carried out on an IONTOF V instrument (IONTOF, GmbH, Münster, Germany). Sample powders were manually pressed with a spatula onto the adhesive part of Post-it® papers. A pulsed Bi^{5+} metal ion source was used to produce a primary beam using an acceleration voltage of 30 kV. An AC target current of 0.06 pA with a bunched pulse width lower than 1.5 ns was used. The analysis was conducted on the positive and negative secondary ion species. For the spectra, a raster of 128 x 128 data points over an area of 150 x 150 μm^2 was used. The total primary ion beam dose for each analysed area was always kept below 1011 ions·cm^{-2}, ensuring static conditions. Lateral resolution of ~3 µm and mass resolution m/Δm > 5000 at 29 m/z were maintained for positive and negative spectra acquisition. Charge compensation was done by interlaced electron flood gun (E_k = 20 eV). All data analyses were carried out using the software supplied by the instrument manufacturer, SurfaceLab (version 6.5). It is important to note here that ToF-SIMS is a semi-quantitative technique and, therefore, can be used to identify the different species present in the material and their relative abundancies, but not for an absolute quantification of their amounts (for which purpose XPS is employed in this work). This also accounts for the differences in the relative abundances of the species that can be detected in the spectra of the negative and the positive secondary ions.[226]

4.2.4 Electrochemical characterisation

Characterisation of electrodes as cathodes for NO-reduction was carried out in an electrochemical half cell and in a single cell. The half cell and the single cell setups used for the electrochemical experiments have been described in detail elsewhere.[15]

The working electrodes (VITO CoRE®) consisted of a current collector (stainless steel gauze), an active layer (*i.e.* the electrocatalyst embedded in a porous PTFE matrix) and a hydrophobic gas diffusion outer layer (porous PTFE). Cold rolling was used to manufacture the VITO CoRE® gas diffusion electrodes.[15,227] The composition of the active layer was 10% PTFE and 90% electrocatalyst powder for the cathode, and 15% PTFE and 85% of 10% Pt on activated charcoal for the anode. An ion-permeable membrane (Zirfon® separator[228]) was cast onto the current collector side of the anode.

The half cell consisted of a cathode (working electrode), a reference electrode and a counter electrode. Ag/Ag_2SO_4 (+0.69 V vs. standard hydrogen electrode (SHE)) was used as a reference electrode (Koslow Scientific) and a Pt disk welded to a titanium (Ti) plate was used as a counter electrode. The cathode and the counter electrode were separated by a liquid electrolyte (3 M sulphuric acid) and a separator membrane.

The single cell consisted of two working electrodes, anode (oxidation of H_2) and cathode (reduction of NO), separated by a liquid electrolyte and an ion-permeable membrane. Besides functioning as a medium for the charge transport, the electrolyte in this case served also to react with the hydroxylamine free base, yielding its sulphate salt.

The cells had a projected electrode surface area of 10 cm². Reactant gases (6% or 18% NO in N_2 (Air Products) for the cathode and 100% H_2 (Air Products) for the anode) were fed to the respective compartments at a flow rate of 10 mL min^{-1} by means of mass flow controllers (In-Flow, Bronkhorst), with an overpressure of 5 mbarg (5 cm water column) at the exhaust. The liquid electrolyte was saturated with N_2 and circulated through the cell with a peristaltic pump (Watson-Marlow).

All the electrochemical measurements were performed at room temperature (18°C) using VersaSTAT 3F potentiostat (Princeton Applied Research) and the VersaStudio software for data acquisition. IR compensation was enabled for the acquisition of the voltammograms. Typical values for internal resistance were 0.15-0.20 and 0.6-0.7 Ohm for the half cell and the single cell, respectively.

The different electrocatalysts were evaluated by means of linear sweep voltammetry (LSV) in the cathode half cell. The voltammograms were recorded by varying the potential of the working electrode (or cathode) from the open circuit potential (OCP) to the hydrogen evolution potential (-0.69 V vs. Ag/Ag_2SO_4) at a scan rate of 1 mV s^{-1}. Prior to recording an LSV under NO flow, the cell was saturated with N_2 for at least 12 h and a blank measurement was performed under nitrogen flow at 5 mbarg.

The performance of the electrocatalysts in the production of hydroxylamine in a fuel cell reactor was assessed by means of chronoamperometry. These experiments were carried out in the single cell setup keeping the cell potential constant. In order to achieve a product concentration that would be high enough for detection by potentiometric titration, the current was collected until the total charge that passed through the electrode was at least 8000 C, while continuously recirculating the electrolyte. Afterwards, the electrolyte solution was analysed by potentiometric titration. Hydroxylamine, which is present as hydroxylammonium sulphate in the 3 M sulphuric acid solutions [$2NH_2OH + H_2SO_4 \rightarrow (NH_3OH)_2SO_4$], was determined by potentiometric titration (DL77 Titrator, Mettler Toledo) with 1 M NaOH (Titripac®, Merck), in the potential range from 325 mV to -280 mV. LabX software was used for data acquisition and analysis. The deviation of the measured values with respect to the theoretical concentration of control solutions was ≤ 2.2%. More details about this procedure can be found elsewhere.[15] Gaseous products (N_2O and N_2) were not analysed.

The current efficiency towards NH_2OH [CE_{NH2OH} (%)] and the yield of NH_2OH [Y_{NH2OH} (%)] were calculated based on the following formulas:

$$CE_{NH_2OH}\ (\%) = \frac{mol_{NH_2OH(exp)}}{mol_{NH_2OH\ max(cal)}} * 100\% \quad (4.6)$$

$$mol_{NH_2OH\ max}(cal) = \frac{Q}{n*F} \quad (4.7)$$

$$Y_{NH_2OH}\ (\%) = \frac{mol_{NH_2OH(exp)}}{mol_{NO(input)}} * 100\% \quad (4.8)$$

where $mol_{NH_2OH}(exp)$ was determined by means of the potentiometric titration of the formed hydroxylammonium sulphate (*vide supra*); and $mol_{NH_2OH\ max}(cal)$ is the maximum number of moles of NH_2OH that can be obtained from the reduction of NO, calculated on the basis of the amount of charge (Q, in Coulomb) collected over the time of the experiment, of the amount of exchanged electrons (n = 3 for $NO + 3H^+ + 3e^- \rightarrow NH_2OH$), and of the constant of Faraday (F = 96485 C mol^{-1}).

The power generated in the fuel cell at steady state (in W m^{-2}) was calculated by multiplying the measured value of the cell potential at steady state (ΔE_{cell}, in V) by the measured value of the current density at steady state (j, in A m^{-2}).

The stability of the different electrocatalysts was evaluated by determining the decay in the current density over time measured by chronoamperometry at a constant potential of -0.1 V vs. Ag/Ag_2SO_4 over the time interval 5000-40000s. The initial part of the measurement (0-5000s) was not included because the decay in current in this period is caused by non-faradaic processes (i.e. the formation of the double layer, which involves a capacitive current).

4.3 Results and discussion

Fe-containing N-doped carbon electrocatalysts were prepared by pyrolysing composite materials consisting of activated carbon and polyaniline (PANI) and incorporating Fe sites (Fe-PANI-AC). The electrocatalysts were tested for the reduction of NO with NH_2OH as target product. FePc/AC, which has been reported to be a very good electrocatalyst for this application,[13] was used as a reference.

The main parameters that are expected to influence the electrocatalytic performance of the Fe-PANI-AC materials in the reduction of NO to NH_2OH are (1) the Fe loading and configuration, (2) the N loading and configuration, (3) the degree of graphitisation and (4) the surface area.[13,153] In order to correlate the physicochemical properties of the Fe-PANI-AC materials with their electrocatalytic performance, the materials were characterised using a combination of techniques.

4.3.1 Physicochemical characterisation of the Fe-PANI-AC materials

Since Fe centres have been proposed to be the active sites on which the electrocatalytic reduction of NO occurs,[13] the influence of the metal loading on the performance of the electrocatalysts in the reduction of NO to hydroxylamine was investigated by employing different amounts of Fe in the synthesis of the Fe-PANI-AC materials (theoretical Fe content: 38 and 11 wt%, corresponding to a metal-to-aniline molar ratio of 1:1 and 1:4, respectively). The final composition of the two Fe-containing N-doped carbon electrocatalysts was determined by means of TGA (metal content) and XPS (carbon, nitrogen, oxygen and metal content). The results are summarised in Table 4.1. The TGA analysis shows that a similar amount of iron is present in the final structure of both electrocatalysts, regardless the large difference in the amount of iron used during the synthesis in the two cases. This suggests that the maximum amount of iron (~5 wt%) that can be retained in the structure is limited by the initial amount of aniline, which was the same for both electrocatalysts. A significant fraction of the iron present in the Fe-PANI-AC materials is expected to be coordinated to N-atoms originating from aniline (Scheme 4.2).[224] Other iron species having a weaker interaction with the N-doped carbon structure, should get largely removed during the acid and thermal treatments. The removal of these iron species is expected to be more efficient from the surface region of the material. Indeed, analysis with a surface technique as XPS (having an analysis depth of only few nm) shows a significantly lower iron content in both samples (Table 4.1). Although the total metal loading is similar in the two materials, the surface content of iron measured by XPS is more than double in Fe-PANI-AC-1 than in Fe-PANI-AC-2. This can significantly affect the electrocatalytic activity of the materials (*vide infra*), because the reduction of NO is expected to occur at the catalysts surface. Also the N-content of Fe-PANI-AC-2 determined by XPS is lower than that of Fe-PANI-AC-1 (Table 4.1). These results can be rationalised on the basis of the pyrolysis temperature, which was 700°C for Fe-PANI-AC-1 and 900°C for Fe-PANI-AC-2. Several reports on N-doped carbon materials demonstrated that at increasingly high temperatures above 650°C less nitrogen is

incorporated in carbon materials, because at these temperatures the formation of C-C and N-N bonds becomes more favourable than that of C-N bonds.[153,229]

Table 4.1. Elemental composition of Fe-PANI-AC-1 and Fe-PANI-AC-2.

	Theoretical Fe wt%	Fe wt% (XPS)	Fe wt% (TGA)	Theoretical N wt%	N wt% (XPS)	Theoretical C wt%	C wt% (XPS)	O wt% (XPS)
Fe-PANI-AC-1	38	3.0	4.2	7.9	12.0	50.5	75.4	7.9
Fe-PANI-AC-2	11	1.3	4.9	11.1	6.4	72.1	81.6	7.6

The fact that iron chloride can act as an oxidant for the polymerisation of aniline might also have contributed to the higher N content in Fe-PANI-AC-1 since a higher amount of iron precursor was present in its synthesis. The N-containing part of these materials is expected to be located at or close to the surface, with the core consisting of activated carbon (Scheme 4.2). Therefore, the lower N content in Fe-PANI-AC-2 also implies less surface sites for coordinating Fe, and can thus account for the lower surface metal content in this sample.

The preparation of the Fe-containing N-doped carbon materials has been reported to lead to a significant decrease in surface area compared to the parent activated carbon.[224] The same trend is observed in this work: the surface area measured by N_2-physisorption is 206 $m^2 g^{-1}$ for Fe-PANI-AC-1 and 197 m^2/g, for Fe-PANI-AC-2 (see Figure S1 for the isotherm of Fe-PANI-AC-2). These values are slightly lower compared to similar materials reported earlier in the literature (270-315 $m^2 g^{-1}$).[224]

XRD was used to investigate the influence of the thermal and acid treatments on the crystalline phases present in the Fe-PANI-AC samples (Fig. 4.1). The XRD patterns of the as-synthesised materials indicate the presence of unreacted oxidant, ammonium persulphate (APS, peaks labelled with Δ in Fig. 4.1), of polyaniline (20.4° and 24.6°, labelled with ○) and of ammonium chloride (peaks labelled with ◊).[224] The relatively higher intensity of the APS peaks in the diffractogram of Fe-PANI-AC-2 is due to the higher APS-to-Fe ratio used in this sample. After the acid treatment and the pyrolysis steps, all the peaks in the diffractogram of the as-synthesised materials (Fig. 4.1) disappear. In the case of Fe-PANI-AC-1, the diffractogram after the second pyrolysis only displays a broad peak around $2\theta = 24°$ (Fig. 4.1.A), which is characteristic for the (002) graphitic plane. Since this peak is rather broad, the graphitic carbon structure of the material has a relatively low degree of crystallinity.[153,176] The absence of any other signals suggests that the acid and thermal treatments efficiently removed the unreacted APS and ammonium chloride. On the other hand, the diffractogram of Fe-PANI-AC-2 displays XRD peaks ascribed to FeS and Fe_3S_4 (□ and ● in Fig. 4.1), together with the broad signal of graphitic carbon at around 24°. These sulphides were generated by the degradation of APS in the presence of iron species. The fact that iron sulphides were found only in Fe-PANI-AC-2 is likely to have been caused by the higher initial APS-to-Fe ratio that was used in this sample. An additional explanation for this behaviour is that a lower amount of N remained in Fe-PANI-AC-2 due to its higher pyrolysis temperature (see Table 4.1). This in turn means that this sample contains fewer sites available to bind Fe, thus favouring the formation of the iron sulphides. In agreement with these results, XPS shows an S content of ~3 wt% for Fe-PANI-AC-2, whereas the very low S content (< 0.1 wt%) in Fe-PANI-AC-1 confirms the absence of iron sulphides.

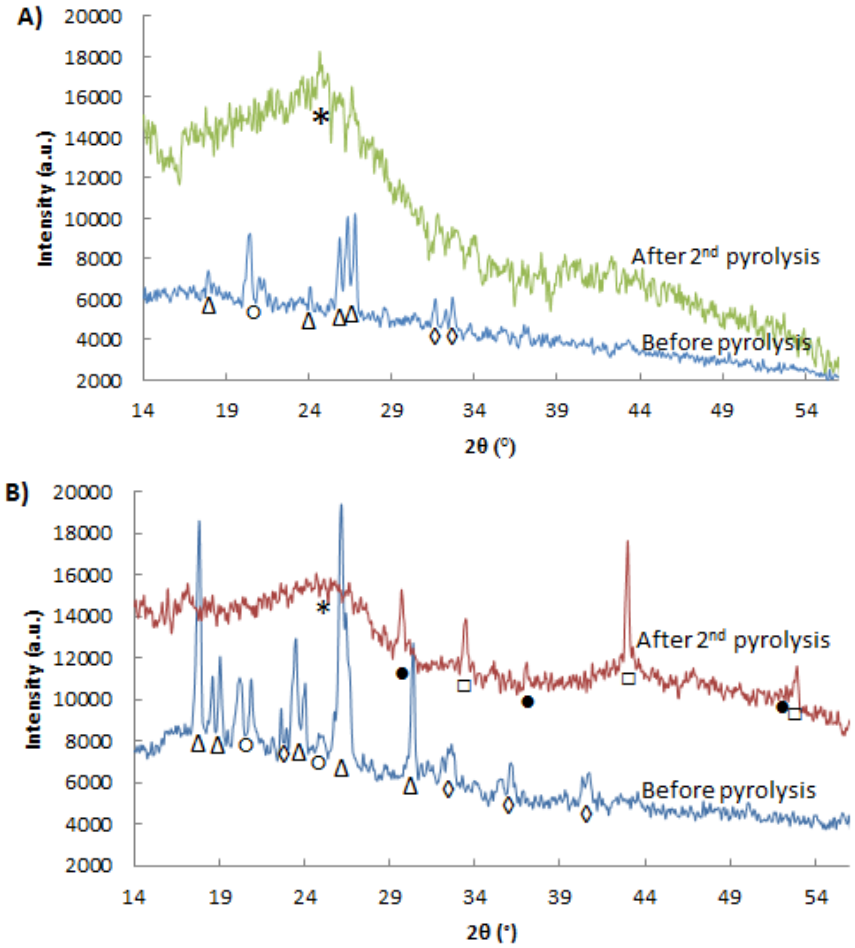

Figure 4.1. X-ray diffractograms of: (A) Fe-PANI-AC-1 and (B) Fe-PANI-AC-2. The peaks in the XRD pattern are identified as follows: Δ is (NH4)2S2O8, ◊ is NH4Cl, ○ is polyaniline, □ is FeS, ● is Fe3S4 and * is graphitic carbon.

Raman spectroscopy provides useful information on the degree of graphitisation of the synthesised electrocatalysts (Fig. 4.2).[153] Two characteristic bands can be distinguished in the Raman spectra of both materials: the D band at 1350 cm^{-1} and the G band at 1590 cm^{-1}. The G band is generally ascribed to the planar vibration of sp^2 C atoms in ideal graphitic layers and thus provides a measure of the amount of graphitic structure in the two materials. As for other carbon materials doped with N, the G band is found at lower wavenumbers than in undoped carbons and this down-shift is caused by an alteration in the electronic structure of the graphitic carbon lattice caused by the electron-donating capability of N atoms.[153,230] The D band is associated with disordered structures at the border of the sp^2 domains. The graphitisation degree can be estimated based on the ratio between the areas of the D and G bands (A_D/A_G).[153] For Fe-PANI-AC-1 and -2, the A_D/A_G values are 1.1 and 1.0, respectively. The slightly lower graphitic degree for Fe-PANI-AC-1 originates from its lower pyrolysis temperature (700°C, compared to 900°C for Fe-PANI-AC-2). These A_D/A_G values are also similar to those reported for graphite (A_D/A_G of 1.0),[231] proving that the prepared materials have a relatively high degree of graphitisation. The apparent discrepancy between this result and the relatively low degree of crystallinity indicated by XRD can be understood considering the composite nature of the Fe-PANI-ACs and the lower analysis depth of Raman (~1-5 µm) compared to XRD (~30 µm), which implies that the latter analysis included a larger fraction of the amorphous activated carbon located in the core of the materials (see Scheme 4.2). The

deconvolution of the Raman spectra shows the presence of two additional peaks, centred at 1200 and 1510 cm^{-1} (Fig. 4.2). These are generally assigned to C atoms outside the perfectly planar graphite network and to heteroatoms present in the graphite lattice, respectively.[176] As expected based on the lower degree of graphitisation for Fe-PANI-AC-1, the combined area of these two bands accounts for a larger fraction of the total area for Fe-PANI-AC-1 than for Fe-PANI-AC-2.

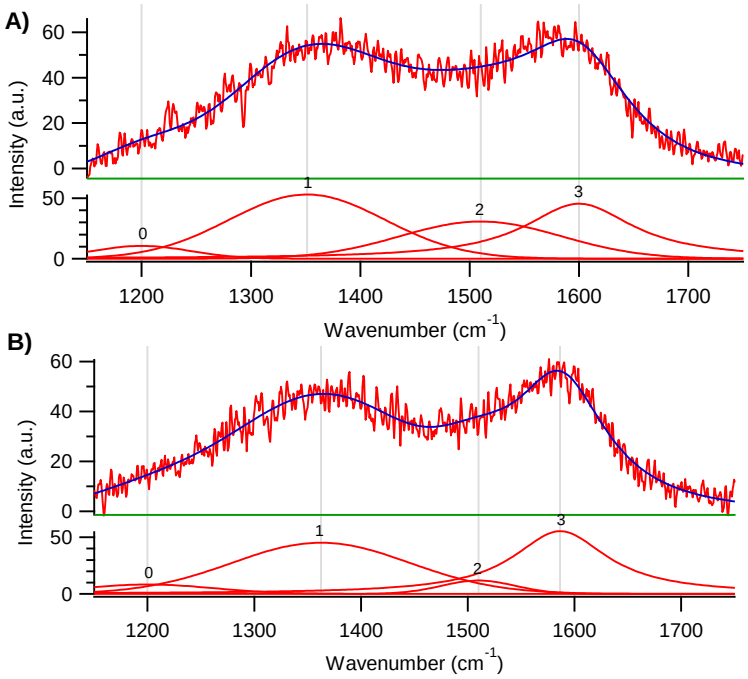

Figure 4.2. Deconvoluted Raman spectra of (A) Fe-PANI-AC-1 and (B) Fe-PANI-AC-2.

The polymerisation of aniline in the initial step of the synthesis procedure was monitored by means of FT-IR before the first pyrolysis step was performed (Fig. 4.3). The spectrum obtained for the non-pyrolysed Fe-PANI-AC-1 is comparable to spectra that were previously reported for pure polyaniline.[224,232,233] The peaks at 1610 (Δ) and 1480 cm^{-1} (◊) are assigned to the C=N stretching in quinoid diimine rings and to the aromatic C=C stretching, respectively. The sharp peak at 1403 cm^{-1} (▪) is ascribed to C-N stretching in the proximity of a quinoid diimine ring. The absorption bands at 1302 (○) and 1232 cm^{-1} (□) are attributed to aromatic C-H bending and aryl C-N stretching, respectively. The broad absorption band at 1134 cm^{-1} (●) is related to the benzenoid C-H in plane-bending and finally the large peak at 797 cm^{-1} (*) is characteristic for the out-of-plane deformations of C-H on 1,4-disubstituted rings.[224,232,233] After the second pyrolysis, all these peaks disappear from the FT-IR spectrum of Fe-PANI-AC-1, thus confirming the XRD analysis (*vide supra*) and demonstrating that polyaniline is fully converted into a new carbon structure upon pyrolysis.

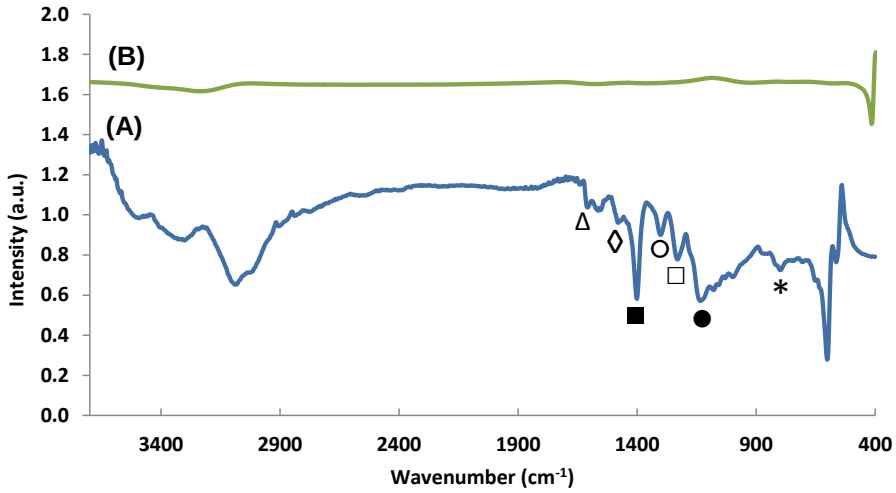

Figure 4.3. FT-IR spectra of Fe-PANI-AC-1 (A) before pyrolysis and (B) after the second pyrolysis.

Further analysis of the XPS data provides information about the configuration of N atoms in the prepared materials.[153,154,224] Figure 4.4 shows the different N configurations that can be typically found in N-doped carbon materials: (N1) pyridinic N, (N2) pyrrolic N, (N3) and (N4) graphitic or quaternary N and (N5) oxidised pyridinic N. In the XPS spectrum they can be found at 398.0-399.3 eV (N1), 399.8-401.2 eV (N2), 401.1-402.7 eV (N3/N4) and >402.8 eV (N5).[153] In the presence of a metal (in this case iron), N can also be present in a configuration bound to the metal (Fig. 4.4). However, this N-Fe peak cannot be distinguished from the pyridinic N peak in XPS since they occur at almost the same binding energy.[224] Therefore, in the following discussion the signals of N-Fe and pyridinic N are considered as a whole. In order to investigate the influence of the temperature on the N content and the N configuration, an extra sample was prepared with the same composition used for Fe-PANI-AC-1 but with a different pyrolysis temperature (400°C). XPS clearly shows that the N content decreases with the temperature from 22 wt% at 400°C to 6 wt% at 900°C, confirming the trend of decreasing N content with increasing pyrolysis temperature (*vide supra*). Furthermore, it is observed that the N configuration is strongly affected by the pyrolysis temperature (Fig. 4.4). No graphitic N species are present in the material pyrolysed at 400°C, whereas a new peak that can be correlated to the formation of graphitic N emerges at higher binding energy in the XPS signal of the material pyrolysed at 700°C. This proves that graphitisation of the Fe-PANI-AC material requires a high pyrolysis temperature. The fraction of graphitic nitrogen further increases in the material pyrolysed at 900°C, as indicated by the deconvolution of the N 1s signal in the XPS spectra (Table 4.2 and Fig. S4.2). The fraction of pyridinic N and pyrrolic N decreases with the pyrolysis temperature, with the effect being much more pronounced for pyrrolic N (Table 4.2). Based on this observation, it can be concluded that pyrrolic N is the least stable species, which is in line with previous reports.[79,153] The higher fraction of pyridinic N/N-Fe in the Fe-PANI-AC pyrolysed at 700°C compared to 900°C can be associated with a higher amount of N-Fe species since more Fe was detected by XPS in Fe-PANI-AC-1 than in Fe-PANI-AC-2 (see Table 4.1). However, the nature of the iron species in the Fe-PANI-AC materials is more complex, as shown by the presence of a contribution assigned to iron oxides (at 530 eV) in the O 1s signal in XPS (Fig. S4.3 and Table S4.1). Based on these XPS data, it was calculated that the fraction of surface iron species that is present as iron oxides is 13% for Fe-PANI-AC-1 and 50% for Fe-PANI-AC-2 (assuming that the Fe-O oxides are Fe_2O_3). The higher fraction of iron oxides in Fe-

PANI-AC-2 can be related to the decrease in number of surface N sites available for coordinating Fe, caused by the higher pyrolysis temperature used in the synthesis of this material. To further evaluate the configuration of Fe inside the electrocatalyst, the high resolution Fe 2p XPS signal was investigated (Fig. 4.4). The two bands at around 711 and 723 eV are assigned to $2p_{3/2}$ and $2p_{1/2}$ photoelectrons from Fe. XPS peaks in this position have been ascribed to several different Fe-containing species, including Fe(II)-N in pyridine-iron complexes,[234] Fe-S species,[235] and Fe-O in iron oxides.[236] Since Fe-PANI-AC-1 does not contain Fe-S species (*vide supra*) we assign the obtained XPS signal to the expected Fe-N species in this material (Scheme 4.2) and to iron oxides (as indicated by the O 1s signal).

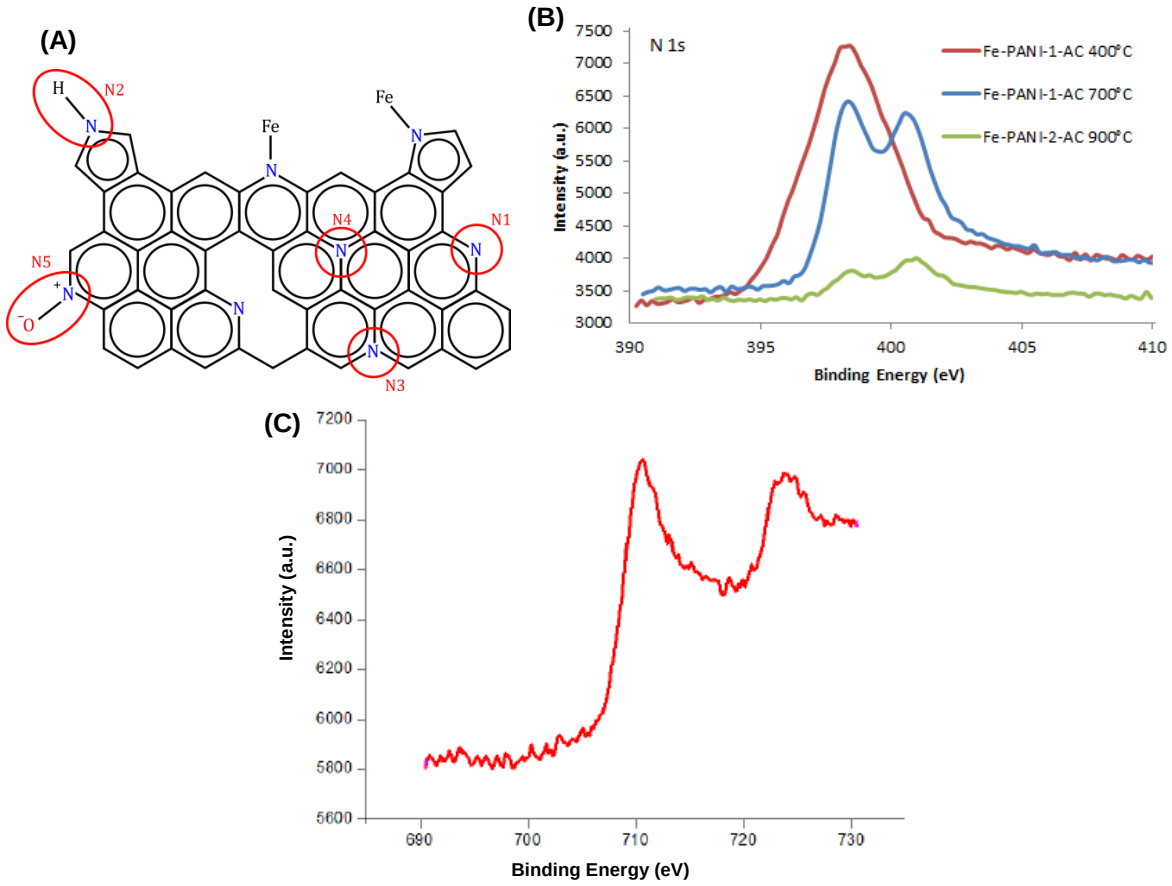

Figure 4.4. (A) Representation of a graphitic carbon material with the different possible N configurations. (B) N1s XPS signal as a function of the pyrolysis temperature used in the synthesis of Fe-PANI-AC. (C) Fe 2p XPS signal of Fe-PANI-AC-1.

Table 4.2. N configurations in the Fe-PANI-AC materials prepared at different pyrolysis temperature.

Sample	Pyridinic N (or N-Fe)	Pyrrolic N	Graphitic N	Oxidised pyr N	N_{pyr}/N_{quat}
Fe-PANI-AC-1 400°C	57%	43%	0%	0%	∞
Fe-PANI-AC-1 (700°C)	44%	14%	32%	10%	1.4
Fe-PANI-AC-2 (900°C)	35%	8%	50%	7%	0.7

The nature of the iron sites in the Fe-PANI-AC materials was further investigated by Time of Flight-Secondary Ion Mass Spectroscopy (ToF-SIMS). This analysis shows that the Fe-PANI-AC materials contain the anticipated FeN_xC_y species, where y is in the range from 1 to 12 (compounds with higher values for y could no longer be distinguished from the background signal) and x is in the range from 1 to 4, since iron can coordinate a maximum of four nitrogen atoms (see Table 4.3).[54]

Table 4.3. Relative abundance of C_xN_yFe ions (in %) for Fe-PANI-AC-1 and -2, as determined by analysis of the negative (top) and positive (bottom) secondary ions by ToF-SIMS.

	$FeNC_y^-$	$FeN_2C_y^-$	$FeN_3C_y^-$	$FeN_4C_y^-$
Fe-PANI-AC-1	26.1	36.7	26.0	11.2
Fe-PANI-AC-2	19.1	43.5	14.2	23.2

	$FeNC_y^+$	$FeN_2C_y^+$	$FeN_3C_y^+$	$FeN_3C_y^+$
Fe-PANI-AC-1	63.1	14.5	11.3	11.2
Fe-PANI-AC-2	50.9	16.0	16.4	16.8

These data lead to an important conclusion: all four possible degrees of coordination of Fe with N are present in the material. The analysis also provides the relative abundance of the FeN_xC_y species. However, these data should be considered with caution, because the analysis with negative secondary ions indicates that FeN_2C_y species are the most abundant type in both materials, whereas $FeNC_y$ species are the major ones when the analysis is carried out with positive secondary ions (Table 4.3). ToF-SIMS also confirms the presence of Fe-O species in both materials (see Table S4.2), while virtually no N-Fe-O species were observed. This supports our assignment of the Fe 2p XPS signal to both Fe-N and Fe-O species. The ratio of Fe-O species to FeN_xC_y species is higher for Fe-PANI-AC-2 (0.76) than for Fe-PANI-AC-1 (0.20) (see Table S4.2), in line with the results obtained by deconvoluting the O 1s XPS signals (*vide supra*). The presence of fragments containing more than one Fe atom (Fe_2O^+, $Fe_2O_2^+$ and $Fe_3O_3^+$) confirms the assignment of these Fe-O species to iron oxides, which are most likely organised in small, amorphous domains, as no peak related to any crystalline iron oxide phase was observed by XRD (Fig. 4.1). On the other hand, no iron sulphides were detected by ToF-SIMS although these species were observed in Fe-PANI-AC-2 by XRD. This suggests that the iron sulphides are not exposed on the surface of the material, since ToF-SIMS has an analysis depth of only 1-3 monolayers. This would also explain why these species did not get removed efficiently by the acid and thermal treatment (*vide supra*).

In summary, the characterisation of Fe-PANI-ACs shows that the materials contain the anticipated Fe-N species, which are expected to be the electrocatalytically active sites.[13,15] The N atoms involved in the coordination of Fe can have pyridinic or pyrrolic configuration (Scheme 4.2 and Fig. 4.4), but if less than two pyrrolic N are involved (*e.g.* in $FeNC_y$), then the positive charge of iron should be compensated by anions, such as chlorides. Indeed, the presence of Cl in both materials was proven by XPS (1.7 wt% for Fe-PANI-AC-1 and <0.5 wt% for Fe-PANI-AC-2). Besides the N-Fe species, the materials contain iron in the form of oxides and, in the case of Fe-PANI-AC-2, of sulphides. The latter are not exposed on the surface and, therefore, will not contribute to the electrocatalytic activity, whereas the iron oxide domains are present at the surface and may contribute to the activity in the NO reduction reaction.

4.3.2 Electrochemical characterisation

Half cell tests

The performance of the Fe-PANI-AC materials as electrocatalysts for the reduction of NO was first assessed by means of linear sweep voltammetry (LSV) in a half cell setup. LSV is often used to screen the activity of electrocatalysts for a certain reaction in order to rank them based on the current density measured in the selected potential region. Four different electrocatalysts were tested: Fe-PANI-AC-1, Fe-PANI-AC-2, FePc/AC and 10 wt% Pt supported on activated carbon (Pt/AC). The latter two were used as reference electrocatalysts: FePc/AC was chosen because it had been identified as a promising electrocatalyst for this reaction,[13] whereas Pt/AC was selected because it is similar to the industrial catalyst for the chemical route to produce NH_2OH and it is also a common benchmark electrocatalyst.

During the LSV measurements, the potential was varied from the open circuit potential to -0.69 V vs. Ag/Ag_2SO_4, while a gas mixture containing 6% or 18% NO in N_2 was continuously cycled over the cathode compartment. Previous experimental research has shown that the selectivity towards hydroxylamine is the highest when 3M H_2SO_4 is used as electrolyte and that the electricity generation increases with the partial pressure of NO up to 25 kPa (*i.e.* ~25%NO), at which it reaches a plateau.[13]

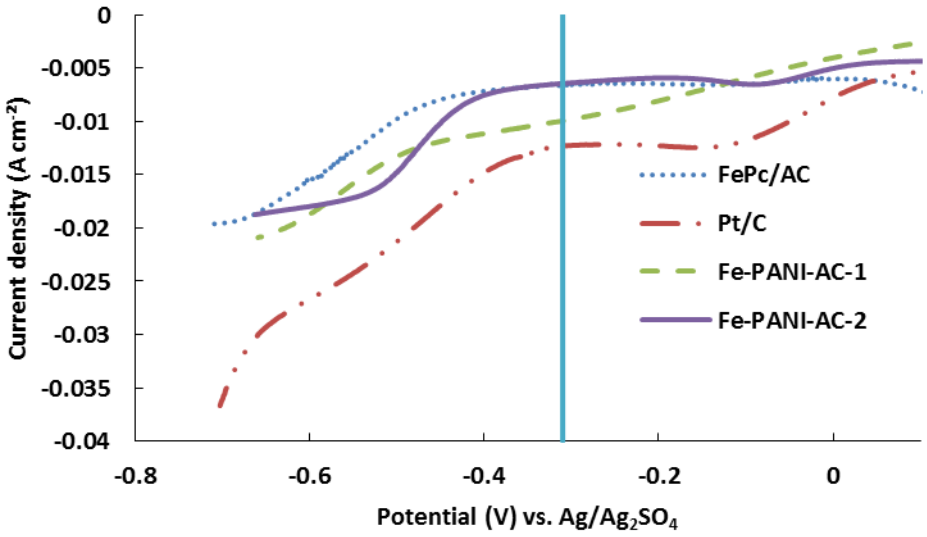

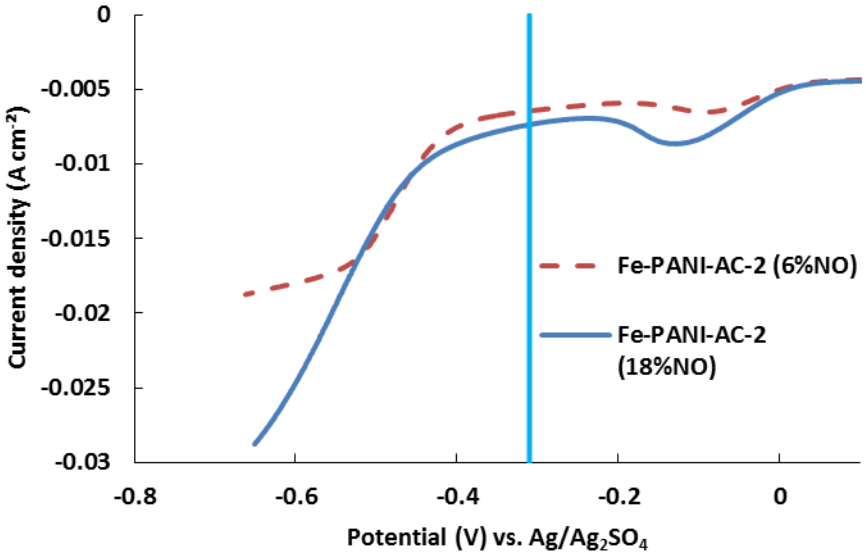

Figure 4.5. Top: LSV plots of the electrocatalysts under study with 6% NO in N2 as a cathode feed. Bottom: LSV plots of Fe-PANI-AC-2 with 6 and 18% NO in the feed and corrected for the iR drop. The first part of the LSV plots from 0.3 to 0.1 V vs. Ag/Ag_2SO_4 has not been represented in the figures. The part of the plot at more negative potential relative to the standard potential for the reduction of NO to NH2OH (marked by the vertical line at 0.31 V vs. Ag/Ag_2SO_4) is the region of interest for this study.

A first indication of the performance of the synthesised electrocatalysts in the production of hydroxylamine is provided by the value of the current density in the region of interest, *i.e.* at a potential below -0.31 V vs. Ag/Ag_2SO_4, which is the standard potential (E^0) for the reduction of NO to NH_2OH (Fig. 4.5, top).[15] The current that is produced at potentials higher than -0.31 V vs. Ag/Ag_2SO_4 is caused by other reduction reactions that are not of interest for this study and which will thus not be discussed further. Based on the current densities in the region of interest, the activity for the reduction of NO increases in the order FePc/AC < Fe-PANI-AC-2 < Fe-PANI-AC-1 < Pt/AC. This trend can be explained based on the metal content of these electrocatalysts, which increases in the same order (from 0.3 wt% for FePc/AC to 1 wt% for Fe-PANI-AC-2, 3 wt% for Fe-PANI-AC-1 and 10 wt% for Pt/AC). Since it is assumed that metals are the active sites promoting the reduction of NO (see Scheme 4.1), it is expected that the electrocatalyst with the highest metal loading leads to the highest current density. It should be noted that for the Fe-PANI-AC electrocatalysts, the surface metal loading (as determined by XPS) was assumed to be the important figure for explaining the NO reduction activity. Although the current density measured by LSV offers a first, rapid evaluation of the electrocatalysts performance in the reduction of NO, it does not provide any information about the selectivity towards the desired hydroxylamine product. Therefore, the Pt-containing electrocatalyst is not necessarily the most suitable for the selective production of hydroxylamine. On the contrary, previous reports showed that Pt electrocatalysts display very poor selectivity towards hydroxylamine and are thus not the best choice for this application.[13,14] In order to get a better idea on the selectivity of the NO reduction on the different electrocatalysts, single cell tests were performed (see next section).

Linear sweep voltammetry in the half cell setup was also employed to study the influence of the NO content in the feed gas on the produced current using Fe-PANI-AC-2 as electrocatalyst (Fig. 4.5, bottom). As expected, the current density at potentials lower than -0.31V vs. Ag/Ag_2SO_4 increases when the concentration of NO in the feed increased from 6 to 18%. However, the current density does not increase by a factor of three upon a threefold

increase in reactant concentration. This suggests that there are not enough active sites available in the electrocatalyst in order to maintain the same reaction rate with the increased concentration of NO in the feed.

Chronoamperometric evaluation of hydroxylamine production in a fuel cell setup

In order to investigate the applicability of the synthesised materials as electrocatalysts for the selective reduction of NO to hydroxylamine (NH_2OH) in a fuel cell, chronoamperometric experiments were performed in a single cell (mimicking the fuel cell conditions) at three different potentials (0; 0.05; 0.10 V) with 6 or 18% NO in N_2 as the cathodic gas feed. The current density was measured for at least 20000 s in order to ensure that a representative amount of data was recorded in a quasi-stationary condition. The electrocatalysts performance can be evaluated based on the rate of hydroxylamine production [$mmol_{NH2OH}$ h^{-1}], on the yield of hydroxylamine [Y_{NH2OH} (%)], on the current efficiency towards hydroxylamine [CE_{NH2OH} (%)], which is a measure of the selectivity towards NH_2OH in the reduction of NO, and on the power generated at steady state (Table 4.4).

Several conclusions can be drawn from the chronoamperometric tests performed with 6% NO in the feed. First of all, the trend already observed by LSV of increasing current density with increasing content of accessible metal (either Fe or Pt) is confirmed in these experiments. Secondly, the selectivity towards hydroxylamine is much higher over FePc/AC than over the Fe-PANI-AC materials (see the current efficiency values in Table 4.4). This behaviour is ascribed to the lower iron content and isolated nature of the iron sites of FePc/AC, and is consistent with previous reports,[13] in which it was proposed that the formation of the main side products in the synthesis of NH_2OH from NO, *i.e.* N_2O and NH_3, requires two neighbouring iron sites. Therefore, a lower metal content will lead to a higher selectivity towards hydroxylamine since the probability to encounter two neighbouring metal sites in the final structure of the electrocatalyst decreases by lowering the metal loading. The current efficiencies achieved with the two Fe-PANI-AC materials are similar to each other, and lower than that achieved with FePc/AC. This suggests that in these two electrocatalysts the iron sites are closer than in FePc/AC, as a consequence of the higher metal loading but also of the absence of the phthalocyanine ligand acting as a spacer. As anticipated, no hydroxylamine was produced when Pt/AC was used as electrocatalyst (Table 4.4). This result is attributed both to the nature of the metal and to its high loading. Based on the discussion above, the ranking of the investigated electrocatalysts differs whether the focus lays on current generation or on selectivity to hydroxylamine. For the former the performance increases in the order FePc/AC < Fe-PANI-AC-2 < Fe-PANI-AC-1 < Pt/AC, while the selectivity increases in the order Pt/AC < Fe-PANI-AC-2 ~ Fe-PANI-AC-1 < FePc/AC. Based on these results, the Fe-PANI-AC materials can be considered promising electrocatalysts for the reduction of NO to NH_2OH, because they lead to a yield of the desired hydroxylamine similar to that obtained with FePc/AC, but they are able to generate significantly higher electric power (Table 4.4). Moreover, these materials have the advantage of a straightforward preparation from inexpensive precursors.

From the perspective of potential industrial application, it is relevant to study the performance of the electrocatalysts also using a higher concentration of NO in the gas feed (18%). These tests were performed by poising the cell at 0, 0.05 and 0.10 V and using either Fe-PANI-AC-2 or the reference FePc/AC as electrocatalyst (Table 4.5). In line with logical expectations and with what was observed in the LSV tests, the current density increases by increasing the concentration of the reactant in the feed (compare entry 1 in Table 4.5 with entry 2 in Table 4.4, and entry 4 in Table 4.5 with entry 3 in Table 4.4).

Table 4.4. Chronoamperometric tests of the electrocatalysts under study, with 6% NO (cathode feed: 6% NO in N2, 10 ml min^{-1}; anode feed: 100% H2, 10 ml min^{-1}; room temperature).

Entry	Electrocatalyst used in the cathode	% NO	ΔE_{cell} poised (V)	ΔE_{cell} at steady state (V)	Current density (j) at steady state (A m^{-2})	Power at steady state (W m^{-2})	Production rate ($mmol_{NH2OH}$ h^{-1})	Y_{NH2OH} (%)	CE_{NH2OH} (%)
1	Fe-PANI-AC-1	6	0	0.018	-115	-2.1	0.46	31	34
2	Fe-PANI-AC-2	6	0	0.014	-98	-1.4	0.27	18	29
3	FePc/AC	6	0	0.010	-76	-0.8	0.60	39	80
4	Pt/AC	6	0	/	-130	/	not detected	0	0

Table 4.5. Chronoamperometric tests of the electrocatalysts under study, with 18% NO (cathode feed: 18% NO in N2, 10 ml/min; anode feed: 100% H2, 10 ml/min; room temperature).

Entry	Electrocatalyst used in the cathode	% NO	ΔE_{cell} poised (V)	ΔE_{cell} at steady state (V)	Current density (j) at steady state (A m^{-2})	Power at steady state (W m^{-2})	Production rate ($mmol_{NH2OH}$ h^{-1})	Y_{NH2OH} (%)	CE_{NH2OH} (%)
1	Fe-PANI-AC-2	18	0	0.020	-153	-3.1	1.23	27	63
2	Fe-PANI-AC-2	18	0.050	0.067	-139	-9.3	0.92	21	53
3	Fe-PANI-AC-2	18	0.100	0.112	-112	-12.5	0.63	14	46
4	FePc/AC	18	0	0.017	-117	-2.0	0.44	9.9	30
5	FePc/AC	18	0.050	0.063	-74	-4.5	0.34	7.6	42
6	FePc/AC	18	0.100	0.108	-64	-7.0	0.32	7.1	40

On the other hand, and quite surprisingly, the selectivity towards hydroxylamine measured in terms of current efficiency increases significantly in the case of Fe-PANI-AC-2, whereas it decreases dramatically in the case of FePc/AC. This results in an almost threefold higher production rate of hydroxylamine over Fe-PANI-AC-2 compared to FePc/AC (Table 4.5). The lower hydroxylamine selectivity with FePc/AC can be explained considering that at low NO concentrations (*e.g.* 6%), the probability that two NO molecules come in contact with each other is very low due to the relatively low number of NO molecules that are being fed to the cathodic compartment and due to the lack of neighbouring iron sites in this type of electrocatalysts. Since an encounter between two NO molecules (or intermediates) is necessary to produce the main side-products (see Introduction), the selectivity towards NH_2OH can decrease by increasing the concentration of reactant (*e.g.* to 18% NO). However, this type of analysis cannot account for the increase in hydroxylamine selectivity observed with Fe-PANI-AC-2. This strongly suggests that the nature of the active sites in the Fe-PANI-AC electrocatalysts is different, and presumably more complex, compared to the well-defined sites in FePc/AC. In this line of reasoning, a possible explanation for the increased selectivity with Fe-PANI-AC-2 is that some active iron sites might be less accessible or might coordinate NO more weakly and thus remain unoccupied at low NO concentrations. At higher NO contents these sites will be utilised as well. In the hypothesis that these sites have lower accessibility, the chance of a second NO molecule approaching them will be low. If these iron sites coordinate NO more weakly, they might be also more prone to release the formed NH_2OH, thus preventing its further reduction to NH_3. Therefore, both types of sites would lead to an increased selectivity towards hydroxylamine, thus explaining the observed behaviour. The existence of active sites with different activity is strongly supported by the ToF-SIMS data, which showed the presence of FeN_xC_y species with different value of x (1 to 4) in the Fe-PANI-AC materials (*vide supra*). However, further research is still necessary to shed more light on the adsorption strength and the location of

the various types of active sites in these electrocatalysts and on the possible contribution of the iron oxide species. Further understanding of the selectivity of the electrocatalysts could also be achieved by analysing the gaseous products of the NO reduction, which was not possible with the setup employed in this work.

The study of Fe-PANI-AC-2 and FePc/AC as electrocatalysts with 18% NO in the feed was completed by investigating the effect of poising the cell at different potentials, *i.e.* 0, 0.05 and 0.10 V. Increasing the cell potential enhanced the power generation at the expense of the hydroxylamine production (Table 4.5). At each potential, the electric power generated as well as the selectivity and yield of the desired hydroxylamine are markedly higher with Fe-PANI-AC-2 compared to those obtained with FePc/AC. These results confirm the superior performance of Fe-PANI-AC-2 when 18% NO is used as gas feed. The gradual decrease in the hydroxylamine selectivity over Fe-PANI-AC-2 by increasing the cell potential, and thus in conditions in which the reaction rate and the current density are lower, is consistent with our hypothesis of different types of active sites in this material. Among the three tested cell potentials, 50 mV might result in the best compromise between power density on one hand, and yield and selectivity towards hydroxylamine on the other hand.

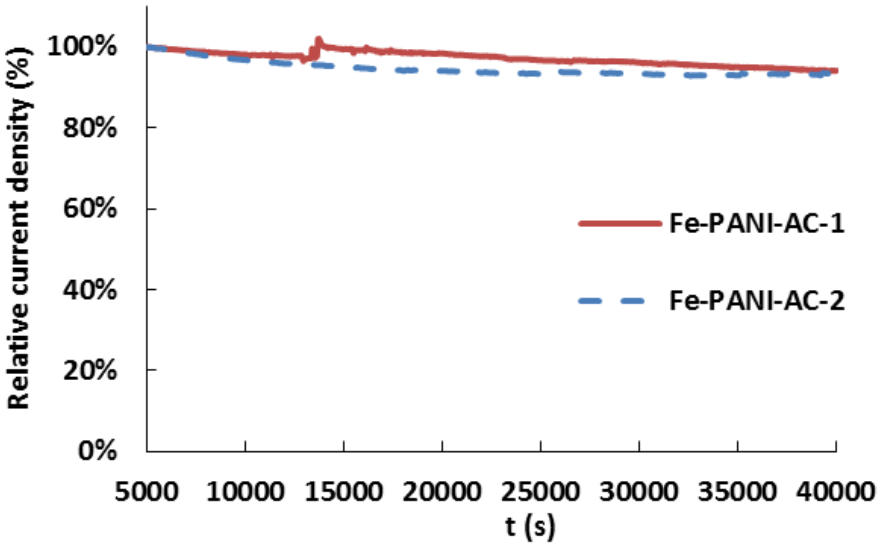

Figure 4.6. Relative current density vs. time (j–t) plot based on chronoamperometric measurements of the Fe-PANI-AC electrocatalysts at 0.01V vs. Ag/Ag_2SO_4 in a 3 M H_2SO_4 solution with 6% NO in the gas feed.

Finally, the stability of the two Fe-PANI-AC electrocatalysts was evaluated based on the chronoamperometric measurements carried out at a constant potential of 0.01 V vs. Ag/Ag_2SO_4 for 40000 s in a 3 M H_2SO_4 solution and with 6% NO in the gas feed. The performance loss between 5000 and 40000 s (*i.e.* after initial stabilisation) is 6% for both Fe-PANI-ACs (Fig. 4.6), which means that our electrocatalysts are rather stable under the fuel cell operating conditions.

4.4 Conclusions

Iron-containing N-doped carbon materials derived from activated carbon and polyaniline incorporating Fe sites (Fe-PANI-AC) were reported here for the first time as electrocatalysts for the reduction of NO with the industrially relevant NH_2OH as target product. The electrochemical synthesis of hydroxylamine in a fuel cell setup is a very attractive option in

the context of green chemistry as it would allow producing this useful compound while converting the energy liberated in the process into electricity. The Fe-PANI-AC electrocatalysts showed very promising results in terms of current density generated, selectivity and yield of the desired hydroxylamine product, particularly when the tests were performed employing a gas feed with higher NO concentration (18%). Under these conditions, the performance of Fe-PANI-AC was much superior to that of the reference FePc/AC (increase of 33% in terms of selectivity towards NH_2OH, 1.5 times higher power generation, and a nearly threefold increase in NH_2OH production rate), which was the most promising electrocatalyst reported so far for this application. Importantly, the Fe-PANI-AC electrocatalysts displayed high stability under fuel cell operating conditions. An additional advantage of the Fe-PANI-AC electrocatalysts is that their synthesis is based on inexpensive precursors, is straightforward and has the potential to be easily up-scalable. The characterisation of the Fe-PANI-AC electrocatalysts indicated that different types of isolated N-coordinated Fe sites are present, alongside with iron oxides. The observed electrocatalytic behaviour could be correlated well with the existence of this variety of active sites. Future research should aim at elucidating further the complex nature of the iron species acting as active sites in the reduction of NO to NH_2OH. This could entail DFT computational modeling of the different FeN_xC_y sites observed in this work, and of their interaction with NO and with the reaction intermediates in the proposed mechanism (Scheme 4.1). Moreover, the optimisation of the synthesis method (*e.g.* pyrolysis temperature, type of activated carbon support and metal loading) is expected to lead to further improvements in the electrocatalytic performance.

Supporting information

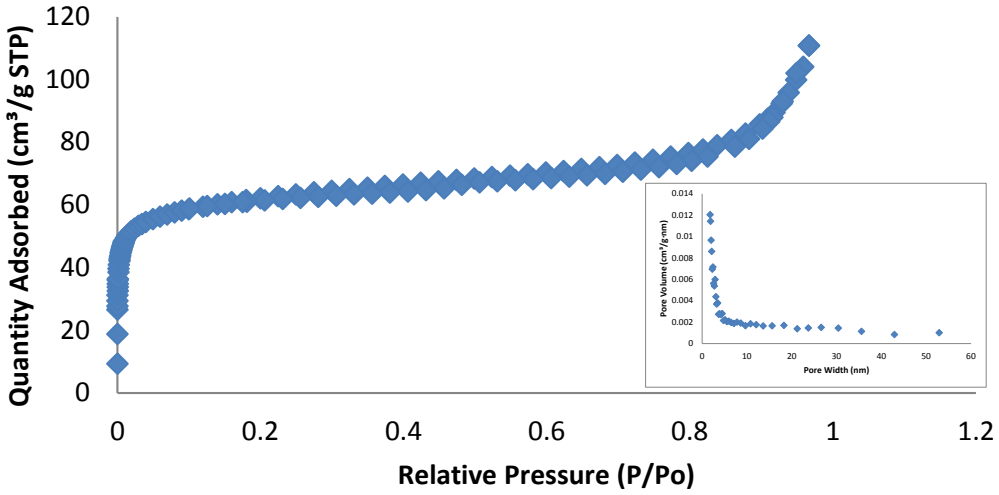

Figure S4.1. N_2 adsorption isotherm and pore size distribution (inset) of Fe-PANI-AC-2.

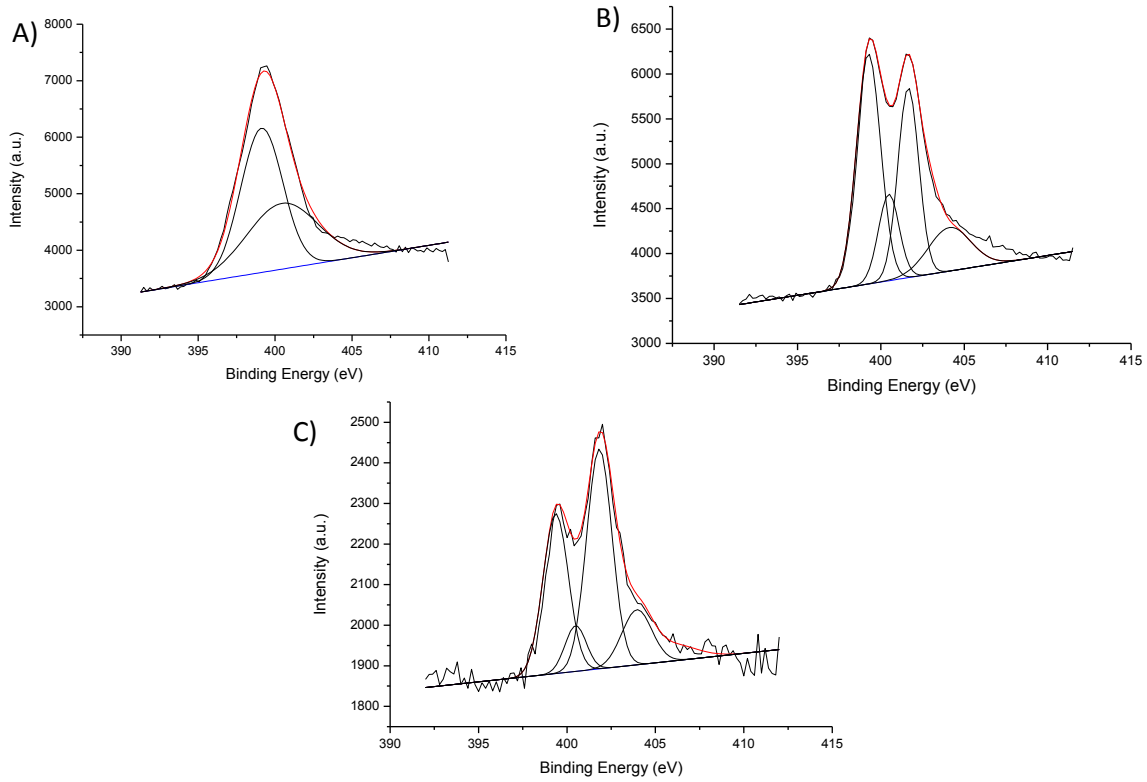

Figure S4.2. Deconvoluted N 1s XPS spectra of (A) Fe-PANI-AC-1 400°C, (B) Fe-PANI-AC - 1 (700°C) and (C) Fe-PANI-AC-2 (900°C).

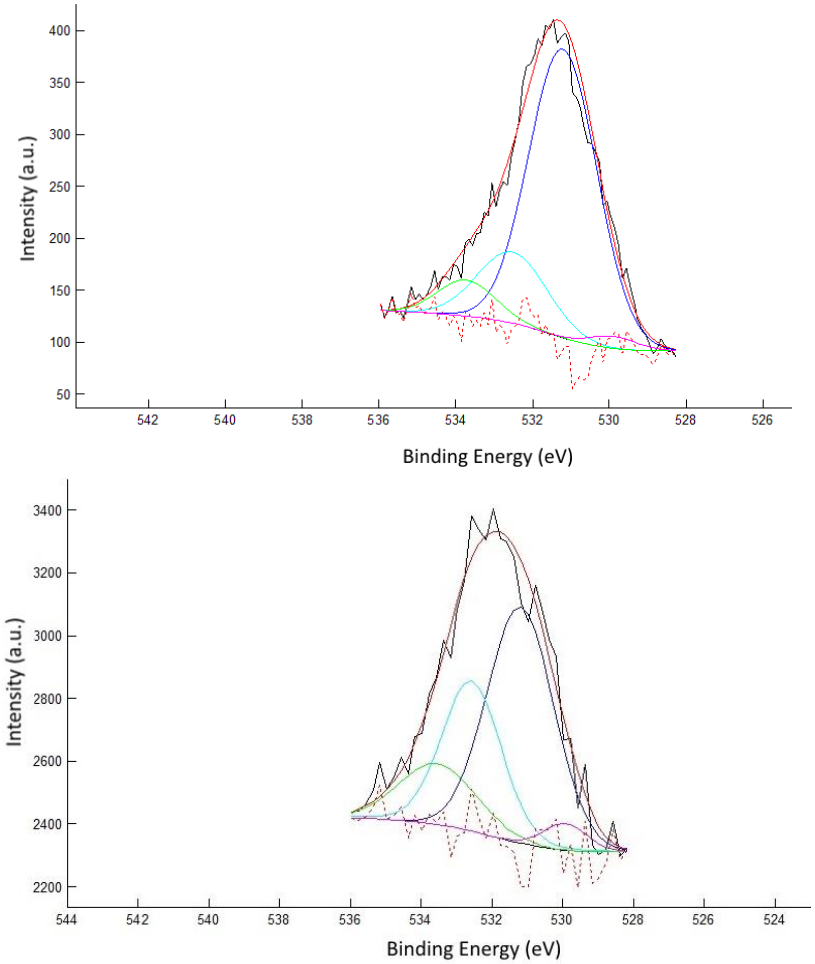

Figure S4.3. Deconvoluted O 1s XPS spectra of (A) Fe-PANI-AC-1 and (B) Fe-PANI-AC-2.

Table S4.1. O configurations in the Fe-PANI-AC materials.

Sample	Fe-O (530.0 eV)	C-O (531.5 eV)	C=O (532.6 eV)	O-C=O (533.8 eV)
Fe-PANI-AC-1	2.1%	72%	18%	7.6%
Fe-PANI-AC-2	3.7%	51%	30%	15%

Table S4.2. Relative abundance of iron species in Fe-PANI-AC-1 and -2, as determined by analysis of the negative secondary ions by ToF-SIMS.

	Fe-PANI-AC-1	Fe-PANI-AC-2
$FeNC^-$	2.8%	2.6%
FeO_2^-	5.7%	14%
FeO_2H^-	2.6%	6.7%
$FeNC_2^-$	1.6%	1.1%
FeN_2C^-	3.9%	9.6%
FeO_3^-	4.6%	12%
FeO_3H^-	3.5%	10%
$FeNC_3^-$	17%	7.0%
$FeN_2C_2^-$	15%	5.1%
FeN_3C^-	0.8%	0.5%
$FeN_2C_3^-$	3.5%	4.8%
$FeN_3C_2^-$	2.0%	1.5%
FeN_4C^-	0.9%	0.4%
$FeN_2C_4^-$	4.3%	2.1%
$FeN_3C_3^-$	7.6%	1.5%
$FeN_4C_2^-$	2.7%	8.7%
$FeN_2C_5^-$	2.5%	1.8%
$FeN_3C_4^-$	2.2%	1.4%
$FeN_4C_3^-$	0.5%	0.5%
$FeN_2C_6^-$	1.8%	1.2%
$FeN_3C_5^-$	3.9%	1.4%
$FeN_4C_4^-$	0.9%	0.3%
$FeN_3C_6^-$	1.8%	0.9%
$FeN_4C_5^-$	0.5%	0.3%
$FeN_3C_7^-$	1.2%	0.3%
$FeN_4C_6^-$	1.0%	0.3%
$FeN_3C_8^-$	1.3%	0.5%
$FeN_4C_7^-$	0.7%	1.6%
$FeN_3C_9^-$	0.8%	0.2%
$FeN_4C_8^-$	0.8%	0.3%
$FeN_4C_9^-$	0.1%	0.1%
$FeN_4C_{10}^-$	0.6%	0.1%
$FeN_4C_{11}^-$	0.3%	0.2%
$FeN_4C_{12}^-$	0.4%	0.5%

Chapter 5

Selective cogeneration of aniline and electricity over electrocatalysts based on nitrogen-doped carbons containing non-noble metals

Abstract

Non-noble metals (Fe, Co or Cu) supported on N-doped carbons are investigated for the first time as electrocatalysts for the reduction of nitrobenzene in a half-cell setup. If applied in a proton-exchange membrane fuel cell, this reaction offers the potential to cogenerate electricity and industrially valuable chemicals at the same time. The electrocatalyst performance was largely determined by the nature of the metal. Furthermore, by testing several synthesis methods, it was determined that each metal had a different optimal method. The Cu-based electrocatalysts, synthesised with a low amount of aniline and Cu, were identified as the best electrocatalysts based on their onset potential, kinetic current density and selectivity to aniline. Most importantly, unprecedented selectivities to aniline were obtained (82% as determined by chronoamperometry) with this electrocatalyst in a half-cell setup. This makes them a promising candidate for the electrochemical cogneration of aniline and electricity in a fuel cell.

Based on:

N. Daems, J. Wouters, K. Baert, C. Poleunis, A. Delcorte, A. Hubin, I.F.J. Vankelecom, P.P. Pescarmona, *in preparation.*

Author contributions

The original idea of this research was developed by N. Daems and P. P. Pescarmona. Electrocatalyst synthesis, physicochemical and electrochemical characterisation were done by N. Daems and J. Wouters. The article was written by N. Daems with editing by P. P. Pescarmona. ToF-SIMS measurements were performed by C. Poleunis under the supervision of A. Delcorte and XPS measurements by K. Baert under the supervision of A. Hubin. GC analysis was performed by N. Daems. The whole work was supervised by P. P. Pescarmona and I. F. J. Vankelecom.

5.1 Introduction

Aniline is an important industrial chemical product,[20] which is largely employed as reagent for the synthesis of polyurethane.[21] In 2010, the world aniline production was ca. $2.3 \cdot 10^6$ tons, of which 2/3 was utilised in the production of polyurethane.[237] Currently, aniline is mainly produced through the hydrogenation of nitrobenzene with Raney nickel or other nickel alloys as a catalyst.[20,238,239] In order to achieve high conversion and selectivity towards aniline (currently between 80 and 90%, with azobenzene and azoxybenzene as the main side-products), the reaction is performed at 35-125°C, at high H_2 pressure (≥ 0.6 MPa) and with long reaction times.[20,21,238,239] Furthermore, since this hydrogenation reaction is exergonic ($\Delta_r G^0 < 0$), a high amount of heat is typically lost in the process. In extreme cases, it might even become difficult to remove heat safely and reactor hot spots might be generated, lowering the reaction yields.[23,240]

The issues discussed above could be avoided by synthesising aniline through an electrochemical approach, where aniline is produced in a fuel cell and the chemical energy liberated by the reaction is converted into electricity. In this way, the synthesis of a valuable product like aniline can be coupled with electricity generation, giving rise to a more sustainable and more energy-efficient process.[24,25] Moreover, the electrochemical aniline production would offer the possibility to control the reaction rate and the selectivity by tuning the electrical potential.[241]

The possibility to reduce nitrobenzene electrochemically was first investigated by Haber *et al.* and has been further developed since then.[22–25] The electrochemical cell typically consists of an anodic and a cathodic compartment, which are separated by a proton exchange membrane (PEM). At the anode, protons and electrons are generated from the oxidation of hydrogen. Both flow to the cathodic compartment, the electrons through an external circuit and the protons through the PEM. Once they reach the cathode, they are involved in the reduction of nitrobenzene. The overall reactions are:

Anode:

$$H_2 \rightarrow 2H^+ + 2e^- \quad E^0 = 0 \text{ V} \tag{5.1}$$

Cathode:

$$PhNO_2 + 6H^+ + 6e^- \rightarrow PhNH_2 + 2H_2O \quad E^0 = 0.82 \text{ V} \tag{5.2}$$

However, the full reaction scheme is more complex and can involve both electrochemical and chemical steps.[23–25,242] It is generally accepted that the reduction of nitrobenzene to aniline consists of two main steps; first, nitrobenzene is reduced to phenylhydroxylamine (PHA) through a four electron exchange, with nitrosobenzene (NSB) as an intermediate. A final 2-electron reduction step then converts PHA to aniline and it benefits from a weakly acidic environment (Scheme 5.1).[243,244] Nitrosobenzene is generally not detected since it is rapidly converted to PHA via a second 2-electron reduction.[244] PHA is a very unstable compound and, besides being reduced to give aniline, it can also react further through three competitive chemical reactions, leading to the formation of side-products as azoxybenzene, azobenzene and para-ethoxyaniline (Scheme 5.1). These competitive reactions have already been discussed in detail elsewhere.[23–25,245–247] If aniline is obtained through the 6-electron reduction of nitrobenzene, care should be taken to avoid further reduction to cylcohexylamine. The formation of this side-product has been reported to take place on carbon supported platinum (Pt/C) electrocatalyts in a fuel cell.[248]

The outcome of the nitrobenzene reduction is strongly influenced by the applied electrocatalyst[23,243,244,246,249–253] and the reaction conditions, such as electrode potential[244,246,251] and the pH.[243,250,251,254] It has already been demonstrated that the selectivity towards aniline can be increased by applying more negative electrode potentials. However, an optimal potential exists since the possibility to further reduce aniline towards cyclohexylamine becomes more likely at increasingly negative potentials. Furthermore, at these potentials another competing reaction, i.e. the hydrogen evolution, can start to dominate the current generation.[244,251] The effect of the pH has also been investigated previously and it was determined that nitrosobenzene is detected in alkaline environments, suggesting slower reaction kinetics[254] and that the third 2-electron reduction step is strongly hindered in alkaline environment compared to acidic or neutral environments.[23,251] In this work, the electrochemical reduction of nitrobenzene will be investigated in acidic ($HClO_4$) ethanolic environment, in a half-cell set-up by means of linear sweep voltammetry (LSV) and chronoamperometry.

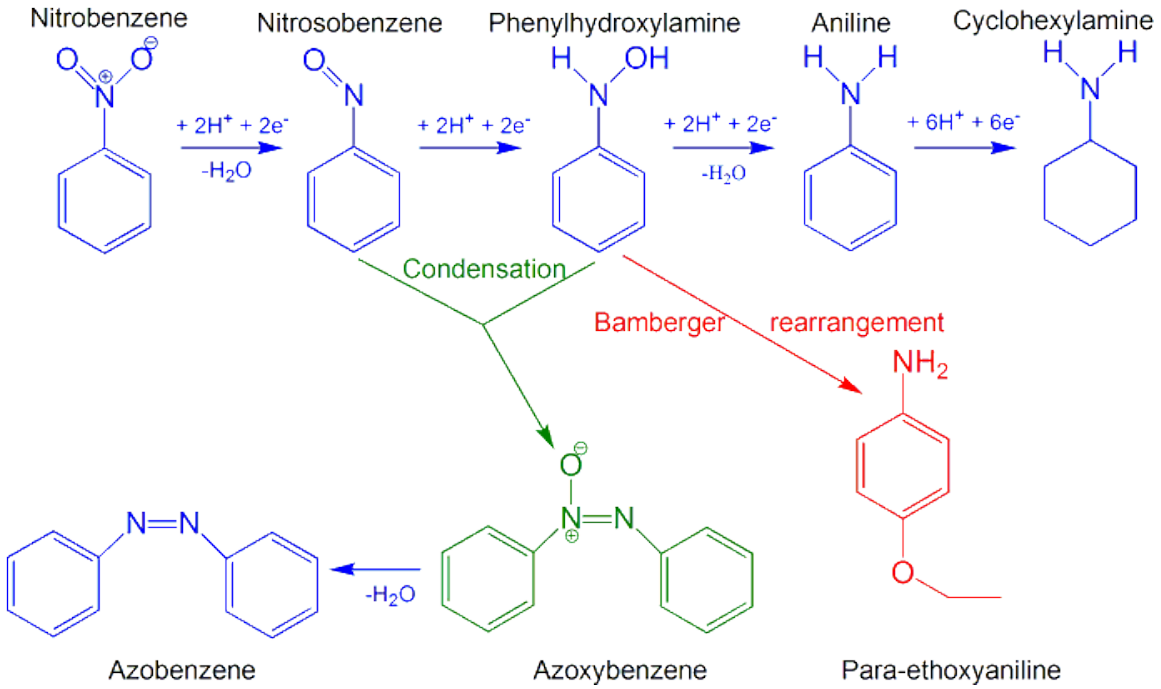

Scheme 5.1. Nitrobenzene reduction reaction scheme

The nature of the electrocatalyst used at the cathode has a crucial impact on the nitrobenzene reduction rate and at the same time on the selectivity of the reaction. Therefore, the development of efficient and cost-effective electrocatalysts is of utmost importance for enabling the practical application of the electrochemical route to produce aniline with cogeneration of electricity. Commonly used cathode electrocatalysts for this specific reaction are noble metals like Pt, Pd, or Au supported on activated carbon or carbon nanotubes.[23,24,248,252] Even if these materials offer a good activity and stability, their high cost is a drawback, which limits commercialisation.[23,244,251] Non-noble metals such as Cu or Fe have been identified as less expensive alternatives to the noble metals but they do not reach sufficiently high selectivities to aniline.[23,251,253] Recently, it was demonstrated that the presence of a metal is not strictly necessary as N-doped diamond was shown to be an efficient electrocatalyst for the production of aniline from nitrobenzene.[251] A drawback of N-doped diamond is that it is synthesised through chemical vapour deposition, which requires

severe conditions and implies a high production cost.[153] In order to make the electrochemical cogeneration approach economically viable, more research is necessary to further enhance the selectivity to the target product, aniline, and this in combination with a reduction of the electrocatalyst manufacturing costs.

In this work, non-noble metals (Fe, Co or Cu) supported on N-doped carbons are investigated for the first time as electrocatalysts for the cogeneration of aniline and electricity. Iron, cobalt and copper were chosen as metal species in the electrocatalysts because they are cheap and abundant and they have several possible oxidation states, which might be beneficial to promote the reduction reaction. Previous work by our group already investigated the use of copper as electrocatalyst for the nitrobenzene reduction reaction.[23–25] However, since the selectivity was still low, further improvements were required. Therefore in this work, it was proposed to replace the multi-walled carbon nanotubes as a support by N-doped carbons. The nitrogen doping is expected to enhance the electrocatalytic performance by improving the interaction between metal and support (possibly easier electron exchange) and to generate extra active sites for the nitrobenzene reduction (N-doping generates partially positively charged carbon atoms, which might act as active sites).[153] Inspired by our previous observations that Cu outperformed Pt as a consequence of its more electropositive behaviour, iron and cobalt, which are both more electropositive than copper, were chosen as alternative metals in an attempt to further enhance the reduction performance.[23] This study combined electrochemical investigation and physiscochemical characterisation of these noble-metal-free materials and led to the identification of novel electrocatalysts for the reduction of nitrobenzene with remarkably high selectivity towards the desired aniline product.

5.2 Experimental

5.2.1 Materials

The following chemicals were used in this work aniline (99.8%, pure, Acros Organics), activated carbon Norit® SX1G (878 m^2 g^{-1}, Norit Americas inc.), iron(III) chloride (97%, reagent grade, Sigma Aldrich), copper(II) chloride (99%, extra pure, anhydrous, Acros Organics), cobalt(II) chloride hexahydrate (98%, reagent grade, Sigma Aldrich), ammonium peroxydisulphate (98%, Acros Organics), sulphuric acid (>95%, Fisher Chemical), hydrochloric acid (37% aqueous solution, Fisher Chemical), perchloric acid (70% aqueous solution, Sigma Aldrich), nitrobenzene (≥99%, Sigma Aldrich) and, phosphate buffer (pH=7, Fisher). All these chemicals were used as received from commercial sources.

5.2.2 Synthesis of the electrocatalyst

Metal-containing N-doped carbon materials were prepared through procedures inspired by a previously reported method (Scheme 2).[8,154] In the first step, activated carbon (AC) was treated with a 6M HCl aqueous solution for 24 h at room temperature to remove impurities. Next, 0.5 g of the purified activated carbon was suspended in 0.5 M HCl at a temperature between 0 and 10°C. After 15 min, aniline (0.2 or 2.5 mL) was added and after another hour, ammonium peroxydisulphate (APS) $(NH_4)_2S_2O_8$, as oxidant, and the metal precursor, (1:1 or 1:4 molar ratio relative to aniline) were added to the synthesis mixture. This suspension was stirred for 24 h. Next, the solvent was evaporated under reduced pressure and the remaining solid was further dried in a vacuum oven at 80°C overnight. Then, the material was subjected to a first pyrolysis under N_2 at 900°C for 1h at a heating rate of 3.3°C min^{-1}. Afterwards, the solid was treated in 0.5 M sulphuric acid at 80°C for 8h to remove unstable surface species,

followed by filtration, washing with deionised water and drying in a vacuum oven. Finally, the material was subjected to a second pyrolysis for 3h at 900°C in order to reduce species that were oxidised during the acid treatment. Three different sets of electrocatalysts were prepared, each with the three different metals (Cu, Co or Fe): (1) Me-PANI-AC-A with 0.2 mL aniline and at a metal to aniline ratio of 1:4; (2) Me-PANI-AC-B with 2.5 mL aniline and at a metal to aniline ratio of 1:1 and (3) Me-PANI-AC-C, same composition as Me-PANI-AC-B but with a second acid treatment and a third pyrolysis step of 3h, to investigate the efficiency of the applied acid treatment to remove unstable metal species (Scheme 5.2).

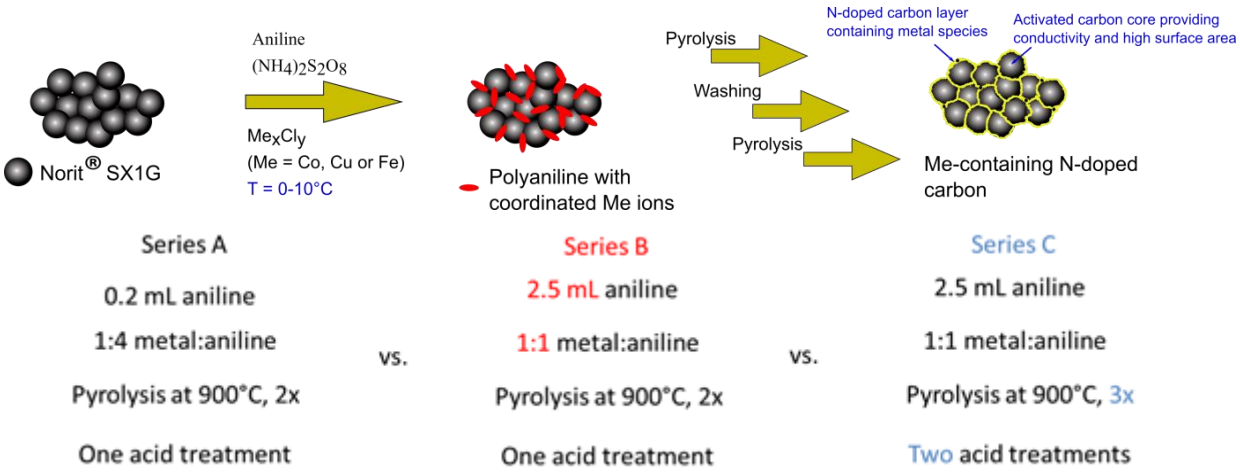

Scheme 5.2. Synthesis of the Me-PANI-AC electrocatalysts and summary of the synthesis conditions of the different series of electrocatalysts.

5.2.3 Physicochemical characterisation

A STOE Stadi P Combi instrument was used in transmission mode to measure the X-ray diffraction (XRD) patterns. The instrument was used in high-throughput mode and was equipped with a Cu-Kα radiation source (λ = 1.54 Å) and a Kα1 Germanium Johann-type monochromator. A high-throughput image plate position detector (IP-PSD) from STOE was used as detector. The XRD instrument was controlled by WinXPOW version 2.20 software from STOE and all the measurements were performed in the 2θ range from 0 to 75°. Nitrogen adsorption-desorption isotherms were measured at 77 K on a Micromeritics Tristar 3000. The pore size distributions were determined using the Barrett-Joyner-Halenda (BJH) method, whereas the Brunauer-Emmett-Teller (BET) method was used to calculate the surface area of the samples. Thermogravimetric analysis (TGA) was performed to determine the metal content. The measurements were carried out under O_2 flow on a TGA Q500 from TA instruments. The temperature was ramped with a heating rate of 5 °C min^{-1} until 1000 °C was reached, and then it was held constant until the mass change was smaller than 0.05% min^{-1}, after which the system was cooled down to room temperature. Previous XRD studies showed that the residual red-orange powder is Fe_2O_3 for the Fe-containing samples.[224] In the case of Cu and Co, XRD showed that the residual powder is CuO and CoO, respectively. The residual mass can thus be used to determine the overall metal content of the sample. Since peaks that could be assigned to trace amounts of quartz wool, which was used during the pyrolysis, could also be detected in the XRD pattern of our materials, the metal content determined by TGA will be a slight overestimation of the actual value. X-ray photoelectron spectroscopy (XPS) measurements were performed by a Physical Electronics PHI 1600 multi-technique system using an Al Kα (1486.6 eV) monochromatic X-ray source, which was operated at 15 kV and 150 W at a base pressure of $2 \cdot 10^{-9}$ Torr. The graphitic C 1s band at

284.6 eV was taken as internal standard, in order to correct possible deviations caused by electric charging of the samples. The MultiPak software was used for the deconvolution and integration of the XPS signals. Room-temperature Raman spectra were recorded on a Dilor XY spectrometer from HORIBA Jobin Yvon Inc.. The spectroscope was equipped with an Olympus BH 2 microscope, a monochromator, a filter and charge-coupled detector with liquid nitrogen cooling (CCD3000 with a resolution of 2 cm^{-1}). A beam originating from an argon/krypton mixed gas laser at a wavelength of 514 nm (Coherent Innova 70C) was sent to the sample. Deconvolution and peak integration was performed by using the IgorPro software. Time of Flight Secondary Ion Mass Spectroscopy (ToF-SIMS) was carried out on an IONTOF V instrument (IONTOF, GmbH, Münster, Germany). Sample powders were manually pressed with a spatula onto the adhesive part of Post-it® papers. A pulsed Bi^{5+} or Bi^{3+} metal ion source was used to produce a primary beam using an acceleration voltage of 30 kV. An AC target current of 0.06 pA with a bunched pulse width lower than 1.5 ns was used. The analysis was conducted on the positive and negative secondary ion species. For the spectra, a raster of 128 x 128 data points over an area of 150 x 150 μm^2 was used. The total primary ion beam dose for each analysed area was always kept below 1011 ions·cm^{-2}, ensuring static conditions. Lateral resolution of ~3 µm and mass resolution m/Δm > 5000 at 29 m/z were maintained for positive and negative spectra acquisition. Charge compensation was done by interlaced electron flood gun (E_k = 20 eV). All data analyses were carried out using the software supplied by the instrument manufacturer, SurfaceLab (version 6.5). It is worth mentioning here that ToF-SIMS is a semi-quantitative technique. It can thus be applied to determine the different species present in the material and their relative abundancies, but it does not offer the possibility to quantify their absolute amounts (for this purpose XPS is used here).[226]

5.2.4 Electrochemical characterisation

All electrochemical measurements were carried out in a half cell set-up using a Gamry Interface 1000E potentiostat. Analysis of the products after chronoamperometry was performed using gas chromatography (GC) (Shimadzu 2010 Plus equipped with a Rtx-5 amine functionalised standard capillary column (15 m, 0.25 mm internal diameter). For all the electrochemical measurements, glassy carbon porous rotating disk electrodes (d = 5 mm) were used. The electrocatalysts were deposited as an ink on the surface of these electrodes. For every measurement, the ink was prepared by dispersing 24.0 mg of electrocatalyst in 900 µL of a 1 wt% solution of polystyrene in toluene. Approximately 3.47 µL of this ink was deposited on the glassy carbon electrode, after which toluene was evaporated at 50°C for 20 min in an oven. For each electrocatalyst, three replicate electrodes were prepared with an average catalyst loading of 0.47 mg/cm². The counter electrode was a Pt grid and the reference electrode was a Fc^+/Fc reference electrode ($E°_{Fc+/Fc}$ = -0.64 vs. S.H.E.). All potentials in this paper are referred to this redox couple. The measurements for the nitrobenzene reduction reaction were carried out in 0.3 M $HClO_4$ in ethanol with traces of water originating from the aqueous solution. To avoid possible interference of the oxygen reduction reaction, nitrogen gas was bubbled through the electrolyte for 30 min to remove O_2 prior to the measurements. A thermostatic bath was used to control the electrolyte temperature, which was set at 25°C. For the linear sweep voltammetry (LSV) measurements, 50 ml of 5 mM nitrobenzene electrolyte solution was used. The potential was scanned in the range from -0.2 to -1.8 V vs. Fc^+/Fc at a rate of 5 mV s^{-1}. Blank measurements were performed before analysing the nitrobenzene reduction performance. Every measurement was carried out three times in order to increase the reliability of the experimental results and

the average values are reported throughout the paper. The reproducibility of the electrocatalyst synthesis was also verified by testing two different batches of Cu-PANI-AC-A, which resulted in a comparable electrocatalytic performance. After each measurement, the potential was corrected for the Ohmic potential drop as a consequence of the electrolyte resistance between the reference and the working electrode. By means of electrochemical impedance spectroscopy an electrolyte resistance of 125 Ohm was found for the 0.3M $HClO_4$ ethanolic solutions.

The Koutécky-Levich equation was used to calculate the number of exchanged electrons and to determine the kinetic current density.[153] The onset potential, i.e. the potential at which the nitrobenzene reduction reaction starts, was determined as the potential at which the slope of the LSV plot exceeded 0.1 mA cm^{-2} V^{-1}. The half-wave potential, i.e. the potential at which the reaction is in the middle of the mixed kinetic-diffusion regime, was determined as the potential corresponding to the inflection point in the LSV plot (i.e. the point at which the second derivative with respect to the potential is zero). The current densities were calculated with respect to the geometric surface area of the glassy carbon electrode disk (A_{geo}) as the actual surface area could not be calculated in an accurate manner (as it depends both on the electrocatalysts specific surface area and on the amounts of electrocatalyst and binder that are applied to the disk). This feature has to be kept in mind when comparing different values for the kinetic current density, as they will not only include contributions of the intrinsic activity (per surface unit) but also of the specific surface area of the electrocatalyst.[23] While this allows a meaningful ranking of the electocatalytic performance of different materials, it should be noted that this ranking is conceptually different from comparisons where the kinetic current density is normalised with respect to the electrochemically active surface area and is thus only a function of the intrinsic activity (per surface unit).

In order to investigate the conversion and the product distribution in the nitrobenzene reduction reaction over the most promising electrocatalysts, chronoamperometric experiments were performed in a cell that was split in an anodic and a cathodic compartment by means of a Zirfon® separator.[228] The rotation speed of the working electrode was set at 500 rpm and the potential was set at -0.75 V vs Fc^+/Fc in 0.3 M $HClO_4$ in ethanol. The volume at the working electrode was 170 ml and a concentration of 15 mM of nitrobenzene was used. After 52h, the pH of the reaction solution was adjusted to 7 in two steps: (1) to a pH between 4 and 5 with 1M KOH ethanolic solution and (2) to a pH of 7 with a phosphate buffer solution (pH = 7). Finally, insoluble $KClO_4$ was filtered out. The product concentrations were measured by GC. Each GC analysis was done in triplicate and the average results were reported. The electrochemical stability for selected electrocatalysts was determined using cyclic voltammetry (CV). The potential was cycled from -0.2 to -1.8 V vs. Fc^+/Fc at a scan rate of 100 mVs^{-1} in a 0.3 M $HClO_4$ electrolyte containing 5 mM nitrobenzene. 1000 cycles were performed and prior to the last scan the solution was stirred in order to homogenise the nitrobenzene concentration in the half-cell. The second and the last scan were compared to evaluate the electrocatalyst stability.

5.3 Results and discussion

Metal-containing N-doped carbon electrocatalysts with a different initial content of N and of non-noble metals (Fe, Co or Cu) were prepared by pyrolysing composite carbon materials consisting of activated carbon, polyaniline and incorporated metal sites (Me-PANI-AC). It is the first time that Cu was used as metal in the synthesis of Me-PANI-AC electrocatalysts. These materials were tested for the electrocatalytic reduction of nitrobenzene, with the industrially relevant aniline as target product.

The major properties that are foreseen to affect the electrocatalytic performance of the Me-PANI-AC materials in the reduction reaction under investigation are (1) the Me loading and its configuration, (2) the N loading and its configuration, (3) the surface area and (4) the degree of graphitisation.[153] To link the physicochemical properties of the electrocatalysts with their performance in the nitrobenzene reduction reaction, the materials were characterised by a set of different techniques.

5.3.1 Physicochemical characterisation

Up to date, almost all reported electrocatalysts for the nitrobenzene reduction reaction contain noble (e.g. Pt[23,248]) or non-noble (e.g. Cu[25,244]) metals as active site. The metal might act as a coordination site for nitrobenzene and as such it might initiate its reduction. Another possibility is that it does not participate in the actual active site itself but that it merely promotes the formation of a more active material. It is thus important to investigate the influence of the metal nature and loading on the electrocatalytic performance in the reduction of nitrobenzene to aniline. Therefore, electrocatalytsts were prepared with different metals (Fe, Co or Cu) and with different initial amounts of metal (lower theoretical loading in Me-PANI-AC-A and higher in Me-PANI-AC-B and -C, see Table 5.1). The composition of the prepared electrocatalysts (Table 5.1) was determined by means of TGA (overall metal content) and XPS (surface carbon, nitrogen, oxygen, sulphur and metal content). TGA analysis shows that the amount of metal that is retained in the final material is higher for the Me-PANI-AC-B and -C electrocatalysts, which was expected based on the higher initial metal and aniline contents. Based on the literature, it is expected that a significant fraction of the metals is present in a coordination with N-atoms, which originate from aniline. A higher aniline content should therefore, allow more metals to be retained. However, for the higher metal loadings, a significant fraction of the initial metals is not incorporated in the final material. This might mean that not enough N atoms are available to bind the metal species. Furthermore, as will be demonstrated in more detail later on, not all metal species are coordinated to nitrogen, but also metal oxides and sulphides exist.

Table 5.1. Elemental composition of Fe-PANI-AC-A and Fe-PANI-AC-B.

	Theoretical Me wt%	Me wt% (XPS)	Me wt% (TGA)	Theoretical N wt%	N wt% (XPS)	Theoretical C wt%	C wt% (XPS)	O wt% (XPS)	S wt% (XPS)
Fe-PANI-AC-A	4.2	1.9	4.6	4.2	4.5	90	88	5.6	0.2
Fe-PANI-AC-B	33	3.8	18	8.4	10	54	80	4.7	1.1
Fe-PANI-AC-C	33	2.4	16	8.4	7.6	54	83	4.9	1.6
Co-PANI-AC-A	4.4	1.2	8.1	4.2	4.0	89	90	4.1	0.8
Co-PANI-AC-B	40	4.4	38	7.6	3.3	49	76	3.3	6.2
Co-PANI-AC-C	40	4.5	18	7.6	2.1	49	81	2.1	6.4
Cu-PANI-AC-A	4.7	1.0	3.9	4.1	5.8	89	88	5.0	0.4
Cu-PANI-AC-B	36	6.1	27	8.0	8.8	52	75	9.4	0.64
Cu-PANI-AC-C	36	4.5	17	8.0	6.1	52	73	16	0.63

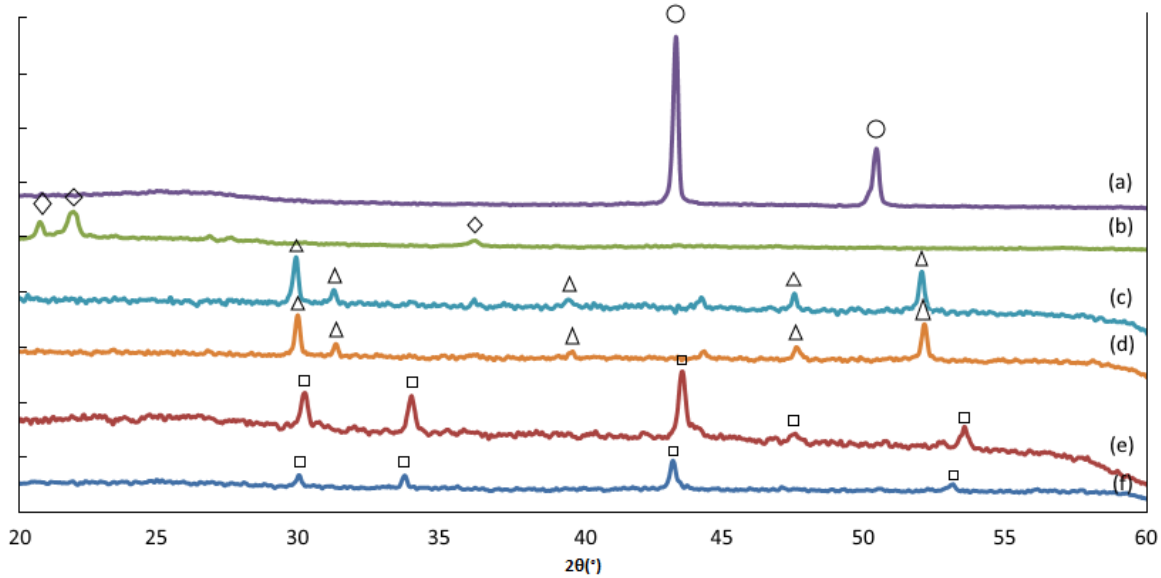

Figure 5.1: X-ray diffractograms of: (a) Cu-PANI-AC-B, (b) Cu-PANI-AC-C, (c) Co-PANI-AC-B, (d) Co-PANI-AC-C, (e) Fe-PANI-AC-B and (f) Fe-PANI-AC-C. The peaks in the XRD pattern are identified as follows: ○ is metallic copper, ◊ is quartz SiO_2, Δ is Co_9S_8 and □ is FeS.

It is expected that these species have a weaker interaction with the carbon framework and should therefore be largely removed by the acid treatment, which is expected to work more efficiently at the surface region. This can explain the lower metal loadings that were detected by XPS (Table 5.1), which is a surface-sensitive technique (analysis depth up to a few nm). For the higher metal loadings, it appears that one acid treatment is not sufficient to remove all unstable metal species, since the metal content further decreases after a second acid treatment. Differences in the surface metal contents can significantly affect the electrocatalytic performance as it is expected that the reduction reaction will occur at the electrocatalysts surface. For both iron and copper also the N/C ratio is higher for the series B and C materials and this was expected based on the higher initial N content. When cobalt was used, an opposite behaviour was observed, indeed the N/C ratio decreased for the electrocatalysts that were prepared with a higher aniline content. This trend can be explained when the standard reduction potentials (E°) of the different metal ions (present during polymerisation) with respect to the standard hydrogen potential (V_{SHE}) are considered. E° decreases from Fe^{3+} (0.77 V_{SHE}) to Cu^{2+} (0.34 V_{SHE}) to Co^{2+} (-0.28 V_{SHE}), which means that cobalt will act as a reductant while copper and iron can act as an oxidant. Thus iron (III) and copper (II) chloride will promote the aniline polymerisation, while cobalt will rather work as an inhibitor. This explains why the increase in the N/C ratio with the metal content is the largest for iron and also why the N/C ratio decreases at higher initial cobalt content.

Table 5.2. BET surface area of Me-PANI-ACs as determined from the N_2 physisorption data.

	Cu-PANI-AC-A	Cu-PANI-AC-B	Cu-PANI-AC-C
S_{BET} (m^2/g)	533	120	373
	Co-PANI-AC-A	Co-PANI-AC-B	Co-PANI-AC-C
S_{BET} (m^2/g)	539	108	342
	Fe-PANI-AC-A	Fe-PANI-AC-B	Fe-PANI-AC-C
S_{BET} (m^2/g)	489	196	358

The surface area of the different electrocatalysts was determined by N_2-physisorption and the results are summarised in Table 5.2. Two trends can be observed for the Me-PANI-ACs: (1) the surface area tends to decrease with the initial metal content because a larger fraction of non-porous metal species (oxides or sulphides) are produced and (2) a second acid treatment partially restores the surface area by further removing the unstable metal species, generating extra porosity.

XRD was used to investigate the presence of crystalline phases in the different Me-PANI-ACs (Fig. 5.1). For the Me-PANI-AC-A samples, the diffractograms only displayed two broad peaks around 2θ = 26 and 44° (Fig. S5.1)., which are characteristic for the (002) and (101) graphitic planes with a rather low degree of crystallinity.[153,176] On the other hand, at higher metal loadings (Me-PANI-AC-B and -C) the diffractograms display peaks ascribed to several different crystalline phases depending on the metal species that was used in the synthesis. For iron and cobalt, all the XRD peaks can be ascribed to FeS and Co_9S_8, respectively. This observation is in agreement with the XPS result, which shows higher S contents for the Co- and Fe-containing electrocatalysts that were prepared with higher metal loadings. Furthermore, it was observed that even after a second acid treatment, these peaks (although less pronounced) remain detectable, which most likely signifies that these remaining sulphides are covered by several carbon layers, impeding its removal. Therefore, these metal species will also not be of significance for the nitrobenzene reduction reaction, which occurs at the surface of the electrocatalysts. The origin of the metal sulphides can be found in the degradation of APS in the presence of cobalt or iron species. The absence of sulphides in Fe- and Co-PANI-AC-A might be caused by the lower APS-to-Fe ratio that was used in the synthesis of these samples. As was already briefly mentioned, another possible explanation is the following: previous ToF-SIMS studies on cobalt-[75] and iron-containing[54] N-doped carbons have shown that both metals tend to be present either as MeN_2 or as MeN_4, which signifies that at least two N sites should be available per metal atom to avoid the formation of other metal-containing species. Considering that the aniline:metal ratio in the Me-PANI-AC-B and -C samples was 1:1, it can be understood that the number of N atoms is insufficient to coordinate all metals, which thus results in the presence of other metal species. In the case of Cu, no sulphides could be detected at higher metal loadings, in agreement with the lower S content detected by XPS (see Table 5.1). The peaks for Cu-PANI-AC-B could be ascribed to metallic copper (○ in Fig. 5.1). After a second acid treatment the metallic copper species appear to be completely removed and the remaining peaks can be ascribed to SiO_2 impurities (Δ in Fig. 1), originating from the quartz wool used during the pyrolysis. As will be discussed later on, based on the XPS measurements, it could be determined that copper does not tend to bind with N, but forms oxides instead at least at the surface. At higher metal loadings, it is possible that the available oxygen content during the synthesis is too low to exclusively form copper oxides, explaining the presence of metallic copper in Cu-PANI-AC-B.

Useful information on the degree of carbonisation and on the extent of defects of the synthesised electrocatalysts can be obtained with Raman spectroscopy (Table 5.3 and Fig. 5.2). The presence of graphitic structures inside the electrocatalysts is evidenced by the presence of the G-band at 1590 to 1600 cm^{-1}, the origin of which can be found in the E_{2g} in-plane vibration of the graphitic carbon framework and is therefore assigned to the planar vibration of sp^2 C atoms in an ideal graphitic plane.[153] Due to a change in the electronic structure of the carbon lattice caused by the presence of the electron-donating N atoms, the peak is blue shifted compared to pure undoped carbons.[230] The other band at approximately 1350 cm^{-1} (D-band) is associated with defects at the edges of the sp^2 domain. After

deconvolution of the Raman spectra two additional peaks, centered at 1200 and 1500 cm^{-1} (A-band) (Fig. 5.2), appeared. These are generally attributed to C atoms outside the perfectly planar graphitic framework and to heteroatoms inside the graphite lattice, respectively.[176] The relative degree of carbonisation can be determined by a set of 3 parameters: (1) the ratio of the areas of the D and G bands (A_D/A_G), which is inversely proportional to the degree of carbonisation, (2) the full-width-half-maximum (FWHM) of the D-band, a higher value generally being correlated with a higher disorder and (3) a smaller A-band (Table 5.3).[153,224,241] Based on these parameters, it was determined that at low metal loadings the highest degree of carbonisation was obtained in the presence of iron, followed by cobalt and copper. This is in accordance with results previously obtained in literature where iron was also identified as the best catalyst to promote carbonisation followed by cobalt. Copper was found to be inactive towards promoting the carbonisation reaction, since it is unable to form metal carbides.[255–258] Furthermore, at higher initial metal contents, it is expected that the degree of carbonisation would increase since the metal acts as a catalyst (at least in the case of iron and cobalt) promoting the carbonisation however, this was only found to be the case for cobalt. For iron a lower degree of carbonisation was observed and most likely this is related with the higher initial aniline to activated carbon ratio of the synthesis mixture. Indeed, it results in a higher amount of N incorporation, thus inducing a higher number of defect sites in the carbon framework, which ultimately results in a less graphitic material. Another option could be that the activated carbon, which forms a smaller fraction in the series B and C materials, is a better starting point to obtain a graphitic end product than polyaniline. For copper the decrease in carbonisation is linked with the higher N incorporation since copper does not tend to catalyse the carbonisation process. Higher cobalt loadings, on the other hand, seem to result in a higher degree of carbonisation and this was actually expected based on the catalytic properties of the metal species in the carbonisation process. The reason why cobalt does seem to behave accordingly while iron does not, is not yet fully clear but there are two possible explanations, (1) the amount of cobalt retained in the system is more than double that of iron, resulting in a more graphitic material. Since metallic cobalt and iron were not found, these species are either sulphides (FeS or Co_9S_8) or oxides (CoO and Fe_2O_3) both of which have a higher melting point in the case of cobalt. While all temperatures lay well above our pyrolysis temperature this might be an indication why cobalt is retained more efficiently. (2) In the case of cobalt, less nitrogen is maintained in the final electrocatalyst even if a higher initial N/C ratio was used (*vide supra*), resulting in a higher degree of carbonisation. A final trend that was observed is that the degree of carbonisation decreases after a second acid treatment, which is a consequence of the removal of both metal species and N atoms from the carbon framework, leaving behind extra defects that could not be fully repaired by the second pyrolysis step.

Table 5.3: N configuration and percentage of surface metal oxides present in the Me-PANI-AC materials as determined with XPS and summary of parameters related with degree of carbonisation as determined by Raman. [a] As determined by deconvolution of the high resolution N1s XPS spectra with MultiPak. [b] Calculated based on the surface metal and oxide contents and on the percentage of oxygen that is in a metal oxide configuration. The latter was determined by deconvoluting the O1s XPS spectra with MultiPak. [c] As derived from the deconvolution of the Raman spectra, which was performed with the IgorPro software.

Sample	Pyridinic N (or N-Fe)[a]	Pyrrolic N[a]	Graphitic N[a]	Oxidised pyr N[a]	N_{pyr}/N_{graph} [a]	% Me in oxides[b]	A_D/A_G [c]	FWHM D-band[c]	Area % of A-band[c]
Fe-PANI-AC-A	40	15	41	5	1.0	13	1.0	11	147
Fe-PANI-AC-B	40	4	45	11	0.9	17	1.1	21	152
Fe-PANI-AC-C	42	1	49	7	0.9	38	1.2	23	155
Co-PANI-AC-A	41	11	40	8	1.0	37	1.1	17	149
Co-PANI-AC-B	26	7	53	14	0.5	66	0.9	16	136
Co-PANI-AC-C	41	0	45	14	0.9	8.0	1.0	17	145
Cu-PANI-AC-A	45	6	43	6	1.0	100	1.3	27	156
Cu-PANI-AC-B	39	10	47	3	0.8	100	1.3	30	169
Cu-PANI-AC-C	43	0	48	10	0.9	100	1.4	30	172

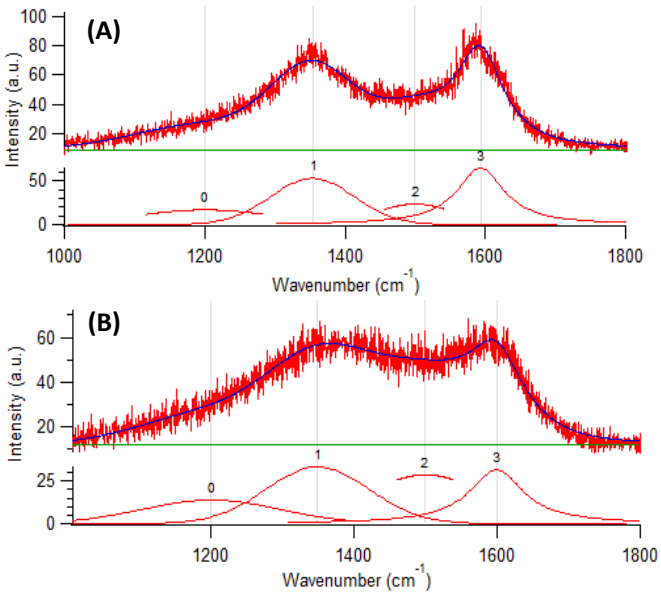

Figure 5.2: Deconvoluted Raman spectra of Co-PANI-AC-B (A) and Cu-PANI-AC-B (B).

The configuration of N atoms inside the electrocatalyst can be further investigated by deconvoluting the high resolution N1s XPS data (Table 5.3). The different N configurations that are typically present in a N-doped sp^2 carbon lattice are represented in Figure 5.3: (N1) pyridinic N, (N2) pyrrolic N, (N3) and (N4) graphitic N and (N5) oxidised pyridinic N.[153,154,224] In the high resolution N1s XPS spectrum they are found at the following electron binding energies: (N1) 398.0-399.3 eV, (N2) 399.8-401.2 eV, (N3/N4) 401.1-402.7 eV and (N5) > 402.8 eV.[153] The difference between N3 and N4 is the location of the graphitic N inside the carbon framework. N3 can be found at the edges of the sp^2 carbon framework, while N4 is located in the bulk of the framework. Since transition metals like iron, cobalt and copper can bind with N (like e.g. in phthalocyanine or porphyrin), another N configuration, where N is bound with the metal (Fig. 5.3), can be present here. Since this N-Me peak can be found at

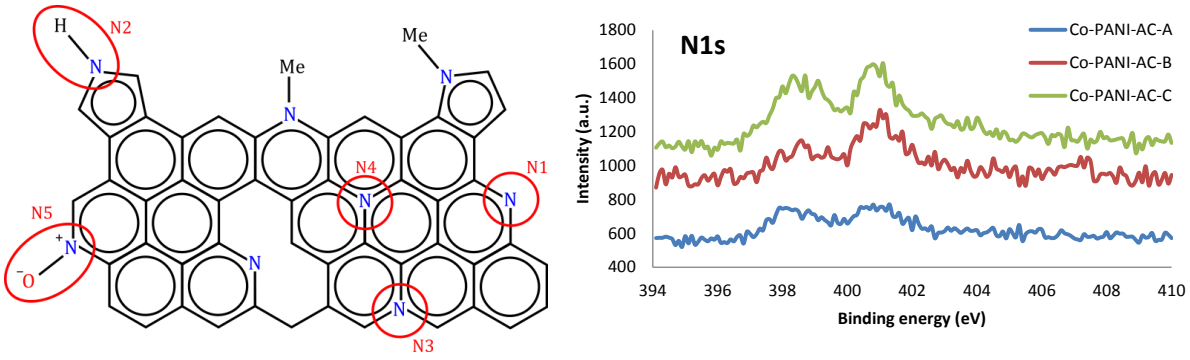

Figure 5.3: Left: illustration of the different possible N configurations inside a graphitic carbon lattice. Right: N1s XPS signal of Co-PANI-AC-A, -B and –C.

around 399.2 eV, it could not be distinguished from the pyridinic N configuration.[224] In the rest of this paper, they will therefore be considered as one peak. When comparing the N configurations for the different metal species no clear trends can be discovered besides the fact that the graphitic and the pyridinic N configurations form the largest fraction in all cases. From Table 5.1, it can further be observed that the N configuration is influenced by the metal content. A higher metal content tends to result in a higher number of graphitic and a lower number of pyridinic and/or pyrrolic N atoms. This might be explained by the role the metal plays in the carbonisation process. Since metals act as carbonisation catalysts, a higher graphitic N fraction can be expected at higher metal loadings. The degree of carbonisation does not necessarily have to increase, as was shown before for iron and copper, because a higher number of N atoms is incorporated in the system. However, since the pyridinic N fraction also consists of the N-Me configuration, an opposite trend for the N configuration could also be expected given that the presence of a higher number of metals could result in a higher number of N-Me species. Since this is not the case, it can be assumed that insufficient N atoms are available and therefore, other metal species (sulphides and oxides) are formed. The presence of sulphides has already been confirmed by XRD and XPS. The presence of oxides or hydroxides, although not visible in XRD, is confirmed by a contribution assigned to metal bound to oxygen (±530 eV) in the deconvoluted O1s XPS spectra. The percentage of surface metal species that is present as oxides and/or hydroxides was calculated based on the results of the deconvoluted O1s XPS spectra and on the surface oxygen and metal contents. For simplicity, it was assumed that the Fe-O signal is Fe_2O_3, the Cu-O signal is CuO and the Co-oxides are CoO. This was assumed because the O1s signals of the most abundant oxide and hydroxide in nature are separated by less than 1 eV. From now on, the ensemble of oxides and hydroxides will simply be referred to as oxides. The results have been summarised in Table 5.3. It can be observed that the ratio of pyridinic over quaternary N appears to be inversely proportional to the fraction of oxides, which is related to the fact that the pyridinic N fraction also includes the Me-N species. The increased presence of metal oxides could be related to a decrease in the number of surface pyridinic or pyrrolic N sites that are available to coordinate Fe or Co, caused by a higher degree of carbonisation and thus less edge and defect sites. The lower pyridinic to graphitic N ratio can be clearly visualised in the case of Co (Fig. 5.3) where Co-PANI-AC-B, clearly shows a smaller peak contributed to pyridinic N atoms. For copper the situation is slightly different since it appears that irrespective of the N configuration, the surface copper is only available as copper oxides. This might also mean that in this case a higher metal content for the series B and C materials is merely caused by a higher amount of available copper during the synthesis and is thus not

necessarily linked with the higher amount of available N as binding site. On the other hand, one might expect that these oxides would be removed during the acid treatment. Since this is not the case, they might still be coordinated to the framework in a certain way, protecting them from the acid treatment. They might be coordinated with carbon or nitrogen directly, or they might as well be covered by a thin carbon layer, which still allows them to be accessible for the reduction reaction. Furthermore, since the copper oxides are not detected by XRD, they might exist as small isolated sites inside the material or they are amorphous. The reason behind this different tendency to form metal oxides and metal-N bonds, is most likely related to the Me-N bond strength. By means of density functional theory studies, it has been determined that the Me-N bond strength decreases in the order Fe-N ≈ Co-N > Cu-N for porphyrins[259], phthalocyanines[260] and in N-doped carbon nanotubes.[261] To further evaluate the configuration of the metals inside the electrocatalyst, the high resolution Me 2p XPS signals were investigated for the Me-PANI-AC-B and -C series (Fig. 5.4 and Fig. S5.2). For copper, the high resolution Cu $2p_{3/2}$ spectrum can be deconvoluted into three peaks at 932.4, 933.7 and 935.0 eV, which are respectively attributed to Cu_2O or Cu; CuO and $Cu(OH)_2$ or Cu-N complexes[262,263]. The satellite peaks (not visible) at 942.4 eV indicate the presence of mainly Cu(II) species.[264] Since Cu-PANI-AC-B contains metallic Cu (XRD) we assign the first peak to metallic Cu. The other two peaks are assigned to CuO and $Cu(OH)_2$ respectively, based on the deconvolution of the O1S XPS spectra and the ToF-SIMS data (*vide infra*). For cobalt, the deconvolution results of Co $2p_{3/2}$ show three or four peaks at 778.4, 780.6, 782.0 and 786.0 eV, which are assigned to Co_9S_8[265], CoO or Co_2O_3[262], Co-N_x[266] and a satellite peak ascribed to the presence of cobalt oxides.[267] Since CoO is expected to be the more stable cobalt oxide, the second peak is mainly ascribed to this specie. In the high resolution Fe2p XPS spectra two bands can be visualised at around 711 and 723 eV, assigned to $2p_{3/2}$ and $2p_{1/2}$ photoelectrons from Fe, respectively. After deconvolution, six peaks could be distinguished at 709.5, 711.2, 714.7, 717.8, 722.9 and 725.1 eV and they are characteristic for Fe^{2+} $2p_{3/2}$ in FeO or FeS_2, for Fe^{3+} $2p_{3/2}$ in Fe_2O_3 or FeS or for Fe-N_x, for $FeSO_4$, for satellite peak confirming presence of Fe^{3+}, for Fe^{2+} $2p_{1/2}$ in FeO and for Fe^{3+} $2p_{1/2}$ in Fe_2O_3, respectively.[235,236,262,268,269] When the deconvolution of the Me-PANI-AC-B and –C series are compared with each other, it is observed that for the copper-series the configuration remains rather similar, while for cobalt and iron some important differences could be distinguished.

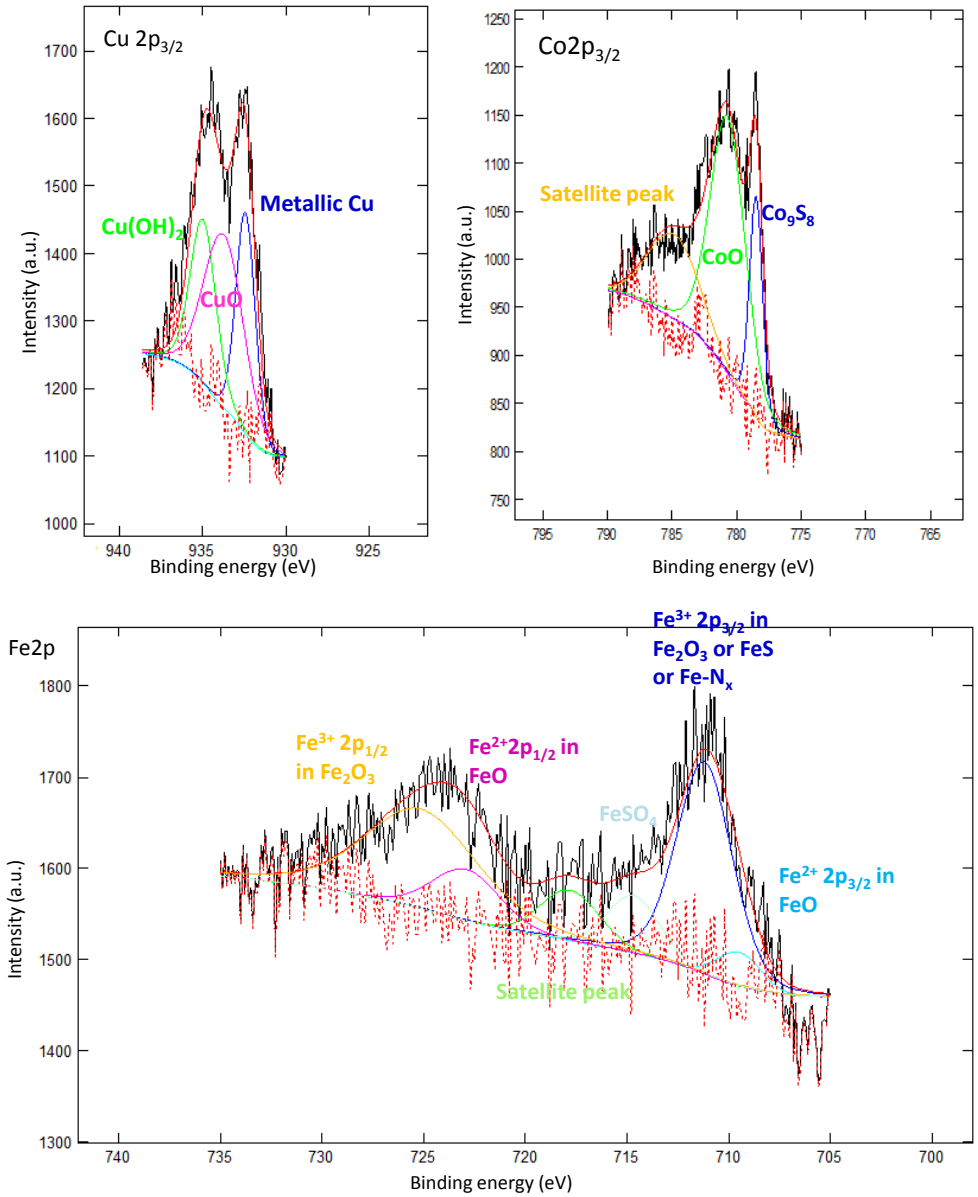

Figure 5.4: Deconvoluted high resolution Me2p XPS spectra of Me-PANI-AC-B series.

After the second acid treatment, a peak ascribed to Co-N_x species appeared and the fraction of cobalt sulphides strongly increased and this at the cost of the cobalt oxides. This confirms the decrease in the fraction of cobalt oxides as determined above based on the deconvoluted O1s XPS spectra. For iron, it appears that those peaks ascribed to FeO tend to increase while the Fe_2O_3 fraction diminishes. These changes might have important implications for the electrochemical performance as will be discussed later on in this work.

The nature of the different metal sites in the Me-PANI-AC-A materials was further investigated by Time of Flight-Secondary Ion Mass Spectroscopy (ToF-SIMS). Only the positive secondary ions were taken into account here since the signal for Cu-PANI-AC-A in the negative mode was much weaker. This analysis reveals that Fe- and Co-PANI-AC-A contain the anticipated MeN_xC_y species, where y is in the range from 0 to 12 (larger compounds could no longer be distinguished from the background signal) and x is in the range from 1 to 4, since metals can coordinate a maximum of four nitrogen atoms (see Table 5.4).[54,75] With Cu as a metal, on the other hand, no MeN_xC_y species seem to form. These results are in accordance with the XPS results reported earlier on where no peaks attributed

to Cu-N species could be found after deconvolution of the Cu XPS spectra while for iron and cobalt peaks assigned to Me-N did appear in the deconvoluted spectra. However, since the outcome of the deconvolution of the XPS spectra is very sensitive to the operator and the exact settings, the presence of CuN_xC_y species cannot be completely excluded, even more so since $CuNC_y$ and CuN_2C_y species were observed in the negative ToF-SIMS mode. Furthermore, ToF-SIMS also confirms the absence of metal sulphides in the series 1 electrocatalysts, which is in accordance with the XRD results. Finally, the decrease in the number of oxides from Cu- to Fe-PANI-AC-A was also confirmed by ToF-SIMS (table 5.4, last column), which reaffirms the assignment of the Me 2p signals to the respective metal oxides. Since no peaks related to crystalline metal oxide phases could be observed in the XRD spectra, these metal oxides are most likely of an amorphous nature or too small to detect.

Table 5.4 Relative abundance of $MeN_xC_y^+$ ions (in %) for Cu-, Co- and Fe-PANI-AC-A, as determined by analysis of the positive secondary ions by ToF-SIMS

	$MeNC_y^+$	$MeN_2C_y^+$	$MeN_3C_y^+$	$MeN_4C_y^+$	$\frac{MeN_xC_y^+}{Me_zO_u}$
Fe-PANI-AC-A	53	19	16	12	0.36
Co-PANI-AC-A	27	24	23	25	0.13
Cu-PANI-AC-A	0	0	0	0	≈0

In summary, the physicochemical features of the as-synthesised electrocatalysts were determined by several aspects as the metal kind and content, the aniline:metal ratio, the aniline content and the extent of the acid treatment. The metal type seemed to have an important role in the resulting metal configuration, iron and cobalt being able to form MeN_X species and copper, being unable to do so, is mainly present as amorphous copper oxides. At higher initial metal and aniline loadings, a larger number of metal species is retained in the final structure, in part due to the larger number of available N sites to produce MeN_X species but also due to the higher number of available metal species and the stronger coordination of metal sulphides and oxides with the carbon framework, which has more functional groups. Finally, a single acid treatment did not seem to be sufficient to remove all unstable metal content. A second acid treatment might thus liberate more active sites, possibly generating a more active material.

5.3.2 Electrochemical characterisation

LSV measurements and Koutécky-Levich analysis

The performance of the different Me-PANI-ACs as electrocatalysts for the cogeneration of electricity and aniline in a fuel cell was first evaluated by means of linear sweep voltammetry (LSV) in a half cell setup. LSV is a suitable technique for the investigation of complex redox reactions as the nitrobenzene reduction reaction. It allows ranking the different electrocatalysts according to activity, which can be compared based on the onset potential and the current generation in the potential range of interest for the aniline production. To further analyse the activity and also to get a first idea on the selectivity the Koutécky-Levich plots are constructed on the basis of the results of the LSV experiments performed at different rotation speeds of the working electrode. Nine different electrocatalysts were tested: Fe-PANI-AC-X, Cu-PANI-AC-X and Co-PANI-AC-X (with X = A, B or C) and the results were

compared with the data available in the literature.[23,24,248] The LSV tests were carried out by varying the potential of the working electrode from -0.2 to -1.8 V vs. Fc^+/Fc at four rotation speeds (500, 1000, 1500 and 2000 rpm, Fig S5.3 to S5.11). In figure 5.5 and S5.12, the polarisation curves for the different electrocatalysts are shown at 2000 rpm.

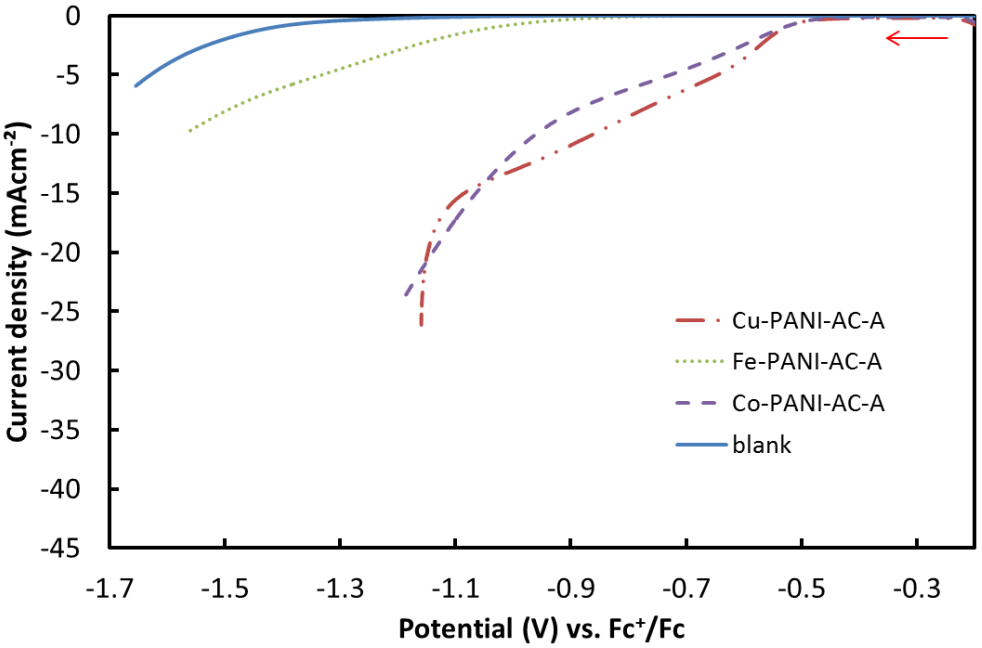

Figure 5.5: LSV plots of Fe-, Co- and Cu-PANI-AC-A, recorded in 5 mM nitrobenzene in 0.3 M $HClO_4$ in ethanol at a scan rate of 5 mVs^{-1}, with a rotation speed of 2000 rpm and corrected for the iR drop.

From Figure 5.5 and S5.12 and in combination with Table 5.5 (onset potentials), some first observations can be made. First of all, for the low metal loadings, the Cu-based electrocatalyst generally gives the highest current densities, followed by Co and finally Fe. With iron as a metal, the activity seems to be rather low, considering the high onset potential and the low current densities. It is possible that the active iron sites are either blocked or leached out in the acidic environment, explaining their poor performance. At higher metal loadings, higher current densities can generally be observed and this is rationalised based on the number of available active sites, which will be higher at higher metal contents. Whether or not the metal plays an active role in the active site, a higher number of metals will either promote the formation of more active sites or will yield more metal-containing sites. Furthermore, a different order in current density can be observed, cobalt gives the highest currents followed by iron and copper. Co-PANI-AC-C does not follow this trend since it generates the lowest currents. It is possible that the active sites, responsible for the activity in Co-PANI-AC-B, were removed in the second acid treatment. The differences in behaviour between the high and the low metal loadings can only be explained by changes in the structure of the active site. This will be discussed in more detail further on in this paragraph.

Secondly, it appears that at low metal loadings, cobalt and copper result in the most positive onset potential and at higher metal loadings, Co-PANI-AC-B outperforms the others. Since a more positive onset potential corresponds to a lower reaction activation energy, the involved sites are more active in initiating the nitrobenzene reduction reaction.

Thus far, we have considered the electrocatalysts activity but to obtain a first indication on the selectivity of the different electrocatalysts, the Koutécky-Levich (K-L) plots (Fig. 5.6 and

Fig. S5.13 to S5.15) have to be constructed based on the following equations (Eqs. (5.1)-(5.3)):

$$\frac{1}{J} = \frac{1}{J_K} + \frac{1}{J_D} = \frac{1}{J_K} + \frac{1}{B\omega^{1/2}} \quad \text{(Eq. 5.1)}$$

where J is the recorded current density, which can be divided in the kinetic current density (J_K) and the diffusion-limited current density (J_D), and ω is the angular velocity of the rotating ring disk electrode. B and J_K are determined by Eqs. (5.2) and (5.3):

$$B = 0.62nFC_0(D_0)^{2/3}v^{-1/6} \quad \text{(Eq. 5.2)}$$

$$J_K = nFkC_0 \quad \text{(Eq. 5.3)}$$

where *n* is the number of exchanged electrons, F is the Faraday constant, *k* is the electron transfer rate constant, C_0 is the bulk concentration of nitrobenzene (5 x 10^{-6} mol cm^{-3}), v is the kinematic viscosity of the electrolyte (0.0152 cm^2 s^{-1}) and D_0 is the diffusion coefficient (4.7 x 10^{-6} cm^2 s^{-1}).[24] The number of exchanged electrons, is a factor for the selectivity of the electrocatalyst, the closer it is to 6, the more selectively aniline should be produced. However, as the plateau of the LSV curves is not well pronounced, it is highly likely that multiple species are produced at the same time. This would mean that *n* represents an average value for the different products. At a certain potential, *n* can be determined from the slope of the K-L plots. The kinetic current density, which is another factor for the activity, can be determined from the intercept.

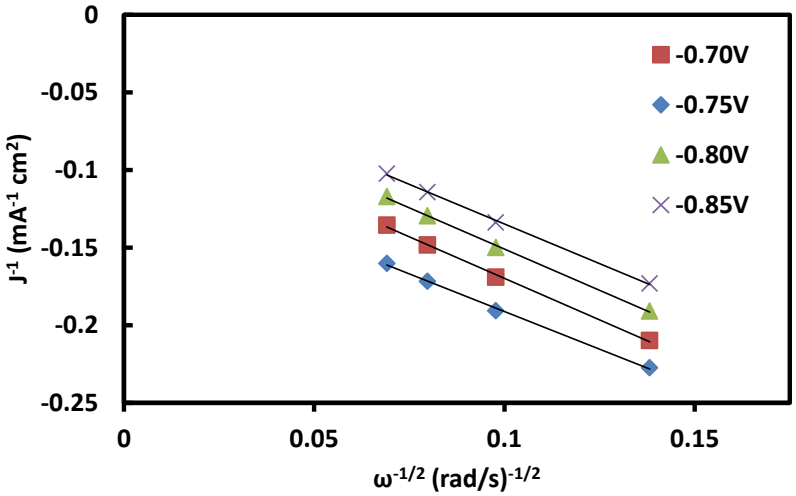

Figure 5.6: Koutécky-Levich plots (J^{-1} vs. $\omega^{-1/2}$) at different electrode potentials (V vs. Fc^+/Fc) for Cu-PANI-AC-A.

The similarity of the slopes of the generated K-L plots (Fig. 5.6 and Fig. S5.13 to S5.15) in the potential range from -0.70 to -0.85 V vs. Fc^+/Fc, indicates that the number of transferred electrons remains rather constant in the selected potential window. For Cu-PANI-AC-A, the slope corresponds to a 6-electron reduction process of nitrobenzene to aniline. The values for *n* for the other electrocatalysts and the kinetic current densities were determined at -0.75 V vs. Fc^+/Fc and are summarised in Table 5.5.

At low metal loading, the selectivity towards aniline decreased from Cu-PANI-AC-A (*n* = 5.8) to Co-PANI-AC-A (*n* = 5.4) to Fe-PANI-AC-A (*n* = 4.2). Thus, it appears that copper is the best metal specie to obtain high selectivities towards aniline. At high metal loading, however, only Co-PANI-AC-B and Fe-PANI-AC-C tend to reduce nitrobenzene although with

a lower selectivity ($n \approx 9$). Indeed since n is higher than six, part of the produced aniline will be further reduced to cylcohexylamine ($n = 12$). Since the limiting current density does not vary with the rotation rate for the remaining electrocatalysts, its current generation is most likely the consequence of the reduction of ethanol. These electrocatalysts are thus not active in the nitrobenzene reduction reaction.

When the electron transfer number of Cu-PANI-AC-A is compared with similar non-noble metal-containing electrocatalysts (e.g. Cu-MWCNTs) in the literature, the selectivity towards aniline is greatly improved ($n \approx 6$ vs. $n \approx 4$).[23,25] This proves the benefits of the applied synthesis method for the synthesis of Cu-containing electrocatalysts for the nitrobenzene reduction reaction.

A first indication for the kinetic current density already follows from the first slope in the LSV plots. The steeper the slope, the higher the kinetic current density will be and this was also confirmed by the values in Table 5.5. The kinetic current density tends to follow the same trend as the overall current, with copper outperforming the other metal species at low loadings and Co-PANI-AC-B giving the highest kinetic current density overall.

A final parameter that can be found in Table 5.5 is the half-wave potential, which is related both with the onset potential and with the kinetic current density. The most positive half-wave potentials are obtained with a combination of either a more positive onset potential or a higher kinetic current density. As for the onset potential, a more positive half-wave potential corresponds with a more active site for the nitrobenzene reduction.

Based on these results, it did indeed prove important to try out different synthesis methods as for every metal, a different synthesis method proved to result in the electrocatalyst with the best performance in the nitrobenzene reduction reaction.

Table 5.5: Summary of nitrobenzene reduction parameters derived from the linear sweep voltammetry results. Average values and standard deviations are reported for n and J_K. For the onset and the half-wave potential the average values are reported (the standard deviation is between 0.005 and 0.01 V).

Electrocatalyst	n @ -0.75V	J_K @ -0.75V ($mAcm^{-2}$)	Onset potential (V)	Half-wave potential (V)
Fe-PANI-AC-A	4.2±0.1	-0.1±0.1	-0.58	-1.27
Fe-PANI-AC-B	/	/	-0.37	-0.90
Fe-PANI-AC-C	8.9±0.5	-8.6±0.4	-0.33	-0.73
Co-PANI-AC-A	5.4±0.2	-9.1±0.3	-0.27	-0.67
Co-PANI-AC-B	9.2±0.5	-20±1.0	-0.30	-0.64
Co-PANI-AC-C	/	/	-0.50	-1.18
Cu-PANI-AC-A	5.8±0.2	-15±0.6	-0.28	-0.64
Cu-PANI-AC-B	/	/	-0.52	-1.16
Cu-PANI-AC-C	/	/	-0.53	-1.17

The results of the electrochemical experiments can be rationalised based on the physicochemical characterisation. First of all, the sulphides can be excluded as active sites since Co-PANI-AC-B and –C have a similar sulphur content but Co-PANI-AC-B is active while the other is not. Secondly, and most importantly, it appears that the activity of the electrocatalysts is strongly related with the fraction of metal oxides. Indeed, for the A-series the activity decreases from Cu to Co to Fe, which is in accordance with the decrease in metal oxides content from 100% to 13%. Furthermore, for the different Co and Fe electrocatalysts this same trend can be observed, both Co-PANI-AC-B and Fe-PANI-AC-C have the highest fraction of oxides and also the highest activity. The inactivity of Co-PANI-AC-C can be linked

with the difference in the contribution of the surface metal species as was observed after deconvoluting the Co2p XPS spectra. It appeared that a second acid treatment mainly removed the active cobalt oxides, while leaving behind Co-N_x species and cobalt sulphides, which were found to be inactive. For Fe-PANI-AC the opposite was observed. In this case, a second acid treatment led to an increased activity and this might again be linked with the surface composition. After a second acid treatment the fraction of FeO becomes larger when compared to Fe_2O_3, suggesting that these species are more active. However, Cu-PANI-AC-B and –C do not follow this trend at all. Their surface metal content exists entirely out of oxides and still they are inactive. A possible hypothesis is that the size of the metal oxides is an important factor determining the electrocatalytic performance. It is possible that the size of the copper oxides in the B- and C-series is too large to be active, possibly because of a lower conductivity of the oxides when compared to the carbon framework. The electrons would thus need more time to travel through the larger oxides to reach the actual active sites, resulting in a lower activity. This would also explain the higher performance of Cu-PANI-AC-A when compared to the Cu-MWCNTs reported in the literature. Since for the latter, the particles could clearly be distinguished in the TEM images while this is not the case for Cu-PANI-AC-A.[23] Another possibility is that the oxides in Cu-PANI-AC-B and –C are covered by a layer of carbon. This carbon layer might then prevent nitrobenzene to reach the active layer. Other factors contributing to the activity are the N content, the fraction of graphitic N, the surface area and the degree of graphitisation. However, since there is no clear trend their contributions are expected to be lower than that of the fraction of oxides. In conclusion, the metal might be more important to determine to what extent the oxides are formed but not to determine the current generation or otherwise stated the oxides will reach similar activities irrespective of the metal type.

To initiate the reaction faster, or to have a lower overpotential, the electrocatalyst should perform the first electron transfer, which is accompanied with the adsorption of nitrobenzene, faster. There are several factors that aid this process (1) a higher degree of graphitisation, (2) a higher surface area and thus a higher number of available active sites, (3) the presence of the appropriate metal coordination and (4) the strength of the reducing agent (metal). For the A-series Co combines a high degree of graphitisation, with the highest surface area and since its most likely configuration is CoO, it can be oxidised to Co^{3+}, to perform the first-electron reduction and adsorption of nitrobenzene. Furthermore, it has a higher number of oxides when compared to iron. Copper and iron are mainly present in their highest oxidation state, CuO and Fe_2O_3, respectively and therefore, need to be reduced prior to the start of the reaction, explaining their higher overpotential. Since the standard reduction potential of the one-electron reduction of both is much more positive than the operating potential, this will be quite a fast process for both. Copper outperforms iron because of the much higher availability of oxides. For the higher metal loadings, the inactive materials have a high onset potential and Co-PANI-AC-B outperforms Fe-PANI-AC-C because it has a higher degree of graphitisation, a higher number of available oxides and because it does not require to be reduced to start the reaction.

Concerning the selectivity, the fact that Cu-PANI-AC-A reaches the highest selectivity to aniline is most likely a consequence of its lower standard reduction potential. In order to terminate the reaction and release the product, the metal specie should return to its initial oxidation state. Since this reduction reaction is less easy (lower E°, 0.16 V) for copper compared to iron and cobalt, the reduction of nitrobenzene will proceed to a further stage on copper than on the other two. In this line, iron having an intermediate E° (0.77 V) should result in a higher selectivity than Co (E° of 1.82 V) but this is not the case because the kinetic

current density of Fe-PANI-AC-A is much lower, which results in a slower reduction reaction. The higher electron transfer number for Co-PANI-AC-B and Fe-PANI-AC-C, might be a consequence of the higher number of available active sites in combination with the relatively thick catalyst layer on the electrode. This means that one reagent might pass several active sites, each advancing the reduction to the next level, prior to finally leaving the active layer.

Chronoamperometic tests for Cu-PANI-AC-A and Co-PANI-AC-B

To confirm the result obtained from the K-L analysis and to determine which products are formed, chronoamperometric measurements in combination with GC analysis were performed for Cu-PANI-AC-A and Co-PANI-AC-B. A potential of -0.75 V vs. Fc^+/Fc was chosen based on the following two criteria: (1) the current in the LSV is high enough to achieve a significant conversion in 52 h and (2) no competing reactions are taking place at this potential.

The results of these tests are summarised in Table 5.6. The reduction of nitrobenzene is clearly faster over Cu-PANI-AC-A than over Co-PANI-AC-B, as the conversion is 2.5 times higher (and accordingly higher currents were generated over Cu-PANI-AC-A during the chronoamperometric tests). At first sight,this might seem to contradict the results obtained for the kinetic current density in the LSV tests, but it can be rationalised considering that the chronoamperometirc tests were carried out at higher nitrobenzene concentration (15 mM). The effect of the nitrobenzene concentration on the elctrocatalysts performance was investigated further by carrying out additional LSV measurements at higher concentration of nitrobenzene (15 and 30 mM, Fig. S5.16) and by combining these data with the pore size distribution curves of Cu-PANI-AC-A and Co-PANI-AC-B (Fig. S5.17). Based on these results, the lower currents for Cu-PANI-AC-A at low concentration of nitrobenzene (5 mM) can be attributed to diffusion limitation in its pores, which are mainly in the microporous and the lower mesoporous range (2-25 nm). At higher concentration, the concentration gradient between bulk solution and electrocatalyst surface becomes larger and thus the driving force for the diffusion of nitrobenzene can become high enough to grant diffusion of nitrobenzene also into the smaller pores. This would result in the utilisation of a larger fraction (or all) of the active sites. As a larger fraction of the pores of Co-PANI-AC-B lays in the mesoporous and even macroporous region, this electrocatalyst is not expected to suffer from diffusion limitations and thus all active sites will already be utilised also with 5 mM nitrobenzene. This would explain the observed much larger increase in current upon increase in nitrobenzene concentration that was observed for Cu-PANI-AC-A compared to Co-PANI-AC-B and that inversion in activity order between the two electrocatalyst as a function of the nitrobenzene concentration, By using the numbers of exchanged electrons, as determined by the K-L equations, and the total charge, which passed through the cell, the Faraday's law could be used to confirm the data for the conversion. This gave a conversion of 55 and 21 % for the Cu- and Co-based electrocatalyst, respectively. As a consequence, the number of exchanged electrons determined by means of the K-L, agrees well with the actual reduction process and this was further evidenced by the values for the selectivity that were determined with the GC analysis (Table 5.6). In the case of Cu-PANI-AC-A, a selectivity of 82% to aniline was obtained, which is in accordance with the value for *n* of 6 for this reaction (Eq. 5.2). For Co-PANI-AC-B, a lower selectivity towards aniline (40%) was obtained and this is mainly due to the further reduction to cyclohexylamine (selectivity of 32%). These results again agree well with the number of exchanged electrons (9) that was obtained for this system. The other major product, para-ethoxyaniline (selectivity around 10% in both cases) can be obtained through a non- electrochemical conversion of the unstable PHA. PHA could not be detected

by means of GC as a consequence of its decomposition to NSB and reaction with another NSB to azoxybenzene under the analysis conditions. The small amount of azoxybenzene and NSB that was thus discovered most likely originated during the GC analysis process.[23–25,245–247]

Based on the number of exchanged electrons during the chronoamperometry experiment and the metal atomic percentages it is possible to determine the turnover frequencies of Cu and Co at the surface. This gave $8.0E^{16}$ and $0.9E^{16}$ electrons per metal site per second, respectively. This signifies that the Cu active sites work almost ten times as efficient as the Co ones.

Table 5.6: Results of GC analysis after chronoamperometry performed at -0.75 V vs. Fc^+/Fc in a 0.3 M $HClO_4$ ethanolic solution containing 15 mM nitrobenzene for 52 h.

	Cu-PANI-AC-A	Co-PANI-AC-B
Conversion	54%	22%
Selectivity		
Aniline	82%	40%
Cyclohexylamine	0%	32%
Nitrosobenzene	3%	8%
Para-ethoxyaniline	11%	12%
Azobenzene	1%	3%
Azoxybenzene	3%	5%

Stability of Cu-PANI-AC-A and Co-PANI-AC-B

Finally, the stability of Cu-PANI-AC-A and Co-PANI-AC-B was evaluated with cyclic voltammetry (Fig. 5.7). The lack of a major difference in the voltammogram between the second curve (after an initial stabilisation of the system) and the last cycle (no. 1000), indicates a good stability of the electrocatalysts under study in the acidic environment (0.3M $HClO_4$), which is a promising feature for their prospective application in a fuel cell for the cogeneration of electricity and aniline.

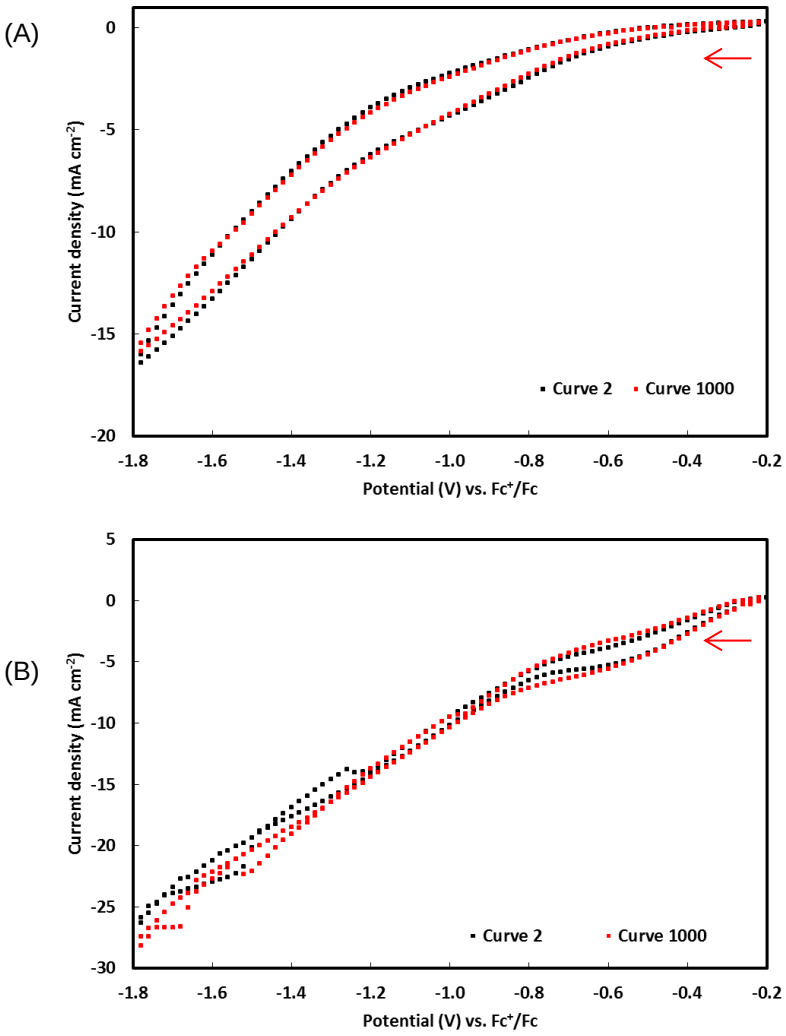

Figure 5.7: Stability test of (A) CuPANI-AC-A and (B) Co-PANI-AC-B by means of cyclic voltammetry. The potential was cycled between -0.2 and -1.8 V vs. Fc^{+}/Fc at a scan rate of 100 mVs^{-1}. Only the second curve (after initial stabilisation of the system) and the last curve are shown. Prior to the last cycle, the measurement was paused and the solution was stirred to ensure a homogeneous distribution of nitrobenzene throughout the medium.

5.4 Conclusions

Electrocatalysts based on non-noble metal-containing (Cu, Co or Fe) N-doped carbons were synthesised, thoroughly characterised and their performance evaluated in a half-cell setup to reduce nitrobenzene to aniline. The activities of the as-synthesised electrocatalysts were ranked on the basis of a combination of their onset potential and kinetic current densities. Remarkably, the ranking of the different metals changed from Cu > Co > Fe at low metal loading to Co > Fe > Cu at high metal loading. The highest selectivity was obtained over Cu-PANI-AC-A. With the physicochemical characterisations in mind, it was determined that this ranking is mostly a consequence of the relative content of small oxides. Bigger oxides and MeN_x species, on the other hand did not seem to contribute to the activitiy. Furthermore, based on the above results it was possible to conclude that the N-containing sites alone could not account for the observed trends in activity as Co-PANI-AC-B, which reaches the highest current densities, has the lowest surface N content. Therefore, it is hypothesised that the metals actively contribute to the reactivity. For Co-PANI-AC-B and Cu-PANI-AC-A a conversion of respectively, 22 and 54% was achieved after 52 h of reaction at -0.75 V vs.

Fc^+/Fc in 0.3M $HClO_4$ at room temperature. For Cu-PANI-AC-A, aniline was identified as the main reaction product with a selectivity of 82%. For Co-PANI-AC-B the selectivity towards aniline was lower (40%) as a consequence of the further reduction reaction yielding hydroxylamine.

The Cu-PANI-AC-A electrocatalyst is a promising candidate for the successful development of a fuel cell that allows the cogeneration of electricity and aniline, as a valuable commodity product, from the reduction of nitrobenzene. Compared to the current industrial aniline production process (see introduction), similar selectivity towards aniline was achieved with our electrochemical approach. In order to further understand the observed behaviour future work will include further analysis of the different electrocatalysts with TEM to test our hypothesis that small oxide particles are the most active sites for the nitrobenzene reduction.

Supporting information

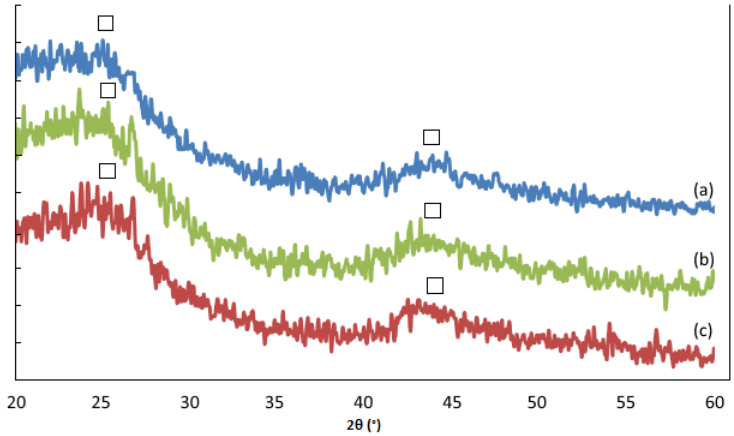

Figure S5.1. XRD diffractograms of: (a) Cu-PANI-AC-A, (b) Co-PANI-AC-A and (c) Fe-PANI-AC-A. The peaks in the XRD pattern are identified as follows: □ is graphitic carbon.

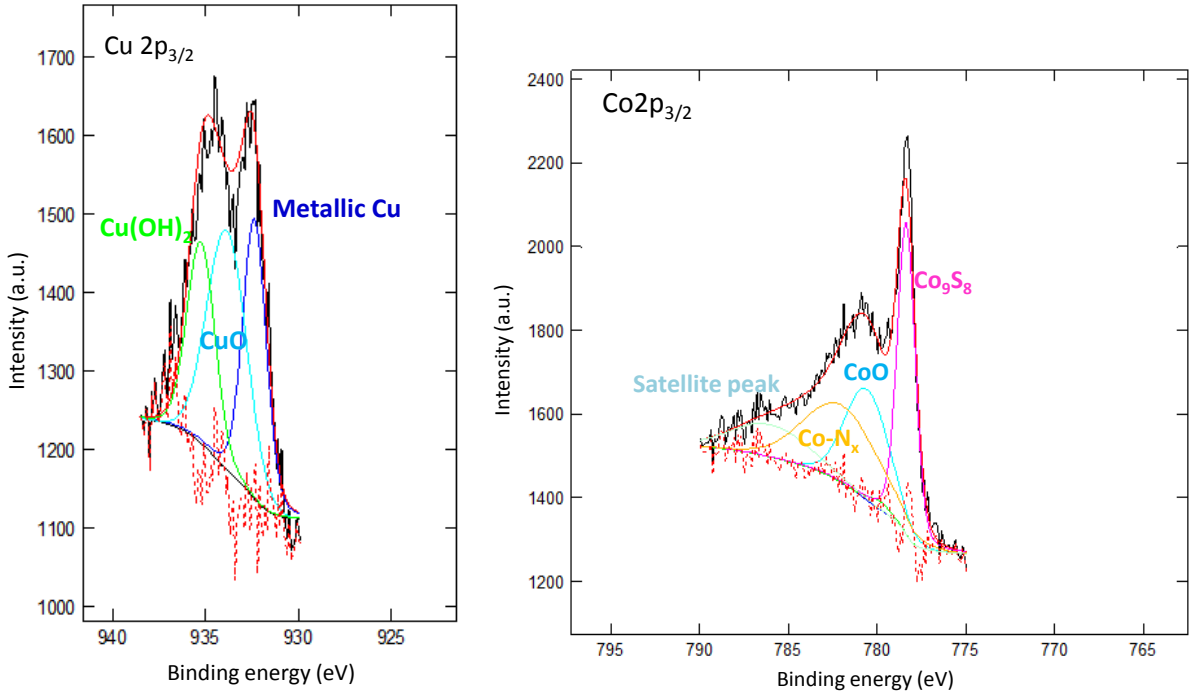

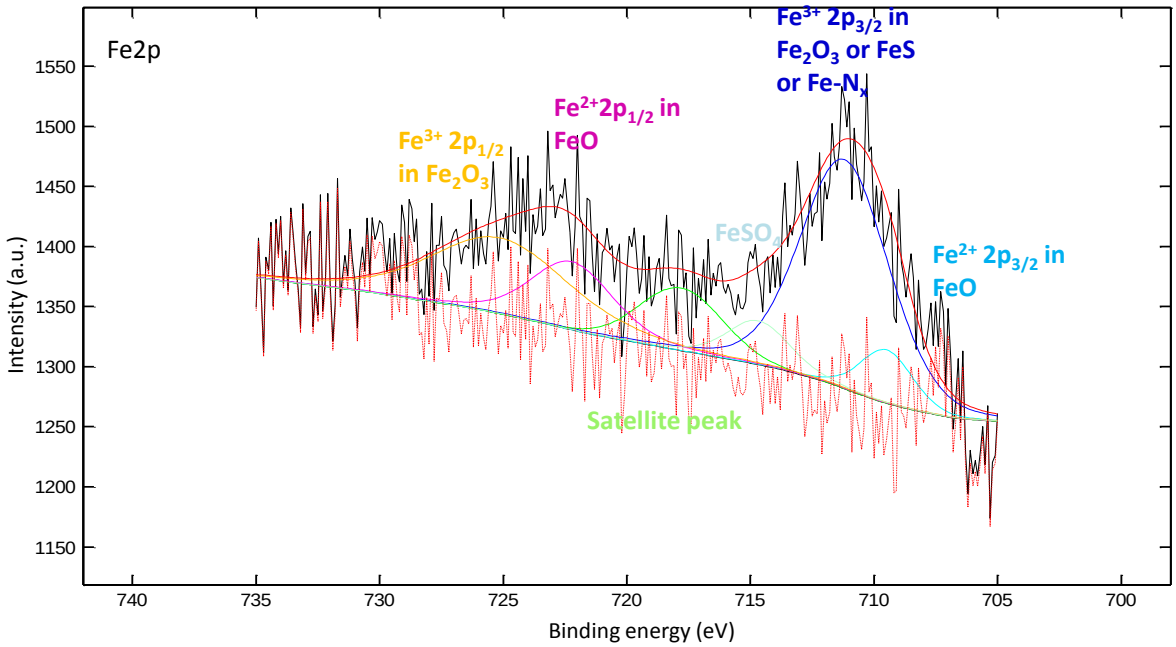

Figure S5.2. Deconvoluted high resolution Me2p XPS spectra of Me-PANI-AC-C series.

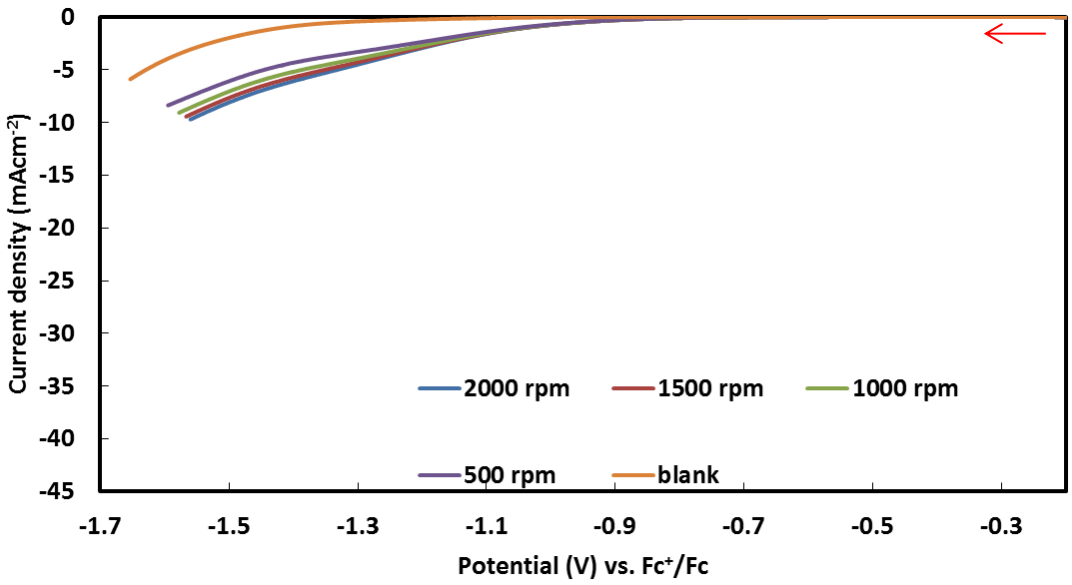

Figure S5.3. LSV plots of Fe-PANI-AC-A recorded in 5 mM nitrobenzene in 0.3 M $HClO_4$ in ethanol at a scan rate of 5 mVs^{-1} at different rotation rates and corrected for the iR drop.

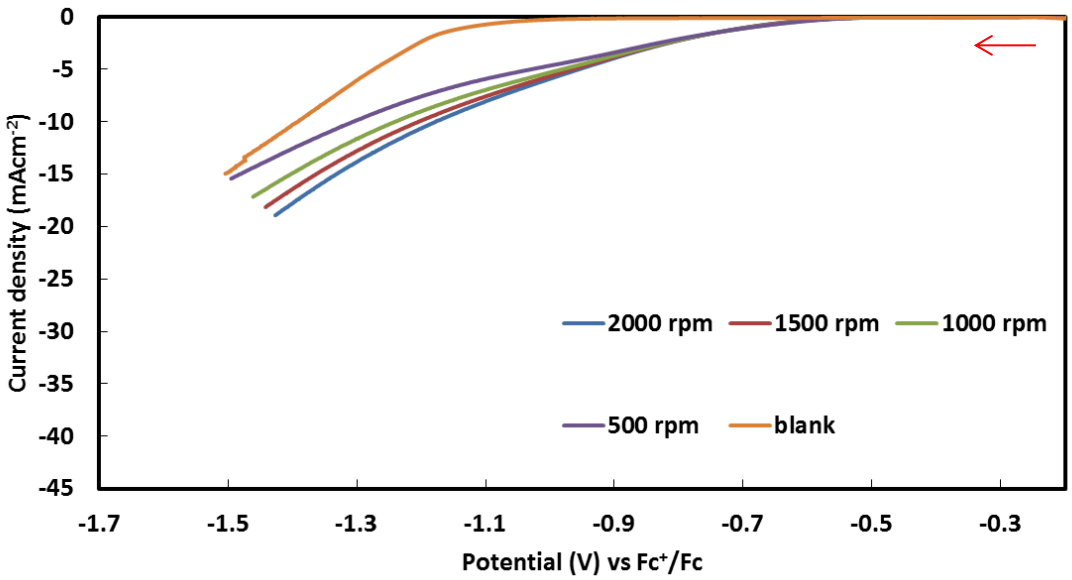

Figure S5.4. LSV plots of Fe-PANI-AC-B recorded in 5 mM nitrobenzene in 0.3 M $HClO_4$ in ethanol at a scan rate of 5 mVs^{-1} at different rotation rates and corrected for the iR drop.

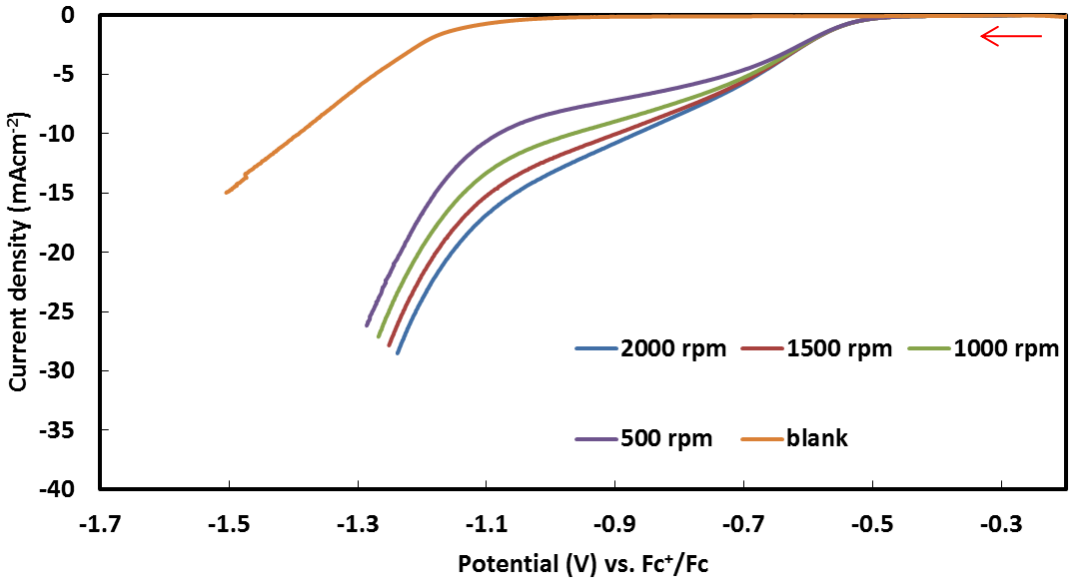

Figure S5.5. LSV plots of Fe-PANI-AC-C recorded in 5 mM nitrobenzene in 0.3 M $HClO_4$ in ethanol at a scan rate of 5 mVs^{-1} at different rotation rates and corrected for the iR drop.

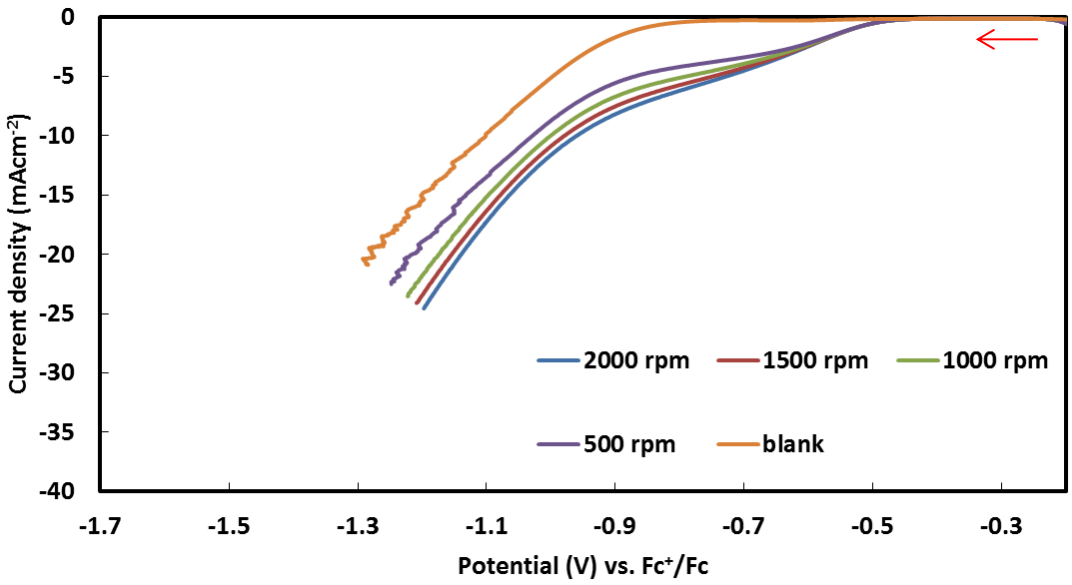

Figure S5.6. LSV plots of Co-PANI-AC-A recorded in 5 mM nitrobenzene in 0.3 M $HClO_4$ in ethanol at a scan rate of 5 mVs^{-1} at different rotation rates and corrected for the iR drop.

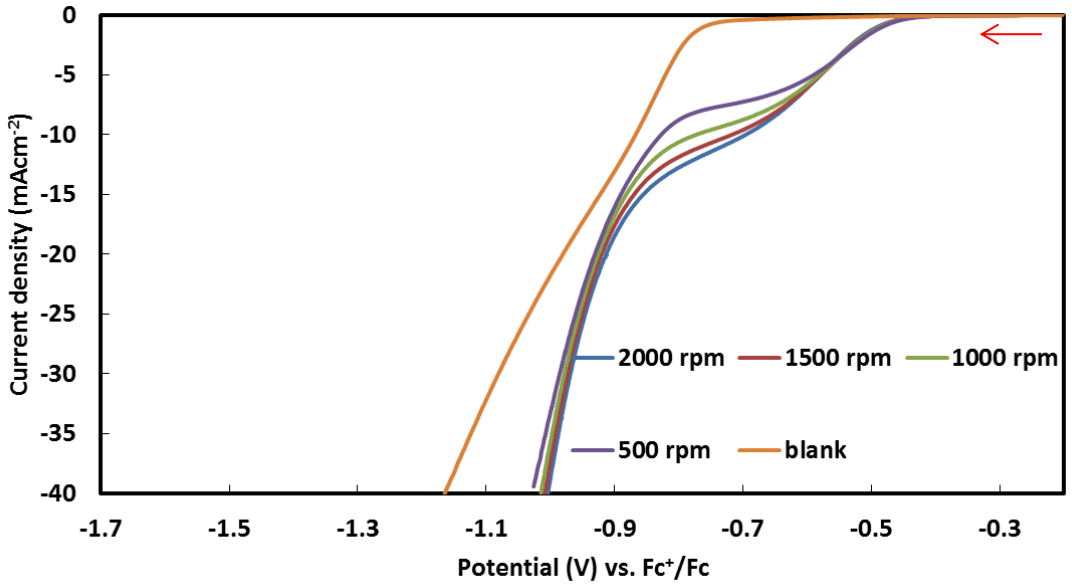

Figure S5.7. LSV plots of Co-PANI-AC-B recorded in 5 mM nitrobenzene in 0.3 M $HClO_4$ in ethanol at a scan rate of 5 mVs^{-1} at different rotation rates and corrected for the iR drop.

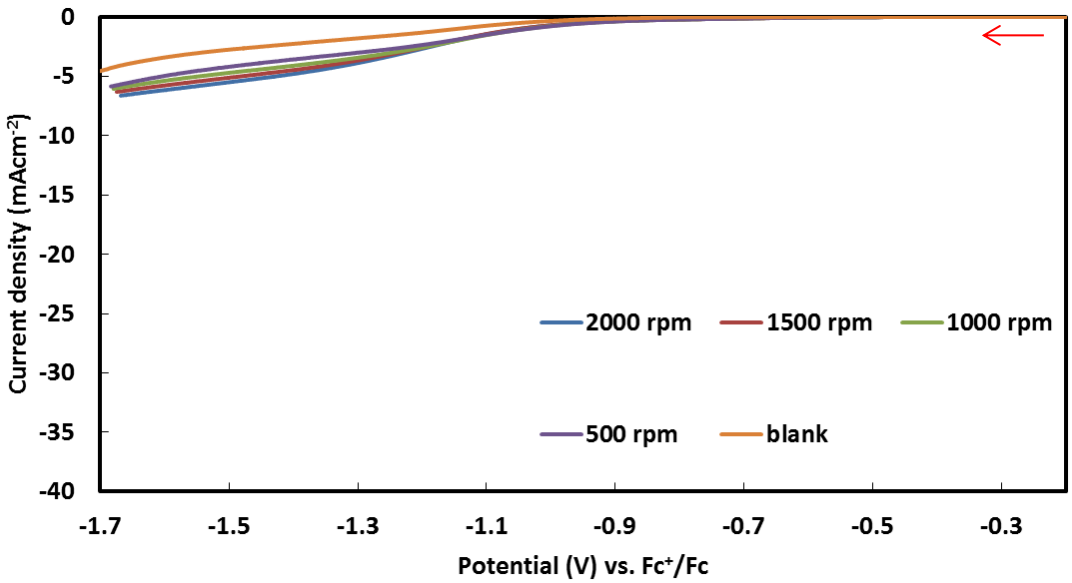

Figure S5.8. LSV plots of Co-PANI-AC-C recorded in 5 mM nitrobenzene in 0.3 M $HClO_4$ in ethanol at a scan rate of 5 mVs^{-1} at different rotation rates and corrected for the iR drop.

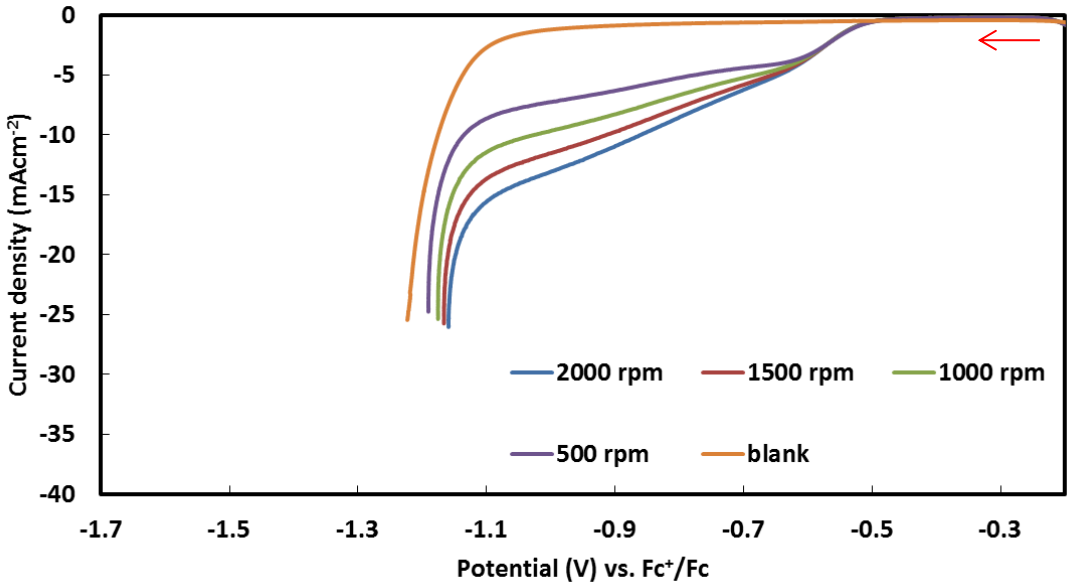

Figure S5.9. LSV plots of Cu-PANI-AC-A recorded in 5 mM nitrobenzene in 0.3 M $HClO_4$ in ethanol at a scan rate of 5 mVs^{-1} at different rotation rates and corrected for the iR drop.

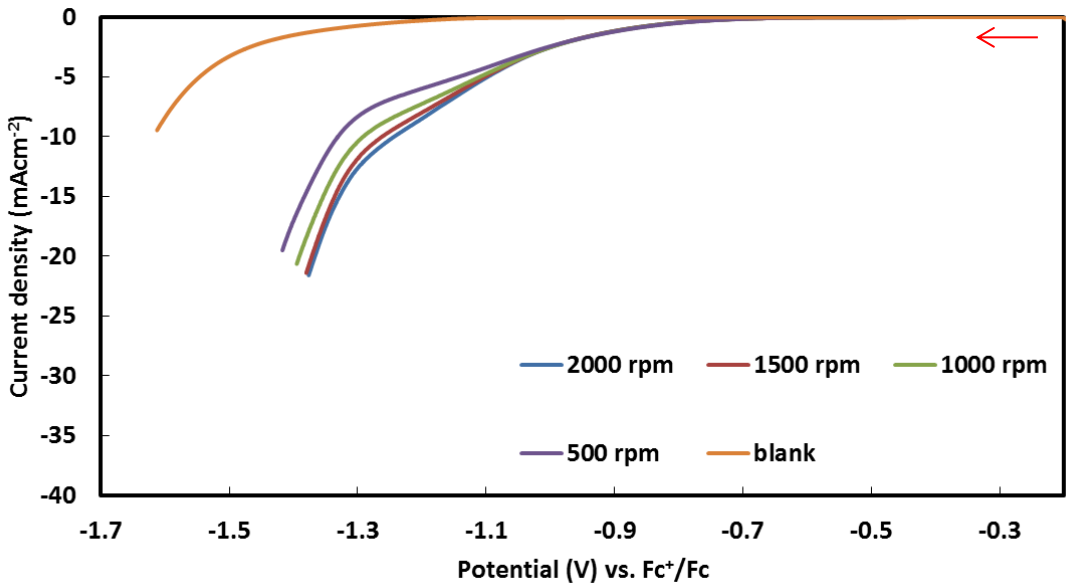

Figure S5.10. LSV plots of Cu-PANI-AC-B recorded in 5 mM nitrobenzene in 0.3 M $HClO_4$ in ethanol at a scan rate of 5 mVs^{-1} at different rotation rates and corrected for the iR drop.

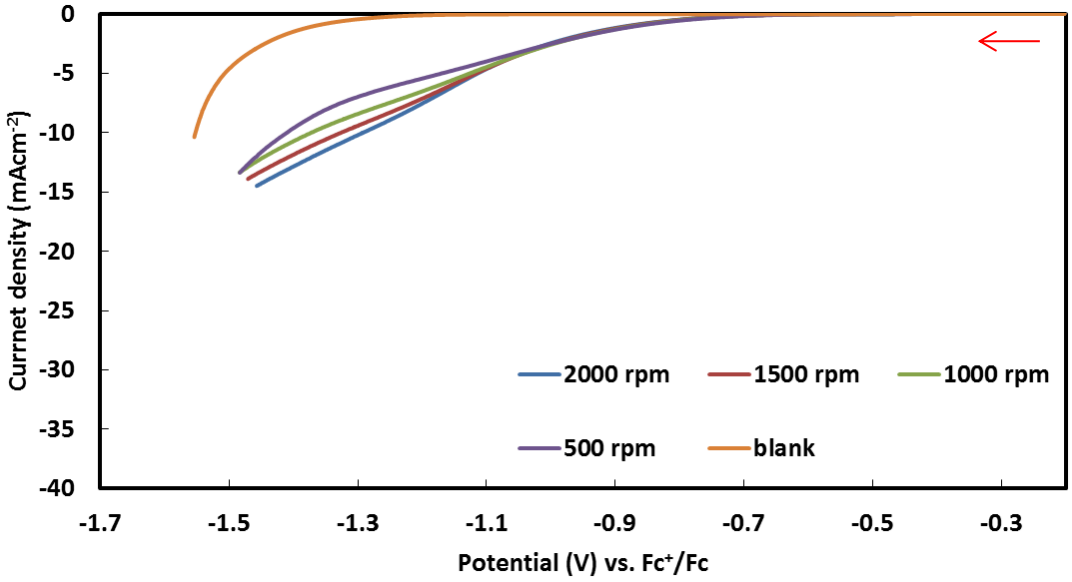

Figure S5.11. LSV plots of Cu-PANI-AC-C recorded in 5 mM nitrobenzene in 0.3 M $HClO_4$ in ethanol at a scan rate of 5 mVs^{-1} at different rotation rates and corrected for the iR drop.

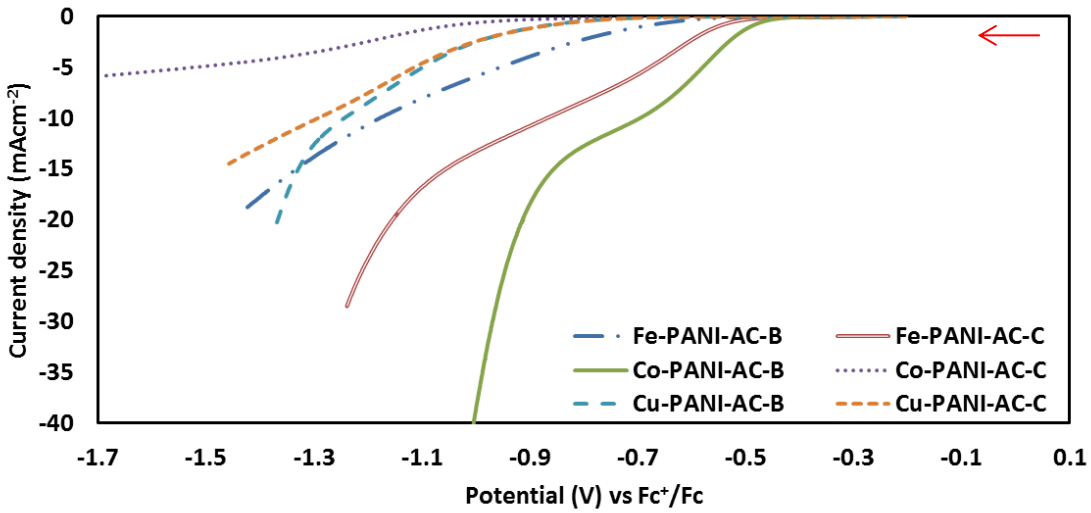

Figure S5.12. LSV plots of Fe-PANI-AC-B & -C, Co-PANI-AC-B & -C and Cu-PANI-AC-B & -C, recorded in 5 mM nitrobenzene in 0.3 M $HClO_4$ in absolute ethanol at a scan rate of 5 mVs^{-1}, with a rotation speed of 2000 rpm and corrected for the iR drop.

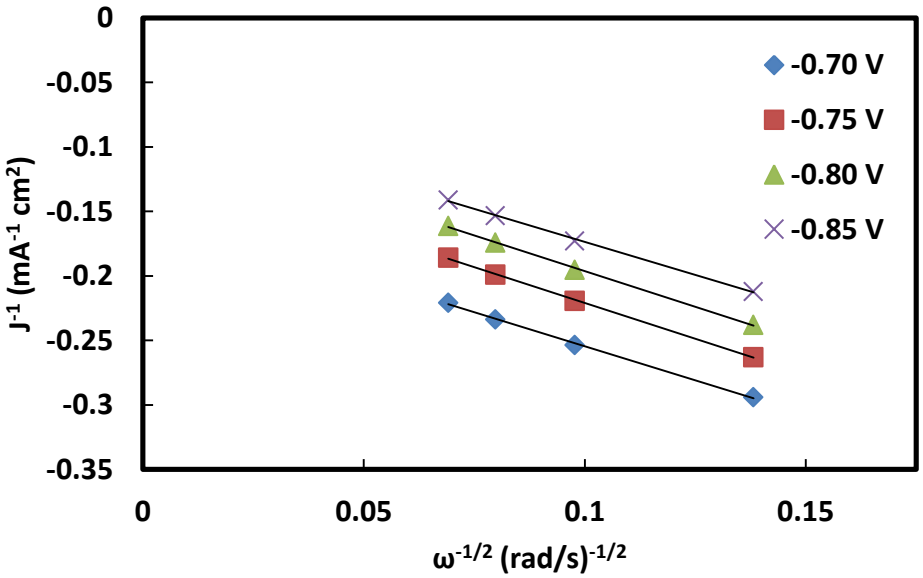

Figure S5.13. Koutécky-Levich plots (J^{-1} vs. $\omega^{-1/2}$) at different electrode potentials (V vs. Fc^{+}/Fc) for Co-PANI-AC-A.

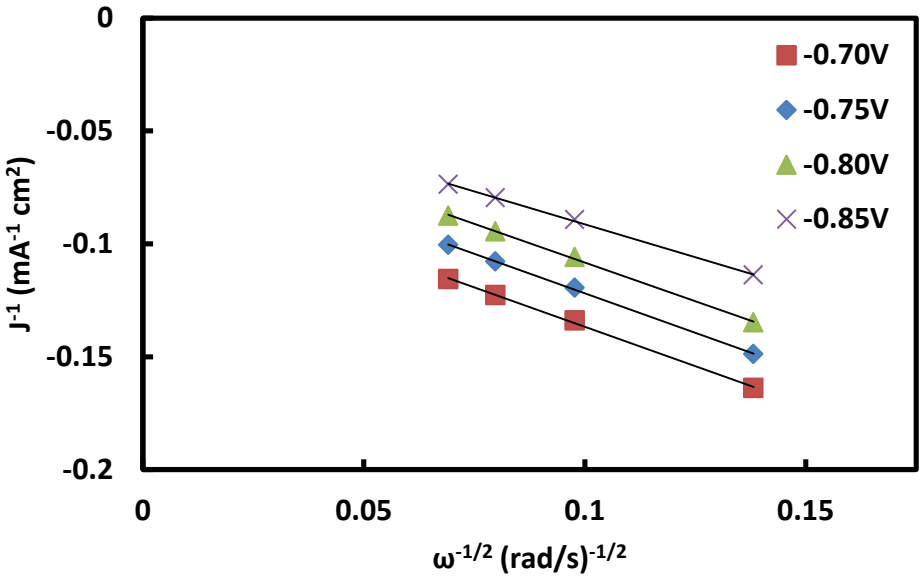

Figure S5.14. Koutécky-Levich plots (J^{-1} vs. $\omega^{-1/2}$) at different electrode potentials (V vs. Fc^{+}/Fc) for Co-PANI-AC-B.

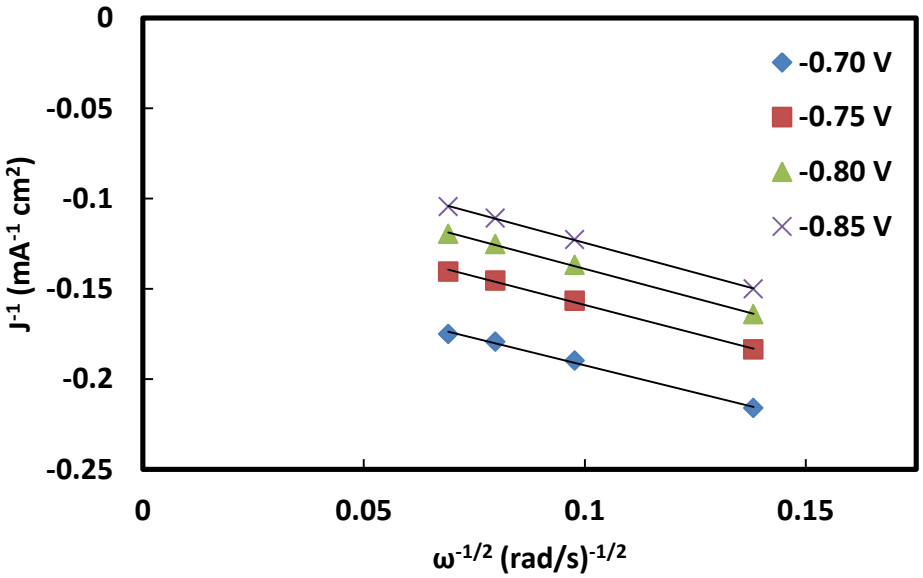

Figure S5.15. Koutécky-Levich plots (J^{-1} vs. $\omega^{-1/2}$) at different electrode potentials (V vs. Fc^{+}/Fc) for Fe-PANI-AC-C.

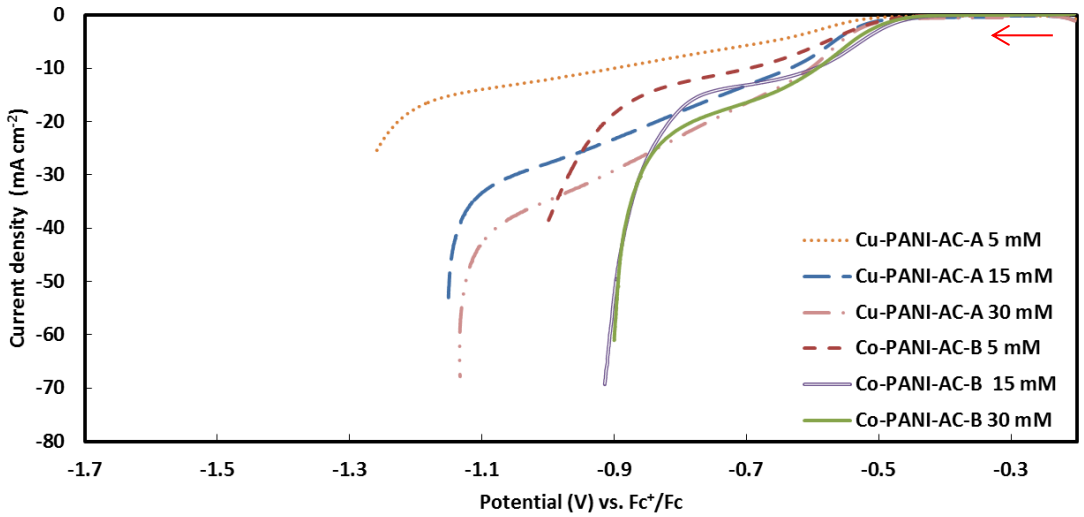

Figure S5.16. LSV plots of Cu-PANI-AC-A & Co-PANI-AC-B, recorded at different concentrations of nitrobenzene (5, 15 and 30 mM) in 0.3 M $HClO_4$ in absolute ethanol at a scan rate of 5 mVs^{-1}, with a rotation speed of 2000 rpm and corrected for the iR drop.

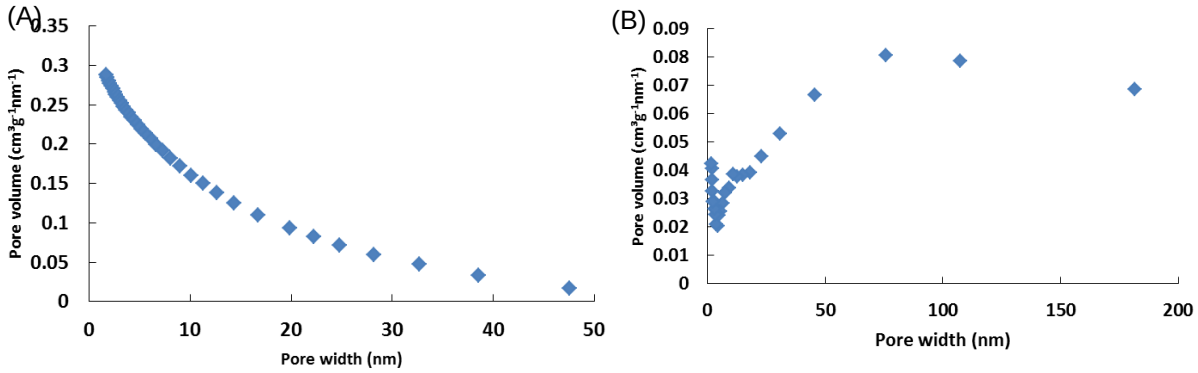

Figure S5.17. Pore size distribution curves of CuPANI-AC-A (A) & Co-PANI-AC-B (B).

Chapter 6

Metal-free doped ordered mesoporous carbons: synthesis and application as selective electrocatalysts for electricity and aniline cogeneration

Abstract

Ordered mesoporous carbons (OMC) doped with nitrogen, phosphorus or boron were synthesised and studied as electroctalalysts for the reduction of nitrobenzene to aniline in a half-cell setup. This exergonic reaction would offer the possibility to generate electricity at the same time as a useful product in a fuel cell set-up. The nature of the dopant played a crucial role in the resulting electrocatalytic performance, which was monitored by LSV with a rotating-disk electrode set-up. While the incorporation of boron generated electrocatalysts with higher reaction rates, phosphorus created sites with a lower overpotential. Doping with nitrogen led to intermediate behaviour in terms of onset potential and kinetic current density but provided the highest selectivity towards aniline and is therefore the most promising electrocatalyst developed in this study. A chronoamperometric experiment over this N-doped OMC performed at -0.75 V vs. Fc^{+}/Fc in acidic environment, resulted in a conversion of 46% with an overall selectivity of 87% to aniline. This is the best performance ever reported for an electrocatalyst for the reduction of nitrobenzene to aniline.

Based on:

N. Daems, K. Baert, A. Hubin, I.F.J. Vankelecom, P.P. Pescarmona, *in preparation.*

Author contributions

The original idea of this research was developed by N. Daems and P. P. Pescarmona. Electrocatalyst synthesis, physicochemical and electrochemical characterisation were done by N. Daems. The article was written by N. Daems with editing by P. P. Pescarmona. XPS measurements were done by K. Baert under the supervision of A. Hubin. GC analysis was performed by N. Daems. The whole work was supervised by P. P. Pescarmona and I. F. J. Vankelecom.

6.1 Introduction

Nowadays, the fuel cell industry and the chemical industry run mainly independently from each other. This means that fuel cells are almost exclusively used for the generation of electricity with water as a side product. However, since a lot of industrially valuable chemicals can be obtained by means of thermodynamically favourable redox reactions, it is possible to replace the reaction occurring at the anode or at the cathode in a fuel cell with one of these exergonic ($\Delta_r G^0 < 0$) reactions. This approach has the advantage that the chemical energy liberated by the reaction, which is typically lost as heat in the commercial process, is converted into electricity. In this way, the electricity generated by a fuel cell can be coupled with the production of industrially valuable products. This cogeneration approach gives rise to more sustainable and energy-efficient processes, which is in line with the current societal and industrial targets.[25] Indeed, as a consequence of the depletion of raw material reserves, the chemical industry has been driven in the direction of alternative technologies with lowered energy demands and increased reaction efficiencies.[187,218] An additional advantage of an electrochemical production process over a conventional process, is the possibility to control the selectivity and the reaction rate through the cell potential.[15,241]

While this is a relatively new and yet unexplored field, several examples do exist in literature. Amongst others they include the reduction of oxygen to hydrogen peroxide,[187,270–273] the reduction of nitrogen monoxide to hydroxylamine,[13–15,241] the reduction of nitrobenzene to aniline[23–25,244,274] and the oxidation of glycerol.[275–279] The focus of this study is on the reduction of nitrobenzene to aniline. Aniline has a broad range of industrial applications,[20] among which the most important is as intermediate in the production of polyurethanes.[21]

The electrochemical reduction of the nitro group was first investigated by Haber *et al.* and has been extensively studied since then, also by our group.[22–25,280] The overall reactions are:

Anode:

$$H_2 \rightarrow 2H^+ + 2e^- \quad E^0 = 0\ V \qquad (6.1)$$

Cathode:

$$PhNO_2 + 6H^+ + 6e^- \rightarrow PhNH_2 + 2H_2O \quad E^0 = 0.82\ V \qquad (6.2)$$

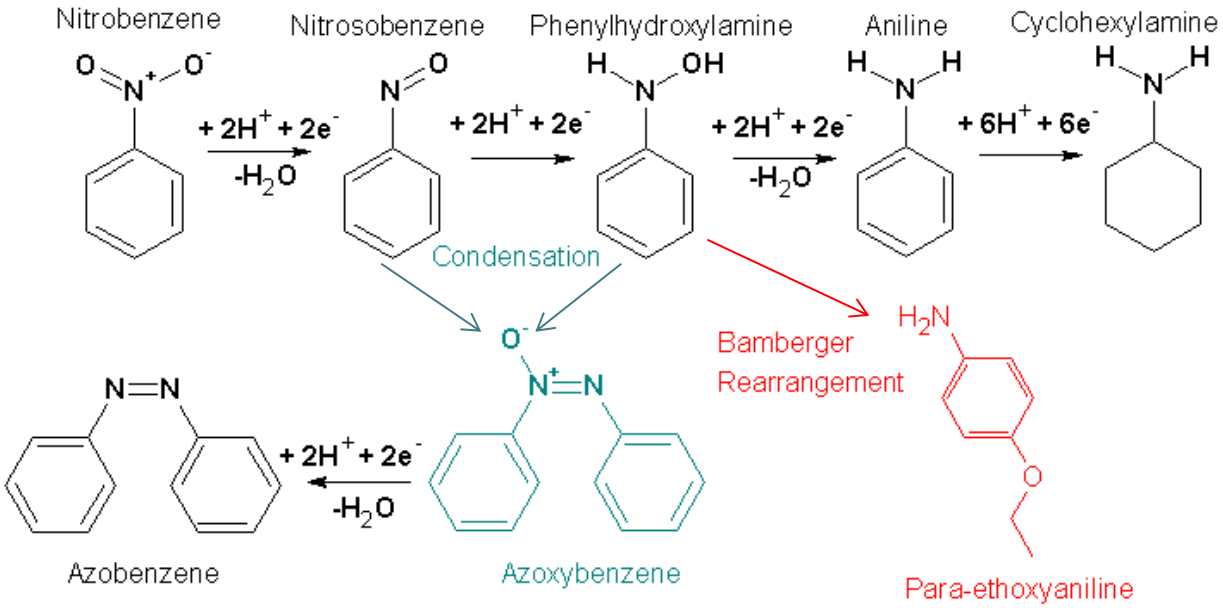

Scheme 6.1. Main and side reaction paths in the electrochemical reduction of nitrobenzene.

As discussed in detail elsewhere,[23] the full reaction scheme is more complex and contains several reaction intermediates and side-products, which originate from both electrochemical and chemical steps (Scheme 6.1).[242] Importantly, the product selectivity and the reaction rate is strongly influenced by the physicochemical features of the electrocatalyst employed at the cathode.[25,243,244,246,249,251–253,281] In order to make this electrochemical route towards aniline economically viable, it is of utmost importance to develop cost-effective and productive electrocatalysts with a high selectivity towards the target product, aniline. Recent research performed by our group has shown that Cu nanoparticles supported on multi-walled carbon nanotubes (MWCNTs) are promising candidates for the selective reduction of nitrobenzene to azoxybenzene. Furthermore, this study also showed that Cu outperformed Pt in terms of onset potential, proving the possibility to use non-noble metals as a less expensive catalytic species.[23–25] In order to further enhance the selectivity to aniline, different non-noble metals, Fe, Co and Cu, and a different support, N-doped carbon, were investigated in a parallel study.[282] This study revealed that the electrocatalyst synthesised with low amounts of copper resulted in the highest selectivity towards aniline (electron exchange number close to six). This study also suggested that non-metallic sites could also play a catalytic role, in analogy to recent results obtained on N-doped diamond.[251] Therefore, and in an attempt to further reduce the electrocatalyst cost, the possibility to use ordered mesoporous carbons (OMCs) doped with nitrogen, boron or phosphorus as electrocatalysts for the nitrobenzene reduction is investigated in this work. Doped carbon materials were chosen since they consist of inexpensive, widely available elements and are devoid of metals. Furthermore, the presence of a graphitic carbon backbone grants a high electrochemical stability and a good electron conductivity.[153,283] Doping the graphitic carbon framework disrupts the electron delocalisation in the graphitic π-system, generating sites with pairs of partial positive and negative charges, which can act as a more active site for the nitrobenzene reduction (easier adsorption of the negatively charged oxygen atom of the nitro-group on the positive sites).[153] There are several reasons why we chose doped OMCs over doped carbon nanotubes or doped graphene. First of all, they possess a higher surface area (up to 1900 m²/g), resulting in a higher number of accessible active sites.[175,184] Furthermore, the presence of mesopores grants easier accessibility of the active sites compared to microporous materials.[79,153] Finally, since they can be prepared in the absence of metals they are truly metal-free, which is not necessarily the case with graphene or carbon nanotubes.[45,104–106] While doped OMCs have been extensively studied for the oxygen reduction reactions (showing promising results),[79,153,184,187,284] they have not yet been applied for the electrochemical cogeneration of electricity and aniline. In this work, a two-step nanocasting method previously developed by our group,[187] was modified to synthesise OMCs doped not only with nitrogen but also with boron or phosphorus. This synthesis method offers several advantages. First of all, by using SBA-15 silica, which has an interconnected two-dimensional mesoporous structure, as hard template, doped OMCs with high surface area can be obtained. Secondly, by covering the template pore walls first with a dopant precursor, a high accessibility of the active sites can be ensured. Finally, compared to the technique that is required to prepare N-doped diamond, this synthesis method requires less severe conditions and is less expensive.[153] The obtained materials presented the desired parallel pore morphology resulting in high specific surface areas (up to 1092 m²/g) and displayed promising electrocatalytic performance with remarkably high selectivity towards the target aniline product.

6.2 Experimental

6.2.1 Materials

The following chemicals were used in this work: aniline (99.8%, pure, Acros Organics), pluronic P123 (Sigma Aldrich), tetraethyl orthosilicate (Sigma Aldrich, reagent grade), glycerol (>99.5%, Sigma Aldrich), benzene-1,4-diboronic acid (≥ 95%, Sigma Aldrich), tris(4-methoxyphenyl)phosphine (98%, Alfa Aesar) ammonium peroxydisulphate (98%, Acros Organics), sulphuric acid (>95%, Fisher Chemical), hydrochloric acid (37% aqueous solution, Fisher Chemical), perchloric acid (70% aqueous solution, Sigma Aldrich), nitrobenzene (≥99%, Sigma Aldrich) and phosphate buffer (pH=7, Fisher). All these chemicals were used as received from commercial sources.

6.2.2 Synthesis of the electrocatalyst

Metal-free doped ordered mesoporous carbon materials were prepared through methods based on a procedure previously developed by our group (Scheme 6.2).[187] Shortly, in the first step, the SBA-15 hard template is synthesised, calcined and then 0.5 g of it (S_{BET} = 819 m^2 g^{-1} and V_{pores} = 0.66 cm^3 g^{-1}) was impregnated with the dopant precursor that is allowed to interact with the template pore walls. Three different dopant precursors were used, one N-containing: aniline (NOMC), one P-containing: tris(4-methoxyphenyl)phosphine (POMC) and one B-containing: benzene-1,4-diboronic acid (BOMC). In each case, the amount of dopant precursor employed was determined as that amount that was necessary to cover the SBA-15 surface with a monolayer. This was 0.17 g for aniline, 0.24 g for tris(4-methoxyphenyl)phosphine and 0.30 g for benzene-1,4-diboronic acid. Afterwards, the material was pyrolysed for a first time at 900°C for 3h. Next, the remaining pore volume was filled up with dihydroxynaphthalene (0.20 g, 0.12 g and 0.13 g for the N-doped, P-doped and B-doped OMCs, respectively), followed by a second pyrolysis. Finally, the SBA-15 template was etched away with a NaOH solution (2.5 wt% in a 50/50 water/ethanol mixture). For a more detailed description we refer to our previous work on N-doped ordered mesoporous carbon materials.[187] As a reference and to investigate the influence of oxygen species, a material was synthesised using only dihydroxynaphthalene (0.44 g) to fill up the complete pore volume (OMC). The materials are further referred to using their respective abbreviations.

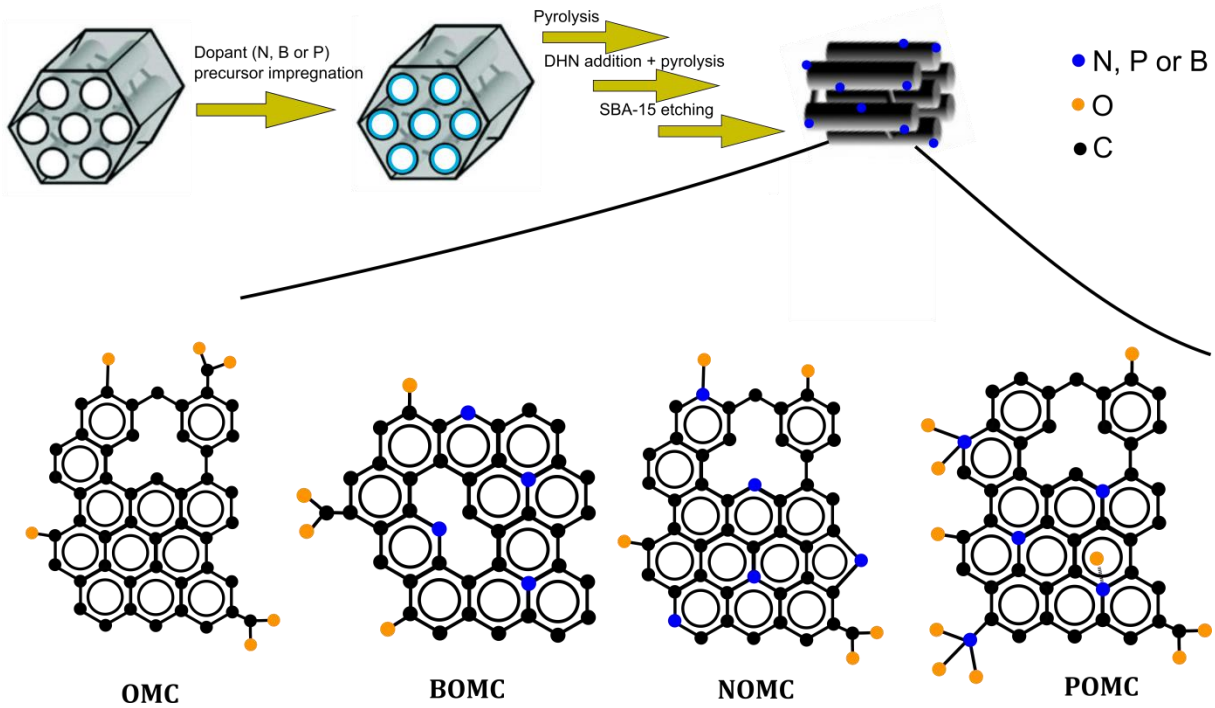

Scheme 6.2. Synthesis route for preparing the doped ordered mesoporous carbon materials.

6.2.3 Physicochemical characterisation

Nitrogen adsorption-desorption isotherms were measured at 77 K on a Micromeritics Tristar 3000. The pore size distributions were determined using the Barrett-Joyner-Halenda (BJH) method, whereas the Brunauer-Emmett-Teller (BET) method was used to calculate the surface area of the samples. Transmission electron microscopy was done at MTM-KU Leuven, using a Philips FEG CM200 operated at 200 kV. Samples were prepared by dispersing the powders in ethanol and placing several drops of the dispersion onto a holey carbon grid. X-ray photoelectron spectroscopy (XPS) measurements were performed by a Physical Electronics PHI 1600 multi-technique system using an Al Kα (1486.6 eV) monochromatic X-ray source, which was operated at 15 kV and 150 W at a base pressure of $2 \cdot 10^{-9}$ Torr. The graphitic C 1s band at 284.6 eV was taken as internal standard, in order to correct possible deviations caused by electric charging of the samples. The multipack software was used for the deconvolution and integration of the XPS signals. Room-temperature Raman spectra were recorded on a Dilor XY spectrometer from HORIBA Jobin Yvon Inc.. The spectroscope was equipped with an Olympus BH 2 microscope, a monochromator, a filter and charge-coupled detector with liquid nitrogen cooling (CCD3000 with a resolution of 2 cm^{-1}). A beam originating from an argon/krypton mixed gas laser at a wavelength of 514 nm (Coherent Innova 70C) was used to visualise the sample. Deconvolution and peak integration was performed by using the Igor pro software.

6.2.4 Electrochemical characterisation

All electrochemical measurements were carried out in a half cell set-up using a Gamry Interface 1000E potentiostat. For all measurements, glassy carbon porous rotating disk electrodes (d = 5 mm) were used. The electrocatalysts were deposited as an ink on the surface of these electrodes. For every measurement, the ink was prepared by dispersing 24.0 mg of electrocatalyst in 900 µL of a 1 wt% solution of polystyrene in toluene. Approximately 3.47 µL of this ink was deposited on the glassy carbon electrode, after which

toluene was evaporated at 50°C for 20 min in a vacuum oven. This resulted in an average catalyst loading of 0.47 mg/cm². The reference electrode was a Fc^+/Fc reference electrode system ($E°_{Fc+/Fc}$ = -0.64 vs. S.H.E.) and the counter electrode was a Pt grid. All potentials in this paper are referred to the Fc/Fc^+ redox couple. The linear sweep voltammetry (LSV) measurements were carried out in 0.3 M $HClO_4$ in ethanol. To avoid possible interference of the oxygen reduction reaction, nitrogen gas was bubbled through the electrolyte for at least 30 min to remove O_2 prior to the measurements. The electrolyte temperature was kept at 25°C with a thermostatic bath. For the LSV measurements, 50 ml of 5 mM nitrobenzene electrolyte solution was used. The potential was scanned in the range from -0.2 to -1.8 V vs. Fc^+/Fc at a rate of 5 mV s^{-1}. Every measurement was carried out three times in order to increase reliability of the experimental results and the average values were reported throughout the paper. The potential of each measurement was corrected for the Ohmic potential drop (equal to 125 Ohm as determined by electrochemical impedance spectroscopy) as a consequence of the electrolyte resistance between the reference and the working electrode.

The Koutécky-Levich equation was used to calculate the number of exchanged electrons and to determine the kinetic current density.[79] The onset potential, i.e. the potential at which the nitrobenzene reduction reaction starts, was determined as the potential at which the slope of the LSV plot exceeded 0.1 mA cm^{-2} V^{-1}. The half-wave potential, i.e. the potential at which the reaction is in the middle of the mixed kinetic-diffusion regime, was determined as the potential corresponding to the inflection point in the LSV plot. The current densities were calculated with respect to the geometric surface area of the glassy carbon electrode(A_{geo}) since it is not possible to accurately determine the actual surface area, which depends both on the electrocatalysts specific surface area and on the amounts of binder and electrocatalyst that are applied to the disk. Therefore, the kinetic current densities reported in this work include contribution of both the intrinsic activity (per surface unit) and of the specific surface area of the electrocatalyst.[23] This allows a meaningful ranking of the electrocatalytic performance of different materials. However, it should be noted that this ranking differs from reports where the electrochemically active surface area is used to normalise the kinetic current density, in which case the kinetic current density is a direct measure of the intrinsic activity (per surface unit).

In order to investigate the conversion and the product selectivity in the nitrobenzene reduction reaction over the most promising electrocatalysts, chronoamperometric experiments were performed in a single cell in which the two half cells are separated by means of a Zirfon® membrane.[228] The rotation speed of the working electrode was set at 500 rpm and the potential was set at -0.75 V vs Fc^+/Fc in 0.3M $HClO_4$ in ethanol. The volume of the half cell with the working electrode was 170 ml and a concentration of 15 mM of nitrobenzene was used. After 52h, the pH of the reaction solution was adjusted to 7 and insoluble $KClO_4$ was filtered out. Analysis of the products after chronoamperometry was performed using gas chromatographyt (GC) on a Shimadzu 2010 Plus equipped with a Rtx-5 amine functionalised standard capillary column (15 m, 0.25 mm internal diameter). Each GC analysis was done in triplicate and the average results were reported. The conversion was calculated based on the GC data and compared to the conversion values calculated with Faraday's law:

$$n_{reacted} = \frac{Q}{F.n} \qquad \text{(Eq. 6.1)}$$

where $n_{reacted}$ is equal to the number of moles that has reacted, Q is the amount of charge that passed through the system (measured using the area under the chronoamperometry

curve), F is the Faraday constant and *n* is the average number of exchanged electrons per molecule of nitrobenzene. The conversion can be calculated by dividing $n_{reacted}$ through the initial number of moles of nitrobenzene.

Cyclic voltammetry (CV) was used to evaluate the electrochemical stability of selected electrocatalysts. The potential was cycled at a scan rate of 100 mV s^{-1} from -0.2 to -1.8 V vs. Fc^+/Fc at in a half-cell containing a 5 mM nitrobenzene in a 0.3 M $HClO_4$ solution. 1000 cycles were performed. Prior to the last scan the solution was stirred to get a homogeneous nitrobenzene distribution. The second and the last scan were compared to evaluate the electrocatalyst stability.

6.3 Results and discussion

Ordered mesoporous carbons doped with different elements (N, B, or P) were prepared by modifying a two-step nanocasting method that was developed by our group.[187] It is the first time that this type of electrocatalysts was tested for the electrocatalytic reduction of nitrobenzene, with the industrially relevant aniline as target product. The electrocatalysts were ranked based on product selectivity (number of exchanged e^-) and activity (onset potential and kinetic current density). The electrocatalyst performance was correlated to the physicochemical properties determined through a combination of techniques in order to understand which features of the materials lead to the most efficient electrocatalyst for the cogeneration of electricity and aniline in a fuel cell.

The success of the applied synthesis strategy in preparing OMCs with a high surface area and with nitrogen-, boron- or phosphorus-doping in the graphitic carbon framework was demonstrated by TEM, N_2 physisorption and XPS. First of all, TEM was used to investigate the pore structure of the different materials (Fig. 6.1). The presence of the characteristic hexagonal arrays of parallel carbon rods unequivocally confirms the successful replication of SBA-15. In addition to the desired structure, small regions containing disordered carbon can also be observed in the TEM images. These species most likely find their origin in the dopant and/or carbon precursor that remain outside the SBA-15 template during the synthesis. Even after a precise fine-tuning of the applied precursors to the pore volume, such species could not be completely avoided. The mesoporous structure observed by TEM is reflected by the very high specific surface of the materials obtained by means of N_2-physisorption. The structural and textural features of the doped OMC materials are summarised in Table 1. The surface area of POMC (1092 m^2 g^{-1}) is remarkably high among doped OMCs obtained with SBA-15 as hard template.[79,153,187] The pore size distributions of the electrocatalysts are narrow (Fig. S6.1) and are centred around 3 to 4 nm (Table 6.1), in line with the expected properties of materials of the OMC type.

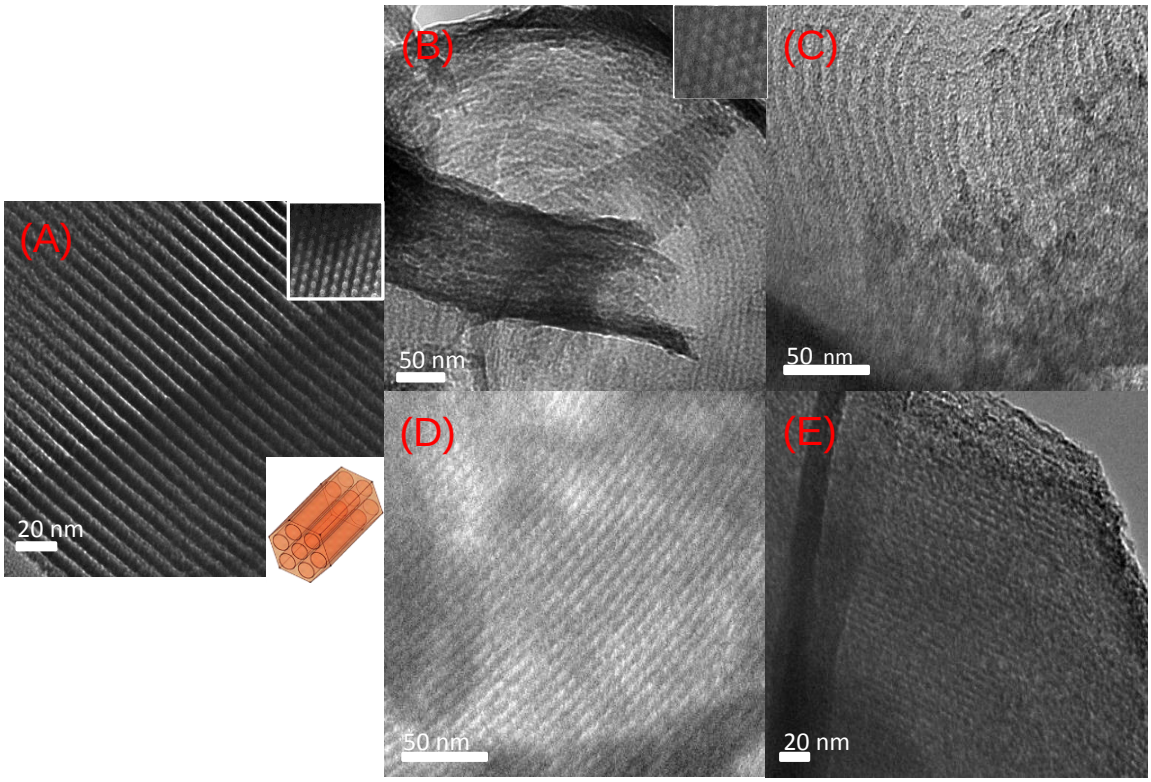

Figure 6.1. TEM images of SBA-15 (A), NOMC (B), BOMC (C), POMC (D) and OMC (E). The inset of image (B) shows a top view of the hexagonal array of rods. All OMC samples were visualised after etching of the silica template.

Table 6.1. Structural and textural properties of SBA-15 and OMCs. [a] S_{BET} is the BET surface area. [b] Total pore volume and pore size calculated with the BJH method. [c] Micropore volume determined from the t-plot.

	S_{BET}[a] (m^2 g^{-1})	Total pore volume[b] (cm^3 g^{-1})	Micropore volume[c] (cm^3 g^{-1})	Pore size[b] (nm)
SBA-15	826	0.76	0.12	7.5
NOMC	745	0.5	0.04	3.1
BOMC	848	0.89	0.03	4.0
POMC	1092	0.36	0.04	2.7
OMC	846	0.57	0.01	3.2

The elemental composition of the active surface layer of the different OMC materials was determined by X-ray photoelectron spectroscopy (XPS). The results confirm that the doping with B,N and P was successful, though in a different extent for each element (Table 6.2). Although phosphorus has the largest mismatch in size with carbon, with our specific synthesis method it is the most efficiently incorporated into the final material, followed by nitrogen and finally boron. In literature, nitrogen is generally more easily incorporated, which is to be expected based on its similar size when compared to carbon.[153,285] Possibly phosphorus is more easily incorporated into the final material because the structure of its precursor (tris(4-methoxyphenyl)phosphine) more closely resembles that of graphitic carbon when compared to that of the other precursors. The low doping levels of boron, on the other hand, can be explained based on its preferential configuration inside the carbon framework, namely replacing a carbon atom in the sp^2 carbon lattice. Compared to nitrogen and

phosphorus, which can also be incorporated at the edges or at defect sites, B incorporation is therefore bound to be more difficult.[285] Further discussion of the XPS data is provided in section 6.3.2

Table 6.2. Surface composition of (doped) OMCs in wt% as determined by XPS.

	N (wt%)	B (wt%)	P (wt%)	C (wt%)	O (wt%)
NOMC	2.7	/	/	85	11
BOMC	0.3	1.1	/	92	5.5
POMC	0.4	/	6.2	76	18
OMC	0.1	/	/	91	8.6

Based on these characterisation results, we can conclude that all the doped OMC display the desired chemical, structural and textural features for the targeted electrocatalytic application.

6.3.1 Electrocatalytic performance of doped OMCs in the nitrobenzene reduction

Linear Sweep Voltammetry (LSV) is typically used to obtain the first ranking of different electrocatalysts in terms of activity (onset potential and generated current density) for a specific reaction, which in this case is the reduction of nitrobenzene. LSV experiments were performed in a half cell setup containing 5 mM nitrobenzene in 0.3 M $HClO_4$ in ethanol. The potential of the working electrode was varied from -0.2 to -1.8 V vs. Fc^+/Fc at four different rotation speeds (500 to 2000 rpm, Fig. S6.2 to S6.5).

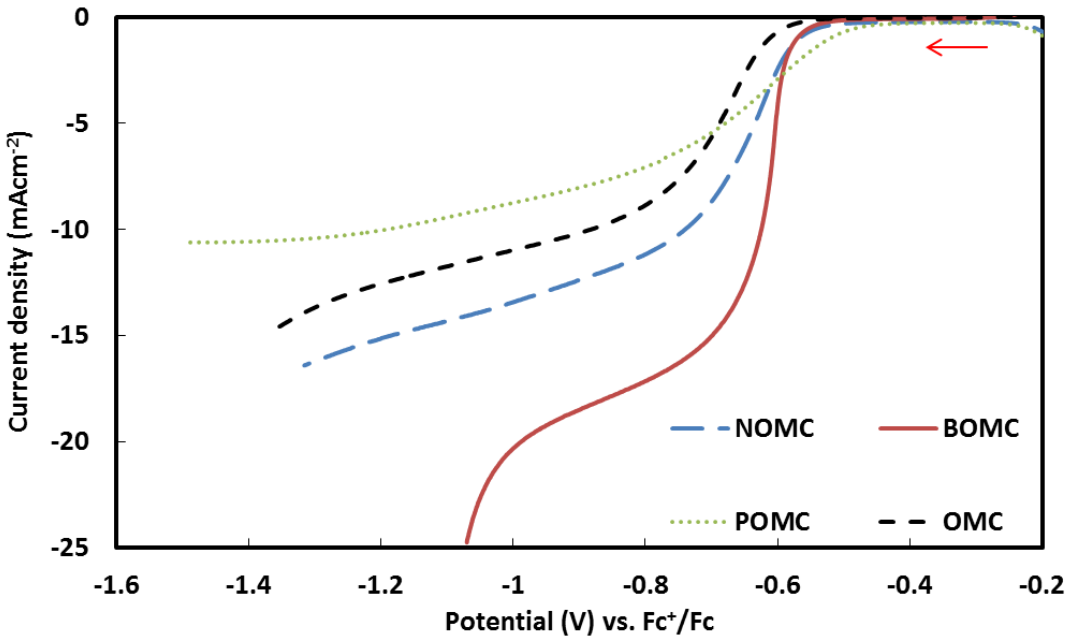

Figure 6.2: LSV plots of NOMC, BOMC, POMC and OMC, recorded in 5 mM nitrobenzene and 0.3 M $HClO_4$ in ethanol at a scan rate of 5 mVs^{-1}, with a rotation speed of 2000 rpm and corrected for the iR drop.

Based on the LSV results (Fig. 6.2 and Table 6.3, column 4), two main observations can be made about the four investigated electrocatalysts. First of all, the onset potential tends to shift to more positive values in the order BOMC to OMC to NOMC to POMC. Since a more positive onset potential corresponds to a lower overpotential, the reaction over the POMC involves a lower activation energy, which means that its sites are more active in initiating the reduction of nitrobenzene. On the other hand, BOMC displays the most negative onset

potential, but leads to the highest current density, followed by NOMC, OMC and POMC. This signifies that the active sites in BOMC, although less easily activated, lead to faster reaction kinetics, resulting in a faster reduction. NOMC and OMC display intermediate values for onset potential and current density. Finally, for all the electrocatalysts the absence of a clear plateau in the LSV curves suggests that more than one chemical is produced at the same time over these kind of materials. This first set of results demonstrates that doping of OMC has a marked influence on the electrocatalytic behaviour of the materials.

However, the results discussed so far, do not include any data or indication on the selectivity of the electrocatalysts. To gain information on the selectivity, Koutécky-Levich (K-L) plots were constructed based on the data from the LSV experiments performed at different rotations and on the equation below (Eq. 6.2):

$$\frac{1}{J} = \frac{1}{J_K} + \frac{1}{J_D} = \frac{1}{nFkC_0} + \frac{1}{0.62nFC_0D_0^{3/2}\nu^{-1/6}\omega^{1/2}} \qquad \text{Eq. (6.2)}$$

where I is the recorded current, which consists of a kinetic factor (J_K) and a diffusion-limited current density (J_D), *n* is the number of transferred electrons, F is the Faraday constant, k is the electron transfer rate constant, C_0 is the concentration of nitrobenzene in the bulk (5 x 10^{-6} mol cm^{-3}), v is the kinematic viscosity of the electrolyte (0.0152 cm^2 s^{-1}), D_0 is the diffusion coefficient (4.7 x 10^{-6} cm^2 s^{-1}) and ω is the rotation speed of the rotating disk electrode.[24] The electrode surface area, used to determine the current densities, was taken as equal to the geometrical surface area of the glassy carbon electrode disk since the real surface area could not be determined, as a consequence of the porosity of the applied electrocatalysts. The Koutécky-Levich plots for the NOMC electrocatalyst is presented in Figure 6.2, those for the other materials can be found in the ESI (S6.6 to S6.8).

Based on these plots and on Eq. 6.2, it is possible to determine *n* from the slope and the kinetic current density (J_K) from the intercept. The number of exchanged electrons allows evaluating the selectivity of the reaction. To have a high selectivity towards aniline, the value for *n* should be as close as possible to 6 (see Scheme 6.1). The kinetic current density is a measure of the activity of the electrocatalysts. Particularly, when comparing two electrocatalysts for which the number of exchanged electrons is the same, a higher kinetic current density can only be a consequence of a higher electron transfer rate constant.

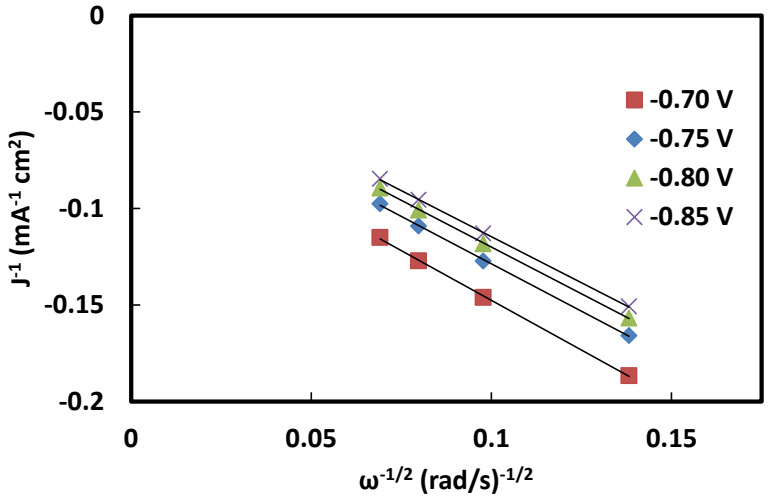

Figure 6.3. Koutécky-Levich plots (J^{-1} vs. $\omega^{-1/2}$) of NOMC at a potential interval from -0.70 to -0.85 V vs. Fc^+/Fc.

The similarity of the slopes in the K-L plot (Fig. 6.3) indicates that the value for *n* remains almost constant in the investigated potential window, which implies that the selectivity of the reduction reaction does not change significantly in this potential range. The values for *n*, J_K, onset potential and half-wave potential are summarised in Table 6.3 for the electrocatalysts under investigation. The half-wave potential ($E_{1/2}$) is correlated both with the onset potential and the current density: a more positive value is the result either of a higher kinetic current density (as in the case of BOMC) or of a more positive onset potential (as in the case of POMC). The fact that $E_{1/2}$ for NOMC, BOMC and POMC are very similar is thus caused by different factors in each case. This also implies that a more balanced and detailed evaluation of the activity of these electrocatalysts can be obtained on the basis of the onset potentials and of the kinetic current densities, rather than of the half-wave potentials.

Table 6.3. Summary of the electrocatalytic performance of the different OMC electrocatalysts. Note: the reported values are the average of at least 2 measurements. The standard deviations are SD(*n*) ≤ 0.3, SD(J_K) ≤ 0.7 mA cm^{-2}, SD(E_{onset}) = 0.01 V and SD($E_{1/2}$) = 0.01 V.

Electrocatalyst	*n* @ -0.75 V	J_K @ -0.75 V (mA cm^{-2})	Onset potential (V)	Half-wave potential (V)
NOMC	6.0	-33	-0.31	-0.62
BOMC	7.5	-110	-0.39	-0.61
POMC	5.8	-9.5	-0.24	-0.62
OMC	6.0	-16	-0.37	-0.67

Comparing the results summarised in Table 6.3, it can be concluded that the best electrocatalyst that was produced in this study is NOMC, since the average number of transferred electrons (*n* = 6.0) suggests an excellent selectivity to aniline, and the activity in terms of current density is much higher compared to the other two electrocatalysts for which *n* is also around 6, *i.e.* POMC and OMC. BOMC reaches the highest kinetic current densities but its selectivity is expected to be inferior due to the too high value of *n*, which suggests that aniline is partially reduced further to cyclohexylamine (Scheme 6.1). It is also worth noting that OMC, which was prepared without a doping element as B, N or P, still displays a relevant activity in the reduction of nitrobenzene.

6.3.2 Correlation between electrocatalytic behaviour and physicochemical properties

The physicochemical properties of the OMC materials that are expected to have a major influence on their electrocatalytic performance in the reduction of nitrobenzene are: (1) the nature of the dopant element, its content and configuration, (2) the surface area and pore size of the material and (3) the degree of carbonisation.[153] The latter can be estimated by Raman spectroscopy, which also provides information about the amount of defects and disordered structures in the material. After deconvolution of the Raman spectra (Table 6.4 and Fig. 6.4 and S6.9), four broad peaks could be distinguished: (i) a peak at 1200 cm^{-1}, attributed to aliphatic species, (ii) a peak at 1350 cm^{-1}, usually referred to as the D-band, which is correlated with defects at the edges of the graphitic domain, (iii) a peak at 1510 cm^{-1} (A-band), originating from heteroatoms or five-membered rings and, (iv) a peak at 1600 cm^{-1} (G-band), which is assigned to C=C vibration modes in an ideal graphitic plane.[153] The presence of the latter is thus a clear indication of the formation of a graphitic carbon structure.[153] Compared to an ideal graphene lattice, this peak is slightly shifted to lower

wavenumbers. This blue shift is a consequence of the electron delocalisation caused by the incorporation of dopant elements inside the carbon framework.[230]

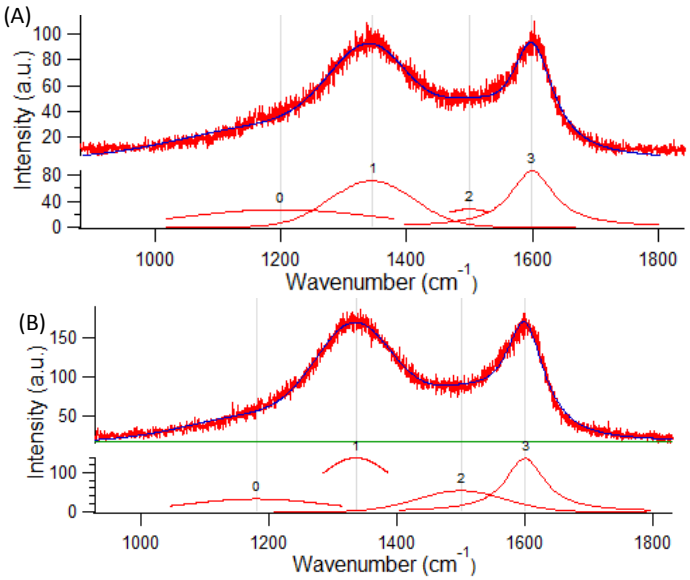

Figure 6.4. Deconvoluted Raman spectra of BOMC (A) and POMC (B). The Raman spectra of NOMC and OMC can be found in Fig. S6 in the ESI.

Table 6.4. Summary of parameters determined by deconvolution of the Raman spectra.

Sample	A_D/A_G	FWHM D-band	Area % of A-band
NOMC	1.16	141	15
BOMC	1.05	123	10
POMC	1.35	145	17
OMC	1.10	134	14

The ratio between the areas of the D and the G band (A_D/A_G) is thus inversely proportional to the degree of carbonisation. Another factor that corresponds to a higher degree of carbonisation is a lower full-width at half-maximum (FWHM) of the D-band. Finally, also a smaller area of the A-band can be linked with a higher degree of order.[153,224,241] The values of these parameters for the studied OMC materials are reported in Table 6.4. The incorporation of boron results in the highest degree of carbonisation, and the A_D/A_G, $FWHM_{D\text{-band}}$ $A_{A\text{-band}}$(%) values of BOMC are even lower compared to those of the OMC material, which was prepared without adding any dopant. It is inferred that the presence of boron promotes the formation of a graphitic carbon structure, in agreement with the observations reported by Choi and co-workers.[85] Moreover, the lower dopant content in BOMC compared to POMC and NOMC observed by XPS (Table 6.2) is also likely to have played a role in the higher carbonisation degree of BOMC. This can be understood considering that the doping elements have different size from C atoms and thus create defect sites. Additionally since the difference in size between phosphorus (106 pm) and carbon (77 pm) is much larger than that between boron (82 pm) or nitrogen (75 pm) and carbon, phosphorus tends to be located slightly above the carbon framework. This results in a more distorted structure and, therefore, can account for the lowest degree of carbonisation observed for POMC (*i.e.* for the highest values for each of the parameters in Table 6.4).[285]

The specific surface areas of all the materials synthesised in this work are high, ranging from 755 m^2 g^{-1} for NOMC to 1092 m^2 g^{-1} for POMC (Table 6.1). All materials have the desired narrow pore size distribution in the mesoporous range (average pore size between 2.7 nm for POMC to 4.0 nm for BOMC – see Table 6.1 and Figure 6.1 and S6.1). These features are expected to grant a good accessibility of the active sites of the electrocatalysts. When comparing the different OMC materials, no specific correlation was found between these structural and textural properties and the electrocatalytic performances. This suggests that even the lowest surface area of the series (NOMC) is sufficiently high to guarantee an optimum accessibility of the active sites, and that for these OMC materials the nature of the doping elements and the carbonisation degree become the factors determining the differences in catalytic behaviour.

Characterisation by XPS did not only provide information about the loading of each doping element in BOMC, NOMC and POMC (*vide supra*) but also evidenced that all the prepared materials display a significant content of oxygen, which most likely originates from the exposure of the electrocatalysts to air during the thermal treatments. The O content varies from 5.5 wt% in BOMC up to 18 wt% in POMC (Table 6.2). It can be inferred that O atoms are more readily incorporated in OMCs with a lower degree of carbonisation (BOMC has the highest and POMC the lowest degree of order - see Table 6.4) as a consequence of the preferential incorporation of oxygen at the edges or at defect sites.[80,286] It is also worth mentioning that even in the absence of N during the synthesis, a small fraction of N was found in BOMC, POMC and OMC (Table 6.2). This is most likely due a minor contamination from previous uses in the tubes used for the pyrolysis step.

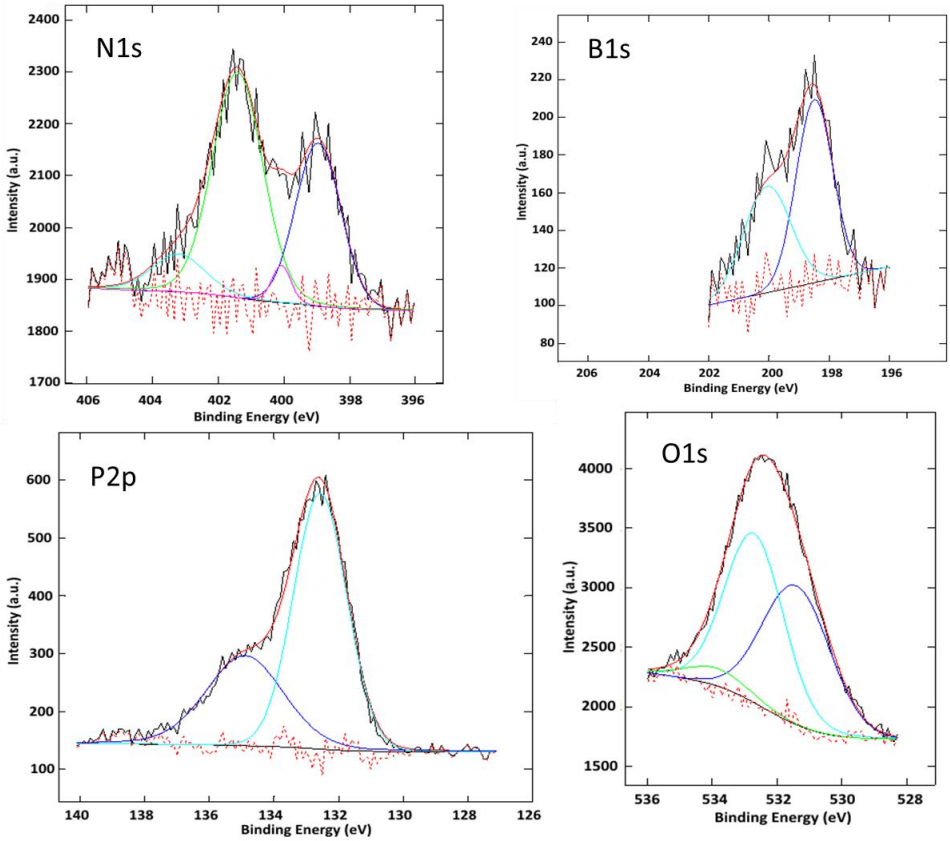

Figure 6.5. Deconvoluted high resolution N1s (NOMC), B1s (BOMC), P2p (POMC) and O1s (OMC) XPS signals.

XPS also provides valuable information about the configuration of the different elements, which is expected to play a role in defining the electrocatalytic behaviour of the OMC materials. The configurations are obtained by deconvoluting the high resolution signals characteristic of each element (Fig. 6.5). The N1s signal is generally deconvoluted into four individual peaks that are attributed to pyridinic N (≈398.7 eV), pyrrolic N (≈400.5 eV), graphitic N (≈401.9 eV) and oxidised pyridinic N (> 402.8 eV).[153,285] In the NOMC material, the largest fraction of N substituted carbon in the sp^2-C plane (graphitic N, 54%), followed by pyridinic N (33%), oxidised pyridinic N (9.8%) and pyrrolic N (3.3%). The oxidised pyridinic N species originate from exposure to air of the pyridinic N sites. The B1s signal of BOMC could be deconvoluted into two peaks, at 200.5 eV (39%) and at 198.5 eV (61%), which are assigned to graphitic B (or boron replacing carbon in hexagonal rings) and to B located in the conjugated π-system but at internal defects or edges (see Scheme 6.2).[287] The latter bears a resemblance to borabenzene, which is a strong Lewis acid. The P2p signal of POMC was deconvoluted into two distinct peaks, one assigned to the P-C bonds (132.6 eV, 64%) and one to P-O bonds (134.9 eV, 36%), in line with the relatively high O content observed in this material. Phophorus can be found either in the bulk of the carbon structure or at the edges, although in the latter location P is expected to be prone to oxidation.[288,289] The P-O configuration is generally attributed to oxidised P atoms that originate from exposure to air of the P sites in the carbon structure, or to $-PO(OH)_2$ functional groups (see Scheme 6.2).[284,288,289]

Table 6.5. Oxygen configuration of the different electrocatalysts as determined by deconvolution of the O1s XPS spectra. [a] C-O and P-O species; [b] C=O and P=O species.

	% C-O	% C=O	% O-C=O
NOMC	77	18	4.8
BOMC	59	29	12
POMC	85[a]	12[b]	3.3
OMC	76	15	5.5

Finally, the O1s XPS signals were deconvoluted for all the studied materials (Fig. 6.5 and Fig. S6.10 in the ESI). In all cases, three distinct peaks were found: one for C-O species (531.5 eV), one for C=O species (532.6 eV) and a final one for O-C=O species (533.8 eV).[34] For POMC, the peak at 531.5 eV can also be due to P-O species and the peak at 532.6 eV to P=O species.[153,290] The actual presence of these P-O and P=O is strongly supported by the P-O peak that was observed in the P2p signal. For all materials, the C-O species make up the largest fraction, followed by C=O and O-C=O (Table 6.5).

The results of the detailed characterisation of the OMC materials allow explaining the performance of the different electrocatalysts in the reduction of nitrobenzene. The electrocatalytic activity of carbon materials doped with P, B or N is generally attributed to the local disruption of the electroneutrality of pure carbon materials.[177] The difference in electronegativity between dopant element and the neighbouring carbon atoms leads to the creation of a partial positive charge on the more electropositive elements and of a partial negative charge on the more electronegative elements. The positively charged sites can act as catalytic sites by interacting with nitrobenzene and thus promoting its subsequent reduction.[153,187,285] B and P are more electropositive than C whereas N is more electronegative. Therefore, each dopant element is expected to have a distinct effect on the electrocatalytic performance of the doped OMCs. First of all, phosphorus and nitrogen

significantly shift the onset potential to more positive values compared to the undoped OMC (oxygen incorporation is not considered as doping in this context). On the other hand, boron-doping generates an electrocatalyst with a higher overpotential (*i.e.* more negative onset potential). An explanation for this behaviour could be found in the ease of accessibility of the active sites (carbon atoms next to dopant atoms or dopant atoms themselves). In the case of phosphorus, the carbon framework is slightly distorted due to the mismatch in size between phosphorus and carbon.[291] Therefore, the active sites are located slightly out of plane compared to the surrounding carbonaceous structure and this can make them more easily accessible for the adsorption of nitrobenzene. Also pyridinic and pyrrolic N (and the C atoms neighbouring them) should be relatively easily accessed since these N configurations are found at the edges or defects of the graphitic lattice. On the other hand, since the most easily accessible B sites are strong Lewis acids, they are most likely coordinated to ethanol, which will have to be removed prior to the start of the nitrobenzene reduction reaction. We propose this extra step to be the reason for the higher overpotential observed over BOMCs.[285,287] Differently from the B-, N- and P-doped materials, the activity of the undoped OMC cannot be attributed to the local disruption of the electroneutrality of the bulk carbon since oxygen only gets incorporated in functional groups and not into the graphitic structure. This typically implies that undoped OMC electrocatalysts display low activity, which mainly originates from defect and edge sites.[286] The trend of kinetic current density is totally different from that observed for the onset potentials: boron tends to generate very active sites, leading to much higher reaction rates (higher J_K) over BOMC compared to the other OMC systems. A straightforward explanation for this behaviour could be that BOMC has the highest number of active sites or the highest value for the number of exchanged electrons. The latter is true (n = 7.5, see Table 6.3), but the difference compared to the other electrocatalysts is not such as to justify the remarkably higher kinetic current density observed for BOMC (Table 6.3). It is difficult to estimate the number of active sites in the doped OMC materials because the activity does not only depend on the dopant content but also on its configuration. However, the fact that BOMC displays the highest kinetic current density while having the lowest dopant content (Table 6.2) suggests that both configurations of B observed by XPS are highly active sites for nitrobenzene reduction. The trends in kinetic current density can be rationalised considering the difference in the partial positive charge density that is generated on B, P or C (in the case of N-doping) and taking into account that the larger is the partial positive charge, the faster the reduction is expected to proceed.[153,285] From theoretical calculations performed in the literature, the partial positive charge decreased from 0.62 on B to 0.28 on C (next to N) to 0.21 on P.[180,291,292] This trend is in line with the observed trends in kinetic current density (Table 6.3). Another factor that most likely contributed to the high J_K over BOMC is its higher carbonisation degree, proven by Raman spectroscopy. A highly graphitic material is more conductive compared to materials with a lower degree of carbonisation, therefore, its electron transport is faster and a faster reduction rate can be achieved.[153] The second highest kinetic current density among the studied OMC electrocatalysts was observed with NOMC (Table 6.3). This is fully in line with the partial positive charge generated by N-doping (see above) and the degree of carbonisation of NOMC estimated by Raman spectroscopy (see Table 6.4), which are both characterised by intermediate values between those of BOMC and POMC. The undoped OMC displayed only moderate activity compared to BOMC and NOMC, but the observed kinetic current is actually slightly higher than that found over POMC (Table 6.3). This is a somewhat unexpected result because the only heteroatom in this material is oxygen, which cannot be incorporated into the graphitic carbon lattice. Therefore, the activity of undoped OMC materials is typically

attributed to defect and edge sites devoid of oxygen, [286] though the possibility of contribution of some of the O-containing functional groups (e.g. phenol) cannot be excluded. The higher J_K found over OMC compared to POMC can be also related to the higher degree of carbonisation and thus the higher electron conductivity of the former.[285]

Most of the studied electrocatalysts (NOMC, POMC and OMC) promoted the reduction of nitrobenzene by transferring the number of electrons that is expected for the selective formation of the desired aniline as product (n = 6). Only BOMC led to a higher average number of exchanged electrons (n = 7.5). This strongly suggests a further reduction of aniline with formation of cyclohexylamine (*vide infra*). This is most likely due to the large partial positive charge generated by boron-doping, which can cause the formed aniline to remain adsorbed on the electrocatalyst surface and thus to undergo further reduction. A similar behaviour was also observed in the oxygen reduction reaction.[96] This effect can be also understood considering that the B-doped sites are expected to bear a resemblance to aromatic compounds containing boron atoms (e.g. borabenzene), which are known to display Lewis acid character and which thus tend to form stable adducts with a Lewis base as aniline.

6.3.3 Cyclic voltammetry and chronoamperometric study of BOMC and NOMC

The two most promising electrocatalysts identified in the LSV study, *i.e.* NOMC and BOMC, were investigated further by means of cyclic voltammetry and chronoamperometry. The former technique allows studying another parameter that is important in view of a practical application of the electrocatalysts: the stability under operating conditions. This parameter was evaluated by comparing the current density of the second cycle (after initial stabilisation) with the 1000th cycle (Fig. 6.6). The rather small difference in current density after 1000 cycles, indicates a good degree of stability of the electrocatalysts under the employed conditions. This is a promising feature in view of a possible application in a fuel cell for the cogeneration of aniline and electricity.

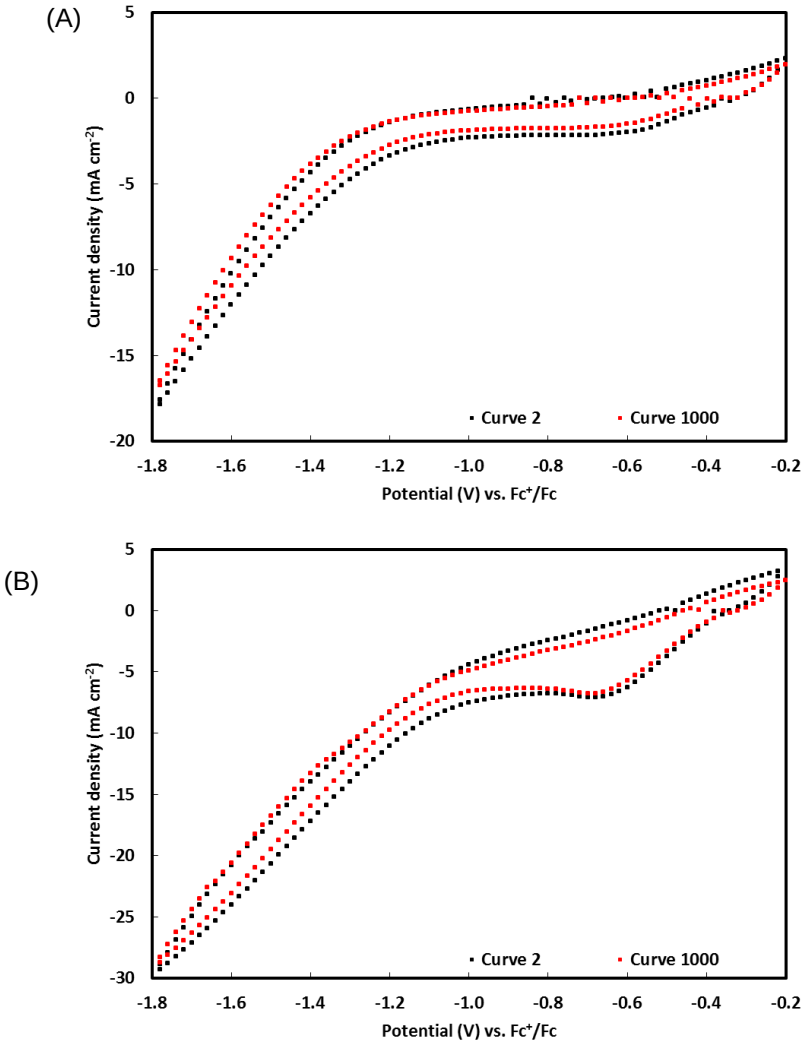

Figure 6.6. Stability test of (A) NOMC and (B) BOMC by cyclic voltammetry. The potential was cycled between -0.2 and -1.8 V vs. $Fc/^{+}Fc$ at a scan rate of 100 mVs^{-1}. Only the second (after initial stabilisation) and the last curve are presented here. After 999 cycles, the measurement was paused and the solution was stirred to ensure a homogeneous nitrobenzene concentration throughout the medium. Afterwards, the last scan was measured.

The chronoamperometric study provides very important information about the activity and selectivity of the electrocatalysts on the basis of the GC analysis of the reaction medium at the end of the experiment (Table 6.6). The nitrobenzene conversion achieved over NOMC (46%) is significantly higher than that over BOMC (30%) as a consequence of the lower current generated over the latter throughout the experiment. This trend is opposite to what would be expected based on the LSV study, in which higher current was generated over BOMC (Fig. 6.2 and Table 6.3). Careful control experiments confirmed the correctness of these trends. The only difference in the experimental conditions was the concentration of nitrobenzene, which was 5 mM in the LSV tests and 15 mM in hte chronoamperometric study. To investigate the observed behaviour in more detail, additional LSV measurements at higher nitrobenzene concentrations (15 and 30 mM) were performed (Fig. S6.11). From these plots it could be observed that the increase in current density for NOMC at higher concentrations is more pronounced than for BOMC, suggesting the presence of diffusion limitations in the pores for NOMC at low concentration. Since the average pore size of BOMC is larger than that of NOMC (see Fig S6.1), it is possible that NOMC, but not BOMC,

is affected by diffusion limitations at a 5 mM nitrobenzene concentration. Increasing the nitrobenzene concentration results in a larger concentration gradient and thus a larger driving force for the diffusion of nitrobenzene. Since the achieved current densities with NOMC are larger than those achieved with BOMC at these higher concentrations, it can be expected that NOMC no longer suffers from diffusion limitations as a consequence of the increased concentration gradient. Therefore, a larger fraction (or all) of the active sites of NOMC will be utilised under these conditions, resulting in a larger current density when compared to BOMC.

The conversion values obtained from the GC analysis were also confirmed with Faraday's law, which gives 46 and 29% for NOMC and BOMC, respectively. The product distributions observed at the end of the chronoamperometric test are reported in Table 6.6. The difference in selectivity between NOMC and BOMC evidenced by the different *n* values obtained from the K-L analysis was confirmed by chronoamperometry. NOMC achieved the expected and desired high selectivity towards aniline (87%), whereas BOMC only reached a selectivity of 37% towards aniline. In accordance with its higher value for *n*, further reduction of aniline to cyclohexylamine was observed over BOMC (selectivity of 37%). Besides a lower selectivity to aniline, BOMC also results in a larger fraction of side-products, including: nitrosobenzene (two-electron reduction), azoxybenzene and para-ethoxyaniline. The latter two side-products are obtained through non-electrochemical conversions of the unstable intermediate phenylhydroxylamine, which could not be detected by means of GC.[23–25,245–247]

Table 6.6. Results of GC analysis after chronoamperometry experiment performed for 52 h at -0.75 V vs. Fc^+/Fc in 15 mM nitrobenzene in 0.3 M $HClO_4$ ethanolic solution.

	NOMC	BOMC
Conversion	46%	30%
Selectivity		
Aniline	87%	37%
Cyclohexylamine	0.0%	37%
Nitrosobenzene	3.6%	13%
Para-ethoxyaniline	5.4%	4.0%
Azobenzene	0.4%	1.0%
Azoxybenzene	3.3%	7.7%

In summary, NOMC was identified as the most promising electrocatalyst for the reduction of nitrobenzene based on the combination of its activity, selectivity and stability, which enabled to reach 46% conversion with 87% selectivity towards the desired aniline after 52h. Only one other metal-free electrocatalyst for nitrobenzene reduction has been reported in the literature (N-doped diamond).[251] However, the comparison with the performance of our NOMC is made virtually impossible by the extremely different and much less challenging conditions used in the literature report, in which the aim was to remove nitrobenzene pollution from a solution and for which purpose much lower nitrobenzene concentration (0.81 mM vs. 15 mM in this work) and much higher electrode surface area (400 mm^2 vs. 20 mm^2) were employed. On the other hand, the performance of our NOMC can be compared to the state-of-the-art non-noble metal-containing electrocatalysts for this reaction, which were tested under analogous conditions.[24,25] NOMC achieved a similar activity but a much better selectivity towards the aniline compared to Cu-Cu_xO nanoparticles supported on carbon nanotubes or on activated carbon. This was demonstrated both by the increased *n* value (from 4 to 6) and by the much higher aniline selectivity measured in the chronoamperometric

tests. The high selectivity towards aniline is highly promising in the perspective of application of NOMC in a fuel cell for the cogeneration of this industrially relevant product and electricity.

6.4 Conclusions

Ordered mesoporous carbons doped with boron, nitrogen or phosphorus were synthesised, thoroughly characterised and tested as electrocatalysts for the cogeneration of aniline and electricity in a half-cell setup. The developed nanocasting synthesis methods using SBA-15 silica as hard template were successful in producing the targeted mesoporous materials with high surface area (up to 1092 m^2/g), uniform pore sizes and containing the desired doping elements. The performance of the electrocatalysts was ranked on the basis of their onset potential, kinetic current densities and number of exchanged electrons. Remarkably, the ranking of the different materials differed for each parameter. Based on the onset potential, POMC emerged as the best material. On the other hand, BOMC outperformed the other materials when the kinetic current density is evaluated. Finally, NOMC and OMC reached the highest selectivities to aniline, based on the number of exchanged electrons. Combining the different catalytic properties, NOMC was identified as the material with the best electrocatalytic performance in the target reaction. In a chronoamperometry test, this electrocatalyst achieved a conversion of 46% with a selectivity of 87% towards aniline after 52 h of reaction at -0.75 V vs. Fc^+/Fc in 0.3M $HClO_4$ at room temperature. This corresponds to the highest yield and selectivity ever reported for the electrochemical reduction of nitrobenzene under comparable conditions. In conclusion, NOMC was identified as a relatively inexpensive material (estimated cost: 22 EUR g^{-1})[293] with promising electrocatalytic performance for the perspective application in a fuel cell allowing the cogeneration of electricity and aniline, as a valuable commodity product. The estimated cost of NOMC is slightly lower compared to the Me-PANI-AC-A electrocatalysts, reported in Chapter 5, (22 EUR g^{-1} for NOMC vs. 26 EUR g^{-1} for Cu-PANI-AC-A[293]), further underlying the benefits of the metal-free materials. Future work should aim at improving further the electrochemical conversion of the doped OMC electrocatalysts, which might be achieved by increasing the number of available active sites by using dopant precursors with a higher N/C atomic ratio.

Supporting information

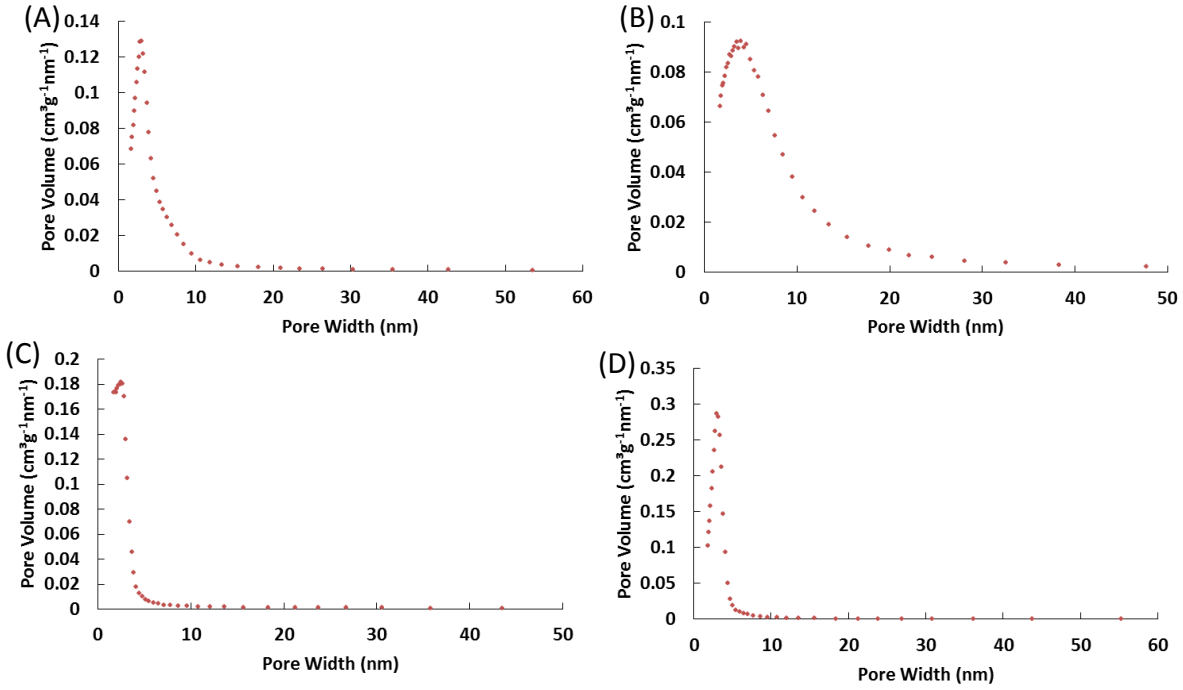

Figure S6.1. Pore size distribution curves of NOMC (A), BOMC (B), POMC (C) and OMC (D).

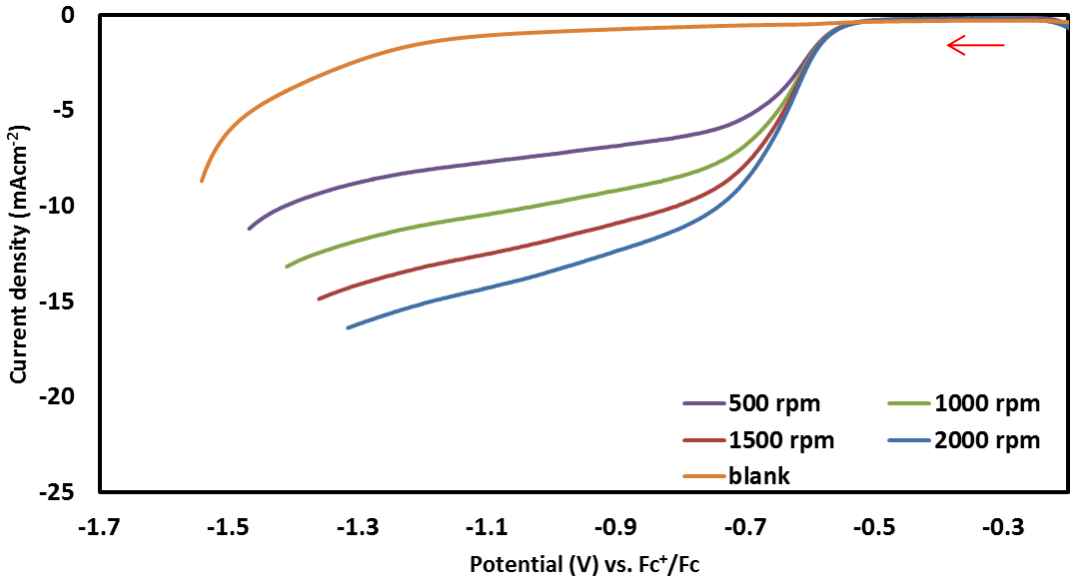

Figure S6.2. LSV plots of NOMC recorded in 5 mM nitrobenzene in 0.3 M $HClO_4$ in ethanol at a scan rate of 5 mVs^{-1} at different rotation rates and corrected for the iR drop.

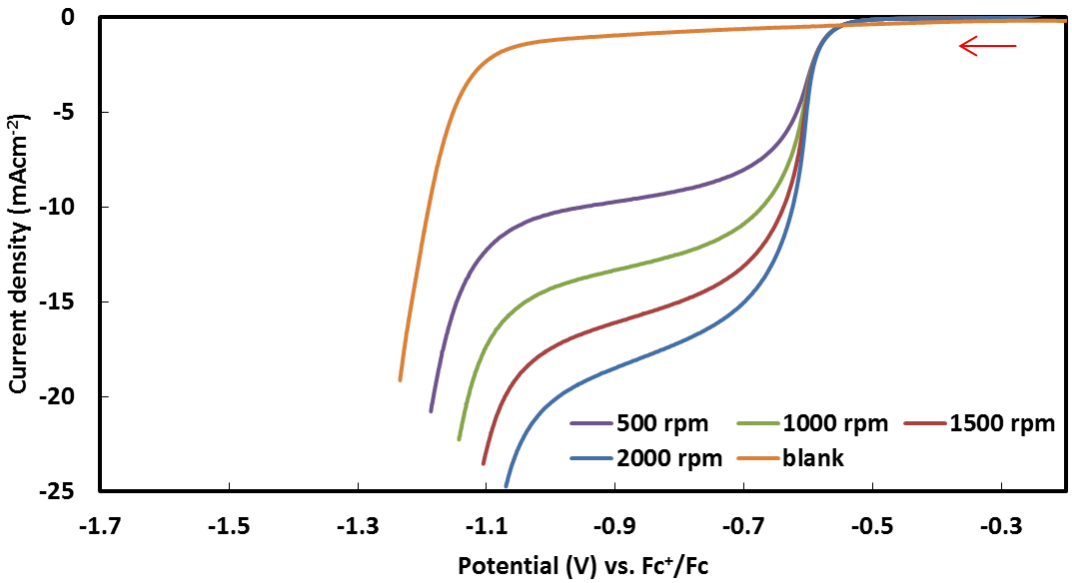

Figure S6.3. LSV plots of BOMC recorded in 5 mM nitrobenzene in 0.3 M $HClO_4$ in ethanol at a scan rate of 5 mVs^{-1} at different rotation rates and corrected for the iR drop.

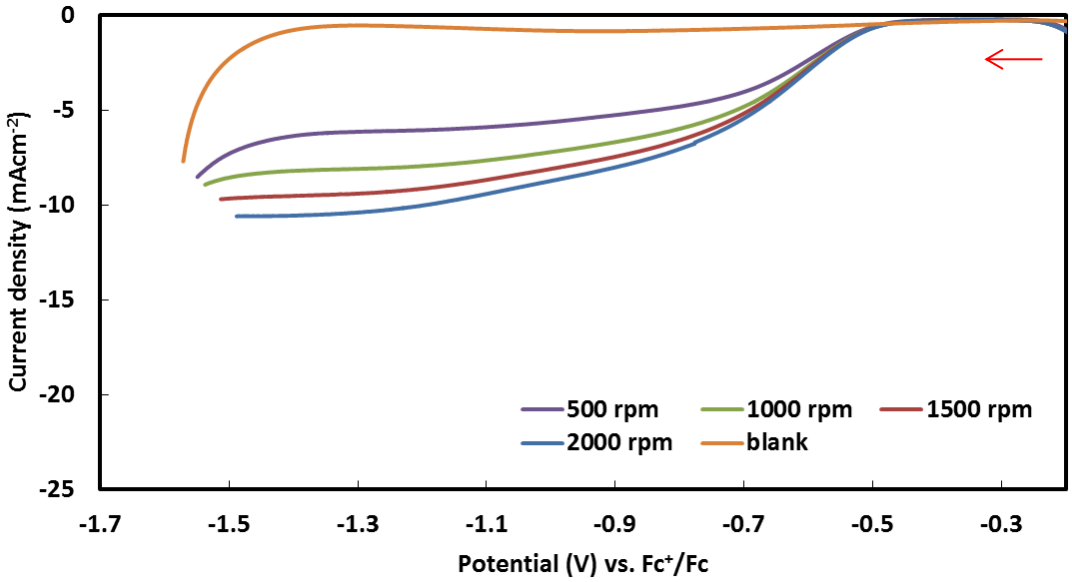

Figure S6.4. LSV plots of POMC recorded in 5 mM nitrobenzene in 0.3 M $HClO_4$ in ethanol at a scan rate of 5 mVs^{-1} at different rotation rates and corrected for the iR drop.

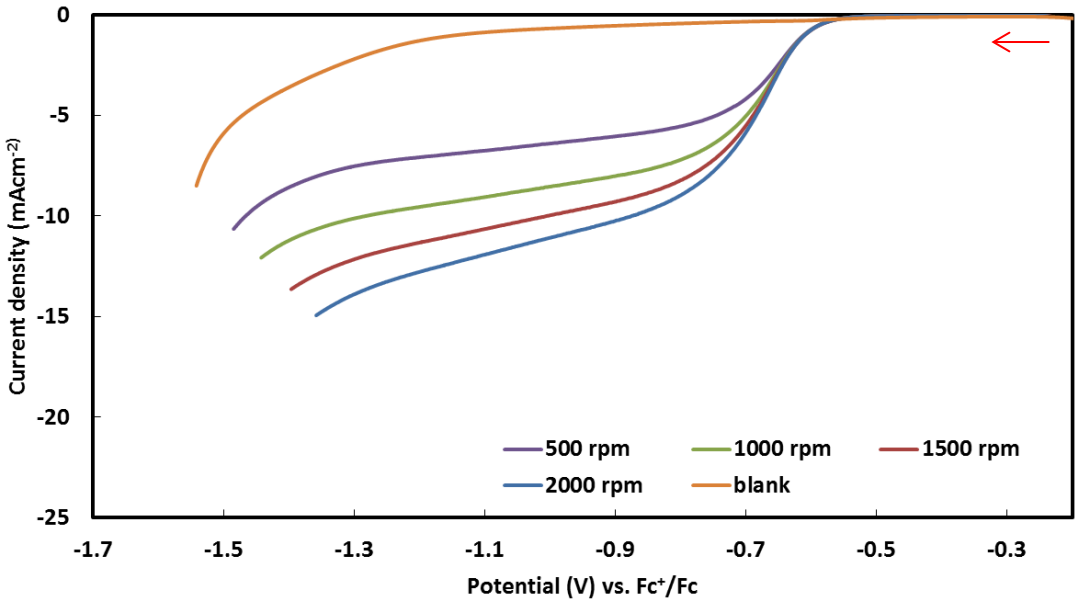

Figure S6.5. LSV plots of OMC recorded in 5 mM nitrobenzene in 0.3 M $HClO_4$ in ethanol at a scan rate of 5 mVs^{-1} at different rotation rates and corrected for the iR drop.

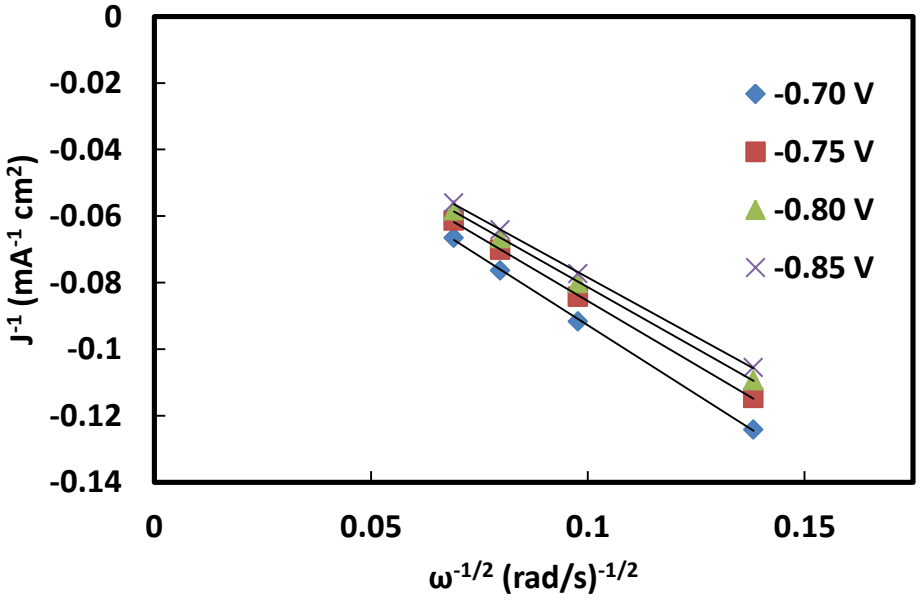

Figure S6.6. Koutécky-Levich plots (J^{-1} vs. $\omega^{-1/2}$) of BOMC at a potential interval from -0.70 to -0.85 V vs. Fc^{+}/Fc.

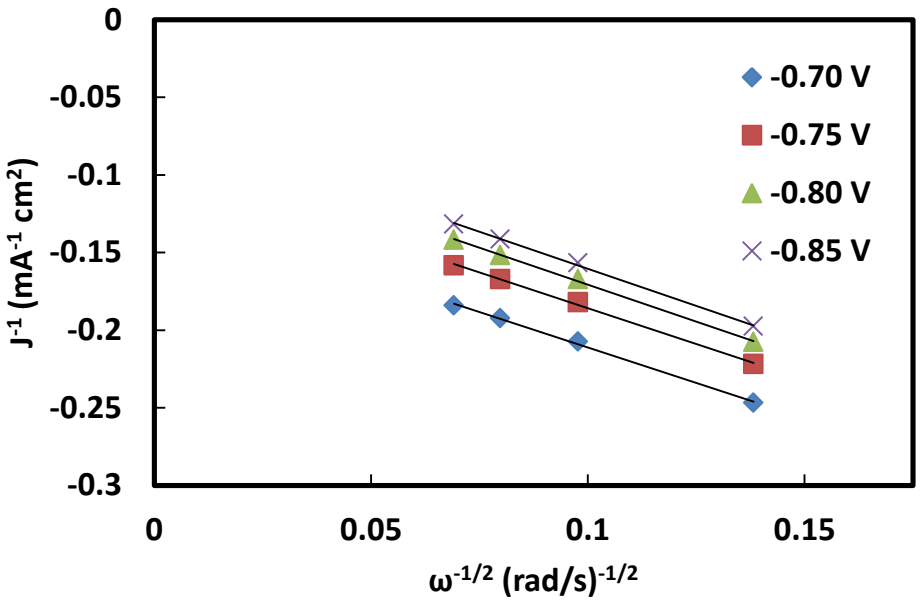

Figure S6.7. Koutécky-Levich plots (J^{-1} vs. $\omega^{-1/2}$) of POMC at a potential interval from -0.70 to -0.85 V vs. Fc^{+}/Fc.

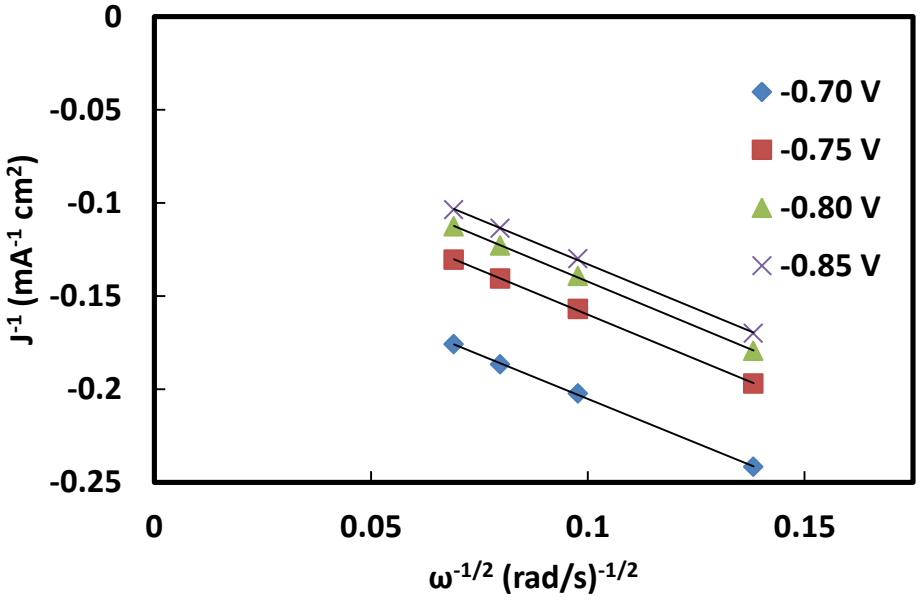

Figure S6.8. Koutécky-Levich plots (J^{-1} vs. $\omega^{-1/2}$) of OMC at a potential interval from -0.70 to -0.85 V vs. Fc^{+}/Fc.

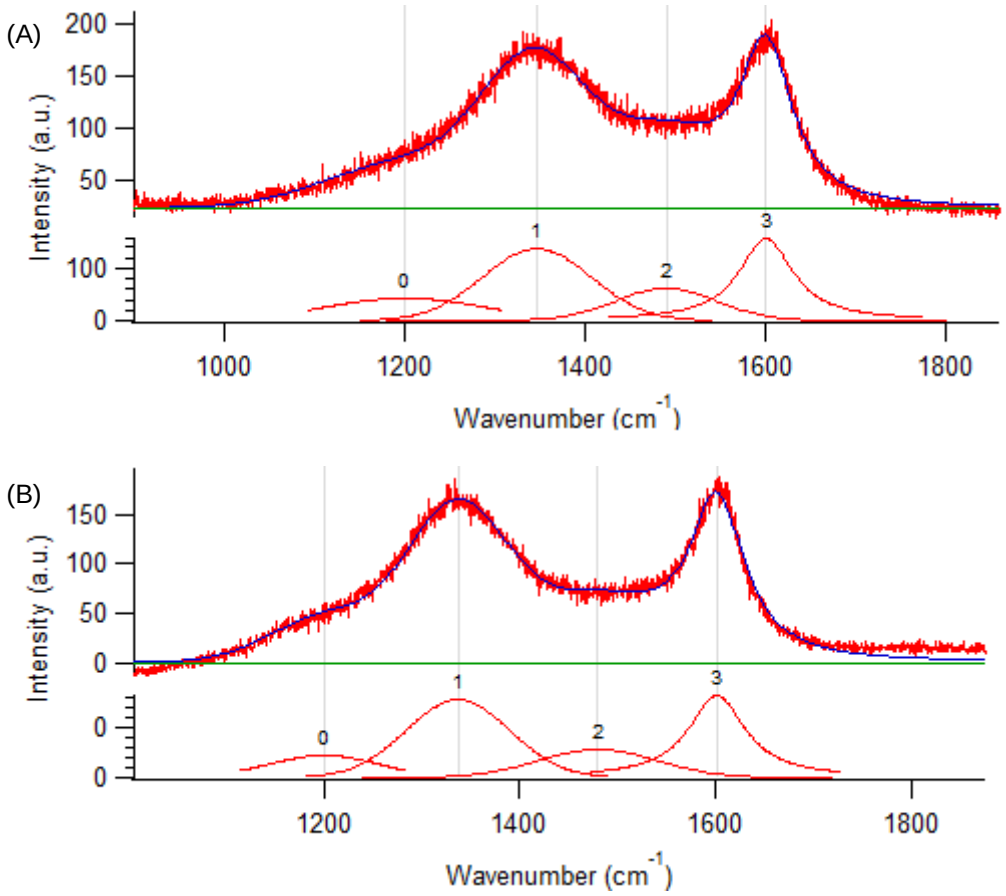

Figure S6.9. Deconvoluted Raman spectra of NOMC (A) and OMC (B).

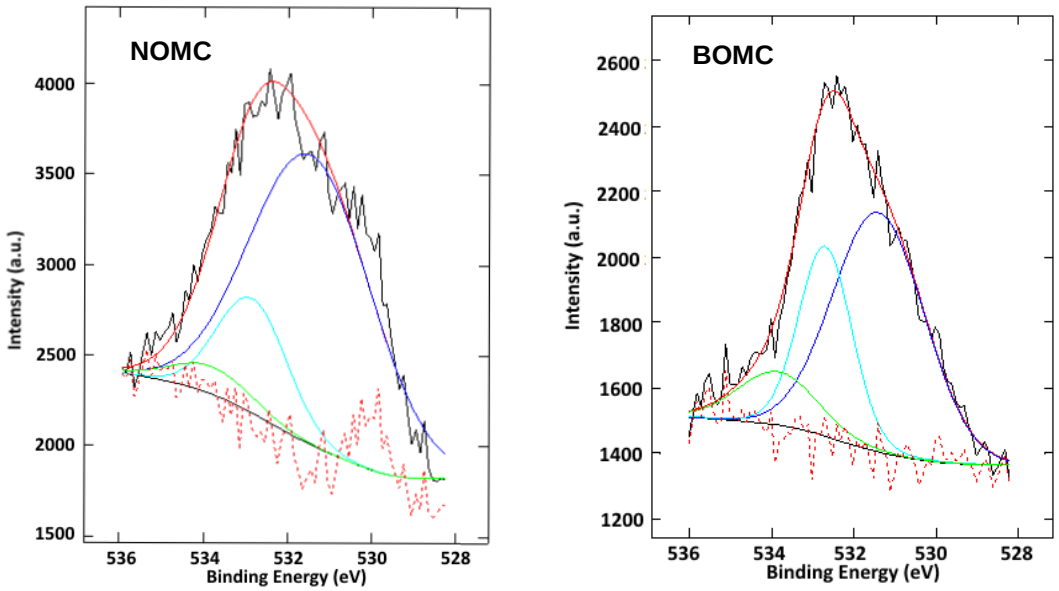

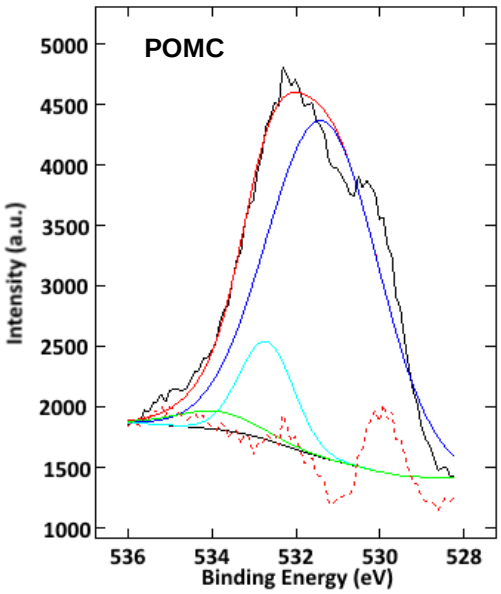

Figure S6.10. Deconvoluted high resolution O1s XPS signals of NOMC, BOMC and POMC.

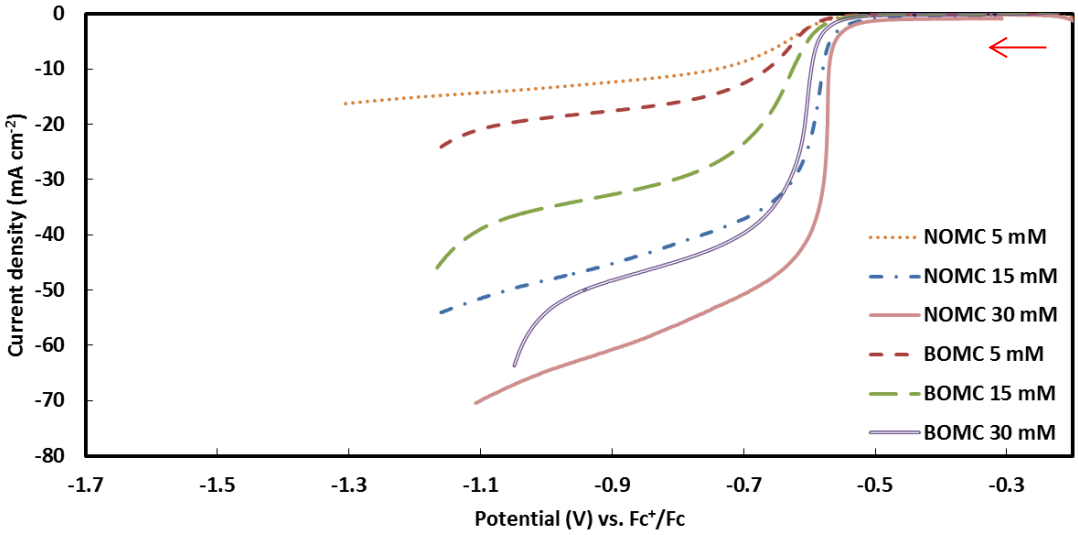

Figure S6.11 LSV plots of NOMC and BOMC, recorded at different concentrations of nitrobenzene (5, 15 and 30 mM) in 0.3 M $HClO_4$ in absolute ethanol at a scan rate of 5 mVs^{-1}, with a rotation speed of 2000 rpm and corrected for the iR drop.

Chapter 7

Optimisation of the synthesis of polyvinylidene membranes grafted with sulphonated polystyrene for application as proton-exchange membranes

Abstract

The synthesis of polyvinylidene membranes grafted with sulphonated polystyrene (PVDF-g-PSSA) was optimised to tune the properties of the material towards application as proton-exchange membrane (PEM) in a fuel cell. The synthesis involves three reaction steps, dehydrofluorination to generate double bonds in the parent PVDF membrane, grafting with polystyrene and sulphonation of these polystyrene chains with chlorosulphonic acid. The change in hydrophobicity and membrane charge was investigated after each step by contact angle and zeta-potential measurements, respectively. The homogeneous distribution of sulphonic groups in the membranes was demonstrated by means of scanning electron microscopy (SEM) and energy-dispersive X-ray spectroscopy (EDX). The influence of the degree of grafting on the ion exchange capacity (IEC) and the proton conductivity was evaluated. The optimum membrane was prepared by an inexpensive procedure involving a dehydrofluorination step at room temperature for 1 h in a 1 M KOH solution, followed by grafting at 60°C for 3 times 6 h from a 80/20 vol% styrene/THF graft solution containing 3.75 x 10^{-3} g mL^{-1} BPO and finally a sulphonation for 24 h in a 1 M chlorosulphonic acid in dichloroethane solution. This membrane showed enhanced proton conductivities (0.25 S cm^{-1}) compared to Nafion® (0.08 S cm^{-1}) and to previously reported for PVDF-g-PSSA membranes (≤ 0.18 S cm^{-1}) and is thus a promising candidate as PEM for fuel cells applications.

Based on:

N. Daems, S. Milis, H. Yu, A. Szymczyk, P.P. Pescarmona, I.F.J. Vankelecom, to be submitted.

Author contributions

The original idea of this research was developed by H. Yu and I.F.J. Vankelecom. Membrane preparation and characterisation were done by N. Daems and S. Milis. The article was written by N. Daems. Zeta-potential measurements were performed by A. Szymczyk. The whole work was supervised by I.F.J. Vankelecom and P.P. Pescarmona.

7.1 Introduction

Over the past decades, proton-exchange membrane fuel cells (PEMFC) became increasingly recognised as an environmentally friendly potential alternative for current power generation processes. Some of the advantages of fuel cells include high energy conversion efficiency, zero emission and low noise.[108,294] One of the key components of PEMFCs is the membrane, which should ideally have the following properties: (1) high proton conductivity, (2) low reagent cross-over, (3) high electric resistance, (4) long-term stability under the harsh fuel cell operating conditions, (5) good water transport and (6) be inexpensive.[108,109] Currently, Nafion®, a perfluorinated sulphonic acid based ionomer developed by DuPont, is the standard membrane in fuel cells.[6] Nafion® has a high proton conductivity and stability, especially at low temperature and high relative humidity.[109,110] However, Nafion®-based membranes have several disadvantages including (1) low proton conductivity at high temperatures,[109] (2) high cost,[110] (3) degradation by H_2O_2 (an intermediate product in H_2/O_2 fuel cells),[111] and (4) drastic decrease in conductivity in the presence of contaminating multi-charge ions.[6]

As a consequence of these drawbacks, numerous attempts have been made to replace Nafion® with partially fluorinated or fully non-fluorinated polymers.[108,295] The largest groups of alternatives to Nafion® include the following: (1) Polystyrene-sulphonic acid membranes, which are rather inexpensive but are not stable under the operation conditions.[113] (2) Sulphonated polyimide membranes, which are advantageous when compared to Nafion® because of their higher stability, lower cost and higher conductivities at elevated temperatures.[114,115] However, they are less stable in water and only achieve high conductivities at high water contents.[116,117] (3) Phosphoric acid-containing poly(benzimidazole)-based membranes, which have a high stability and a high conductivity at temperatures as high as 160-180°C.[118,119] Their main drawback is related to the presence of phosphoric acid as its leaching can corrode the electrodes and inhibit the electrocatalysts.[122] (4) The last group contains several kinds of sulphonated membranes with aromatic carbon backbones (poly(arylene ethers), polysulphones, etc.), which gained interest as a consequence of their stability and low cost.[108]

To increase the stability of polystyrene sulphonic acid membranes, styrene sulphonic acid monomers can be grafted onto a more stable backbone polymer like polyvinylidene fluoride (PVDF-g-PSSA). Generally, these materials are synthesised by polymerisation of styrene on an existing PVDF framework, initiated either by radiation or by a radical initiator like benzoyl peroxide. This is then followed by a sulphonation of the grafted polystyrene chains.[128,296] These membranes have good physico-mechanical stabilities and are inexpensive as compared to Nafion®. Thus far, promising conductivities (up to 0.13 S cm^{-1}) were already obtained for this kind of materials.[109,125–128] In this work, we aim at achieving PEMs with better performance than those in the literature in terms of conductivity and stability, by systematically investigating and tuning the three steps involved in the synthesis of these membranes, *i.e.* the dehydrofluorination, the grafting of styrene and finally its sulphonation.

7.2 Experimental

7.2.1 Materials

PVDF powder (M_w = 534,000 Da), styrene, 1,2-dichlorethane, sulphuric acid (95-98%), benzoyl peroxide (BPO), chlorosulphonic acid (70% in water), magnesium sulphate (>=97%), sodium chloride and potassium hydroxide (KOH) were purchased from Sigma-Aldrich and used without further modification. Bengal Rose (M_w = 973.67 Da) and Rhodamine B (M_w =

479.02 Da) were purchased from FlukaN-methyl-2-pyrrolidone (NMP), tetrahydrofuran (THF), chloroform, 1,2-dichloroethane, and ethanol were obtained from Acros as analytical grade.

7.2.2 Membrane preparation

The parent PVDF membranes were prepared from (20 wt% PVDF) (64 wt% NMP) (16 wt% THF) casting solutions by phase inversion.[297] The casting solution was stirred until homogeneous and left to rest overnight to remove all air bubbles. The solution was then cast onto a glass plate with a 250 µm wet thickness using a casting knife. After an evaporation period of 15 s, it was immersed into de-ionised water for about 15 min to allow phase-inversion.

The membrane was then grafted with polystyrene following a sequence of steps. The membranes were first washed three times with ethanol to remove all water trapped inside the pores. Afterwards, they were immersed into a KOH/ethanol solution which generates double bonds in the membrane matrix by eliminating several H and F atoms from the PVDF backbone.[298] These double bonds will be the starting point for the grafting step. The concentration of the KOH solution was 0.1 or 1 M and the membranes were immersed for 60, 250 or 1440 min at room temperature. After thoroughly washing the membranes with de-ionised water until neutral pH, they were immersed in the grafting solution, the composition of which was varied to investigate the influence of several parameters on the degree of grafting of styrene. It contained 80 or 50 vol% styrene and 20 or 50 vol% THF, and the radical initiator BPO with a concentration of 2.25, 3 or 3.75 x 10^{-3} g mL^{-1}. The grafting reaction was performed at 60, 80 or 100°C for 1, 2 or 3 separate steps of 6 h. Finally, the membrane was extracted with chloroform overnight at 120°C to remove unreacted monomer and uncoupled polystyrene.

As a final modification, the membranes were sulphonated in order to obtain proton-exchange groups in the membrane matrix. To achieve this, the membranes were first pre-wetted in 1,2-dichloroethane and afterwards immersed in 0.1, 0.5 or 1 M chlorosulphonic acid in 1,2-dichloroethane at ambient temperature for 12, 24 or 45 h. The sulphonated membranes were thoroughly rinsed with tetrahydrofuran and distilled water. The final membranes were stored in deionised water.

The standard method for the synthesis of PVDF-g-PSSA membranes, used in this research, was inspired by the method of Lehtinen *et al.*.[126] The membranes were first washed with ethanol. Afterwards, the membrane was immersed in a 0.1 M KOH in ethanol solution for 250 min. After neutralisation, the membranes were immersed into the grafting solution (80/20 vol% styrene/THF and 3 g L^{-1} BPO), which was previously purged with N_2 for 30 min, for 6h at 80°C. The unreacted monomer and homopolymers, were then removed through a Soxhlet extraction with chloroform. Finally, after a pre-wetting step in 1,2-dichloroethane, the membranes were immersed in a 0.5 M chlorosulphonic acid in 1,2-dichloroethane solution for 24 h at room temperature to obtain a proton-exchange membrane.

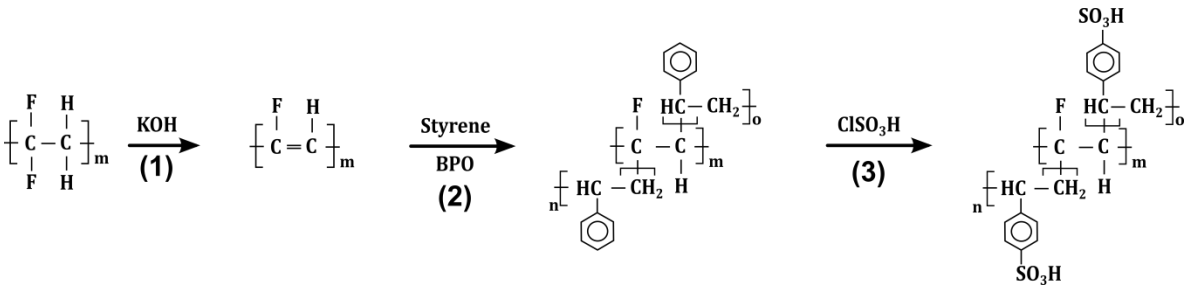

Scheme 7.1. Schematic representation of the different steps:dehydrofluorination (1), grafting with styrene (2) and sulphonation (3) in the synthesis method of PVDF-g-PSSA.

7.2.3 Degree of grafting

The degree of grafting (%) was determined gravimetrically:

$$\text{degree of grafting} = \frac{m_1 - m_0}{m_0} \times 100\% \qquad \text{(Eq. 7.1)}$$

where m_0 is the original mass and m_1 is the mass after grafting.

7.2.4 Scanning electron microscopy (SEM) and energy-dispersive X-ray (EDX) spectroscopy.

The membrane surface and cross-sections were imaged with scanning electron microscopy (SEM) using a Philips XL30 FEG scanning electron microscope. The cross-sections were obtained after breaking the dried membranes. The samples, top and cross sections, were glued on a sample holder, dried and coated with a thin gold layer via a high resolution sputter coater (JEOL JFC-1300).

Energy-dispersive X-ray (EDX) spectroscopy was used in combination with SEM to visualise the distribution of the sulphonic groups throughout the membrane. The elemental distribution was recorded with an EDAX energy dispersive X-ray detector with an ultra-thin window from phoenix. Data analysis was performed with Genesis spectrum version 6.46.

7.2.5 Contact angle measurements

Contact angle measurements were conducted to investigate the hydrophilic/hydrophobic character at different stages during the membrane synthesis. The measurements were conducted with a high resolution camera linked to a computer (Drop Shape Analysis system, DSA 10 Mk2 from Kruss). Prior to the measurements, the membrane samples were dried overnight at 100°C.

7.2.6 Zeta-potential measurements

Membrane charge properties were characterised from streaming current measurements performed with a SurPASS electrokinetic analyser (Anton Paar GmbH, Austria) equipped with an adjustable-gap cell. All measurements were carried out by setting the distance between the two membrane coupons in the measuring cell to 100 ± 5 µm. Streaming current was measured with a pair of Ag/AgCl electrodes by applying pressure ramps of 300 mbar. Visiolab software was used for data analysis (zeta potential determination). All experiments were performed with 10^{-3} M KCl background solutions at room temperature (25 ± 2 °C) following the experimental protocol described by Mouhoumed *et al.*.[299] Membranes were first equilibrated with the background solution at pH~9 (pH was adjusted with 0.1 M KOH) and then streaming current measurements were performed by progressively decreasing the pH down to about 3 by additions of 0.1 M HCl.

7.2.7 Ion-exchange capacity (IEC)

The ion-exchange capacity (IEC) was measured on membrane samples in the H^+ form by treating them with a 0.5 M H_2SO_4 solution for 24 h. After washing them several times with de-ionised water until a neutral pH was obtained, they were immersed in a 1 M NaCl aqueous solution at room temperature overnight under stirring. The released H^+ was titrated against a 0.5 M NaOH solution using an automatic titrator (Titrino Plus 848) from Metrohm until a pH of 7 was achieved. The IEC was then calculated by the following equation:

$$\text{IEC (meq g}^{-1}) = \frac{V_{NaOH} x\, C_{NaOH}}{m_{dry}}$$

where V_{NaOH} is the volume in mL of NaOH solution added to reach a pH of 7, C_{NaOH} is the concentration in molar of the NaOH solution that was used and m_{dry} is the dry mass in g of the membrane.

7.2.8 Membrane resistance measurement and proton conductivity calculation

The resistance of the membranes in H^+ form was measured through an impedance measurement using an interface 1000 potentiostat manufactured by Gamry in an in-house constructed setup (Scheme 1). The setup consists of two Teflon parts that are connected with screws and have a small container in it for the electrolyte. The membrane is placed between the two Teflon parts. The stainless steel electrodes are connected to the potentiostat to measure the impedance. Prior to the impedance test, the membranes were equilibrated for at least 24 h in 0.5 M H_2SO_4. The spectra were recorded at room temperature at 60°C and at 80°C in the frequency range of 1 Hz to 0.1 MHz. The resistance was determined as the intercept with the real axis. To obtain the cell resistance (containing the electrolyte resistance), an impedance measurement was also performed in the absence of the membrane. The obtained value for the cell resistance was subtracted from the total resistance obtained in the presence of a membrane to get a value for the membrane resistance. The proton conductivity was then calculated according to the following formula:

$$\sigma(\text{S cm}^{-1}) = \frac{d}{R.A}$$

where d is the membrane thickness in cm, R is the membrane resistance in Ohm and A is the area of the membrane that is in contact with the electrolyte in cm².

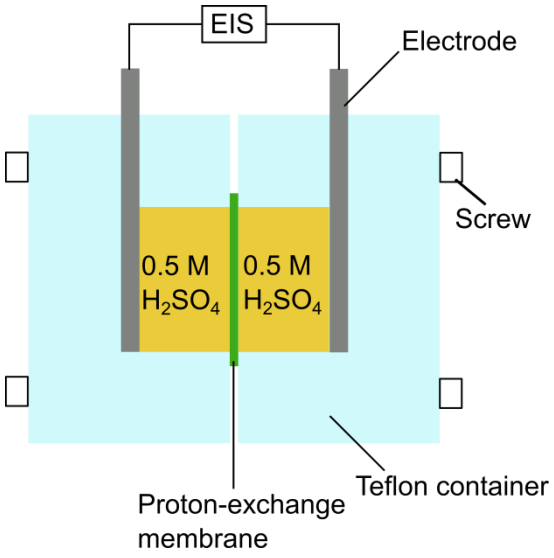

Scheme 1. Schematical representation of the setup that was used for the impedance measurements.

7.3 Results and discussion

In a previous study performed by our group, the synthesis of the parent PVDF membrane was optimised with respect to its Rose Bengal retention and water permeance. It was found that the optimal composition of the casting solution was 20 wt% PVDF, 64 wt% NMP and 16 wt% THF. Several batches of this casting solution were prepared and cast on a glass plate, followed by phase inversion. The membranes were then used as such for grafting and subsequent sulphonation.

7.3.1 Proof of concept

The influence of the three different steps (dehydrofluorination, grafting with styrene and sulphonation) on the membrane properties (hydrophilicity, sulphur content and distribution and charge) was monitored by a combination of techniques (contact angle measurements, SEM/EDX and zeta potential measurements).

Contact angle measurements

To investigate the influence of the grafting and the sulphonation on the hydrophilicity of the membranes, contact angle measurements were performed. For pristine PVDF, a contact angle of 75° was recorded, which increased to 85° after grafting the membrane with polystyrene (PVDF-g-PS) and decreased to almost 0° for the sulphonated membranes (PVDF-g-PSSA). The increase in contact angle after grafting confirms the more hydrophobic nature of polystyrene compared to PVDF. Furthermore, the sulphonation is considered successful since the contact angle decreases to almost 0°, suggesting a very hydrophilic character of the membrane, which can only be caused by the presence of the hydrophilic sulphonic acid groups.

SEM/EDX

SEM was used in combination with EDX to investigate the distribution of the sulphonic acid groups across the PVDF matrix (Fig. 7.1). In the SEM image, the asymmetric membrane morphology typical for membranes prepared by phase inversion can be observed clearly. A dense skin layer, which is responsible for the separation properties of the membrane, is supported by a more porous layer consisting of fingerlike macro-voids. The stars in the image mark the positions at different distances from the top layer where the EDX measurements were performed. The results of these measurements are summarised in Table 7.1.

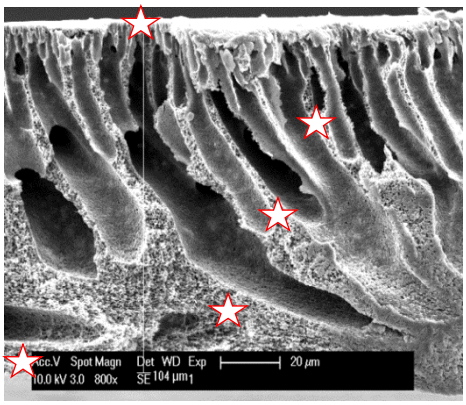

Figure 7.1. SEM image of the cross-section of a PVDF-g-PSSA membrane with the positions where EDX was measured marked with a star.

From Table 7.1, it can be concluded that sulphur is distributed rather homogeneously throughout the membrane cross-section. Since the sulphonation can occur from both top and bottom layer, the risk existed of a lower sulphonation degree in the middle sections of the membrane. However, this is not the case as the lowest at% of sulphur was found in the top layer, which is most likely caused by the more dense nature of this layer, hindering the diffusion of the chlorosulphonic acid.

Table 7.1. Elemental composition at different distances from the skin layer as determined by EDX measurements

Distance from top (µm)	C (at%)	O (at%)	F (at%)	S (at%)
0	77	7.2	14	1.6
36	67	4.5	24	4.1
59	68	5.9	23	3.1
89	67	6.1	23	3.5
104	70	4.6	21	4.2

Zeta-potential measurements

Figure 7.2 shows the zeta potential of the PVDF membrane after each modification. The pristine PVDF membrane surface is predominantly negatively charged until it reaches its isoelectric point at a pH of 3-4 . This behaviour is similar to that observed for other uncharged membranes and is attributed to the adsorption of hydroxide ions, which originate from the water self-ionisation.[300] The KOH treatment results in a decrease in the electrokinetic charge density as a consequence of the removal of functional fluoride groups, which are the most likely groups to coordinate with the hydroxide anions due to their high electronegativity. After grafting with polystyrene, the charge density increases again to a value comparable to that of the pristine PVDF, indicating that the polystyrene modification did not introduce additional charged groups to the system.[301] After sulphonation, the isoelectric point disappears and the negative charge density becomes almost independent of the pH of the solution, which indicates an efficient sulphonation of polystyrene as it points out the presence of sulphonic groups that behave as strong acids.[302]

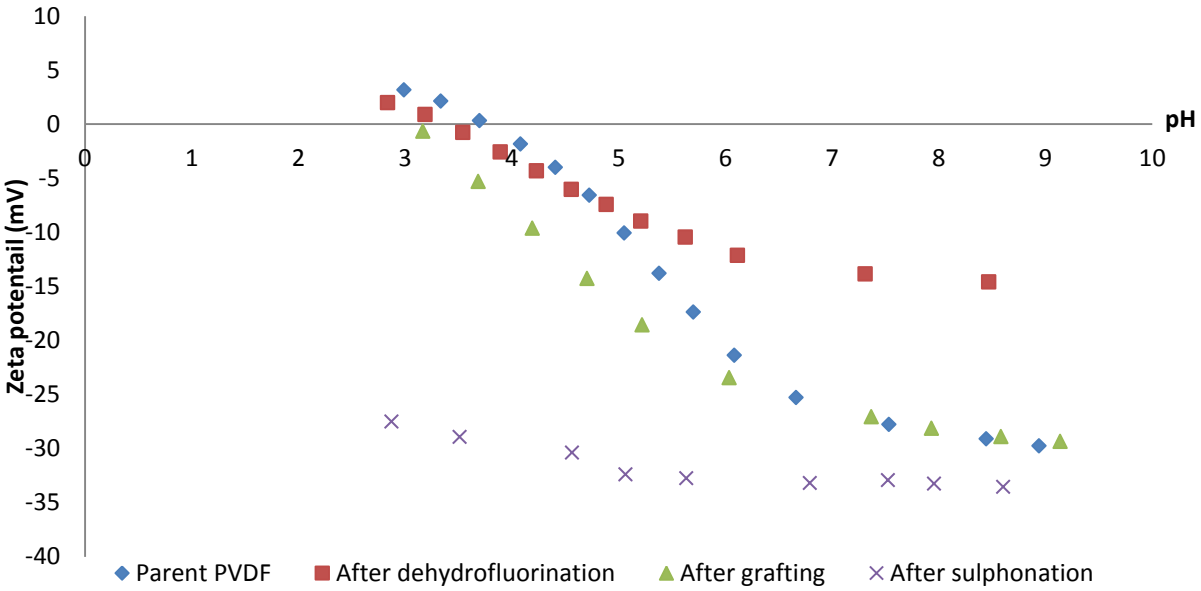

Figure 7.2. Zeta-potential measurements after the different modificationsteps: parent PVDF, after dehydrofluorination, after grafting and after sulphonation.

7.3.2 Modification of dehydrofluorination step

As a first attempt to improve the membrane performance (i.e. its proton conductivity), the dehydrofluorination step (see Scheme 7.1) was modified in an effort to increase the number of double bonds that is generated during this step. Since the double bonds form the starting point for the styrene grafting, it is expected that a higher number of double bonds will result in a higher degree of grafting. This should then result in a higher number of sites available for sulphonation and thus a higher conductivity.[109,296,303] Two different ways to increase the yield of the dehydrofluorination were investigated: (1) the duration was increased from 60 to 250 to 1440 min and (2) the KOH concentration was increased from 0.1 to 1 M for a duration of 60 min. When a 0.1 M KOH solution was used, it was observed that the degree of grafting increased with the duration from 8.8% after 60 min to 10.7% after 250 min, after which it remained rather constant, indicating that the maximum degree of dehydrofluorination was reached under these conditions. However, at higher KOH concentration, more double bonds could be generated, as indicated by the higher degree of styrene grafting (16.5%) obtained with 1 M KOH after 60 min. This would mean that the maximum degree of dehydrofluorination for these membranes could not be reached with 0.1 M KOH, which suggests that harsher dehydrofluorination conditions (1 M KOH) are necessary to penetrate all areas of the membrane, including the most dense ones. As not all fluorine atoms are removed even with a 1 M KOH solution (see Table 7.1), a further increase in the concentration might lead to a higher degree ofdehydrofluorination of the membrane. This was not further investigated here, as the applied conditions already gave a substantial improvement.[304]

In Figure 7.3, the ion exchange capacity and the proton conductivity are plotted as a function of the degree of grafting that results from this particular modifications. As expected,[134] it can be observed that both the ion exchange capacity and the proton conductivity increase in a similar manner with the degree of grafting. The degree of grafting can be used as an indicator for the ion exchange capacity and the proton conductivity if it is assumed that the sulphonation proceeds to the same extent, irrespective of the degree of

grafting. This is generally the case as the sulphonation conditions were not altered in this set of experiments. A higher degree of grafting thus results in a higher number of sites available for sulphonation and thus in a higher ion exchange capacitiy and proton conductivity, as was observed here. Another consequence is that the degree of grafting can be considered as an indication of a higher sulphonation as long as the sulphonation conditions remain the same. The results in Figure 7.3 also prove our hypothesis that the proton conductivity of the PVDF-g-PSSA membranes can be further improved by increasing the degree of grafting.

In summary, this study showed that the best conditions to perform the dehydrofluorination in order to maximise the proton conductivity consist in immersing pristine PVDF for 60 min in a 1 M KOH solution at room temperature.

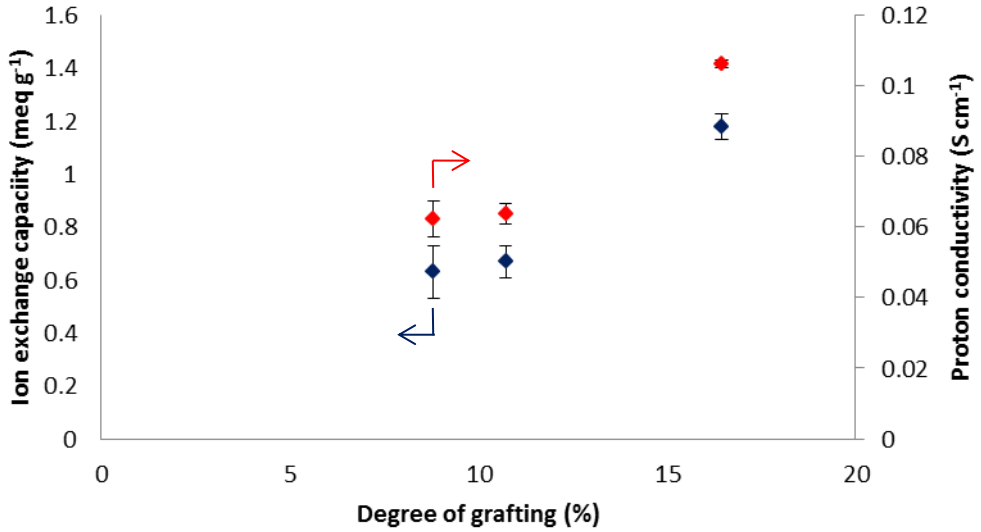

Figure 7.3. IEC and proton conductivity as a function of the degree of grafting as realised by modifying the dehydrofluorination step.

7.3.3 Modification of the grafting method

To further improve the proton conductivity of the membrane, the grafting step (see Scheme 7.1) was optimised in order to obtain membranes with a higher degree of styrene grafting and thus a higher number of aromatic groups available for sulphonation. Several parameters were investigated: (1) the composition of the grafting solution (80/20 or 50/50 vol% styrene/THF); (2) the content of initiator (2.25 to 3.75 x 10^{-3} g mL^{-1}); (3) the temperature (60 to 100°C); and (4) the number of grafting steps (1 to 3). The results are summarised in table 7.2.

Table 7.2. Change in degree of grafting, IEC and proton conductivity as a function of the grafting conditions. The dehydrofluorination step was performed with a 0.1 M KOH solution for 250 min. Average values and standard deviations are reported where available. The proton conductivity was calculated from the average value of the membrane resistance and therefore it does not have a standard deviation.

Parameter modified*	Degree of grafting (%)	IEC (meq g^{-1})	Membrane resistance (Ohm)	Proton conductivity (S cm^{-1})
/	11	0.67±0.05	0.45±0.03	0.06
50/50 vol% styrene/THF	7.7	0.49±0.03	0.51±0.03	0.06
60°C	27	1.97±0.10	0.13±0.01	0.22
100°C	4.4	0.23±0.01	0.59±0.03	0.05
[BPO] = 2.25 x 10^{-3} g ml^{-1}	8.7	0.57±0.05	0.48±0.02	0.06
[BPO] = 3.75 x 10^{-3} g ml^{-1}	20	1.46±0.03	0.18±0.01	0.16
2 times 6 h	17	1.16±0.02	0.28±0.02	0.10
3 times 6 h	22	1.56±0.05	0.15±0.01	0.20

*All other parameters except the one mentioned in the table were kept constant. The standard grafting conditions are: 80/20 vol% styrene/THF, 3 x 10^{-3} g ml^{-1} BPO, at 80°C for 6 h.

As expected, the degree of grafting increased with the number of grafting treatments, indicating an incomplete grafting after one or two subsequent grafting periods of 6 h. Furthermore, an increase in the BPO content also yielded membranes with a higher grafting degree, which could be anticipated as BPO serves as an initiator. The higher its concentration, the more grafting sites will be generated in the same time interval. At lower vol% of styrene, the grafting was less successful, which is obviously due to a lower reactant availability.[128] Finally, while it was expected that an increase in the reaction temperature would result in a higher reaction rate and thus a faster grafting, the opposite behaviour was observed here as the degree of grafting decreased when changing from 60 to 100°C. This can be explained based on visual observations during the course of the grafting experiment. At higher temperatures, the grafting solution became more viscous at a faster rate due to the faster polymerisation of styrene in the solution, which overcompensates the expected decrease in viscosity with the temperature. It is thus proposed that the grafting of the membrane does not proceed further once the solution is no longer properly mixed. This might explain the lower degree of graftingachieved at higher temperatures together with the fact that the styrene monomers that polymerised in solution are obviously no longer available for reaction with the membrane. Furthermore, from Table 7.2 it can be observed that the ion exchange capacity and the proton conductivity increase similarly with the degree of grafting, which further confirms the possibility to improve the performance of the PVDF-g-PSSA membranes in terms of proton conductivity by increasing the degree of grafting.

7.3.4 Modification of sulphonation process

As a final approach to enhance the membrane proton conductivity, it was investigated whether the sulphonation step (see Scheme 7.1) could be optimised by varying (1) the duration (from 12 to 45 h) and (2) the concentration of chlorosulphonic acid (from 0.1 to 1 M in dichloroethane). The results are summarised in table 7.3. While the duration of the sulphonation only has a minor effect on the final proton conductivity (sulphonation is typically a fast process), an increase in concentration from 0.5 to 1 M of chlorosulphonic acid does have a major positive impact. It is possible that under these harsher conditions,

chlorosulphonic acid is able to access even the most difficult to reach areas as a consequence of the higher concentration gradient and thus the higher driving force for the sulphonic acid diffusion. This would explain the higher ion exchange capacity and conductivity, even if the degree of grafting remains the same.

Table 7.3. Change in IEC and proton conductivity as a function of the sulphonation conditions. The dehydrofluorination and grafting step were performed with the starting conditions. Average values and standard deviations are reported where available. The proton conductivity was calculated from the average value of the membrane resistance and therefore it does not have a standard deviation.

Parameter modified*	Degree of grafting (%)	IEC (meq g^{-1})	Membrane resistance (Ohm)	Proton conductivity (S cm^{-1})
/	11	0.67±0.03	0.45±0.02	0.06
Reaction time = 12 h	11	0.85±0.06	0.49±0.01	0.06
Reaction time = 45 h	11	0.50±0.02	0.46±0.03	0.06
Reagent concentration= 0.1 M	11	0.58±0.05	0.47±0.02	0.06
Reagent concentration = 1 M	11	1.20±0.08	0.27±0.05	0.11

* All other parameters except the one mentioned in the table were kept constant. The standard sulphonation conditions are: 0.5 M chlorosulphonic acid in 1,2-dichloroethane at room temperature for 24 h.

After optimising the different steps in the synthesis procedure, a membrane was prepared using the optimal conditions: (1) dehydrofluorination at room temperature for 1 h in a 1 M KOH solution; (2) grafting at 60°C for 3 times 6 h from a 80/20 vol% styrene/THF solution containing 3.75 x 10^{-3} g mL^{-1} BPO; and (3) sulphonation for 24 h in a 1 M chlorosulphonic acid in dichloroethane solution. The resulting ion exchange capacity and conductivity reached values of 2.3 meq g^{-1} and 0.25 S cm^{-1}, respectively. This indicated that a PVDF-g-PSSA membrane with a significantly enhanced performance was achieved by using a combination of the optimised parameters for the different steps. In figure 7.4, the Nyquist plots of Nafion® and of the optimal PVDF-g-PSSA membrane are given together with the Nyquist plot of the cell without membrane. In the insert, a close-up is given showing the intercept with the x-axis, which is the value of the resistance that is used to determine the proton conductivities after subtracting the resistance of the cell and the electrolyte.

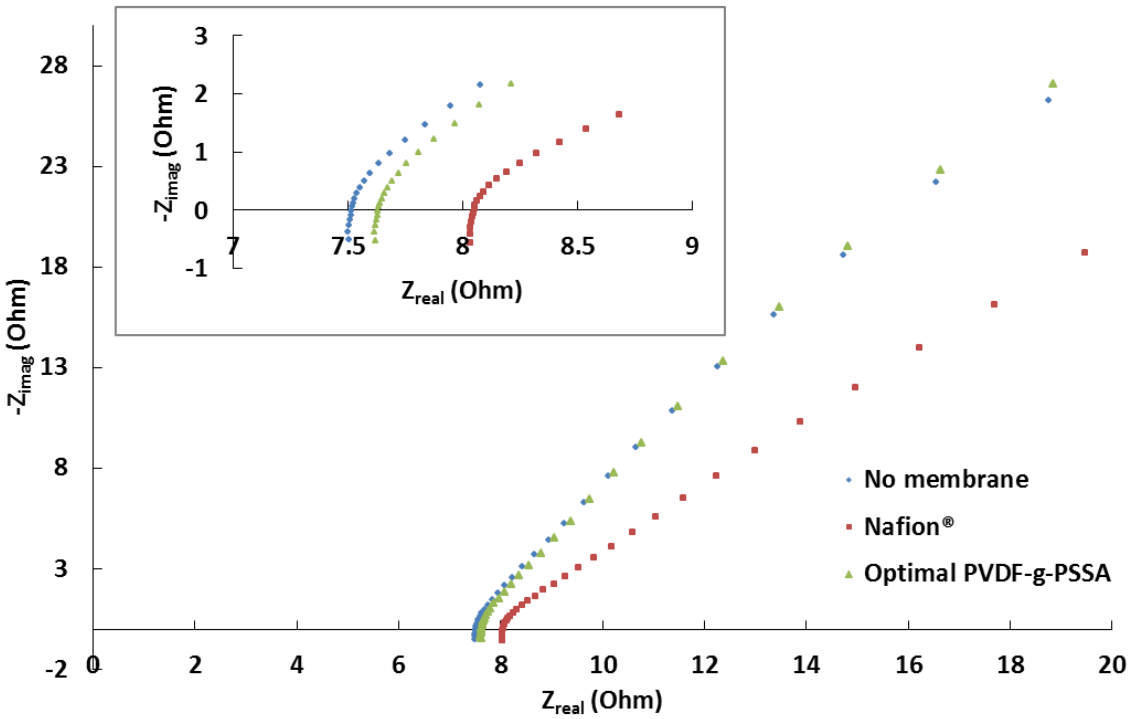

Figure 7.4. Nyquist plots for the cell without membrane, with Nafion and with the optimal PVDF-g-PSSA membrane. The inset is an enlarged image of the area of interest to determine the membrane resistance, in essence the intercept with the x-axis.

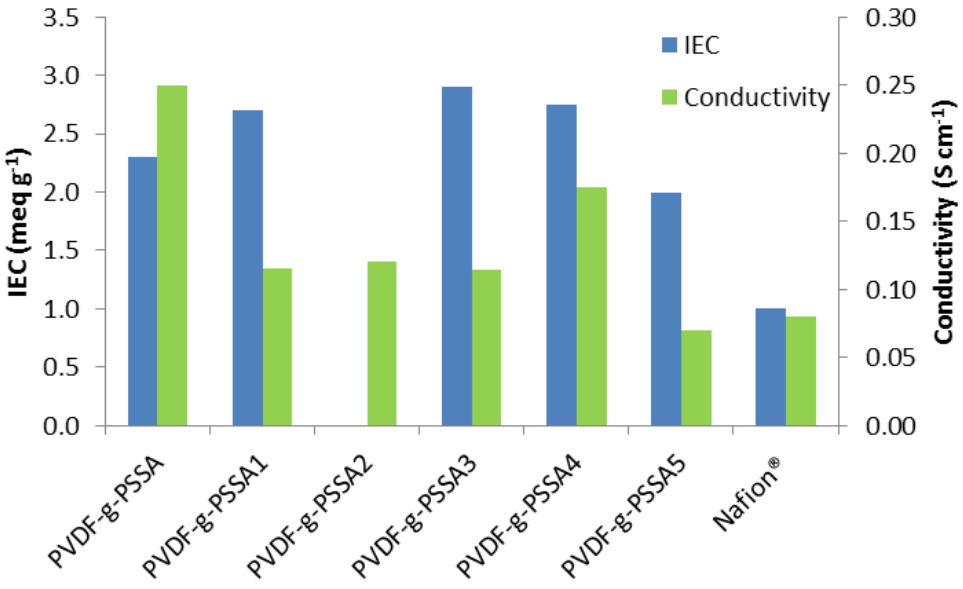

Figure 7.5. IEC and proton conductivity for optimised PVDF-g-PSSA compared with results found in literature (PVDF-g-PSSA 1 to 5) and with Nafion®.

In figure 7.5, the ion exchange capacity and the proton conductivity of this optimised membrane was compared with various results obtained in the literature and with Nafion® (values from own resistance measurements under equal conditions).[109,125,126,128,303] While it appears that after a thorough optimisation of the synthesis method, a higher conductivity

compared to the best results in literature could be obtained, the ion-exchange capacity lags behind some of the literature values. Since this is contrary to what is expected, as normally the IEC and the conductivity increase proportionally,[134] an explanation for this behaviour is proposed. The degree of grafting of the membrane (≤ 25%) is lower compared with that of memebrnaes reported in (generally ≥ 50%) .[128,296,305] As was demonstrated in this work, the IEC tends to increase with the degree of grafting as a consequence of a higher availability of anchoring points for sulphonic groups. This would explain why the membranes reported in literature reach a higher IEC. However, since the synthesised membranes result in higher proton conductivities than those achieved in literature, it is likely that the IEC and thus the number of sulphonic acid groups is sufficiently high such that a homogeneous distribution is achieved across the membrane, providing channels with high ionic mobilities.[126,128] A possible explanation for the combination of a higher proton conductivity and a lower IEC for the prepared PVDF-g-PSSA membranes compared to the literature could stem from the lower degree of grafting of our material, generating a less rigid structure, which would allow higher mobility of the polystyrene units and thus result in a higher proton mobility and conductivity. As one of the mechanisms of proton transport through charged membranes is the proton hopping mechanism, where the proton moves from one sulphonic group to the other, it is clear that an increased mobility of the polystyrene chains would allow this proton hopping to occur faster. Since the proton conductivity is directly related with the proton diffusion rate, a higher proton mobility will result in a higher proton conductivity.[306] Other possible explanations are related to the differences in the conditions for the proton conductivity tests. Although important, they are not expected to lead to such an increase in proton conductivity since they were already corrected by subtracting the value of the cell and electrolyte resistance from the total resistance. These differences include relative humidity (100% vs ≤ 75%), temperature (20°C vs 25 °C) and test medium (0.5 M H_2SO_4 vs. humidified gas or water). A higher humidity and a higher availability of protons (0.5 M H_2SO_4) are beneficial for the proton conductivity while a lower temperature should decrease the proton mobility.[109,128] Another factor that could impact the proton conductivity is the degree of swelling of the membrane which differs from pure water to the acidic environment. A higher degree of swelling would result in a higher resistance, as the length of the path that the protons have to travel increases. As the swelling generally increases with the deviation from neutral pH, a higher membrane swelling is expected under our test conditions and therefore, a lower conductivity would be expected.[307]

Finally, the influence of temperature on the proton conductivity of PVDF-g-PSSA was investigated and compared with the effect on Nafion® (Fig. 7.6). It was observed that the difference in performance in favour of the grafted PVDF membrane became much more significant at higher temperatures. The difference in conductivity increased from 3-fold at room temperature to more than 6-fold at 80°C. This most likely signifies that the PVDF-g-PSSA membranes manage better to keep water sorbed to ensure proton conductivity at higher temperatures than Nafion®.[109] This is a highly promising property of these PVDF-g-PSSA membranes. Higher temperatures were not investigated here but as the membranes are stable up until 250°C (as determined by thermogravimetric analysis), at which point the sulphonic acid groups decompose. It is expected that the conductivity would further increase with temperature if the membranes manage to keep enough water sorbed to ensure the proton conductivity as the proton mobility would further increase at higher temperatures. However, as the water management of the membranes becomes increasingly difficult at higher temperatures, it is expected that there is a treshold temperature above which the

conductivity no longer increases as a consequence of the lower water content at these elevated temperatures.[109]

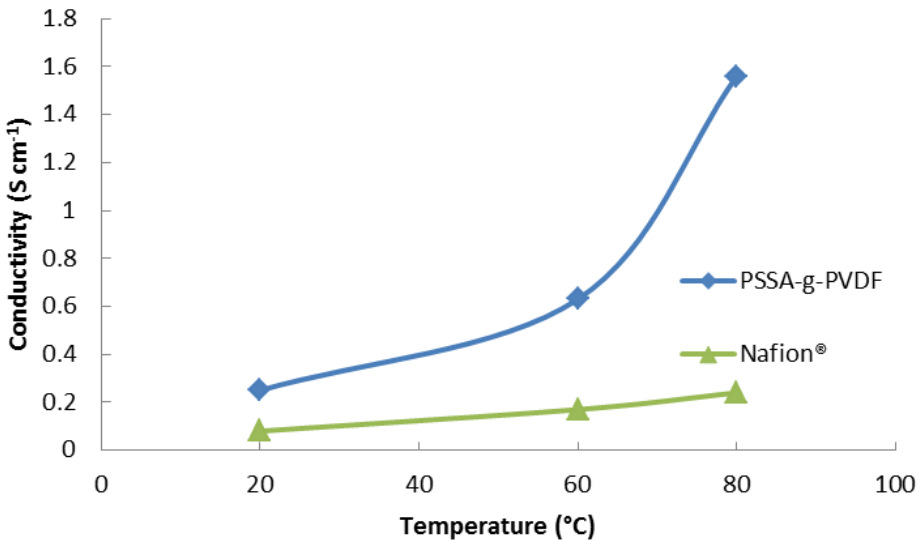

Figure 7.6. Influence of the temperature on the proton conductivity of PVDF-g-PSSA and Nafion®. The standard deviation for the conductivity is always smaller than 0.02 S cm^{-1}.

Overall, by optimising the synthesis method of PVDF-g-PSSA membranes, a clear enhancement in performance was achieved with respect to the existing membranes and also when compared to the commercial Nafion® 117 membrane, especially at elevated temperatures. These membranes are thus potential candidates to replace the expensive Nafion® inside PEM fuel cells. However, actual fuel cell tests should still be performed to investigate whether they can also outperform Nafion® under such conditions. Furthermore, in the future also long-term stability tests of the PVDF-g-PSSA membranes should be performed.

7.4 Conclusions

An improved method to synthesise sulphonic acid-containing proton-exchange membranes with enhanced degree of grafting, charge introduction, and consequently, proton conductivity was developed. This was achieved by the systematic optimisation of the different steps involved in the synthesis of these PVDF-G-PSSA membranes . SEM-EDX showed that the sulphonation groups are homogeneously distributed throughout the membrane, resulting in good pathways for the proton conduction. It was observed that the IEC and proton conductivity increase proportionally with the degree of grafting, which is ascribed to a higher availability of anchoring points for the sulphonic acid groups. The benefit of the optimisation process lies in the creation of membranes with a higher proton conductivity even at lower values of IECs when compared to literature, which was ascribed to the less rigid structure. Moreover, the membranes manage to further increase their conductivity at higher temperatures to levels that exceed the Nafion® conductivity more than 6-fold. These PVDF-g-PSSA membranes are thus promising candidates to replace the expensive Nafion® in the future as proton-exchange membrane in fuel cells.

Chapter 8

Polyvinylidene membranes grafted with sulphonated polystyrene for nanofiltration in a broad pH-range

Abstract

A polyvinylidene fluoride membrane grafted with polystyrene sulphonic acid was evaluated as a nanofiltration membrane for operation under extreme pH-conditions. The best performing membrane had a water permeance of 2.4 l $h^{-1}.m^{-2}.bar^{-1}$ and a > 96% retention for Rhodamine B (480 g mol^{-1}), while NaCl and $MgSO_4$ were retained for ≈60% and ≈80%, respectively. Most importantly, after prolonged exposure to extreme pH (both alkaline and acidic), the membrane performance hardly changed, which makes these membranes extremely interesting candidates as pH-resistant nanofiltration membranes.

Based on:

N. Daems, S. Milis, P.P. Pescarmona, I.F.J. Vankelecom, *in preparation.*

Author contributions

The original idea of this research was developed by N. Daems and I. Vankelecom. Membrane preparation, characterisation, filtration experiments were done by N. Daems and S. Milis. The article was written by N. Daems.. Valuable discussions on further improvement possibilities were held with I. F. J. Vankelecom. The whole work was supervised by I. F. J. Vankelecom and P. P. Pescarmona.

8.1 Introduction

Currently, nanofiltration (NF) membranes attract a lot of interest, as they are able to separate molecules of 200-1000 g mol^{-1} (as sugars, micropollutants, dyes or multi-avlent ions) from water or other liquids and could thus offer an economic and ecologic viable alternative to conventional separation technologies considering all advantages of membrane technology in general as e.g. being easily upscalable, creating no waste and requiring less energy.[308–311] In terms of retention, NF falls in between ultrafiltration, retaining macromolecules, and reverse osmosis, rejecting even monovalent salts.[308,312,313] However, compared to reverse osmosis, NF membranes reach higher fluxes.[313] This allows these membranes to be used in a broad range of areas, including water treatment, food engineering and biotechnology.[313]

Most commercially available NF membranes have thus far limited stability at extreme pH conditions (above 12 or below 2). Especially membranes that can withstand extreme alkaline conditions (pH 12 or higher) are scarce.[310,311,314] Since many industrial applications are operated at these more aggressive conditions, the possibility to use membranes in these cases is currently excluded. Developing membranes that are stable in a wider pH-window, would thus largely expand the potential use of NF membranes.[309–311] At low pH conditions, possible applications include metal ion removal from metallurgy process streams[315] or sulphate ion removal from streams originating from the mining industry.[316] At high pH, filtration and reuse of cleaning solutions from the food and dairy industry, or the effluent treatment in pulp, paper and textile industry could potentially benefit from the possibility to use NF membranes.[311,317–319] In addition, pH-stability might not be of prime importance during the actual filtration, but could allow implementation of more aggressive, hence more effective, cleaning procedures to fully recover original membrane performances.[320] Even though the range of potential applications is thus rather broad, the search for pH-resistant NF membranes has been rather limited up until now, mainly because it is so difficult to find materials with intrinsic stability that can still be turned into dense membranes.

Currently there are only few commercially available membranes that allow operation under extreme pH's. NP030 from Hydranautics, a sulphonated polyethersulphone membrane, is one of them. Duracid® from GE, MPF-34 from Koch Membrane systems and A3014 from Advanced Membrane System Technologies have undisclosed compositions. B4022 from Advanced Membrane System Technologies is a melamine-polyamine membrane that is stable at alkaline pH's. (4) Inopor® has ceramic membranes with a good stability (SiO_2 or TiO_2, both pH 0-14).[310,321] However, they all have their specific drawbacks. Either they have a rather high molecular weight cut-off (≥ 500 g mol^{-1}) or their permeance remains at the lower limits (< 1.5 l $h^{-1}.m^{-2}.bar^{-1}$). Furthermore, they often require complex synthesis methods making them expensive to procedure.[310,322] All of the above drawbacks limit their commercialisation and broad-scale application. The search for alternative pH-resistant NF membranes thus remains of high importance.

Several of these commercial membranes consist of sulphonated aromatic polymers, which have the advantage of being intrinsically chemically much more stable than for instance the standard polyamide NF membranes.[321] Another group of stable membranes that has achieved attention in the recent past and that contains sulphonic acid groups is polyvinylidene fluoride grafted with sulphonated polystyrene (PVDF-g-PSSA). While these membranes were mainly applied as ion-exchange membranes in fuel cells as an alternative to Nafion®,[109,125–128] they also have promising properties to be applied as pH-resistant NF membranes. Indeed, PVDF, a semicrystalline fluoropolymer, already provides the membrane with a stable backbone as a consequence of its excellent thermal, mechanical and chemical

stability.[298] However, PVDF membranes as such can not be used to retain salts as they can not be prepared dense enough via conventional phase inversion.[323–326] Moreover, PVDF is unstable at high pH (pH > 12) as a base can dehydrofluorinate the polymer.[298,304] On the other hand, Nafion®, while stable in a broad pH range, is not suitable for nanofiltration as it is too dense to allow water to pass through the membrane at acceptable rates. Moreover, Nafion® can not be prepared in an asymmetric structure thus rendering NF-applications not feasible.

To further extend the use of PVDF to the NF range, the rather large pores of such treated PVDF membranes were grafted in present work with polystyrene to create a dense enough structure inside the original pores and on top of the membrane. Subsequent introduction of charges into this polystyrene should further increase the retention of salts through Donnan exclusion. pH-stability of these membranes should be ensured as the backbone is largely dehydrofluorinated and the presence of the polystyrene graft might also prevent further attacks by a base on the PVDF backbone. The performance of these PVDF-g-PSSA membranes was investigated by means of high-throughput filtration experiments with aqueous solutions of dyes of different size as well as with salts. Their pH-stability was evaluated by repeating the same filtration experiments after long-term exposure to extreme pH-conditions (pH = 0-14).

8.2 Experimental

8.2.1 Materials

PVDF powder (M_w = 534,000 Da), styrene, 1,2-dichlorethane, sulphuric acid (95-98%) and benzoyl peroxide (BPO), were purchased from Sigma-Aldrich and used without further modification. Bengal Rose (M_w = 973.67 g mol^{-1}) and Rhodamine B (M_w = 479.02 g mol^{-1}) were purchased from Fluka. Magnesium sulphate (>=97%), sodium chloride and potassium hydroxide (KOH) were purchased from Sigma Aldrich. N-methyl-2-pyrrolidone (NMP), tetrahydrofuran (THF), chloroform, 1,2-dichloroethane, and ethanol were obtained from Acros as analytical grade. Chlorosulphonic acid (70%) was obtained from Sigma Aldrich.

8.2.2 Membrane preparation

Basic membrane

The parent PVDF membranes were prepared by phase inversion from PVDF/NMP/THF casting solutions with 15, 18 or 20 wt% PVDF concentrations.[297] The solution was cast onto a glass plate at a 250 µm wet thickness by using a lab-made casting knife. After an evaporation period of 15 s, it was immersed into distilled water for about 15 min to allow phase-inversion.[326] The membranes were then washed three times with ethanol to remove all water. Afterwards, they were immersed into a KOH/ethanol solution which generates double bonds in the membrane matrix by eliminating H and F atoms from the PVDF backbone. These double bonds will be the starting point for the grafting step. The concentration of the KOH solution was 1 M and the membranes were immersed for 60 min. After thoroughly washing the membranes with distilled water until neutral pH, they were immersed in the grafting solution. This solution was composed of 80 vol% styrene, 20 vol% THF and the radical initiator BPO in a 3.75 x 10^{-3} g mL^{-1} concentration. The grafting reaction was performed at 60°C for 6 h. The membrane was then extracted with chloroform overnight at 120°C to remove unreacted monomer and uncoupled polystyrene. Finally, the polystyrene graft was sulphonated through immersion in a 1 M chlorosulphonic acid in 1,2-dichloroethane solution for 24 h to obtain a negatively charged membrane. The sulphonated membranes

were thoroughly rinsed with THF and distilled water, and then stored in distilled water (Scheme 1).

Post-synthesis modifications

To further enhance the salt retention two post-synthesis modifications were performed.

Annealing

The membrane was annealed at 80°C in a water bath for 15 min [326,327] (referred to as PVDF-g-PSSA-A, Scheme 1).

Extra grafting

The membrane was submitted to 1 (referred to as PVDF-g-PSSA-2) or 2 (referred to as PVDF-g-PSSA-3) additional grafting steps (Scheme 1), either before or after the sulphonation of the membrane.

8.2.3 Filtration experiments

The membrane performance was tested in a high throughput filtration module with a water feed and a dye (Rose Bengal or Rhodamine B) and/or a salt (NaCl or $MgSO_4$). Rose Bengal (RB) and NaCl were permeated simultaneously. The active membrane area was 2.01 x 10^{-4} m². The setup allowed simultaneous dead-end filtrations of eight membranes under the same operating conditions. In order to minimise concentration polarisation, the feed solution was continuously stirred at 400 rpm. A nitrogen pressure of 10 bar was supplied for the parent PVDF membranes and 20-30 bar for the modified PVDF membranes. To obtain reproducible results, at least three coupons of each membrane were tested.

Membrane permeance (L_p) was calculated using:

$$L_p = \frac{V}{A*t*\Delta P} \quad \text{(Eq. 8.1)}$$

where V is the permeate volume (L), A is the membrane area (m²), t is the time (h) and ΔP is the applied pressure (bar).

The retention was calculated using:

$$R = \frac{c_f - c_p}{c_f} * 100 \quad \text{(Eq. 8.2)}$$

where c_f and c_p are the feed and the permeate concentration, respectively. Dye concentrations were measured on a UV-1800 UV-vis spectrophotometer (Shimadzu). Salt concentrations were measured with a Consort multi parameter analyser C3010 conductivity meter.

8.2.4 Scanning electron microscopy and energy-dispersive X-ray spectroscopy

Experimental details can be found in chapter 7 under paragraph 7.2.4.

8.2.5 Attenuated Total Reflectance Fourier Transform Infrared Spectroscopy (ATR-FTIR)

The chemical structure of the sample was analysed by Attenuated Total Reflectance Fourier Transform Infrared (ATR-FTIR) spectroscopy using a VARIAN 620-IR FT-IR spectrometer (Agilent). Prior to measurements, the membranes were dried for 45 minutes in an oven at 100°C to remove excess water.

8.2.6 Long term pH-stability tests

After an initial filtration experiment, the used membrane coupons were immersed in 100 mL of either 1 M HCl or NaOH at room temperature for one week. Subsequently, the membranes were rinsed with distilled water until a neutral pH was obtained. Hereafter the membrane performance was evaluated again using the very same membrane coupons.

8.3 Results and discussion

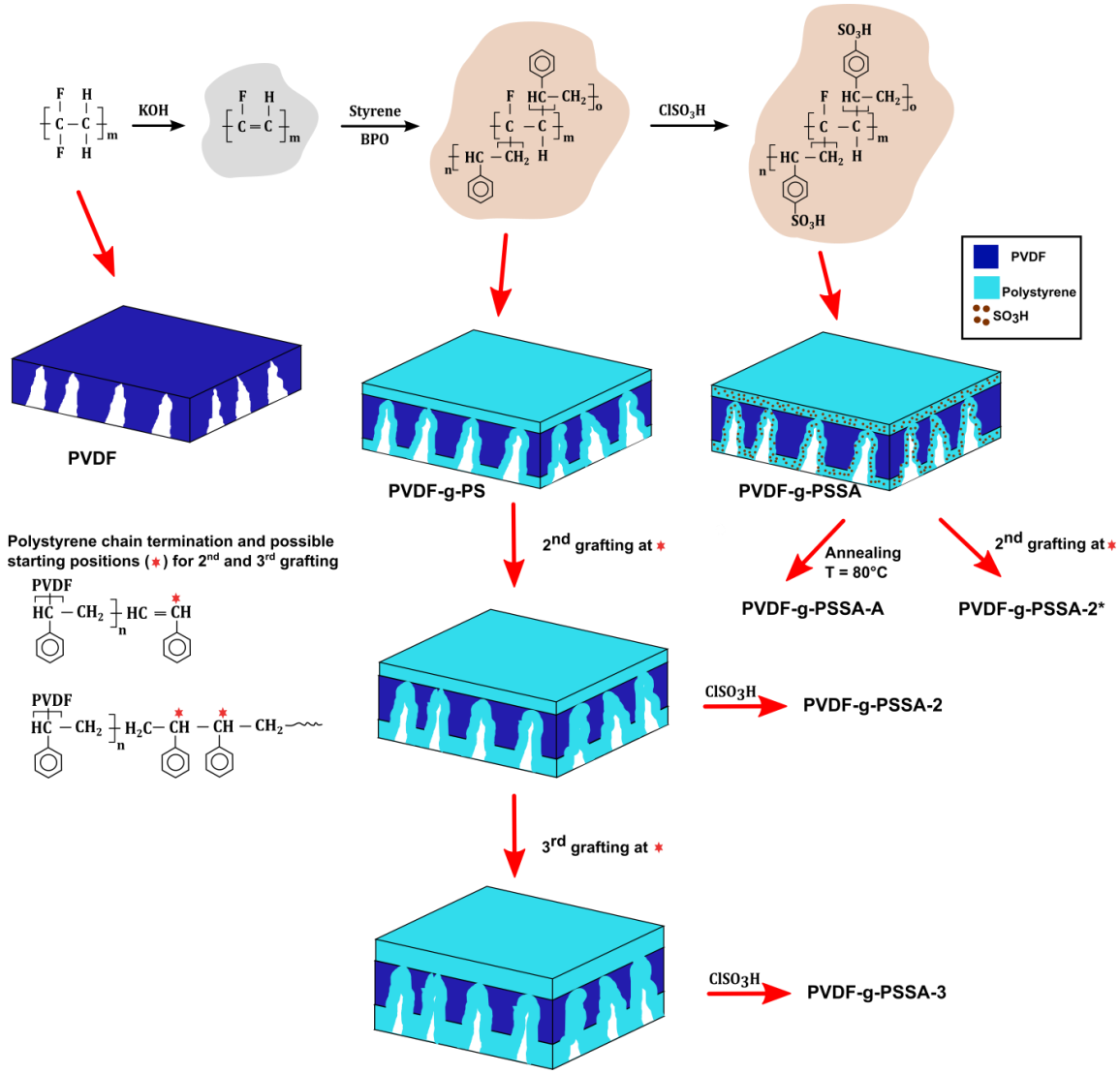

Scheme 8.1. Schematic representation of the synthesis method of the different PVDF-g-PSSA membranes prepared and tested in this work.

The different membranes were synthesised according to Scheme 8.1. The grafting is expected to narrow down the pores of the parent PVDF-membranes and also create an extra layer on top of the dense layer, generating a denser and slightly thicker membrane with a better retention for smaller molecules. The negative charges, created by the sulphonation, should result in higher salt retentions as a consequence of the Donnan exclusion principle. In an attempt to further enhance the salt retention, two different post-synthesis methods to densify the membranes were investigated. The membrane was either annealed after the sulphonation (PVDF-g-PSSA-A) or it was grafted a second (PVDF-g-PSSA-2) and a third (PVDF-g-PSSA-3) time prior to performing the sulphonation. As an extra test, a second

grafting step was also performed after the sulphonation step (PVDF-g-PSSA-2*). This membrane was not sulphonated a second time.

8.3.1 Parent PVDF membrane

Three PVDF-membranes were prepared by phase inversion from solutions with different PVDF concentrations and their performance was investigated by filtering an aqueous RB solution (Figure 8.1). As anticipated, the results show that the retention increases and the permeance decreases with the PVDF concentration in the casting solution.[326,328,329] Since the best retention of RB was achieved with 20 wt% PVDF in the casting solution, only this membrane was further modified through grafting and sulphonation to render it still more selective.

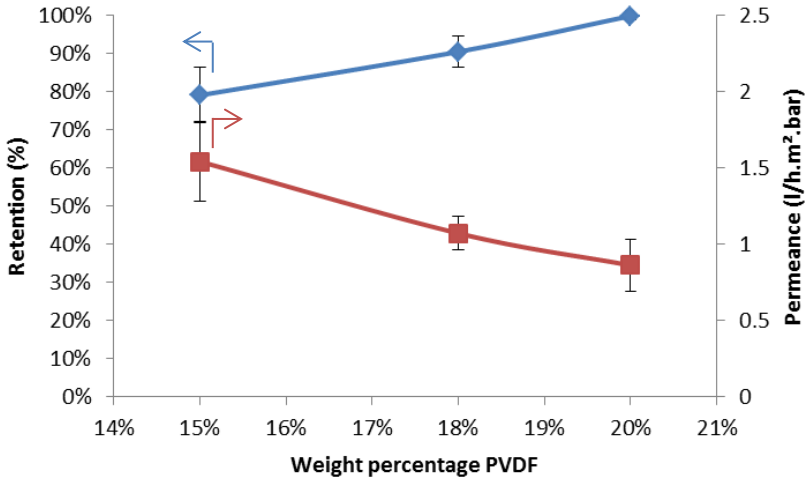

Figure 8.1. Rose Bengal retention and water permeance as a function of weight percentage of PVDF in the casting solution.

Based on the SEM images in figure 8.2, no clear effect of the casting film concentration on the membrane structure and morphology could be observed. However, based on the increased performance at higher concentration of PVDF in the casting solution, smaller pores in the selective layer of these membranes can be expected. In all cases, the substructure consists of fingerlike macrovoids.

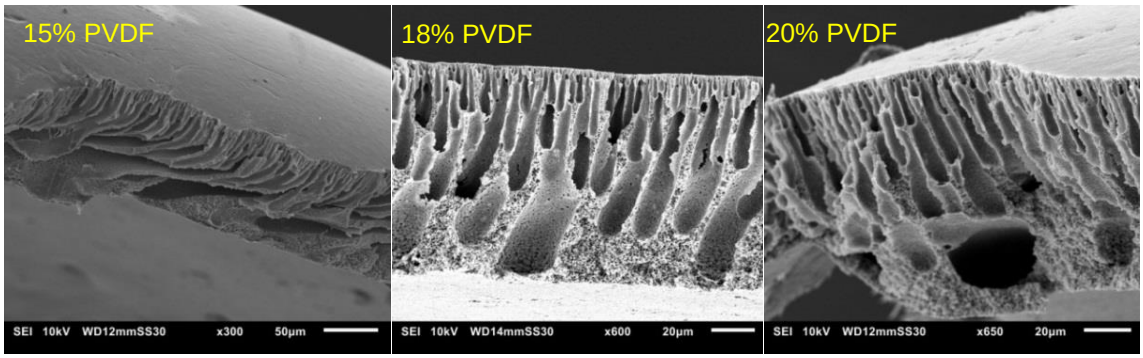

Figure 8.2. SEM images of the cross-sections of the membranes prepared with different weight percentages of PVDF in the casting solutions.

8.3.2 PVDF-g-PSSA membrane

The success of the dehydrofluorination step could easily be followed qualitatively by mere visual observation. The more advanced the dehydrofluorination, the more the membrane

darkened (Fig. 8.3). This follows from the formation of a more conjugated system as a consequence of the formation of double and even triple bonds after HF elimination. The black colour indicates that the conjugated system is long enough to cause such darkening or a substantial presence of triple bonds. After the grafting, the colour of the membranes changed to brown, which remained the same also after the sulphonation step (Scheme 8.1, Fig. 8.3). This indicates the disappearance of the triple bonds and of the majority of the double bonds.

Figure 8.3. Photographs of the membrane (A) parent, (B) after dehydrofluorination and (C) after grafting and sulphonation.

ATR-FTIR spectra were recorded after the different stages in the synthesis to confirm the visual observations and to verify whether PVDF was successfully grafted with polystyrene and subsequently sulphonated (Fig. 8.4). Besides the characteristic peaks of pristine PVDF (C-H bending (1400 cm^{-1}), C-F stretching (1180 cm^{-1}), C-H wagging (870 cm^{-1}) and C-F bending (830 cm^{-1})[330]), one extra, broad peak appears after the dehydrofluorination step at 1640 cm^{-1} and this can be assigned to the C=C bond stretching modes. After the grafting, two additional peaks appear at 698 and 1490 cm^{-1}, which can be assigned to the out of plane ring deformation of mono-substituted phenyl groups[331] and the C=C in-plane stretching vibration modes of the phenyl rings,[332] respectively. The bond at 1640 cm^{-1} dissapears upon grafting, suggesting that most of the double bonds reacted in the grafting of polystyrene. The C≡C bond (2100-2260 cm^{-1}) could not be observed in the IR spectra because of its weak dipole and the weak IR signal as a result. As a consequence, IR is not a suitable technique to detect alkyne bonds, especially when they are symmetrical (even weaker signal).[333] After sulphonation, the peaks at 698 and 1490 cm^{-1} disappear since the phenyl rings are no longer mono-substituted. Furthermore, three additional peaks appear, which can be assigned to the symmetric (1009 and 1039 cm^{-1}) and the asymmetric (1128 cm^{-1}) stretching vibration of the S=O bond.[334]

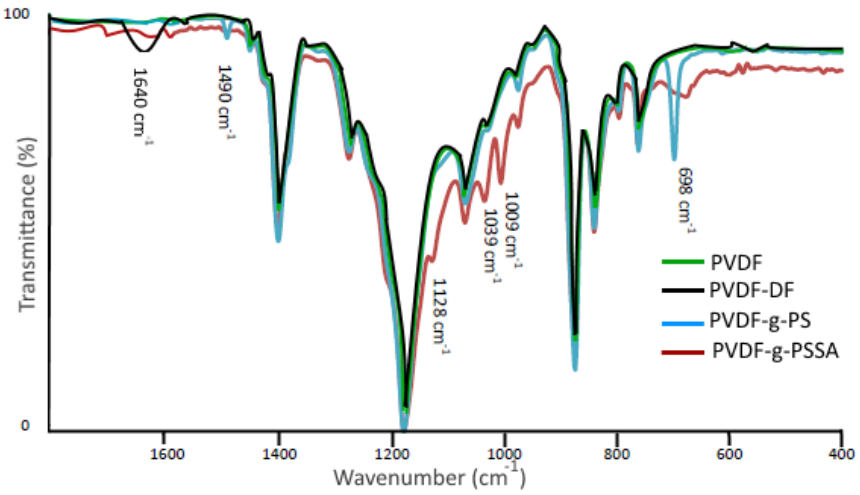

Figure 8.4. ATR-FTIR spectra of PVDF, PVDF-g-PS and PVDF-g-PSSA.

SEM was used in combination with EDX to investigate the distribution of sulphur (and thus the sulphonic acid groups) across the PVDF matrix. It was found that the sulphur is distributed rather homogeneously throughout the membrane (between 3 and 4 at%), with the exception of the top zone of the membrane where only 1.6 at% of sulphur could be found. Under the applied conditions, the EDX probing is assumed to penetrate to a depth of about 1 µm. This lower sulphur content is most likely caused by the more dense nature of the top of the membrane where the most narrow pores are located, hindering the styrene grafting and the chlorosulphonic acid diffusion to the phenyl rings.

The membrane performance was investigated to follow the effects of the grafting and after the sulphonation (Table 8.1). After grafting, the membrane permeance clearly decreased by a factor of 15, which can be related to the presence of an extra layer on top of the membrane and inside its pores, creating a more dense membrane. This layer thus forms an extra barrier against the water permeance through the membrane. Furthermore, since polystyrene is much more hydrophobic than PVDF (contact angle of 85° vs. 75° for PVDF), this layer will repel water more significantly. By sulphonation, the hydrophilicity of the membrane increases drastically (contact angle decreases to 0°) due to the presence of charges (Scheme 8.1) and as a consequence, the water permeance increases strongly. In addition, the salt rejection increases because of the Donnan exclusion that was added to the system through the charge introduction.

Table 8.1. Retention for the different solutes and water permeance for membranes obtained after different steps in the synthesis method of the PVDF-g-PSSA membrane. Filtration conditions: operating pressure: 20-30 bar, rotation speed: 500 rpm and feed: 35 µM RB and 1 g L^{-1} NaCl in milliQ water.

Solute	Permeance (L $h^{-1}.m^{-2}.bar^{-1}$)	Retention (%)	
		Rose Bengal	NaCl
PVDF	3.0±0.5	99.9±1.0	17.9±8.2
PVDF-g-PS	0.2±0.1	99.9±0.5	18.4±2.5
PVDF-g-PSSA-original*	4.4±0.5	99.8±0.3	30.7±0.8
PVDF-g-PSSA	3.0±0.5	99.9±0.4	39.7±0.8

*This membrane was prepared as follows: (1) dehydrofluorination for 250 min in a 0.1 M KOH in ethanol solution; (2) grafting for 16 h at 80°C with 80/20 vol% styrene/THF solution containing 3 x 10^{-3} g mL^{-1} BPO and (3) sulphonation for 24 h in a 0.1 M chlorosulphonic acid in dichloroethane solution.

In a parallel study, the parameters of the different membrane modification steps (dehydrofluorination, grafting and sulphonation) were altered and the conditions were made more extreme in an attempt to achieve NaCl retentions above 30% and thus to bring the membrane performance to the level of tighter NF. Based on visual observations, the grafting step was reduced from 18 to 6 h since a complete solidification of the reaction environment was already observed after 6 h. With as aim to achieve a higher degree of grafting and sulphonation and thus to increase salt retention, the concentrations of KOH, BPO and chlorosulphonic acid were increased from 0.1 to 1 M, from 3 to 3.75 g ml^{-1} and from 0.5 to 1 M, respectively. Based on the last entry in table 8.1, the salt retention remains rather low even after applying the more extreme conditions, although a certain improvement can be seen.[312,313]

The influence of the membrane modifcations on the membrane morphology can be observed in Figure 8.5. While no clear changes in the morphology can be seen from the pictures of the membrane cross-sections, the images of the surface of the PVDF and PVDF-

g-PSSA do look different. It appears that the PVDF surface is successfully covered with a grafted sulphonated polystyrene layer.

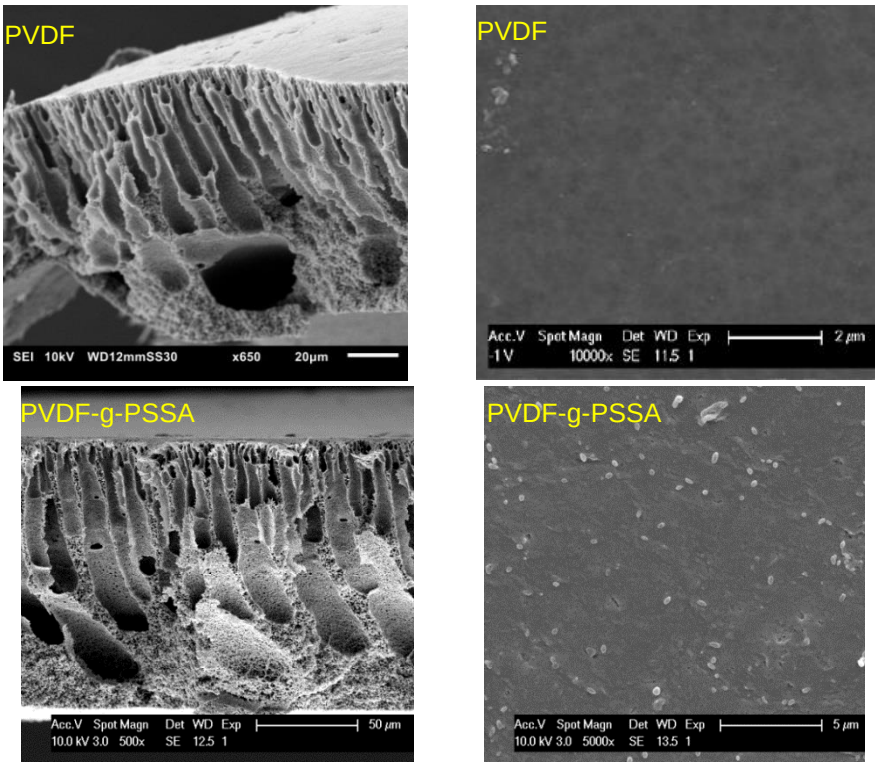

Figure 8.5. SEM images of the cross-sections and surfaces of the parent PVDF membranes and of the PVDF-g-PSSA membranes.

Using these more intensified reaction conditions, the polystyrene grafting process was repeated a second and third time, prior to performing the sulphonation step to further improve the salt rejection. This would occur through an attack by BPO at the sites marked with an * in scheme 8.1, generating free radical sites that can be further grafted with polystyrene. This would result in the creation of extended and/or branched polystyrene chains, which would lead to thicker and/or denser grafted layers on the PVDF.

Table 8.2. Retention and permeance of PVDF-g-PSSA membranes after further modifications. Filtration conditions: operating pressure: 20 bar, rotation speed: 500 rpm and feed: 35 µM RB and 1 g L^{-1} NaCl in milliQ water or 1 g L^{-1} $MgSO_4$ in miliQ water.

	Permeance ($l\ h^{-1}.m^{-2}.bar^{-1}$)	Retention (%)		
		Rose Bengal	NaCl	$MgSO_4$
PVDF-g-PSSA	3.0±0.5	99.9±0.4	39.7±0.8	61.3±0.7
PVDF-g-PSSA-2	2.4±0.3	97.0±4.0	48.3±2.6	66.4±0.8
PVDF-g-PSSA-2*	2.1±0.2	61.2±6.2	8.8±1.2	19.6±1.1
PVDF-g-PSSA-3	2.4±0.6	99.4±1.3	57.1±0.4	77.4±0.5
PVDF-g-PSSA-A	2.6±0.8	81.8±7.4	6.0±2.2	14.8±1.5

After a second and a third grafting step and subsequent sulphonation, the salt retention further increased while the permeance decreased (Table 8.2), caused by the formation of a more dense and thicker layer on top of the membrane and inside the membrane pores. Indeed, it can be expected that the second and third grafting step will take place wherever

the initiator and the monomers can still reach, hence filling up the remaining voids with extra polystyrene or extending the polystyrene chains that lay on top of the dense layer. However, this could not be confirmed by the SEM images as they all look quite similar (Fig. 8.6). A close-up of the dense layer of the PVDF-g-PSSA membranes with different number of grafting steps could also not give closure on the formation of a thicker polystyrene top layer (Fig. 8.7). But when the surface layers of the membranes were visualised, the increase in the fraction of polystyrene could be observed by an increase in the number of surface features (white fragments in Fig. 8.8), suggesting that the degree of grafting could further be increased by performing several separate grafting steps of 6h.

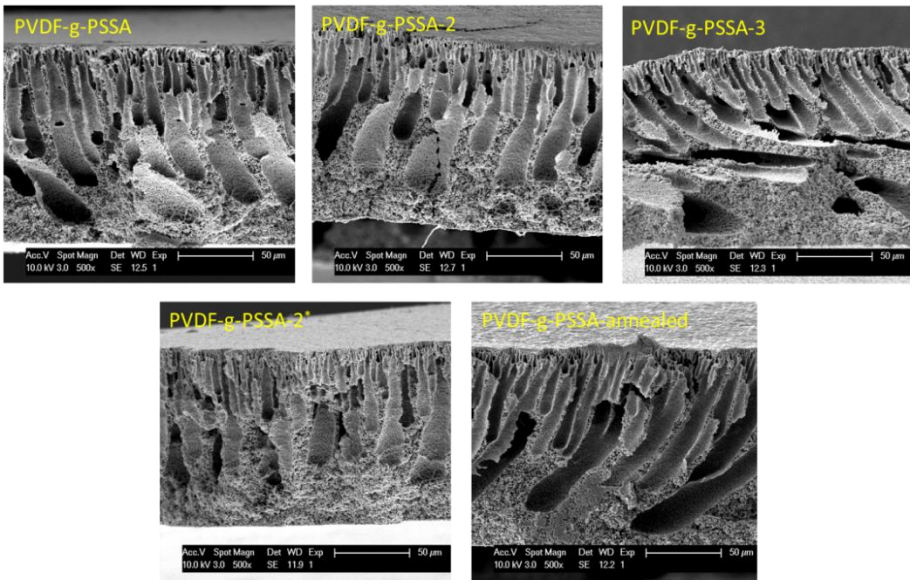

Figure 8.6. SEM images of the cross-sections of the different PVDF-g-PSSA membranes.

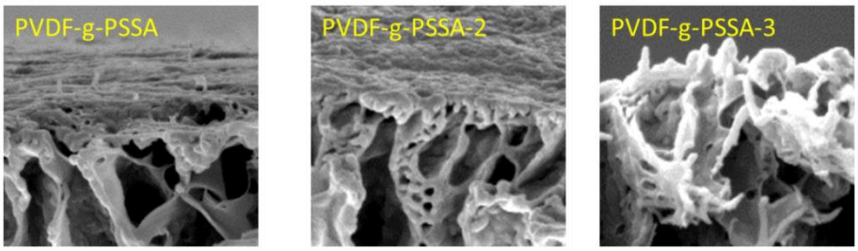

Figure 8.7. Close-up SEM images of the dense layer of the PVDF-g-PSSA membranes with different number of grafting steps.

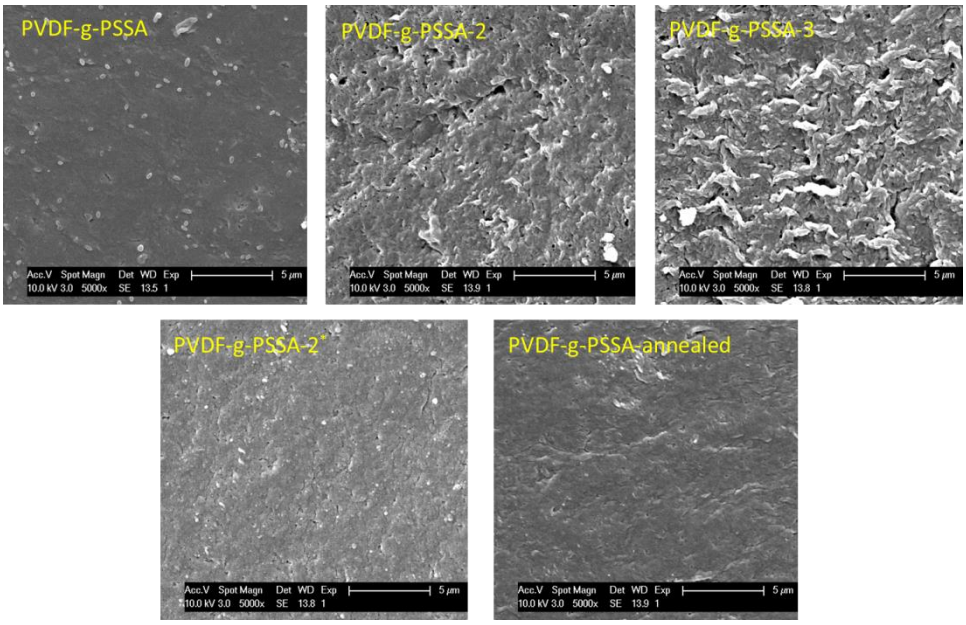

Figure 8.8. SEM images of the surface areas of the different PVDF-g-PSSA membranes.

If the second grafting step is performed after the sulphonation step and without further sulphonation afterwards, a decrease in performance is observed. Indeed, both the Rose Bengal and the NaCl retention go down. This can be explained based on the high hydrophobicity of polystyrene and thus the outer layers of the membrane. While handling this membrane, it could be noted that it was rather brittle. So it can be assumed that several microcracks might have been created when increasing the trans-membrane pressure during the filtration experiments. Finally, for the annealed membranes also a decrease in performance was observed, which contradicts the knowledge available in the literature. Indeed, it would be expected that the salt rejection would increase after annealing since it causes void shrinkage through a better chain stacking.[326] Since each membrane was tested 3 times and the performance of the annealed membrane was compared with the parent PVDF-g-PSSA membrane, an experimental error could not be at the origin of this unexpected behaviour. A possible hypothesis for this behaviour could be that the charges cluster during the annealing step, generating some kind of ion channels. This is well known for related Nafion® type membranes.[335] These channels would facilitate transport of charged components through the membrane with a lower retention as result.

8.3.3 pH-stability

It has been shown that PVDF membranes are not stable under alkaline conditions as a consequence of the dehydrofluorination reaction, which generates carbon-carbon double and triple bonds with the elimination of HF molecules. This process deteriorates the membrane structure by generating a more open structure with wider and larger pores.[298] This deterioration was also observed experimentally by a decline in the salt and dye retention and an increase in the permeance for the parent PVDF membrane after exposure to alkaline conditions (1 M NaOH solution, Fig. 8.9).

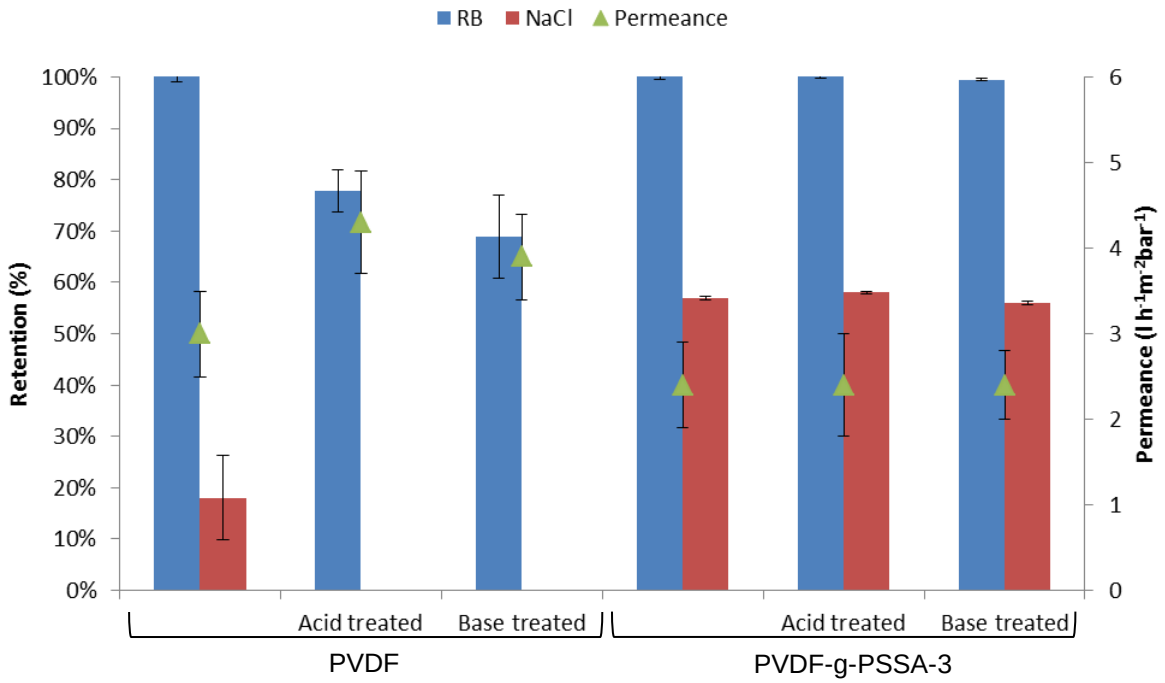

Figure 8.9. Influence of pH on the permeance and on the salt and dye retention for PVDF and PVDF-g-PSSA-3.

From Figure 8.9, it can be observed that the retentions of both RB and NaCl decrease for the parent PVDF membrane upon soaking for 1 week at extreme pH, both acidic and basic, while it remains constant for the PVDF-g-PSSA-3 after such treatments. Even during such long exposure, the sulphonated polystyrene thus either protects the PVDF backbone from deterioration in the presence of acid or base, or the dehydrofluorination had reached completion already during the membrane preparation. The permeance of PVDF-g-PSSA-3 remained constant around 2.4 l $h^{-1}.m^{-2}.bar^{-1}$, while the permeance for PVDF increased after acid and base treatments indicating a loss of membrane integrity. By grafting the PVDF membrane with sulphonated polystyrene, exceptional membranes that are stable in both acidic and alkaline environment were thus obtained.

8.4 Conclusions

PVDF-g-PSSA NF-membranes were prepared by grafting polystyrene on dehydrofluorinated polyvinylidene fluoride membranes, followed by a subsequent sulphonation of the styrene groups. By means of a prolonged exposure to extreme pH-conditions, it was demonstrated that these membranes are remarkably resistant towards chemical attack instigated by these conditions. This was verified by the stable performance (salt, dye rejection and permeance) before and after exposure of the membrane to pH =0 and 14 for more than one week. Furthermore, it was demonstrated that extra grafting steps could further enh densify the membranes, improving the salt rejections (up to ≈60% for NaCl), while keeping the permeance at decent level (from 3.0 to 2.4 l $h^{-1}.m^{-2}.bar^{-1}$). Possibly even higher salt retentions can be realised still by better fixing the selective layer through crosslinking and by further increasing the charge density.

Chapter 9

Conclusions and perspectives

9.1 Conclusions

With the target of bridging the gap between the fuel cell industry and the chemical industry, this Ph.D. project aimed to improve two of the main components for the H_2-O_2 fuel cell, namely the electrocatalysts and the proton-exchange membrane. At the same time the possibility to perform other redox reactions in a half-cell setup was investigated. This could then ultimately result in the expansion of the use of fuel cells from its sole role of electricity generation to the simultaneous generation (or so-called cogeneration) of industrially valuable products and electricity. This approach will not only lead to more sustainable production processes, converting the reaction energy that would otherwise be lost as heat into valuable electricity, but also to a more efficient use of reagents by increasing the product selectivity by controlling the cell potential. The fuel cell industry will benefit from this approach as a consequence of the added value of the product compared to water. In this context, it was investigated if hydrogen peroxide, hydroxylamine or aniline could be successfully obtained from the cathodic reduction of oxygen, nitrogen monoxide and nitrobenzene, respectively. To reach the first goal of improving the electrocatalysts, non-noble metal-containing or metal-free electrocatalysts were investigated as candidates to perform these reactions. As for the proton-exchange membranes, polyvinylidene membranes grafted with sulphonated polystyrene were tested as alternatives for Nafion® to improve the fuel cell performance.

9.1.1 Electrocatalysts

Hydrogen peroxide production

Metal-free NOMCs were prepared by using a novel nanocasting method, thoroughly characterised and subsequently evaluated as electrocatalysts for the reduction of O_2 to H_2O_2 in a fuel cell. Our novel nanocasting method resulted in several properties advantageous for the electrocatalytic performance, (1) by using SBA-15, which has a two-dimensional, interconnected pore structure, a high surface area (> 750 m²/g) was ensured, (2) the N-dopants were made readily available by covering the surface of SBA-15 first with the dopant precursor alone and (3) by filling up the remaining pore volume with dihydroxynaphthalene a high degree of graphitisation was achieved. From the electrochemical tests, it could then be deduced that the above properties were indeed important to obtain a N-doped carbon with an excellent performance for the cogeneration of electricity and hydrogen peroxide. The NOMC with the best performance had an electron transfer number close to two (92% selectivity to H_2O_2) and exhibited remarkably high kinetic current densities (-16 mA/cm²) and long-term stability (10% decay in current after 5h) when compared to results previously published in literature.

From a thorough investigation of the influence of the electrode composition on the electrochemical performance, it was learned that of the five investigated parameters, there were two with a big impact on the selectivity towards H_2O_2, the catalyst and the ionomer loadings. An increase in both resulted in a decreased selectivity to hydrogen peroxide. This underlines the importance of a uniform method to prepare the electrodes for electrochemical testing, as this would allow comparing different electrocatalysts for the same reduction reaction. Thus far its influence was underestimated and not often taken into account when comparing different electrocatalysts.

Hydroxylamine production

Iron-containing N-doped carbons (Fe-PANI-AC) were synthesised according to a procedure inspired by the literature and their electrocatalytic performance in the reduction of NO to hydroxylamine was investigated and compared with the reference electrocatalyst iron

phthalocyanine supported on activated carbon (FePc/AC). The most optimal Fe-PANI-AC was obtained with a pyrolysis temperature of 900°C and with an initial metal:aniline molar ratio of 1:4. Based on the results of the chronoamperometric experiments performed with a 6 or 18% NO in N_2 feed and the physicochemical characterisation, it could be concluded that Fe-PANI-AC outperformed the reference electrocatalyst at higher NO concentrations (increase of 33% in terms of selectivity towards NH_2OH, 1.5 times higher power generation, and a nearly threefold increase in NH_2OH production rate) as a consequence of the presence of different types of active sites. Whether they are less accessible or whether they adsorb NO more weakly, could not be determined yet but both types of sites would result in higher selectivity to aniline at higher NO concentrations in the feed. From an industrial point of view, this enhanced performance at higher NO concentrations is more interesting as more product could be obtained in a shorter period.

Aniline production

For the reduction of nitrobenzene to aniline both non-noble metal-containing N-doped carbons and metal-free doped ordered mesoporous carbons were evaluated. The selectivity towards the desired aniline could be enhanced by using Cu-containing N-doped carbons compared to the electrocatalysts applied in literature. This was attributed to the presence of small copper oxides inside the final material. The best non-noble metal-containing N-doped carbon composite electrocatalyst was achieved with a low aniline loading (0.2 mL per 0.5 g activated carbon), an aniline:metal molar ratio of 4:1 and copper as metal species (Cu-PANI-AC-A). By evaluating the performance of doped ordered mesoporous carbons, it could furthermore be concluded that the presence of metals is not a requirement to obtain an active electrocatalyst for the nitrobenzene reduction reaction. In this case, the best performance was obtained with the N-doped ordered mesoporous carbon (NOMC) electrocatalyst. The selectivity to aniline was enhanced from <20% to 82% with Cu-PANI-AC-A and further to 86% with NOMC. This increase in selectivity is advantageous with respect to the aim of cogenerating aniline and electricity in a fuel cell.

9.1.2 Proton-exchange membrane

For all the above reactions, it is important to have an efficient and cost-effective proton-exchange membrane, which separates the two half-cells in a fuel cell. As such direct contact between the two reagents is avoided and electricity is generated by the flow of electrons, which are liberated by the oxidation of one reagent at the anode and which flow to the cathode to perform the reduction reaction. Therefore, the three different steps (dehydrofluorination, grafting and sulphonation) of the synthesis method of PVDF-g-PSSA were optimised with respect to the proton conductivity in attempt to replace Nafion® as proton-exchange membrane in a fuel cell. Of the eight different parameters that were investigated, three were found having the largest influence on the proton conductivity, namely (1) the concentration of KOH solution used to perform the dehydrofluorination, (2) the temperature at which the grafting step was performed and (3) the chlorosulphonic acid concentration during the sulhponation step. The best result was obtained by performing the dehyrofluorination at room temperature in a 1 M KOH solution for 1 h, followed by 3 subsequent grafting steps, each performed at 60°C for 6 h in a 80/20 col% styrene/tetrahydrofuran solution containing 3.75 x 10^{-3} g ml^{-1} of benzoylperoxide and terminated by a sulphonation for 24 h in a 1 M chlorosulphonic acid in dichlorethane solution. This gave a proton conductivity of 0.25 S/cm, which is a 4-fold increase with respect to the

published results with the same class of membranes. Based on a comparison with the commercial Nafion® membrane, it could be concluded that the best PVDF-g-PSSA membrane reached higher proton conductivities, up to a 6-fold increase at elevated temperatures (80°C) and, therefore, can be considered as potential replacement for the expensive Nafion®. This enhanced performance was linked with the better water management of the PVDF-g-PSSA membranes resulting in a higher water retention inside its pores at higher temperatures as compared to Nafion®.

By evaluating the filtration performance before and after prolonged exposure to extreme pH's (0 or 14), it was also established that this type of membrane is also a promising candidate as a pH resistant nanofiltration membrane as no decline in salt rejections was observed. The optimal membrane reached NaCl rejections up to 60% and a water permeance of about 2.4 l/h.m².bar.

9.2 Perspectives

While this Ph.D. thesis underlined the possibility to perform other reduction reactions besides the reduction of oxygen in a fuel cell, validating the so-called cogeneration approach, there is still room for improvement. The selectivity towards the target products can be further enhanced while at the same time maximising the current generation and thus the reagent conversion.

For the ORR, NOMCs were shown to combine a high stability with a high selectivity to H_2O_2 in an alkaline environment. However, as a consequence of the scarce availability of commercial anion-exchange membranes, the most commonly applied fuel cells work under acidic conditions. Future work should thus investigate the possibility to use these NOMCs as electrocatalysts in an acidic medium or an attempt should be made to synthesise better anion-exchange membranes. While the non-noble metal-containing electrocatalysts were originally intended for the other two reduction reactions, future work should investigate their applicability in the ORR in both alkaline and acidic environment since electrocatalysts with comparable compositions showed promising results in literature for this specific reaction. Furthermore, since a lot of research on doped carbon materials revealed that they are not active or less active in an acidic environment, it might also be necessary to try and enhance the performance of the NOMCs by incorporating small amounts of non-noble metals in the final structure.

Due to practical problems with the experimental setup for the NO reduction reaction it was not possible to evaluate the performance of all the prepared electrocatalysts. Only Fe-PANI-AC could be evaluated, leaving a lot of room for improvement in this field. The selectivity and the current generation can still be improved, for example other metal species with similar oxidation states as iron (e.g. cobalt or manganese) could be investigated for this purpose. Moreover, the optimisation of the synthesis method (*e.g.* pyrolysis temperature, type of activated carbon support and metal loading) is expected to lead to further improvements in the electrocatalytic performance. Finally, the applicability of the doped OMCs with or without coordinated metals should still be investigated for this reduction reaction.

Although significant progress has been made in terms of performance for the electrochemical reduction of nitrobenzene to aniline, there are still some routes left unexplored. It was demonstrated in this work that the activity and especially the selectivity towards aniline of the nitrobenzene reduction reaction could be significantly enhanced to 82% by substituting the previous optimum Cu nanoparticles supported on undoped MWCNTs with Cu-containing N-doped carbons. It was further established that metals were not absolutely necessary as N-doped ordered mesoporous carbons were able to perform the reduction of nitrobenzene with an even higher selectivity (87%) towards aniline, while achieving equally high kinetic current densities and low overpotentials. It was also shown that each dopant resulted in the improvement of a different aspect of the electrochemical performance. The incorporation of boron led to enhanced kinetic current densities, nitrogen doping gave higher selectivity to aniline and the presence of phosphorus resulted in the lowest overpotential. Therefore, an interesting strategy to further enhance the performance might be to investigate the possible synergetic effects between the different dopant elements by preparing dual- or ternary-doped ordered mesoporous carbon materials.

As the applications of the investigated electrocatalysts are not limited to the reactions under study, future investigations could extend their use to other applications or other reactions. Another promising cogeneration example is the oxidation of glycerol to dihydroxyacetone which could replace the hydrogen oxidation reaction. Glycerol has the

advantage that it is produced in excess as a by-product of biodiesel production making it less useful for industry than hydrogen, which has many other fields of applications, e.g. as the steam reforming reaction to generate natural gas or methane. Furthermore, as pyridinic and pyrrolic N are basic sites, the N-doped OMCs could potentially be applied as base catalysts for example in the Knoevenagel condensation reaction. Finally, instead of applying the investigated electrocatalysts for the cogeneration of electricity and valuable chemicals in a fuel cell, they can also be applied in electrolysis cells, which can e.g. use renewable power sources to enable the efficient use of CO_2 and H_2O as renewable feedstock for energy storage and fuel production. Water can be split into hydrogen and oxygen during the energy peaks to store the excess energy as chemical, which can then be used again in a fuel cell to generate electricity with water as a side-product. In the case of CO_2, the aim is to reduce it to methane, ethylene or longer chain organics with as goal to obtain a circular carbon chemistry and to decrease the CO_2 content in the atmosphere. Finally, it is not expected that the proton conductivity of the PVDF-g-PSSA membranes can still be further improved since a thorough optimisation of the synthesis method was performed during this thesis. However, the proton conductivity, while important, is not the only relevant parameter for the fuel cell performance; also its long-term stability is important. In the future, it is thus crucial to investigate the changes of the membrane performance as a function of time in a real fuel cell setup as part of the membrane electrode assembly (MEA). Also the effect of temperature on the proton conductivity should be investigated at temperatures above 80°C to confirm the lower dependence of the PVDF-g-PSSA membranes of water for their proton conductivity when compared with commercial Nafion®. To further improve the salt rejection of PVDF-g-PSSA membranes, the possibility to cross-link the parent PVDF and the grafted polystyrene could be investigated. Besides for the investigated applications, future work could also focus on the application of these membranes in other research areas as for example reverse osmosis or electrodialysis, the most common use of which is in the desalination of sea water.

The work presented here explored the initial performance of two classes of electrocatalysts and one proton-exchange membrane with as aim their use in a fuel cell for the cogeneration of electricity and valuable chemicals. However, to really move to commersialisation the developed materials (membranes and electrocatalysts) should be subjected to actual fuel cell tests. For this purpose, the materials have to be combined together with a gas diffusion layer and a current collector into MEAs. Since a lot of parameters (as water management, catalyst accessibility, cross-over, etc.) have to be taken into account, this is not a straightforward process. Therefore, some of the future work should focus on developing a suitable synthesis method for the MEAs. These MEAs can then be tested in an actual fuel cell to investigate the performance of the ensemble under the real application conditions and no longer under half-cell conditions. This will give a better idea about the potential use of the investigated electrocatalysts and membrane for cogeneration purposes. These MEAs should further also be investigated by means of accelerated degradation tests to investigate the materials durability.

Once the MEAs pass the above-mentioned tests, future steps towards industrialisation of this electrochemical cogeneration approach should include the following: (1) scaling-up of the production process, which will require more efforts for the N-doped electrocatalysts as it includes a larger number of production steps, (2) in the case of the nitrobenzene reduction reaction, it is important to further improve the reaction rate as incomplete conversions (up to 50%) are obtained after long reaction times (52 h), which could be achieved either by further improving the active sites or by increasing the number of available active sites, (3) both for the oxygen reduction reaction and the nitrogen monoxide reaction, it is important to further

screen the different electrocatalysts to discover the optimal composition to selectively obtain the respective target products at a fast enough rate, and (4) for the nitrobenzene reduction it is also important to investigate the compatibility of the ethanolic reaction environment with the membranes as some parameters, like swelling and proton conductivity, might differ from an aqueous to an ethanolic environment.

Bibliography

1 Y. Shao, J. Sui, G. Yin and Y. Gao, *Appl. Catal. B Environ.*, 2008, **79**, 89–99.
2 Y. Zheng, Y. Jiao, M. Jaroniec, Y. Jin and S. Z. Qiao, *Small*, 2012, **8**, 3550–3566.
3 M. S. Larminie, J., Dicks, A., McDonald, *Fuel cell systems explained*, 2003, vol. 2.
4 J. Benziger, J. Nehlsen, D. Blackwell, T. Brennan and J. Itescu, *J. Memb. Sci.*, 2005, **261**, 98–106.
5 J. R. Varcoe and R. C. T. Slade, *Fuel Cells*, 2005, **5**, 187–200.
6 R. Borup, J. Meyers, B. Pivovar, Y. S. Kim, R. Mukundan, N. Garland, D. Myers, M. Wilson, F. Garzon, D. Wood, P. Zelenay, K. More, K. Stroh, T. Zawodzinski, X. J. Boncella, J. E. Mcgrath, O. M. Inaba, K. Miyatake, M. Hori, K. Ota, Z. Ogumi, S. Miyata, A. Nishikata, Z. Siroma, Y. Uchimoto, K. Yasuda, K. Kimijima and N. Iwashita, *Chem. Rev.*, 2007, **107**, 3904–3951.
7 Y.-J. Wang, J. Qiao, R. Baker and J. Zhang, *Chem. Soc. Rev.*, 2013, **42**, 5768–5787.
8 A. Verdaguer-Casadevall, D. Deiana, M. Karamad, S. Siahrostami, P. Malacrida, T. W. Hansen, J. Rossmeisl, I. Chorkendorff and I. E. L. Stephens, *Nano Lett.*, 2014, **14**, 1603–1608.
9 C. W. Jones and H. J. Clark, in *Applications of hydrogen peroxide and derivatives, RSC, UK*, 1999, pp. 1–36.
10 J. M. Campos-Martin, G. Blanco-Brieva and J. L. G. Fierro, *Angew. Chemie - Int. Ed.*, 2006, **45**, 6962–6984.
11 I. Yamanaka, T. Onizawa, S. Takenaka and K. Otsuka, *Angew. Chemie - Int. Ed.*, 2003, **42**, 3653–3655.
12 I. Yamanaka, S. Tazawa, T. Murayama, R. Ichihashi and N. Hanaizumi, *ChemSusChem*, 2008, **1**, 988–992.
13 K. Otsuka, H. Sawada and I. Yamanaka, *J. Electrochem. Soc.*, 1996, **143**, 3491–3497.
14 W. Lewdorowicz, W. Tokarz, P. Piela and P. K. Wrona, *J. New Mater. Electrochem. Syst.*, 2006, **9**, 339–343.
15 Y. Alvarez-Gallego, X. Dominguez-Benetton, D. Pant, L. Diels, K. Vanbroekhoven, I. Genné and P. Vermeiren, *Electrochim. Acta*, 2012, **82**, 415–426.
16 S. Polizzi, A. Benedetti, G. Fagherazzi, C. Goatin, R. Strozzi, G. Talamini and L. Toniolo, *J. Catal.*, 1987, **106**, 494–499.
17 M. T. de Groot, M. Merkx, A. H. Wonders and M. T. M. Koper, *J. Am. Chem. Soc.*, 2005, **127**, 7579–7586.
18 W. B. Fisher and L. Crescentini, *Kirk-Othmer Encyclopedia of Chemical Technology*, Wiley Interscience, 5th edn., 2011.
19 M. J. Foral and S. H. Langer, *Electrochim. Acta*, 1991, **36**, 299–307.
20 J. Wang, Z. Yuan, R. Nie, Z. Hou and X. Zheng, *Ind. Eng. Chem. Res.*, 2010, **49**, 4664–4669.
21 X. Meng, H. Cheng, Y. Akiyama, Y. Hao, W. Qiao, Y. Yu, F. Zhao, S. ichiro Fujita and M. Arai, *J. Catal.*, 2009, **264**, 1–10.
22 A. Furst, R. C. Berlo and S. Hooton, *Chem. Rev.*, 1965, **65**, 51–68.
23 X. Sheng, B. Wouters, T. Breugelmans, A. Hubin, I. F. J. Vankelecom and P. P. Pescarmona, *Appl. Catal. B Environ.*, 2014, **147**, 330–339.
24 B. Wouters, X. Sheng, A. Boschin, T. Breugelman, E. Ahlberg, I. F. J. Vankelecom, P. P. Pescarmona and A. Hubin, *Electrochim. Acta*, 2013, **111**, 405–410.
25 X. Sheng, B. Wouters, T. Breugelmans, A. Hubin, I. F. J. Vankelecom and P. P. Pescarmona, *ChemElectroChem*, 2014, **1**, 1198–1210.
26 Y. Nie, L. Li and Z. Wei, *Chem. Soc. Rev.*, 2015, **44**, 2168–2201.
27 X. Ge, A. Sumboja, D. Wuu, T. An, B. Li, F. W. T. Goh, T. S. A. Hor, Y. Zong and Z. Liu, *ACS Catal.*, 2015, **5**, 4643–4667.
28 Y. Jiao, Y. Zheng, M. Jaroniec and S. Z. Qiao, *Chem. Soc. Rev.*, 2015, **44**, 2060–2086.
29 L. Zhang and Z. Xia, *J. Phys. Chem. C*, 2011, **115**, 11170–11176.

30 P. H. Matter and U. S. Ozkan, *Catal. Letters*, 2006, **109**, 115–123.
31 J. K. Nørskov, J. Ressmeisl, A. Logadottir, L. Lindqvist, J. R. Kitchin, T. Bligaard and H. Jonsson, *J. Phys. Chem. B*, 2004, **108**, 17886–17892.
32 I. Katsounaros, S. Cherevko, A. R. Zeradjanin and K. J. J. Mayrhofer, *Angew. Chemie - Int. Ed.*, 2014, **53**, 102–121.
33 S. Mukerjee, S. Mukerjee, J. Ziegelbauer, J. Ziegelbauer, T. Arruda, T. Arruda, D. Ramaker, D. Ramaker, B. Shyam and B. Shyam, *Electrochem. Soc. Interface*, 2008, 46–52.
34 F. Jaouen, E. Proietti, M. Lefèvre, R. Chenitz, J.-P. Dodelet, G. Wu, H. T. Chung, C. M. Johnston and P. Zelenay, *Energy Environ. Sci.*, 2011, **4**, 114–130.
35 C. W. B. Bezerra, L. Zhang, K. Lee, H. Liu, A. L. B. Marques, E. P. Marques, H. Wang and J. Zhang, *Electrochim. Acta*, 2008, **53**, 4937–4951.
36 W. Wang, R. Wang, S. Ji, H. Feng, H. Wang and Z. Lei, *J. Power Sources*, 2010, **195**, 3498–3503.
37 G. S. Karlberg, *Phys. Rev. B - Condens. Matter Mater. Phys.*, 2006, **74**, 3–6.
38 Z. Quan, Y. Wang and J. Fang, *Acc. Chem. Res.*, 2013, **46**, 191–202.
39 Y. Bing, H. Liu, L. Zhang, D. Ghosh and J. Zhang, *Chem. Soc. Rev.*, 2010, **39**, 2184–2202.
40 V. R. Stamenkovic, B. Fowler, B. S. Mun, G. Wang, P. N. Ross, C. a Lucas and N. M. Marković, *Science*, 2007, **315**, 493–497.
41 V. R. Stamenkovic, B. S. Mun, M. Arenz, K. J. J. Mayrhofer, C. a Lucas, G. F. Wang, P. N. Ross and N. M. Markovic, *Nat. Mater.*, 2007, **6**, 241–247.
42 B. Geboes, I. Mintsouli, B. Wouters, J. Georgieva, A. Kakaroglou, S. Sotiropoulos, E. Valova, S. Armyanov, A. Hubin and T. Breugelmans, *Appl. Catal. B Environ.*, 2014, **150-151**, 249–256.
43 L. Gan, M. Heggen, R. O'Malley, B. Theobald and P. Strasser, *Nano Lett.*, 2013, **13**, 1131–1138.
44 Z. Chen, D. Higgins, A. Yu, L. Zhang and J. Zhang, *Energy Environ. Sci.*, 2011, **4**, 3167–3192.
45 J. Masa, W. Xia, M. Muhler and W. Schuhmann, *Angew. Chemie - Int. Ed.*, 2015, **54**, 10102–10120.
46 Q. Li, R. Cao, J. Cho and G. Wu, *Adv. Energy Mater.*, 2014, **4**, 1301415–1301434.
47 R. Jasinski, *Nature*, 1964, **201**, 1212–1213.
48 a. L. Bouwkamp-Wijnoltz, W. Visscher, J. a R. Van Veen and S. C. Tang, *Electrochim. Acta*, 1999, **45**, 379–386.
49 a. Biloul, F. Coowar, O. Contamin, G. Scarbeck, M. Savy, D. van den Ham, J. Riga and J. J. Verbist, *J. Electroanal. Chem. Interfacial Electrochem.*, 1990, **289**, 189–201.
50 a. Biloul, F. Coowar, O. Contamin, G. Scarbeck, M. Savy, D. van den Ham, J. Riga and J. J. Verbist, *J. Electroanal. Chem.*, 1992, **328**, 219–232.
51 a. Biloul, O. Contamin, G. Scarbeck, M. Savy, D. van den Ham, J. Riga and J. J. Verbist, *J. Electroanal. Chem.*, 1992, **335**, 163–186.
52 a. Biloul, F. Coowar, O. Contamin, G. Scarbeck, M. Savy, D. van den Ham, J. Riga and J. J. Verbist, *J. Electroanal. Chem.*, 1993, **350**, 189–204.
53 a. Biloul, O. Contamin, G. Scarbeck, M. Savy, B. Palys, J. Riga and J. Verbist, *J. Electroanal. Chem.*, 1994, **365**, 239–246.
54 M. Lefèvre, J. P. Dodelet and P. Bertrand, *J. Phys. Chem. B*, 2002, **106**, 8705–8713.
55 T. S. Olson, S. Pylypenko, P. Atanassov, K. Asazawa, K. Yamada and H. Tanaka, *J. Phys. Chem. C*, 2010, **114**, 5049–5059.
56 B. Wang, *J. Power Sources*, 2005, **152**, 1–15.
57 V. S. Bagotzky, M. R. Tarasevich, K. A. Radyushkina, O. A. Levina and S. I. Andrusyova, *J. Power Sources*, 1978, **2**, 233–240.
58 R. Franke, D. Ohms and K. Wiesener, *J. Electroanal. Chem. Interfacial Electrochem.*, 1989, **260**, 63–73.
59 J. a. R. van Veen, H. A. Colijn and J. F. Van Baar, *Electrochim. Acta*, 1988, **33**, 801–804.

60 D. Scherson, a. a. Tanaka, S. L. Gupta, D. Tryk, C. Fierro, R. Holze, E. B. Yeager and R. P. Lattimer, *Electrochim. Acta*, 1986, **31**, 1247–1258.
61 A. Van Der Putten, A. Elzing, W. Visscher and E. Barendrecht, *J. Electroanal. Chem.*, 1986, **205**, 233–244.
62 K. Wiesener, *Electrochim. Acta*, 1986, **31**, 1073–1078.
63 E. Yeager, *Electrochim. Acta*, 1984, **29**, 1527–1537.
64 S. Gupta, D. Tryk, I. Bae, W. Aldred and E. Yeager, *J. Appl. Electrochem.*, 1989, **19**, 19–27.
65 Y. Qian, P. Du, P. Wu, C. Cai and D. F. Gervasio, 2016.
66 F. Charreteur, F. Jaouen, S. Ruggeri and J. P. Dodelet, *Electrochim. Acta*, 2008, **53**, 2925–2938.
67 F. Charreteur, S. Ruggeri, F. Jaouen and J. P. Dodelet, *Electrochim. Acta*, 2008, **53**, 6881–6889.
68 U. I. Kramm, J. Herranz, N. Larouche, T. M. Arruda, M. Lefèvre, F. Jaouen, P. Bogdanoff, S. Fiechter, I. Abs-Wurmbach, S. Mukerjee and J.-P. Dodelet, *Phys. Chem. Chem. Phys.*, 2012, **14**, 11673–11688.
69 A. Zitolo, V. Goellner, V. Armel, M.-T. Sougrati, T. Mineva, L. Stievano, E. Fonda and F. Jaouen, *Nat. Mater.*, 2015, **14**, 937–42.
70 U. Tylus, Q. Jia, K. Strickland, N. Ramaswamy, A. Serov, P. Atanassov and S. Mukerjee, *J. Phys. Chem. C*, 2014, **118**, 8999–9008.
71 Y. Zhu, B. Zhang, X. Liu, D. W. Wang and D. S. Su, *Angew. Chemie - Int. Ed.*, 2014, **53**, 10673–10677.
72 E. F. Holby, G. Wu, P. Zelenay and C. D. Taylor, *J. Phys. Chem. C*, 2014, **118**, 14388–14393.
73 C. E. Szakacs, M. Lefèvre, U. I. Kramm, J.-P. Dodelet and F. Vidal, *Phys. Chem. Chem. Phys.*, 2014, **16**, 13654.
74 R. Zhou, M. Jaroniec and S. Z. Qiao, *ChemCatChem*, 2015, **44242**.
75 M. Lefvre, J. P. Dodelet, P. Bertrand, C. Electrocatalysts and B. L. Boulet, *J. Phys. Chem. B*, 2005, 16718–16724.
76 H. Alt, H. Binder and G. Sandstede, *J. Catal.*, 1973, **28**, 8–19.
77 C. Zhang, R. Hao, H. Yin, F. Liu and Y. Hou, *Nanoscale*, 2012, 7326–7329.
78 D.-W. Wang and D. Su, *Energy Environ. Sci.*, 2014, **7**, 576.
79 R. Liu, D. Wu, X. Feng and K. Müllen, *Angew. Chemie - Int. Ed.*, 2010, **49**, 2565–2569.
80 H. Wang, T. Maiyalagan and X. Wang, *Acs Catal.*, 2012, **2**, 781–794.
81 Z. Jin, J. Yao, C. Kittrell and J. M. Tour, *ACS Nano*, 2011, **5**, 4112–4117.
82 T. Sharifi, G. Hu, X. Jia and T. Wagberg, *Prepr. - Am. Chem. Soc. Div. Energy Fuels*, 2013, **58**, 1203–1204.
83 G. Liu, X. Li, P. Ganesan and B. N. Popov, *Electrochim. Acta*, 2010, **55**, 2853–2858.
84 D. Higgins, Z. Chen and Z. Chen, *Electrochim. Acta*, 2011, **56**, 1570–1575.
85 C. H. Choi, S. H. Park and S. I. Woo, *ACS Nano*, 2012, **6**, 7084–7091.
86 K. R. Lee, K. U. Lee, J. W. Lee, B. T. Ahn and S. I. Woo, *Electrochem. commun.*, 2010, **12**, 1052–1055.
87 N. P. Subramanian, X. Li, V. Nallathambi, S. P. Kumaraguru, H. Colon-Mercado, G. Wu, J. W. Lee and B. N. Popov, *J. Power Sources*, 2009, **188**, 38–44.
88 T. Xing, Y. Zheng, L. H. Li, B. C. C. Cowie, D. Gunzelmann, S. Z. Qiao, S. Huang and Y. Chen, *ACS Nano*, 2014, **8**, 6856–6862.
89 D. Guo, R. Shibuya, C. Akiba, S. Saji, T. Kondo and J. Nakamura, *Science (80-.).*, 2015, **351**, 1–24.
90 S. Yasuda, L. Yu, J. Kim and K. Murakoshi, *Chem. Commun. (Camb).*, 2013, **49**, 9627–9629.
91 Z. Luo, S. Lim, Z. Tian, J. Shang, L. Lai, B. MacDonald, C. Fu, Z. Shen, T. Yu and J. Lin, *J. Mater. Chem.*, 2011, **21**, 8038.
92 H. Niwa, K. Horiba, Y. Harada, M. Oshima, T. Ikeda, K. Terakura, J. I. Ozaki and S. Miyata, *J. Power Sources*, 2009, **187**, 93–97.

93 H. Kim, K. Lee, S. I. Woo and Y. Jung, *Phys. Chem. Chem. Phys.*, 2011, **13**, 17505.
94 J. Zhang and L. Dai, *ACS Catal.*, 2015, **5**, 7244–7253.
95 J. Liu, P. Song, Z. Ning and W. Xu, *Electrocatalysis*, 2015, **6**, 132–147.
96 Y. Jiao, Y. Zheng, M. Jaroniec and S. Z. Qiao, *J. Am. Chem. Soc.*, 2014, **136**, 4394–4403.
97 D. Geng, N. Ding, T. S. A. Hor, Z. Liu, X. Sun and Y. Zong, *J. Mater. Chem. A*, 2015, **3**, 1795–1810.
98 I.-Y. Jeon, H.-J. Choi, M. Choi, J.-M. Seo, S.-M. Jung, M.-J. Kim, S. Zhang, L. Zhang, Z. Xia, L. Dai, N. Park and J.-B. Baek, *Sci. Rep.*, 2013, **3**, 1810.
99 Y. Zheng, Y. Jiao and S. Z. Qiao, *Adv. Mater.*, 2015, **27**, 5372–5378.
100 Z. Guo, G. Ren, C. Jiang, X. Lu, Y. Zhu, L. Jiang and L. Dai, *Sci. Rep.*, 2015, **5**, 17064.
101 Y. Xue, D. Yu, L. Dai, ab R. Wang, D. Li, A. Roy, F. Lu, H. Chen, Y. Liu and J. Qu, *Phys.Chem.Phys.Chem.Chem.Phys.*, 2013, **15**, 12220–12226.
102 C. Domínguez, F. J. Pérez-Alonso, S. A. Al-Thabaiti, S. N. Basahel, A. Y. Obaid, A. O. Alyoubi, J. L. Gómez De La Fuente and S. Rojas, *Electrochim. Acta*, 2015, **157**, 158–165.
103 V. Perazzolo, C. Durante, R. Pilot, A. Paduano, J. Zheng, G. A. Rizzi, A. Martucci, G. Granozzi and A. Gennaro, *Carbon N. Y.*, 2015, **95**, 949–963.
104 L. Wang and M. Pumera, *Chem. Commun.*, 2014, **50**, 12662–12664.
105 J. Masa, A. Zhao, W. Xia, Z. Sun, B. Mei, M. Muhler and W. Schuhmann, *Electrochem. commun.*, 2013, **34**, 113–116.
106 H. Shi, Y. Shen, F. He, Y. Li, A. Liu, S. Liu and Y. Zhang, *J. Mater. Chem. A*, 2014, **2**, 15704–15716.
107 M. S. Thorum, J. M. Hankett and A. A. Gewirth, *J. Phys. Chem. Lett.*, 2011, **2**, 295–298.
108 A. Kraytsberg and Y. Ein-Eli, *Energy & Fuels*, 2014, **28**, 7303–7330.
109 Z. Zhang, E. Chalkova, M. Fedkin, C. Wang, S. N. Lvov, S. Komarneni and T. C. M. Chung, *Macromolecules*, 2008, **41**, 9130–9139.
110 N. Kang, J. Shin, T. S. Hwang and Y. S. Lee, *React. Funct. Polym.*, 2016, **99**, 42–48.
111 J. Healy, C. Hayden, T. Xie, K. Olson, R. Waldo, M. Brundage, H. Gasteiger and J. Abbott, *Fuel Cells*, 2005, **5**, 302–308.
112 H. Zhang and P. K. Shen, *Chem. Rev.*, 2012, **112**, 2780–2832.
113 S. L. Chen, L. Krishnan, S. Srinivasan, J. Benziger and A. B. Bocarsly, *J. Memb. Sci.*, 2004, **243**, 327–333.
114 M. A. Hickner, H. Ghassemi, Y. S. Kim, B. R. Einsla and J. E. McGrath, *Chem. Rev.*, 2004, **104**, 4587–4611.
115 K. Miyatake, H. Zhou, H. Uchida and M. Watanabe, *Chem. Commun. (Camb).*, 2003, 368–369.
116 Y. He, C. Tong, L. Geng, L. Liu and C. Lü, *J. Memb. Sci.*, 2014, **458**, 36–46.
117 Y. Yin, J. Fang, T. Watari, K. Tanaka, H. Kita and K. Okamoto, *J. Mater. Chem.*, 2004, **14**, 1062–1070.
118 H. Vogel and C. S. Marvel, *J. Polym. Sci.*, 1961, **50**, 511–539.
119 M. Kawahara, J. Morita, M. Rikukawa, K. Sanui and N. Ogata, *Electrochim. Acta*, 2000, **45**, 1395–1398.
120 K. A. Perry, K. L. More, E. Andrew Payzant, R. a. Meisner, B. G. Sumpter and B. C. Benicewicz, *J. Polym. Sci. Part B Polym. Phys.*, 2014, **52**, 26–35.
121 S. Matar, A. Higier and H. Liu, *J. Power Sources*, 2010, **195**, 181–184.
122 M. Mamlouk and K. Scott, *Int. J. Hydrogen Energy*, 2010, **35**, 784–793.
123 S. Swier, Y. S. Chun, J. Gasa, M. T. Shaw and R. A. Weiss, *Polym. Eng. Sci.*, 2005, **45**, 1081–1091.
124 C. Perrot, L. Gonon, M. Bardet, C. Marestin, A. Pierre-Bayle and G. Gebel, *Polymer (Guildf).*, 2009, **50**, 1671–1681.
125 S. Holmberg, T. Lehtinen, J. Nasman, D. Ostrovskii, M. Paronen, R. Serimaa, F. Sundholm, G. Sundholm, L. Torell and M. Torkkeli, *J. Mater. Chem.*, 1996, **6**, 1309.

126 T. Lehtinen, G. Sundholm, S. Holmberg, F. Sundholm, P. Björnbom and M. Bursell, *Electrochim. Acta*, 1998, **43**, 1881–1890.
127 Y. W. Kim, D. K. Lee, K. J. Lee and J. H. Kim, *Eur. Polym. J.*, 2008, **44**, 932–939.
128 M. M. Nasef, H. Saidi and K. Z. M. Dahlan, *J. Memb. Sci.*, 2009, **339**, 115–119.
129 M. Mamlouk, J. A. Horsfall, C. Williams and K. Scott, *Int. J. Hydrogen Energy*, 2012, **37**, 11912–11920.
130 J. R. Varcoe, R. C. T. Slade and E. Lam How Yee, *Chem. Commun. (Camb).*, 2006, 1428–1429.
131 M. Mamlouk and K. Scott, *J. Power Sources*, 2012, **211**, 140–146.
132 S. Chempath, B. R. Einsla, L. R. Pratt, C. S. Macomber, J. M. Boncella, J. A. Rau and B. S. Pivovar, *J. Phys. Chem. C*, 2008, **112**, 3179–3182.
133 H. Hou, G. Sun, R. He, Z. Wu and B. Sun, *J. Power Sources*, 2008, **182**, 95–99.
134 J. Pan, C. Chen, L. Zhuang and J. Lu, *Acc. Chem. Res.*, 2012, **45**, 473–481.
135 J. Yan and M. A. Hickner, *Macromolecules*, 2010, **43**, 2349–2356.
136 J. Li, X. Yan, Y. Zhang, B. Zhao and G. He, *RSC Adv.*, 2016, **6**, 58380–58386.
137 M. Tomoi, K. Yamaguchi, R. Ando, Y. Kantake, Y. Aosaki and H. Kubota, *J. Appl. Polym. Sci.*, 1997, **64**, 1161–1167.
138 L. Sun, J. Guo, J. Zhou, Q. Xu, D. Chu and R. Chen, *J. Power Sources*, 2012, **202**, 70–77.
139 W. Chen, X. Yan, X. Wu, S. Huang, Y. Luo, X. Gong and G. He, *J. Memb. Sci.*, 2016, **514**, 613–621.
140 G. Merle, M. Wessling and K. Nijmeijer, *J. Memb. Sci.*, 2011, **377**, 1–35.
141 G. Couture, A. Alaaeddine, F. Boschet and B. Ameduri, *Prog. Polym. Sci.*, 2011, **36**, 1521–1557.
142 A. L. Ong, S. Saad, R. Lan, R. J. Goodfellow and S. Tao, *J. Power Sources*, 2011, **196**, 8272–8279.
143 Z. Hu, W. Tang, D. Ning, X. Zhang, H. Bi and S. Chen, *Fuel Cells*, 2016, 1–11.
144 T. P. Pandey, H. N. Sarode, Y. Yang, Y. Yang, K. Vezzù, V. Di Noto, S. Seifert, D. M. Knauss, M. W. Liberatore and A. M. Herring, *J. Electrochem. Soc.*, 2016, **163**, H513–H520.
145 D. Geng, Y. Chen, Y. Chen, Y. Li, R. Li, X. Sun, S. Ye and S. Knights, *Energy Environ. Sci.*, 2011, **4**, 760.
146 I. Yamanaka, S. Tazawa, T. Murayama, T. Iwasaki and S. Takenaka, *ChemSusChem*, 2010, **3**, 59–62.
147 P. Landon, P. J. Collier, A. J. Papworth, J. Kiely and J. Graham, 2002, 2058–2059.
148 S. Guo, S. Zhang and S. Sun, *Angew. Chemie - Int. Ed.*, 2013, **52**, 8526–8544.
149 T. Murayama, S. Tazawa, S. Takenaka and I. Yamanaka, *Catal. Today*, 2011, **164**, 163–168.
150 H. A. Gasteiger, S. S. Kocha, B. Sompalli and F. T. Wagner, *Appl. Catal. B Environ.*, 2005, **56**, 9–35.
151 M. Schulze, N. Wagner, T. Kaz and K. A. Friedrich, *Electrochim. Acta*, 2007, **52**, 2328–2336.
152 E. Gülzow, M. Schulze, N. Wagner, T. Kaz, R. Reissner, G. Steinhilber and A. Schneider, *J. Power Sources*, 2000, **86**, 352–362.
153 N. Daems, X. Sheng, I. F. J. Vankelecom and P. P. Pescarmona, *J. Mater. Chem. A*, 2014, **2**, 4085–4110.
154 G. Wu, K. L. More, C. M. Johnston and P. Zelenay, *Science*, 2011, **332**, 443–447.
155 L. Wang, L. Zhang and J. Zhang, *Electrochem. commun.*, 2011, **13**, 447–449.
156 T.-P. Fellinger, F. Hasché, P. Strasser and M. Antonietti, *J. Am. Chem. Soc.*, 2012, 4072–4075.
157 S. Mao, Z. Wen, T. Huang, Y. Hou and J. Chen, *Energy Environ. Sci.*, 2014, **7**, 609–616.
158 N. Gokulakrishnan, N. Kania, B. Léger, C. Lancelot, D. Grosso, E. Monflier and A. Ponchel, *Carbon N. Y.*, 2011, **49**, 1290–1298.
159 Y. Wang, F. Zhang, Y. Wang, J. Ren, C. Li, X. Liu, Y. Guo, Y. Guo and G. Lu, *Mater.*

Chem. Phys., 2009, **115**, 649–655.
160 F. Rouquerol, J. Rouquerol and K. Sing, in *Adsorption by Powders and Porous solids*, eds. F. Rouquerol, J. Rouquerol and K. Sing, Academic Press, London, 1999, pp. 165–189.
161 C. Yu, S. Koh, J. E. Leisch, M. F. Toney and P. Strasser, *Faraday Discuss.*, 2008, **140**, 283–296.
162 J. J. Hernández, M. C. García-Gutiérrez, a. Nogales, D. R. Rueda and T. a. Ezquerra, *Compos. Sci. Technol.*, 2006, **66**, 2629–2632.
163 S. Lowell and E. J. Shields, in *Powder Surface Area and Porosity*, Chapman & Hall, New York, 3rd ed., 1991.
164 C. Carkeet, S. R. Dueker, J. R. Follett, T. E. Correa and A. J. Clifford, *FASEB*, 2001, **15**, A260–A260.
165 P. Gilbert, *J. Theor. Biol.*, 1972, **36**, 105–117.
166 N. Liu, L. Yin, C. Wang, L. Zhang, N. Lun, D. Xiang, Y. Qi and R. Gao, *Carbon N. Y.*, 2010, **48**, 3579–3591.
167 Z. Lei, L. An, L. Dang, M. Zhao, J. Shi, S. Bai and Y. Cao, *Microporous Mesoporous Mater.*, 2009, **119**, 30–38.
168 H. Nishihara, Y. Fukura, K. Inde, K. Tsuji, M. Takeuchi and T. Kyotani, *Carbon N. Y.*, 2008, **46**, 48–53.
169 W. Zou, X. Yuan, F. Zeng, X. Huang, S. Mo and D. Yuan, *Mater. Lett.*, 2012, **79**, 195–198.
170 H. Chang, S. H. Joo and C. Pak, *J. Mater. Chem.*, 2007, **17**, 3078.
171 C. Jin, G. Li, X. Wang, L. Zhao, Y. Wang and D. Sun, *Top. Catal.*, 2008, **49**, 118–124.
172 D. H. Lin, Y. X. Jiang, Y. Wang and S. G. Sun, *J. Nanomater.*, 2008, **2008**, 473791–473801.
173 W. Schmidt, *Microporous Mesoporous Mater.*, 2009, **117**, 372–379.
174 K. Lund, N. Muroyama and O. Terasaki, *Microporous Mesoporous Mater.*, 2010, **128**, 71–77.
175 Y. Xia and R. Mokaya, *Chem. Mater.*, 2005, **17**, 1553–1560.
176 I. Herrmann, U. I. Kramm, J. Radnik, S. Fiechter and P. Bogdanoff, *J. Electrochem. Soc.*, 2009, **156**, B1283–B1292.
177 Y. Okamoto, *Appl. Surf. Sci.*, 2009, **256**, 335–341.
178 C. Zhang, R. Hao, H. Liao and Y. Hou, *Nano Energy*, 2013, **2**, 88–97.
179 H. Liu, Y. Liu and D. Zhu, *J. Mater. Chem.*, 2011, **21**, 3335.
180 J. Liang, Y. Jiao, M. Jaroniec and S. Z. Qiao, *Angew. Chemie - Int. Ed.*, 2012, **51**, 11496–11500.
181 Z. H. Sheng, L. Shao, J. J. Chen, W. J. Bao, F. Bin Wang and X. H. Xia, *ACS Nano*, 2011, **5**, 4350–4358.
182 L. Braeken, R. Ramaekers, Y. Zhang, G. Maes, B. Van Der Bruggen and C. Vandecasteele, *J. Memb. Sci.*, 2005, **252**, 195–203.
183 P. Zhang, F. Sun, Z. Xiang, Z. Shen, J. Yun and D. Cao, *Energy Environ. Sci.*, 2014, **7**, 442–450.
184 X. Wang, J. S. Lee, Q. Zhu, J. Liu, Y. Wang and S. Dai, *Chem. Mater.*, 2010, **22**, 2178–2180.
185 Y. Zhang, K. Fugane, T. Mori, L. Niu and J. Ye, *J. Mater. Chem.*, 2012, **22**, 6575–6580.
186 S. Srinivasan, *Fuel Cells: From Fundamentals to Applications*, 2006.
187 X. Sheng, N. Daems, B. Geboes, M. Kurttepeli, S. Bals, T. Breugelmans, A. Hubin, I. F. J. Vankelecom and P. P. Pescarmona, *Appl. Catal. B Environ.*, 2015, **176-177**, 212–224.
188 A. J. Lemke, A. W. O'Toole, R. S. Phillips and E. T. Eisenbraun, *J. Power Sources*, 2014, **256**, 319–323.
189 S. J. Hamrock and M. a. Yandrasits, *J. Macromol. Sci. Part C*, 2006, **46**, 219–244.
190 A. Bonakdarpour, C. Delacote, R. Yang, A. Wieckowski and J. R. Dahn, *Electrochem. commun.*, 2008, **10**, 611–615.

191 A. Bonakdarpour, M. Lefevre, R. Yang, F. Jaouen, T. Dahn, J.-P. Dodelet and J. R. Dahn, *Electrochem. Solid-State Lett.*, 2008, **11**, B105.
192 University of York, *Hydrog. Peroxide*, 2014, 1–6.
193 J. Pan, C. Chen, Y. Li, L. Wang, L. Tan, G. Li, X. Tang, L. Xiao, J. Lu and L. Zhuang, *Energy Environ. Sci.*, 2014, **7**, 354.
194 J. Wang, S. Gu, R. B. Kaspar, B. Zhang and Y. Yan, *ChemSusChem*, 2013, **6**, 2079–2082.
195 O. D. Thomas, K. J. W. Y. Soo, T. J. Peckham, M. P. Kulkarni and S. Holdcroft, *J. Am. Chem. Soc.*, 2012, **134**, 10753–10756.
196 N. Ramaswamy and S. Mukerjee, *J. Phys. Chem. C*, 2011, **115**, 18015–18026.
197 I. Takahashi and S. S. Kocha, *J. Power Sources*, 2010, **195**, 6312–6322.
198 W. Jin, H. Du, S. Zheng, H. Xu and Y. Zhang, *J. Phys. Chem. B*, 2010, **114**, 6542–6548.
199 J. S. Spendelow and A. Wieckowski, *Phys. Chem. Chem. Phys.*, 2007, **9**, 2654–2675.
200 N. Ramaswamy and S. Mukerjee, *Adv. Phys. Chem.*, 2012, **2012**, 17.
201 Z. Yang, H. Nie, X. Chen, X. Chen and S. Huang, *J. Power Sources*, 2013, **236**, 238–249.
202 J. P. Paraknowitsch and A. Thomas, *Energy Environ. Sci.*, 2013, **6**, 2839–2855.
203 A. J. Bard and L. R. Faulkner, *Electrochemical methos: Fundamentals and Applications*, 2000, vol. 30.
204 A. J. Bard and L. R. Faulkner, *Electrochemical methods : fundamentals and applications*, Wiley, 2nd ed., 2001.
205 E. J. Biddinger, D. Von Deak, D. Singh, H. Marsh, B. Tan, D. S. Knapke and U. S. Ozkan, *J. Electrochem. Soc.*, 2011, **158**, B402.
206 D. Shin, B. Jeong, M. Choun, J. D. Ocon and J. Lee, *RSC Adv.*, 2015, **5**, 1571–1580.
207 S. S. Kocha, J. W. Zack, S. M. Alia, K. C. Neyerlin and B. S. Pivovar, *ECS Trans.*, 2012, **50**, 1475–1485.
208 F. Jaouen and J. P. Dodelet, *J. Phys. Chem. C*, 2009, **113**, 15422–15432.
209 J. M. Song, S. Y. Cha and W. M. Lee, *J. Power Sources*, 2001, **94**, 78–84.
210 D. G. Lee, O. Gwon, H. S. Park, S. H. Kim, J. Yang, S. K. Kwak, G. Kim and H. K. Song, *Angew. Chemie - Int. Ed.*, 2015, **54**, 15730–15733.
211 K. J. J. Mayrhofer, D. Strmcnik, B. B. Blizanac, V. Stamenkovic, M. Arenz and N. M. Markovic, *Electrochim. Acta*, 2008, **53**, 3181–3188.
212 U. a. Paulus, T. J. Schmidt, H. a. Gasteiger and R. J. Behm, *J. Electroanal. Chem.*, 2001, **495**, 134–145.
213 1–2.
214 C. S. Fadley and R. A. Wallace, *J. Electrochem. Soc.*, 1968, **115**, 1264–1270.
215 B. Britton and S. Holdcroft, *J. Electrochem. Soc.*, 2016, **163**, F353–F358.
216 T. P. Pandey, A. M. Maes, H. N. Sarode, B. D. Peters, S. Lavina, K. Vezzù, Y. Yang, S. D. Poynton, J. R. Varcoe, S. Seifert, M. W. Liberatore, V. Di Noto and A. M. Herring, *Phys. Chem. Chem. Phys. Phys. Chem. Chem. Phys*, 2015, **17**, 4367–4378.
217 M. Eikerling, A. A. Kornyshev, A. M. Kuznetsov, J. Ulstrup and S. Walbran, *J. Phys. Chem. B*, 2002, **105**, 3646–3662.
218 D. S. Su and G. Centi, *J. Energy Chem.*, 2013, **22**, 151–173.
219 S. H. Langer and H. P. Landi, *J Am Chem Soc*, 1986, **86**, 4694–4698.
220 F. Alcaide, P. L. Cabot and E. Brillas, *J. Power Sources*, 2006, **153**, 47–60.
221 A. C. A. de Vooys, G. L. Beltramo, B. Van Riet, J. A. R. van Veen and M. T. M. Koper, *Electrochim. Acta*, 2004, **49**, 1307–1314.
222 A. C. A. de Vooys, M. T. M. Koper, R. A. van Santen and J. A. R. van Veen, *J. Catal.*, 2001, **202**, 387–394.
223 B. G. Snider and D. C. Johnson, *Anal. Chim. Acta*, 1979, **105**, 9–23.
224 G. Wu, C. M. Johnston, N. H. Mack, K. Artyushkova, M. Ferrandon, M. Nelson, J. S. Lezama-Pacheco, S. D. Conradson, K. L. More, D. J. Myers and P. Zelenay, *J. Mater. Chem.*, 2011, **21**, 11392–11405.
225 R. Chen, H. Li, D. Chu and G. Wang, *J. Phys. Chem. C*, 2009, **113**, 20689–20697.

226 J. C. Vicker and D. Briggs, *ToF-SIMS: Materials Analysis by Mass Spectrometry*, IM Publications LLP, 2nd edn., 2013.
227 F. Zhang, S. Cheng, D. Pant, G. Van Bogaert and B. E. Logan, *Electrochem. commun.*, 2009, **11**, 2177–2179.
228 P. Vermeiren, R. Leysen, H. Beckers, J. P. Moreels and a. Claes, *J. Porous Mater.*, 2008, **15**, 259–264.
229 L. Roldán, S. Armenise, Y. Marco and E. García-Bordejé, *Phys. Chem. Chem. Phys.*, 2012, **14**, 3568–3575.
230 Z. Lin, G. Waller, Y. Liu, M. Liu and C. P. Wong, *Adv. Energy Mater.*, 2012, **2**, 884–888.
231 Y. Wang, D. C. Alsmeyer and R. L. McCreery, *Chem. Mater.*, 1990, **2**, 557–563.
232 S. Quillard, G. Louarn, S. Lefrant and A. G. Macdiarmid, *Phys. Rev. B*, 1994, **50**, 496–508.
233 M. Trchová, P. Matějka, J. Brodinová, A. Kalendová, J. Prokeš and J. Stejskal, *Polym. Degrad. Stab.*, 2006, **91**, 114–121.
234 M. Salavati-Niasari, M. Shakouri-Arani and F. Davar, *Microporous Mesoporous Mater.*, 2008, **116**, 77–85.
235 X. Wang, Q. Xiang, B. Liu, L. Wang, T. Luo, D. Chen and G. Shen, *Sci. Rep.*, 2013, **3**, 1–8.
236 A. E. Bocquet, T. Mizokawa, T. Saitoh, H. Namatame and A. Fujimori, *Phys. Rev. B*, 1992, **46**, 3771–3784.
237 T. Kahl, K.-W. Schröder, F. R. Lawrence, W. J. Marshall, H. Höke and R. Jäckh, in *Kirk-Othmer Encyclopedia of Chemical Technology*, Wiley Interscience, 5th edn., 2011.
238 H. Li, Q. Zhao, Y. Wan, W. Dai and M. Qiao, *J. Catal.*, 2006, **244**, 251–254.
239 S. Lee and Y. Chen, *J. Mol. Catal. A Chem.*, 2000, **152**, 213–223.
240 T. Niknam, M. Bornapour, A. Gheisari and B. Bahmani-Firouzi, *Int. J. Hydrogen Energy*, 2013, **38**, 1111–1127.
241 N. Daems, X. Sheng, Y. Alvarez-Gallego, I. F. J. Vankelecom and P. P. Pescarmona, *Green Chem.*, 2016, **18**, 1547–1559.
242 Y. P. Sun, W. L. Xu and K. Scott, *Electrochim. Acta*, 1993, **38**, 1753–1759.
243 J. Jiang, R. Zhai and X. Bao, *J. Alloys Compd.*, 2003, **354**, 248–258.
244 Y. Chen, L. Xiong, W. Wang, X. Zhang and H. Yu, *Front. Environ. Sci. Eng.*, 2015, **9**, 897–904.
245 A. R. Becker and L. A. Sternson, *Proc. Natl. Acad. Sci. U. S. A.*, 1981, **78**, 2003–2007.
246 G. Kokkinidis and K. Jüttner, *Electrochim. Acta*, 1981, **26**, 971–977.
247 D. Groskova, M. Stolcova and M. Hronec, *Catal. Letters*, 2000, **69**, 113–116.
248 X. Z. Yuan, Z. F. Ma, Q. Z. Jiang and W. S. Wu, *Electrochem. commun.*, 2001, **3**, 599–602.
249 S. Jayabal and R. Ramaraj, *Appl. Catal. A Gen.*, 2014, **470**, 369–375.
250 A. Cyr, P. Huot, J.-F. Marcoux, G. Belot, E. Laviron and J. Lessard, *Electrochim. Acta*, 1989, **34**, 439–445.
251 Q. Zhang, Y. Liu, S. Chen, X. Quan and H. Yu, *J. Hazard. Mater.*, 2014, **265**, 185–190.
252 Z. Y. Sun, Y. F. Zhao, Y. Xie, R. T. Tao, H. Y. Zhang, C. L. Huang and Z. M. Liu, *Green Chem.*, 2010, **12**, 1007–1011.
253 L. Z. Huang, H. C. B. Hansen and M. J. Bjerrum, *J. Hazard. Mater.*, 2016, **306**, 175–183.
254 Z. Chen, Z. Wang, D. Wu and L. Ma, *J. Hazard. Mater.*, 2011, **197**, 424–429.
255 J. Hoekstra, A. M. Beale, F. Soulimani, M. Versluijs-Helder, J. W. Geus and L. W. Jenneskens, *J. Phys. Chem. C*, 2015, **119**, 10653–10661.
256 F. Vallejos-Burgos, S. Utsumi, Y. Hattori, X. Garc??a, A. L. Gordon, H. Kanoh, K. Kaneko and L. R. Radovic, *Fuel*, 2012, **99**, 106–117.
257 K. T. Lee, X. Ji, M. Rault and L. F. Nazar, *Angew. Chemie - Int. Ed.*, 2009, **48**, 5661–5665.

258 a Moisala, a G. Nasibulin and E. I. Kauppinen, *J. Phys. - Condens. Matter*, 2003, **15**, S3011.
259 M. Liao and S. Scheiner, *Chem. Phys.*, 2001, **114**, 9780–9791.
260 M. S. Liao and S. Scheiner, *J. Chem. Phys.*, 2001, **114**, 9780–9791.
261 M. Mananghaya, *J. Chem. Sci.*, 2015, **127**, 751–759.
262 M. C. Biesinger, B. P. Payne, A. P. Grosvenor, L. W. M. Lau, A. R. Gerson and R. S. C. Smart, *Appl. Surf. Sci.*, 2011, **257**, 2717–2730.
263 L. Lozzi, S. Picozzi, S. Santucci, C. Cantalini and B. Delley, *J. Electron Spectros. Relat. Phenomena*, 2004, **137-140**, 101–105.
264 O. Akhavan, R. Azimirad, S. Safa and E. Hasani, *J. Mater. Chem.*, 2011, **21**, 9634.
265 A. D. S. Cells, S. Chang, M. Lu, Y. Tung and H. Tuan, *ACS Nano*, 2013, 9443–9451.
266 R. L. Arechederra, K. Artyushkova, P. Atanassov and S. D. Minteer, *ACS Appl. Mater. Interfaces*, 2010, **2**, 3295–3302.
267 P. Chen, F. Yang, A. Kostka and W. Xia, *ACS Catal.*, 2014, **4**, 1478–1486.
268 H. Peng, Z. Mo, S. Liao, H. Liang, L. Yang, F. Luo, H. Song, Y. Zhong and B. Zhang, *Sci. Rep.*, 2013, **3**, 1765.
269 M. Salavati-Niasari, *J. Mol. Catal. A Chem.*, 2009, **310**, 51–58.
270 W. R. P. Barros, R. M. Reis, R. S. Rocha and M. R. V Lanza, *Electrochim. Acta*, 2013, **104**, 12–18.
271 R. M. Reis, A. a G. F. Beati, R. S. Rocha, M. H. M. T. Assumpção, M. C. Santos, R. Bertazzoli and M. R. V Lanza, *Ind. Eng. Chem. Res.*, 2012, **51**, 649–654.
272 E. Brillas, F. Alcaide and P. L. Cabot, *Electrochim. Acta*, 2002, **48**, 331–340.
273 M. H. M. T. Assumpção, R. F. B. De Souza, D. C. Rascio, J. C. M. Silva, M. L. Calegaro, I. Gaubeur, T. R. L. C. Paixão, P. Hammer, M. R. V Lanza and M. C. Santos, *Carbon N. Y.*, 2011, **49**, 2842–2851.
274 Y. Sang, B. Wang, Q. Wang, G. Zhao and P. Guo, *Sci. Rep.*, 2014, **4**, 6321.
275 P. S. Fernández, M. E. Martins and G. a. Camara, *Electrochim. Acta*, 2012, **66**, 180–187.
276 L. Roquet, E. M. Belgsir, J.-M. Léger and C. Lamy, *Electrochim. Acta*, 1994, **39**, 2387–2394.
277 M. Simões, S. Baranton and C. Coutanceau, *Appl. Catal. B Environ.*, 2011, **110**, 40–49.
278 A. Zalineeva, A. Serov, M. Padilla, U. Martinez, K. Artyushkova, S. Baranton, C. Coutanceau and P. Atanassov, *J Am Chem Soc*, 2014, **136**, 3937–3945.
279 M. Simões, S. Baranton and C. Coutanceau, *ChemSusChem*, 2012, **5**, 2106–2124.
280 J. W. Larsen, M. Freund, K. Y. Kim, M. Sidovar and J. L. Stuart, *Carbon N. Y.*, 2000, **38**, 655–661.
281 A. Cyr, P. Huot, J. F. Marcoux, G. Belot, E. Laviron and J. Lessard, *Electrochim. Acta*, 1989, **34**, 439–445.
282 N. Daems, J. Wouters, K. Baert, C. Poleunis, A. Delcorte, A. Hubin, I. F. J. Vankelecom and P. P. Pescarmona, *submitted*.
283 C. M. Yang, C. Weidenthaler, B. Spliethoff, M. Mayanna and F. Schuth, *Chem. Mater.*, 2005, **17**, 355–358.
284 D. Yang, J. Park, D. Bhattacharjya, S. Inamdar and J. Yu, *J. Am. Chem. Soc.*, 2012, **134**, 16127–16130.
285 J. Duan, S. Chen, M. Jaroniec and S. Z. Qiao, *ACS Catal.*, 2015, **5**, 5207–5234.
286 K. Waki, R. A. Wong, H. S. Oktaviano, T. Fujio, T. Nagai, K. Kimoto and K. Yamada, *Energy Environ. Sci.*, 2014, **7**, 1950–1958.
287 X. Li, L. Fan, Z. Li, K. Wang, M. Zhong, J. Wei, D. Wu and H. Zhu, *Adv. Energy Mater.*, 2012, **2**, 425–429.
288 F. Niu, L.-M. Tao, Y.-C. Deng, Q.-H. Wang and W.-G. Song, *New J. Chem.*, 2014, **38**, 2269.
289 R. Li, Z. Wei, X. Gou and W. Xu, *RSC Adv.*, 2013, **3**, 9978–9984.
290 J. Liu, H. Liu, Y. Zhang, R. Li, G. Liang, M. Gauthier and X. Sun, *Carbon N. Y.*, 2011, **49**, 5014–5021.

291 H. H. Wang, H. H. Wang, Y. Chen, Y. Liu, J. Zhao, Q. Cai and X. Wang, *Appl. Surf. Sci.*, 2013, **273**, 302–309.
292 X. Kong, Q. Chen and Z. Sun, *ChemPhysChem*, 2013, **14**, 514–519.
293 The electrocatalyst cost was calculated based on the amount of chemicals that is necessary to obtain 1 g of NOMC and Cu-PANI-AC-A, respectively, and the price of the chemicals, which was acquired from the website of Sigma Aldrich on 27-10-2016.
294 B. Smitha, S. Sridhar and a. a. Khan, *J. Memb. Sci.*, 2005, **259**, 10–26.
295 C. H. Park, C. H. Lee, M. D. Guiver and Y. M. Lee, *Prog. Polym. Sci.*, 2011, **36**, 1443–1498.
296 E. F. Abdrashitov, V. C. Bokun, D. A. Kritskaya, E. A. Sanginov, A. N. Ponomarev and Y. A. Dobrovolsky, *Solid State Ionics*, 2013, **251**, 9–12.
297 A. I. Schäfer, A. G. Fane and T. D. Waite, *Nanofiltration: principles and applications*, Elsevier, Amsterdam, The Netherlands, 2004.
298 M. F. Rabuni, N. M. Nik Sulaiman, M. K. Aroua and N. A. Hashim, *Ind. Eng. Chem. Res.*, 2013, **52**, 15874–15882.
299 E. Idil Mouhoumed, A. Szymczyk, A. Schäfer, L. Paugam and Y. H. La, *J. Memb. Sci.*, 2014, **461**, 130–138.
300 R. Zimmermann, S. Dukhin and C. Werner, *J. Phys. Chem. B*, 2001, **105**, 8544–8549.
301 D. Breite, M. Went, A. Prager and A. Schulze, *Polymers (Basel).*, 2015, **7**, 2017–2030.
302 J. J. Shyue, M. R. De Guire, T. Nakanishi, Y. Masuda, K. Koumoto and C. N. Sukenik, *Langmuir*, 2004, **20**, 8693–8698.
303 E. F. Abdrashitov, V. C. Bokun, D. A. Kritskaya, E. A. Sanginov, A. N. Ponomarev and Y. A. Dobrovol'Skii, *Russ. J. Electrochem.*, 2011, **47**, 387–394.
304 X. Zhao, L. Song, J. Fu, P. Tang and F. Liu, *Surf. Sci.*, 2011, **605**, 1005–1015.
305 Y. Shen, X. Qiu, J. Shen, J. Xi and W. Zhu, *J. Power Sources*, 2006, **161**, 54–60.
306 P. Choi, N. H. Jalani and R. Datta, *J. Electrochem. Soc.*, 2005, **152**, A1548.
307 J. Luo and Y. Wan, *J. Memb. Sci.*, 2013, **438**, 18–28.
308 M. Mulder, *Basic Principles of Membrane Technology*, Kluwer Academic Publishers, Dordrecht, second ed., 1996.
309 P. Vandezande, L. E. M. Gevers and I. F. J. Vankelecom, *Chem. Soc. Rev.*, 2008, **37**, 365–405.
310 K. P. Lee, J. Zheng, G. Bargeman, A. J. B. Kemperman and N. E. Benes, *J. Memb. Sci.*, 2015, **478**, 75–84.
311 M. Dalwani, G. Bargeman, S. S. Hosseiny, M. Boerrigter, M. Wessling and N. E. Benes, *J. Memb. Sci.*, 2011, **381**, 81–89.
312 M. M. Pendergast and E. M. V. Hoek, *Energy Environ. Sci.*, 2011, **4**, 1946.
313 A. W. Mohammad, Y. H. Teow, W. L. Ang, Y. T. Chung, D. L. Oatley-Radcliffe and N. Hilal, *Desalination*, 2015, **356**, 226–254.
314 M. Dalwani, N. E. Benes, G. Bargeman, D. Stamatialis and M. Wessling, *J. Memb. Sci.*, 2010, **363**, 188–194.
315 S. Platt, M. Nyström, A. Bottino and G. Capannelli, *J. Memb. Sci.*, 2004, **239**, 91–103.
316 T. J. K. Visser, S. J. Modise, H. M. Krieg and K. Keizer, *Desalination*, 2001, **140**, 79–86.
317 M. Nyström, L. Kaipia and S. Luque, *J. Memb. Sci.*, 1995, **98**, 249–262.
318 G. Trägardh and D. Johansson, *Desalination*, 1998, **119**, 21–29.
319 G. Gésan-Guiziou, N. Alvarez, D. Jacob and G. Daufin, *Sep. Purif. Technol.*, 2007, **54**, 329–339.
320 E. Arkhangelsky, D. Kuzmenko and V. Gitis, *J. Memb. Sci.*, 2007, **305**, 176–184.
321 K. Boussu, B. Van der Bruggen, A. Volodin, C. Van Haesendonck, J. A. Delcour, P. Van der Meeren and C. Vandecasteele, *Desalination*, 2006, **191**, 245–253.
322 V. Freger, A. Bottino, G. Capannelli, M. Perry, V. Gitis and S. Belfer, *J. Memb. Sci.*, 2005, **256**, 134–142.
323 S. Munari, A. Bottino, G. C. Roda and G. Capannelli, *Desalination*, 1990, **77**, 85–100.
324 M. Khayet, C. Y. Feng, K. C. Khulbe and T. Matsuura, *Polymer (Guildf).*, 2002, **43**, 3879–3890.

325 S. Munari, A. Bottino and G. Capannelli, *J. Memb. Sci.*, 1983, 16, 181–193.
326 A. K. Holda and I. F. J. Vankelecom, *J. Appl. Polym. Sci.*, 2015, **132**, 1–17.
327 A. Cano-Odena, M. Spilliers, T. Dedroog, K. De Grave, J. Ramon and I. F. J. Vankelecom, *J. Memb. Sci.*, 2011, **366**, 25–32.
328 P. Vandezande, X. Li, L. E. M. Gevers and I. F. J. Vankelecom, *J. Memb. Sci.*, 2009, **330**, 307–318.
329 T. Uragami, M. Fujimoto and M. Sugihara, *Polymer (Guildf).*, 1980, **21**, 1047–1051.
330 N. Durand, B. Ameduri, K. Takashima, K. Ishida, S. Horie and Y. Ueda, *Polym. J.*, 2011, **43**, 171–179.
331 J. Jang and K. Lee, *Chem. Commun. (Camb).*, 2002, 1098–1099.
332 J. Qiu, J. Zhang, J. Chen, J. Peng, L. Xu, M. Zhai, J. Li and G. Wei, *J. Memb. Sci.*, 2009, **334**, 9–15.
333 P. Graham, *Organic Chemistry*, Taylor & Francis, Boston, 2nd editio., 2004.
334 Y. L. Lei, Y. J. Luo, F. Chen and L. H. Mei, *Polymers (Basel).*, 2014, **6**, 1914–1928.
335 H. L. Lin, T. L. Yu and F. H. Han, *J. Polym. Res.*, 2006, **13**, 379–385.

Appendix 1

A RDE study of electrocatalysts for the cogeneration of hydroxylamine and electricity in a fuel cell

Abstract

In an attempt to move to the industrially more relevant conditions (100% NO feed) and to speed-up the electrocatalyst screening for the reduction of NO to hydroxylamine in a fuel cell setup, a setup with four operating rotating disk electrodes was constructed at the Vrije Universiteit Brussel. In this chapter, the successes and setbacks of this setup are discussed. In the end, these experiments were stopped as a consequence of a too high level of noise on the measurements. The attempts to adapt the electrodes in order to resolve this issue are described in this chapter.

Author contribution

Electrocatalysts preparation and writing of the chapter was done by N. Daems. Electrochemical tests were performed at the Vrije Universiteit Brussel by N. Daems in close collaboration with P. Steegstra. Adaptations to the setup were performed by M. Depauw. Valuable discussions were held with P. Steegstra and A. Hubin. Editing of the work and the supervision was done by A. Hubin.

Within the same context of increasing energy demands and raw material depletion and bearing in mind the promising results that were obtained in the chapter 4, the possibility to reduce nitrogen monoxide in a fuel cell was further investigated in this chapter. In the future this cogeneration approach might pose a solution to both problematics since it allows the simultaneous generation of electricity and industrially valuable chemicals, in this case with hydroxylamine as target product [15,241]. Industrially, hydroxylamine is commonly applied in the synthesis of carprolactam, which in turn is mainly applied in the production of nylon 6 [13–17]. The cogeneration of hydroxylamine and electricity in a H_2-NO fuel cell was first studied by Langer *et al.* [19] and has been further investigated since then [13–15,17]. The electrochemical cell is typically composed of two compartments, an anodic and a cathodic section, which are separated by an electrolyte (most commonly a proton-exchange membrane). Nitrogen monoxide is reduced at the cathode and hydrogen is oxidised at the anode. The overall reactions are:

Anode:

$$H_2 \longrightarrow 2H^+ + 2e^- \quad E° = 0\ V \qquad (A1.1)$$

Cathode:

$$2NO + 2H^+ + 2e^- \longrightarrow N_2O + H_2 \quad E° = 1.59\ V \qquad (A1.2)$$

$$2NO + 4H^+ + 4e^- \longrightarrow N_2 + 2H_2O \quad E° = 1.68\ V \qquad (A1.3)$$

$$NO + 3H^+ + 3e^- \longrightarrow NH_2OH \quad E° = 0.38\ V \qquad (A1.4)$$

$$NO + 5H^+ + 5e^- \longrightarrow NH_3 + H_2O \quad E° = 0.73\ V \qquad (A1.5)$$

While this process has already been investigated previously, further research to improve its efficiency is still necessary before this approach can become economically viable and one prime factor that needs further study and improvement is the electrocatalyst. As was shown in the chapter 4, the proposed electrocatalysts (iron-containing N-doped carbons) have some promising features (straightforward, up-scalable and tunable synthesis method based on cheap precursors, high stability, decent current generation) but there is still room for improvement in terms of hydroxylamine yield and current efficiencies. Based on the results mentioned in previous chapters, two types of electrocatalysts will be investigated as electrocatalysts for the nitrogen monoxide reduction reaction: (1) non-noble metals supported on N-containing carbons and (2) non-noble metals coordinated to N-doped ordered mesoporous carbons. The synthesis method of the former was already detailed in chapter 4, but several aspects were modified (e.g. metal specie, pyrolysis temperature, extent of acid treatment, aniline to activated carbon ratio). Only one electrocatalyst of the second set (Fe-NOMC) was investigated for this purpose and it was synthesised with the nanocasting method that is mentioned in chapter 2, with as only difference that the surface of SBA-15 was covered with iron-phthalocyanine instead of aniline.

In an attempt to discover a more efficient electrocatalyst to cogenerate hydroxylamine and electricity in a H_2-NO fuel cell in a fast and efficient way, a unique setup (figure A1.1), which was previously designed and constructed at the Vrije Universiteit Brussel (VUB) as part of an SBO project (OCPEC, contract number 090027), was used for this purpose. With this setup four different electrocatalysts could be tested simultaneously in a controlled environment. The electrocatalytic performance in the NO reduction reaction was evaluated by means of rotating disk electrode (RDE) linear sweep voltammetry (LSV). The measurements were conducted at various rotation speeds (300-2500 rpm). The experiments were carried out at 25°C, using a thermostatic bath, in the three-electrode cells, depicted in figure A1.1, with rotating-disk electrodes, constructed in house and connected to a Biologic VMP3 Potentiostat. Pt wire counter electrodes were used in combination with an Ag/AgCl (3M KCl)

reference electrode. A glassy carbon RDE disk (with a diameter of 6 mm) was utilised as an inert carrier for the investigated electrocatalysts. Catalyst ink solutions were prepared by suspending 3 mg of ground electrocatalyst powder in 1.3 ml isopropanol and 0.15 ml of a 5 wt% Nafion® suspension from Sigma Aldrich. After sonication for 1 h, 5 µl of the catalyst ink was deposited onto the mirror-polished glassy carbon surface, yielding an approximate electrocatalyst loading of 37 µg cm^{-2}. The first experiments were performed under neutral conditions using an aqueous phosphate buffer of pH seven saturated with NO. The NO saturation was achieved by bubbling the solution with pure NO gas for 45 min, after which a NO blanket was maintained above the solution during the whole time of the LSV measurement. The potential was varied from 0.3 to -1.4 V vs. Ag/AgCl at a potential sweep rate of 10 mV s^{-1}.

Figure A1.1: Half-cell setup with four separate units at the VUB used to investigate electrocatalytic performance in the NO reduction reaction.

The electrocatalysts are ranked based on a set of three parameters, the onset potential, the kinetic current density and the number of exchanged electrons. The onset potential, or that potential where the NO reduction reaction is initiated, was determined as that potential where the slope of the LSV plot exceeded 0.1 mA cm^{-2} V^{-1}. The Koutécky-Levich equations (Eqs. (A1.1)-(A1.3)) were used to determine the kinetic current density and the electron transfer number.

$$\frac{1}{J} = \frac{1}{J_K} + \frac{1}{J_D} = \frac{1}{J_K} + \frac{1}{B\omega^{1/2}} \qquad \text{Eq. (A1.1)}$$

where J is the recorded current density, which can be divided in the kinetic current density (J_K) and the diffusion-limited current density (J_D), and ω is the angular velocity of the rotating ring disk electrode. In this case, the current densities were calculated with respect to the geometrical surface area of the glassy carbon disk since the real surface area could not be determined as a consequence of the complex nature of the electrocatalysts. B and J_K are determined by Eqs. (2) and (3):

$$B = 0.62nFC_0(D_0)^{2/3}v^{-1/6} \qquad \text{Eq. (A1.2)}$$

$$J_K = nFkC_0 \qquad \text{Eq. (A1.3)}$$

where *n* is the number of exchanged electrons, F is the Faraday constant, *k* is the electron transfer rate constant, C_0 is the bulk concentration of nitrogen monoxide (1.76 x 10^{-9} mol cm^{-3}), v is the kinematic viscosity of the electrolyte (0.0102 cm^2s^{-1}) and D_0 is the diffusion coefficient (2.9 x 10^{-5} cm^2s^{-1}) . The number of exchanged electrons, is a factor for the selectivity of the electrocatalyst, the closer it is to 3, the more selectively hydroxylamine will be produced. *n* can be determined from the slope of the K-L plots. The kinetic current density, which is another factor for the activity, can be determined from the intercept.

At first some promising results were obtained with several electrocatalysts (*n* close to three). The most promising material was Fe-NOMC, which had an onset potential of 0.09 V, a kinetic current density of -9.3 mA cm^{-2} and an electron transfer number of 3.0 or a 100% selectivity towards the target product, hydroxylamine. To evaluate the reproducibility of this first tests, two different inks were tested several times over the course of time, giving a wide range of results (see figure A1.2, (A to H)).

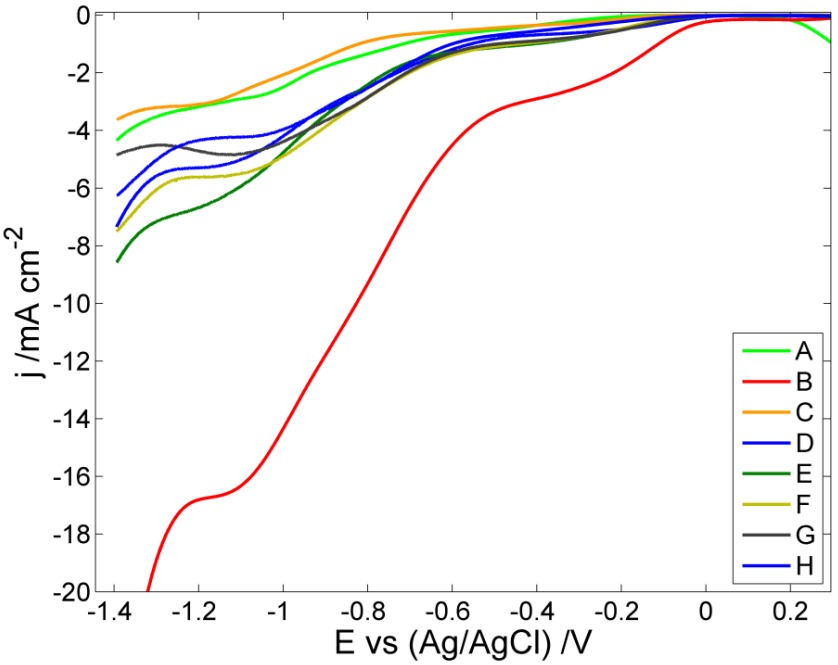

Figure A1.2: LSV plots of different measurements of Fe-NOMC with two different inks over the course of time (first ink: A to D and second ink: E to H).

While something might have gone wrong (contamination on GC disk) in measurement B (too large of a difference), the other measurements still lay too far apart to draw a good conclusion. This can also be seen in the relatively large standard deviations on the mean values for the different parameters, 0.05 ± 0.05 V for the onset potential, -6.5 ± 2.1 mA cm^{-2} for the kinetic current density and 3.6 ± 1.7 for the electron transfer number. Possible explanations for this large standard deviations are the instability of the electrocatalyst ink or the electrocatalyst itself in the ink or inhomogeneous composition of the electrocatalyst. The latter could be discarded based on the reproducible results that could be obtained utilising these electrocatalysts in the oxygen reduction reaction. Unfortunately, the lack of reproducability was only observed after a relatively large amount of experiments. In order to overcome this problem, it was planned to perform four simultaneous tests of the same electrocatalytic ink at the same time, with a freshly prepared ink. At the same time and because of the promising results, it was also decided to pass to an acidic testing environment (0.5 M H_2SO_4). This type of environment was chosen since the most easily

available and most advanced fuel cell system is the proton-exchange membrane fuel cell, which uses an acidic electrolyte (most commonly Nafion®). Another advantage of the acidic environment lies in the reaction of the as-synthesised hydroxylamine with sulphuric acid to give the more stable and easier to handle hydroxylamine sulphate salt. This transformation is advantageous since the free hydroxylamine decomposes violently at elevated temperatures (> 50°C) [15].

Unfortunately, once these experiments in an acidic electrolyte started, a new problem occurred, as there was too much noise on the LSV measurements to allow correct analysis of the data and accurately determine the values for the onset potential, the kinetic current density and the number of exchanged electrons. Several attempts were made to determine the origin of the noise and to try and solve it. First, on opening the RDE's and connecting them to a multimiter, it was discovered that the contact between the carbon brushes, connected with the potentiostat, and the rotating rod, connected with the electrode tip, was not good enough. The resistance varied between mΩ and Ω upon rotation. It was attempted to solve this problem by placing the brushes closer to the rotator, by making them more concave and ultimately by using two brushes one on each side of the rotator. While all of these attempts seemed to work initially (low resistance even upon rotation), after several CVs the noise kept coming back. After cleaning the insides of the RDE and running them again for a certain time, it was discovered that an oily substance was leaking down from the engines, creating a resistance between brush and rod. It could thus be concluded that the engines of the RDEs were destroyed and the RDEs could thus no longer be used. The main cause for the malfunctioning of the engines is the production of the aggressive HNO_3. In the presence of oxygen NO is easily transformed to NO_2, which further transforms to HNO_3 with water. Most likely, the engines are not completely closed off from the NO in the cells and thus HNO_3 can be produced here. The fact that the problem only started occurring when an acidic electrolyte was utilised might be a mere coincidence since sulphuric acid has a low vapor pressure and will therefore not reach the engines easily. The engines were thus gradually affected by HNO_3 until the point that they started leaking and caused the noise on the measurements. A solution to this problem, would be to flow N_2 through the electrode housing, to avoid contact between NO and oxygen. However, in the light of the limited amount of remaining time and since new engines had to be ordered and placed into the RDEs, it was decided to stop the NO reduction experiments.

In conclusion, despite the availability of a setup that allows the simultaneous testing of four electrocatalysts at the same time for the NO reduction reaction and the promising, preliminary results, it was not possible to determine a more efficient electrocatalyst, which could possibly have led to the commercialisation of the electrochemical hydroxylamine production process. Two problems lay at the origin of this failure: a first one related to the ink stability and a second one related to the negative impact of HNO_3 on the RDE engine lifetime.